

Quantum Gates for Superconducting Qubits

A Dissertation
Presented to the Faculty of the Graduate School
of
Yale University
in Candidacy for the Degree of
Doctor of Philosophy

by
Chad Tyler Rigetti

Dissertation Director: Professor Michel Devoret

May 2009

Abstract

Quantum Gates for Superconducting Qubits

Chad Tyler Rigetti

2009

Josephson junction-based devices offer the potential to process information with the electromagnetic modes of an engineered quantum circuit. Doing so requires the subtle application of control signals to induce arbitrary transformations of the associated Hilbert space – or quantum gates – without causing the system to decohere. But there are strict constraints on the dynamical control we can exert over the circuit Hamiltonian, and given a practical set of controls, it is in general difficult to extract a particular desired transformation. Of the possible strategies to address this quantum gate problem, those requiring the fewest control parameters, the least relative control bandwidth, and the minimal number of non-linear circuit elements are particularly interesting, as they would reduce experimental complexity and minimize unwanted interactions with degrees of freedom in the environment.

We show how microwave signals and fixed weak linear coupling elements can be used to effectively switch on and off an interaction and tune its strength and direction in the on state, and we derive specific irradiation protocols that use these interactions to implement universal two-qubit gates.

These results emerge from Fourier analysis of the circuit Hamiltonian in a particular multiply-rotating reference frame. We develop and formalize this approach, then apply it to two- and three-qubit systems. In the two-qubit case, the theory succinctly reproduces many earlier results, and reveals new methods of entangling pairs of superconducting quantum bits. For example, a static weak linear coupling reactance can give rise to an effective interaction that turns on linearly with the drive ampli-

tude when one qubit is simply irradiated at the transition frequency of the other. In the three-qubit case, it describes how a very weak off-diagonal three-body coupling Hamiltonian can be exploited to controllably and directly produce pure tripartite entanglement, even when the qubits are far detuned from one another.

We describe efforts to experimentally observe some of these effects in two-qubit systems. The results provide preliminary evidence for the microwave-tuned interaction of qubits with fixed linear couplings.

Copyright © 2009 by Chad Tyler Rigetti

All rights reserved.

Contents

Acknowledgements	i
Notation	ii
List of symbols and abbreviations	iv
1 Introduction	1
1.1 Overview	1
1.2 Quantum computation	7
1.3 Superconducting quantum circuits	11
1.3.1 The Josephson junction	11
1.3.2 Charge Qubits	14
1.3.3 Flux Qubits	15
1.3.4 Phase Qubits	16
1.3.5 The Quantronium	16
1.4 Coupling Schemes	19
1.4.1 Fixed linear coupling, DC controlled qubits	22
1.4.2 DC controlled coupling, fixed qubits	22
1.4.3 Fixed linear coupling, RF controlled qubits	23
1.4.4 RF controlled coupling, fixed qubits	24

1.4.5	Quantum bus	25
1.5	Summary of key results	25
1.5.1	The discrete Hilbert space \mathfrak{H}_n	25
1.5.2	Visual representation of two-qubit gates	27
1.5.3	Continuous two-qubit dynamics	29
1.5.4	Two-qubit gates at optimal bias point	31
1.5.5	Fourier approach to quantum gates	37
1.5.6	GHZ state production	40
1.5.7	Circuit design and fabrication	42
1.5.8	Experimental results	44
1.6	Conclusion	46
2	Two-Qubit Toolkit	49
2.1	Introduction	49
2.2	Discrete Hilbert space	49
2.2.1	Discretization based on stabilizer theory	54
2.2.2	The generalized $\pi/2$ rotations generate the n -qubit Clifford group	70
2.2.3	Sample application of digital quantum information: Gottesman tables and synonyms for CNOT	74
2.2.4	Conclusion	76
2.3	Generalized Bloch equations	77
2.3.1	One-qubit dynamics: Bloch equations	79
2.3.2	General two-qubit dynamics	81
2.3.3	Graphical representation of the dynamical equations	84
2.3.4	n -qubit dynamics	85
2.3.5	Lindblad form	88

2.3.6	Conclusion	90
2.4	Visual representation of two-qubit states	91
2.4.1	Bloch sphere revisited	91
2.4.2	Two-qubit representation	93
2.4.3	Applications of the two-qubit representation: illustration of CNOT gate	97
2.5	Conclusion	100
3	Two-Qubit Gates at Optimal Bias Point	101
3.1	Introduction	101
3.2	The FLICFORQ system	101
3.3	Entanglement by double-resonant irradiation	104
3.4	Gate fidelity under double-resonant irradiation	113
3.4.1	Errors in one-qubit rotations due to fixed coupling	113
3.4.2	Leakage due to strong driving	114
3.4.3	The rotating wave approximation	114
3.4.4	Other sources of error	116
3.4.5	Entanglement modulation depth and bandwidth	117
3.5	Other protocols for gates at optimal bias	118
3.5.1	Generalization to off-resonant drive	118
3.5.2	Driven non-linear coupling	120
3.6	Limitations	122
4	Fourier Approach to The Quantum Gate Problem	124
4.1	Fourier Analysis of the Transformed Hamiltonian	126
4.1.1	Multiply-rotating references frames	126
4.1.2	The coupling matrix	132

4.1.3	Fourier analysis	133
4.1.4	Extraction of the effective Hamiltonian	135
5	Application of Fourier Approach	137
5.1	Two-Qubit Gates	137
5.1.1	Generalized FLICFORQ Protocols	137
5.1.2	Protocols involving DC control of transition frequencies	155
5.1.3	Protocols involving AC control of transition frequencies	156
5.1.4	Protocols involving harmonic variation of the coupling	157
5.2	Three-Qubit Gates	158
5.2.1	GHZ state production with DC control	160
5.2.2	GHZ state production with AC control	165
6	Device fabrication	170
6.1	Overview	170
6.2	Standard fabrication techniques	171
6.2.1	Typical device fabrication by e-beam lithography and shadow mask evaporation	171
6.2.2	Bridge/ledge hybrid	174
7	Experiments	177
7.1	Introduction	177
7.1.1	Previous Measurements	177
7.1.2	Aims	184
7.2	Experiment design	185
7.2.1	Measurement setup	185
7.3	Measurement Results	188

7.3.1	Qubit Readout	188
7.3.2	Qubit Control	191
7.3.3	Qubit–qubit Coupling	194
8	Conclusion	198
8.1	Conclusions	198
8.2	Future work	200
8.2.1	Gate strategies for cQED with flux bias lines	200
8.2.2	Active cancellation of fixed coupling	201
8.2.3	Architectures for direct multi-qubit gates	202
8.2.4	Quantum gates in a dynamically decoupled subspace	203
A	The Quantronium qubit	204
A.1	Cooper pair box (CPB)	204
A.1.1	Phase basis	205
A.2	Split Cooper pair box (sCPB)	207
A.3	Energy Surfaces of the sCPB	208
B	Mathematica code	210
B.1	The n-qubit Pauli matrices	210
B.2	The n-qubit super-operator	211
C	A wideband IQ modulator for microwave pulse generation	213

List of Figures

1.1	Quantum logic circuits and gates	10
1.2	The Josephson junction.	13
1.3	Three main types of superconducting qubit and their potential energy landscapes.	17
1.4	Artificial atom "quantronium" qubit circuit.	18
1.5	Coupling schemes for superconducting qubits.	20
1.6	Taxonomy of proposals to couple superconducting qubits.	21
1.7	Graph of the set \mathcal{S}_2 of two-qubit generalized Pauli matrices and their geometric relation to one another.	28
1.8	Representation of a two-qubit state in three real dimensions.	30
1.9	Superconducting two-qubit circuits for performing universal quantum gates at optimal bias point with linear fixed couplings.	32
1.10	Dressed state picture of double-resonant irradiation and Rabi sideband resonance.	34
1.11	Effective interaction strength generated by cross-resonance irradiation.	36
1.12	Superconducting circuit implementing coupled quantronia in coplanar stripline (CPS) geometry	44
1.13	High raw visibility readout of coplanar stripline quantronium circuit.	45

1.14	Simultaneous independent control and readout of two coupled superconducting qubits.	46
1.15	Rabi beating of two superconducting qubits subject to cross-resonance irradiation.	47
2.1	Graph of the set \mathcal{S}_2 of two-qubit generalized Pauli matrices and their geometric relation to one another.	66
2.2	Graphical representation of continuous one-qubit dynamics.	85
2.3	Graphical representation of continuous two-qubit dynamics.	86
2.4	Representation of a two-qubit state in three real dimensions.	96
2.5	Use of the real space representation to identify local measurements that will reveal the maximal Bell inequality violation for arbitrary entangled states.	98
2.6	Real space illustration of CNOT gate and its "phase kickback."	99
3.1	Superconducting two-qubit circuits for performing universal quantum gates at optimal bias point with linear fixed couplings.	104
3.2	Dressed state picture of double-resonant irradiation and Rabi sideband resonance.	105
3.3	Explicit control sequence to implement universal two-qubit gate with FLICFORQ.	112
3.4	Leakage probability for charge qubits under strong resonant driving as a function of E_J/E_{CP} .	115
3.5	Sidebands of the doubly driven two-qubit system generalized to off-resonant microwave signals.	119
3.6	Schematic circuits for implementing two-qubit gates at optimal bias with parametric driving of a non-linear coupling subcircuit.	121

4.1	Illustration of the transformations to null out the driven local qubit dynamics.	127
5.1	Cross-resonance effect in the dressed state picture.	144
5.2	Effective interaction strength generated by cross-resonance irradiation.	146
5.3	Verification of Fourier approach results for cross-resonance effect through numerical simulations of master equation in the lab frame.	148
5.4	Intrinsic crosstalk in practical superconducting quantum circuits.	151
5.5	Effective coupling strength under cross resonance in presence of microwave control signal crosstalk.	153
5.6	Equivalent circuit diagrams for three-qubit FLICFORQ systems.	160
5.7	Generation of entangled three-qubit states by DC tuning to $\omega_1 = \omega_2 = \omega_3$	164
5.8	Generation of maximally entangled three-qubit states by exploiting a weak three-body coupling term with DC control in far-detuned qubits.	166
5.9	Generation of maximally entangled three-qubit states by exploiting a weak three-body coupling term with microwave control in far-detuned qubits.	169
6.1	Optical image of a shadow mask for a coupled qubit device.	173
6.2	Double angle evaporation using a bridge/ledge hybrid shadow mask.	175
7.1	Non-linear resonance curves in a driven Josephson oscillator.	179
7.2	Schematic of a JBA coupled to a quantronium qubit.	180
7.3	Superconducting circuit implementing coupled quantronia in coplanar stripline (CPS) geometry	184
7.4	Cryogenic microwave measurement setup for two-qubit experiments.	186

7.5	Characteristic phase diagram for CPS resonator implementation of the JBA/CBA.	189
7.6	High raw visibility readout of coplanar stripline quantronium circuit.	191
7.7	Gate and flux modulations of a quantronium with CPS readout resonator.	192
7.8	Pulse protocol for Rabi oscillations experiment.	193
7.9	Simultaneous independent control and readout of two coupled superconducting qubits.	194
7.10	Rabi beating of two superconducting qubits subject to cross-resonance irradiation.	196
7.11	Observed effective coupling strength under cross-resonance vs. drive signal amplitude.	197
A.1	Energy levels of the Cooper pair box.	206
A.2	Energy surfaces of the two lowest-lying states of the split Cooper pair box.	209
C.1	Schematic black box modulator.	214

Acknowledgements

Foremost I would like to thank my advisor Michel for his continued and extraordinary encouragement and support throughout this work. I have learned a great deal about physics and the art of doing research from him. I wish I could have absorbed more. I would like to thank all the members of our group, past and present, especially my compatriot graduate students Vijay, Mike and Vlad. I would like to thank my committee members Dan, Rob and Steve for taking time to oversee the work, and also Dan for his support and guidance since before my day one at Yale. I would like to thank Alexandre for some essential lessons towards my humble aspirations as a theorist.

This would not have been possible without the support and enduring love of my parents Milt and Nola, brother Rob and sister Sara, my grandparents Goldie and Alfred, and the rest of my wonderful family. The friends and loved ones I have met here and along the way have been more important to me and to the completion of this work than I can explain. Thank you. I hope I can someday return all the kindness and support you have given me.

Notation

We make extensive use of the Pauli spin 1/2 operators, and through the different sections we use the following naming conventions,

$$\begin{aligned}\sigma_w &= W = \begin{bmatrix} 1 & 0 \\ 0 & 1 \end{bmatrix}, & \sigma_x &= X = \begin{bmatrix} 0 & 1 \\ 1 & 0 \end{bmatrix} \\ \sigma_y &= Y = \begin{bmatrix} 0 & -i \\ i & 0 \end{bmatrix}, & \sigma_z &= Z = \begin{bmatrix} 1 & 0 \\ 0 & -1 \end{bmatrix}.\end{aligned}$$

Multi-qubit operators are written with an implied tensor product, i.e. $\sigma_a \otimes \sigma_b = \sigma_a \sigma_b = AB$. For clarity and bookkeeping, we on occasion append a numerical subscript to disambiguate the system on which the particular operator acts, and in this case the alphabetical tag will appear instead as a superscript. In a three-qubit system, for example, two-body coupling terms can include all pairs, so we will write e.g. $\sigma_1^x \sigma_2^x$ as distinct from $\sigma_2^x \sigma_3^x$.

It is helpful to identify each Pauli operator acting on a particular Hilbert space with a unique tag, and in that case we will on occasion opt for the following alternative to the obvious but verbose string $\sigma_a \sigma_b \cdots \sigma_k = AB \cdots K$. We assign the Pauli matrices a number according to

$$\sigma_w = \sigma_0, \sigma_z = \sigma_1, \sigma_x = \sigma_2, \sigma_y = \sigma_3,$$

then concatenate the numerical strings in base two and reading off the result in base ten. e.g. $\sigma_y\sigma_z=\sigma_3\sigma_1=\sigma_{11}\sigma_{01}=\Sigma_{1101}^{(2)}=\Sigma_{13}^{(2)}$. This makes it easier to carry out calculations involving the many Pauli operators in large systems. We will make extensive use of it in Chapter Two and Chapter Four but otherwise stick to the lower case σ 's.

We define the charging energy E_C and the dimensionless charge N_g in units of $2e$, i.e. $E_C = \frac{(2e)^2}{2C_\Sigma}$ and $N_g = \frac{C_g V_g}{2e}$.

List of symbols and abbreviations

C_g	Gate capacitance
C_J	Josephson capacitance
C_Σ	Total capacitance of an island
E_C	Cooper pair charging energy
E_J	Josephson energy
\mathcal{F}	Symbolic Fourier transform
FLICFORQ	Fixed linear couplings between fixed off-resonant qubits
\mathcal{G}	Fourier-space non-local Hamiltonian as a matrix of Pauli coefficients
\mathcal{H}	Hamiltonian
\mathcal{H}^{eff}	Effective Hamiltonian
\mathfrak{H}_n	Discrete Hilbert space of n qubits
I_o	Josephson junction critical current
L_J	Josephson inductance
CPB	Cooper pair box
$sCPB$	Split Cooper pair box
\mathcal{M}	Non-local Hamiltonian as a matrix of Pauli coefficients
CNOT	Controlled-NOT quantum logic gate

φ_o	Reduced flux quantum = $\phi_o/2\pi$
ϕ_o	Flux quantum $h/2e$
ρ	Density operator
JBA	Josephson Bifurcation Amplifier
CBA	Cavity Bifurcation Amplifier
QFH	Quad frame Hamiltonian
$ \psi_k\rangle$	Energy eigenstate
$ \psi_N\rangle$	Charge eigenstate
$ \psi_\theta\rangle$	Phase eigenstate
$ 0\rangle$	Quantum logic ‘0’ state
$ 1\rangle$	Quantum logic ‘1’ state
\mathcal{L}	Lindblad operator
\mathbf{g}	Entanglement vector
Ω	Drive signal amplitude, Rabi frequency
η	Generalized Rabi frequency
QED	Quantum electrodynamics
σ_{\pm}	Qubit excitation creation and annihilation operators
$\sigma_{w,x,y,z}$	Pauli spin- $\frac{1}{2}$ operators
ω_p	Plasma frequency
ω_{xx}	Qubit–qubit coupling strength along $\sigma_x\sigma_x$
ω_{xxx}	Three-qubit coupling strength along $\sigma_x\sigma_x\sigma_x$
ω_j	Qubit j transition frequency

Δ	Qubit–qubit detuning
δ	Qubit–signal detuning
ϕ	Drive signal phase
ω_{rf}	Drive signal frequency
Σ	Generalized Pauli multi-spin- $\frac{1}{2}$ operators

Chapter 1

Introduction

1.1 Overview

The discovery of quantum algorithms capable of solving certain problems exponentially faster than their classical counterparts—and of methods to inoculate quantum systems against noise and decoherence—has engendered a broad effort to build a useful quantum computer[1, 2, 3, 5, 6, 7, 8, 9, 10, 11, 12]. Though such a device is likely yet a generation away, small prototype systems of a handful of quantum bits offer the potential for pioneering studies of strange phenomena such as parallelism and entanglement that emerge from quantum theory. These fragile effects, destroyed by interaction with the classical macroscopic world, would form the green heart of a functional quantum computer, yet little is known about them in systems with more than a few degrees of freedom.

But even small scale quantum information processors push the limits of present technologies. They require a delicate quantum island in a tide of noise and macroscopic control signals. Countless designs, originating from nearly every field of lab-based experimental physics, have been put forth. Indeed, most any quantum mechan-

ical system has the basic attributes. The challenge comes primarily in coupling to them the external signals used for state manipulation and readout without degrading too much the valued quantum behavior.

Most of the proposed technologies, such as those based on nuclear or electron spins [14, 15, 16, 17], trapped ions [18, 19], and neutral atoms [20] among many others, are based on microscopic and *a priori* quantum mechanical systems. There, the information-storing physical degrees of freedom have tiny electromagnetic cross-sections that allow them to remain isolated from the environment. Though it makes them hard to manipulate, this has the benefit of only modestly endangering their quantum behavior. Implementations of this style are usually characterized by long coherence times but also long gate times, and the highly specialized equipment and techniques needed to interface with them make scaling a major challenge.

The contrasting approach is to represent quantum information with physical degrees of freedom which are typically classical, but may be coaxed into quantum behavior under suitable conditions. These modes are neither macroscopic and classical, nor microscopic and quantum mechanical. They are somewhere in between, in the realm of *mesoscopic* physics, where a system's behavior cannot *a priori* be separated from the characteristics of or couplings to the environment [21]. As a quantum computing technology, mesoscopic systems present a different bargain. They tend to be well coupled to their electromagnetic environment, making them easy to access with control signals. But their quantum behavior tends to be all the more delicate and fleeting.

The most advanced mesoscopic quantum computing technology is that based on superconducting integrated electrical circuits [24, 25, 26, 27, 28, 30]. Like all mesoscopic systems, these are man-made devices, and this again presents a bargain. Whereas intrinsically microscopic objects such as electrons, nuclei, atoms and

molecules have fundamental properties which are determined once and for all by nature, the mesoscopic system may be designed to have certain desirable properties. Most important, the energy landscape—the surfaces of allowed energy states and their derivatives with respect to any number of control parameters—may be engineered through design and fabrication. This capability offers a distinct advantage that has been exploited to wonderful ends in the superconducting qubit community [26, 22, 32].

Like the classical electrical circuits of present day information processing technologies, superconducting integrated electrical circuits represent information in the collective modes of a lithographically defined electrical circuit. In the classical systems, these modes are necessarily dissipative. Switching the state of a transistor-based logic circuit requires driving current through a resistive path. In classical computing, dissipation is both a blessing and a curse. It provides robustness by making the information-storing modes immune to noise and environmental fluctuations. But it also places rigorous demands on the thermal engineering of the chip itself, as the heat must be shuttled away through available phonon modes to maintain acceptable operating temperatures.

To quantum computing systems, dissipation is a robe of the reaper, as information-storing quantum states meet a classical end when they share energy with the environment. Superconducting circuits are advantageous in this regard, as the collectivity of their modes derives from underlying quantum mechanical effects, not from lossy elements in the system. They thus offer a great compromise: addressable with simple currents and voltages, not plagued by intrinsic dissipation.

When this quality is taken together with the capability for Hamiltonian engineering [32], the excitement over superconducting systems for quantum computation becomes clear. In essence, they can be designer atoms with large electromagnetic

cross-sections, capable of being wired directly to control-signal-carrying transmission lines, and with the promise of being mass fabricated with advanced lithography techniques borrowed from the silicon-based integrated circuit industry.

To be used as a quantum bit, we must operate such an artificial atom as a virtual two-level system¹. The two lowest-lying energy states under particular circuit bias conditions are retained from the full Hilbert space. These two states, taken to represent logical 0 and 1, form a non-restrictive *computational subspace*. We must initialize the system by reliably preparing some fiducial state within the computational subspace. In mesoscopic circuits, whose quantum coherences are typically short-lived, this is trivial, as we may simply let the system relax to its ground state. We must deploy electromagnetic signals to exact subtle but precise control of the circuit Hamiltonian, giving rise to unitary transformations of the quantum state. These quantum gates—rotations of the state vector in Hilbert space implemented by real-world control fields—are the mathematical elements from which a quantum algorithm is constructed. Last, we must be able to measure the logical quantum state of the system by coupling to the input of an amplification chain some circuit variable which depends upon it.

In order to implement a system of two or more qubits – a quantum register – each individual qubit must meet these requirements. The initialization and readout strategies may be, for the most part, directly extended and applied to each qubit in turn. The quantum gates, though, become notably more complex. One-qubit gates are *local* operations. Acting on one qubit at a time, they transfer quantum information from one local observable to another, but they always leave the information in that qubit’s local subspace where it is accessible through one-qubit measurements.

¹Higher level systems can be used, either explicitly – leading to a larger computational space – or to assist with transformations or measurements in the traditional 2^n -dimensional computational subspace.

But full control of a multiqubit state requires couplings *between* the individual qubits so we can realize conditional quantum state evolution. These two-qubit gates are also rotations of the state vector in Hilbert space, but here, they transfer information from local observables to non-local ones via the inter-qubit couplings.

In fact, it is through two-qubit gates that the strange effect of quantum entanglement first emerges. In this synthetic light, quantum entanglement may be viewed as the distribution of information, which would classically be localized, across multiple quantum systems. Once distributed, the information may only be retrieved through simultaneous measurements of multiple qubits. This special quantum capability implies a collection of behaviors and attributes that are outside the classical realm, and it imbues two-qubit rotations with special importance: they allow us to generate and study effects that are impossible not only in the classical world, but in single qubit systems as well.

Furthermore, unitary transformations of any number of quantum bits may be constructed by concatenating one- and two-qubit gates and applying them to the different qubits in the register. Two-qubit gates are thus *universal* for quantum computation [7, 12]: once we learn to control each qubit individually and to do pairwise two-qubit gates, we may implement any quantum algorithm on any number of quantum bits. For these reasons, moving from one- to two-qubit systems is a hurdle of special significance. Furthermore, we in principle need only learn how to perform a single two-qubit gate corresponding to a $\pi/2$ rotation, as it may then be transformed into any other two-qubit gate by dressing it with arbitrary individual qubit rotations, which are generally much simpler.

Even so, there is no established recipe for developing such a two-qubit gate protocol. Mathematically, the question is posed only in sketch, so we may not seek a solution by straightforward derivation. The unconstrained parameter space is typi-

cally too large and the dynamics too complex for automated search [23]. But more important, each technology – trapped ions, quantum electronic circuits, NMR, etc. – presents the experimentalist with a unique constellation of lab-level knobs with which to guide the system’s dynamics. So though the question is of general interest, solutions to the quantum gate problem are typically specific to narrow classes of qubit implementations, and each strategy presents a unique bargain.

The task may be understood as follows. Appearing in the Hamiltonian of a quantum register are terms describing the interaction of the quantum systems with externally controlled fields, and a set of parameters $\boldsymbol{\lambda} = \{\lambda_1(t), \lambda_2(t) \dots \lambda_k(t)\}$ over which we can exert dynamic control. The λ_k ’s, through a generally non-linear functional dependence, imbue some terms in the Hamiltonian with time dependence. We wish to implement over the interval (t_o, t) a transformation \mathcal{U} of the n -qubit Hilbert space. . We must, in essence, invert the time-dependent Schrödinger equation to find a solution to the equation²,

$$\mathcal{U}(t - t_o) = e^{i\mathcal{H}(\lambda_1(t-t_o), \lambda_2(t-t_o) \dots \lambda_k(t-t_o))/\hbar}, \quad (1.1)$$

in terms of the control vector trajectory $\boldsymbol{\lambda}(t - t_o)$, subject to the practical constraints on the system. This task is in general very difficult, and no closed form solution is expected in all but the most trivial cases. Ideally, the Hamiltonian’s functional dependence on $\boldsymbol{\lambda}$ would allow various terms to be directly switched on and off. It is never this simple. The parameters most often allow an existing term to only be enhanced or weakened, relative to the others, or to be made oscillating rather than static.

²It is important to note that the opposite problem—to calculate the unitary transformation $\mathcal{U}(t - t_o)$ engendered by a specified trajectory $\boldsymbol{\lambda} = \{\lambda_1(t - t_o), \lambda_2(t - t_o) \dots \lambda_k(t - t_o)\}$ —is straightforward. A solution may be obtained through standard numerical integration if it is not analytically tractable.

Furthermore, practical quantum computing systems are yet far from ideal. Noise, energy relaxation, dephasing, signal cross coupling, and imperfect control pulses conspire to make the problem more challenging yet.

This thesis describes our efforts to advance the state of the art in solving the quantum gate problem for Josephson junction-based quantum circuits. We develop a framework to approach the problem for a broad class of systems, and present novel methods of entangling two- and three-qubit systems. We describe the design and fabrication of the circuits, and experiments to test the schemes, with the aim of controllably generating quantum entanglement in superconducting qubits. Though I have made my best effort at each of these, I suspect the reader will agree that the most interesting and useful results center around the theoretical work.

We now turn to a brief introduction to the concepts that come together in this thesis – quantum information and computation, and superconducting quantum circuits.

1.2 Quantum computation

Quantum states live in a continuous complex vector space [33]. A single two-level quantum system, or quantum bit by analogy with the classical bit, is described by a unit vector $|\psi\rangle$ that may take on an arbitrary complex superposition,

$$|\psi\rangle = \alpha|0\rangle + \beta|1\rangle, \quad (1.2)$$

of the classically allowed states $|0\rangle$ and $|1\rangle$, and where α and β obey the constraint

$$\alpha^2 + \beta^2 = 1$$

that allows $|\psi\rangle$ to be interpreted as a probability density.

If a quantum system is built up of multiple sub-systems with independent local observables, its dimensionality is the product of the dimensionality of the subsystems. The state of n quantum bits, or *qubits*, is described by a 2^n -component complex superposition of the classically allowed states. An n classical bit system, by contrast, is an n -dimensional vector over \mathbf{Z}_2 . The exponential scaling of the dimensionality of composite quantum systems relative to classical ones is the reason classical computers have a hard time simulating even fairly small quantum systems.

This idea led Feynman to suggest that a computer using quantum mechanical degrees of freedom could efficiently simulate other quantum systems, and might generally be more powerful than a classical one [1]. The most dramatic known example of this is Shor's algorithm for factoring large numbers on a quantum computer in polynomial time in the number of digits [3]. Another example is Grover's search algorithm, which identifies an item from an unsorted n -item list in $\mathcal{O}(\sqrt{n})$ steps.

Some of the most subtle properties of quantum mechanics center on the distinction between states of composite systems that can be factored into products of states of the individual subsystems, and those that cannot. For a composite system of two quantum bits in the state

$$|\psi_{21}\rangle = \frac{1}{\sqrt{2}}(|00\rangle + |11\rangle), \quad (1.3)$$

there exists no valid factorizing states $|\psi_1\rangle$ and $|\psi_2\rangle$ such that,

$$|\psi_{21}\rangle = |\psi_2\rangle \otimes |\psi_1\rangle.$$

This amazing property amounts to the *entire* information content of the composite quantum system $|\psi_{21}\rangle$ residing in *correlations* between the individual observable

properties of the constituent systems. And yet, any and all of those individual observables contain precisely zero information when examined independently. Such a state is said to be *entangled*. The properties and their implications were first pointed out by Einstein, Podolsky and Rosen [34], and the state 1.3 is consequently known as an *EPR pair*.

Quantum computation aims to exploit the properties of quantum mechanics that give rise to these strange properties in order to more efficiently process information. This calls for seemingly paradoxical requirements. One must exert subtle control over the system to carry out transformations according to the famous Schrödinger equation,

$$\mathcal{H}|\psi\rangle = i\hbar \frac{\partial}{\partial t}|\psi\rangle,$$

where \mathcal{H} is the Hamiltonian operator governing the system dynamics, all the while ensuring that the quantum effects are not destroyed through interactions with uncontrolled degrees of freedom in the environment. Provided no information is lost from the quantum system over the interval, the evolution between two times t and t' of the full 2^n -dimensional space is,

$$\begin{aligned} |\psi(t')\rangle &= \exp\left[\frac{-i}{\hbar}\mathcal{H}(t'-t)\right]|\psi(t)\rangle \\ &= \mathcal{U}(t,t')|\psi(t)\rangle. \end{aligned}$$

In the standard language of quantum computing, the transformation $\mathcal{U}(t,t')$ is decomposed into a concatenated string of quantum gates, chosen from some universal set [12], that address the subsystems individually or pair-wise, as only one- and two-qubit gates are needed to build up an arbitrary unitary transformation of the full computational space. Universal sets can be stated as a finite number of quantum logical transformations, with the insinuation that they can be applied to any subspace

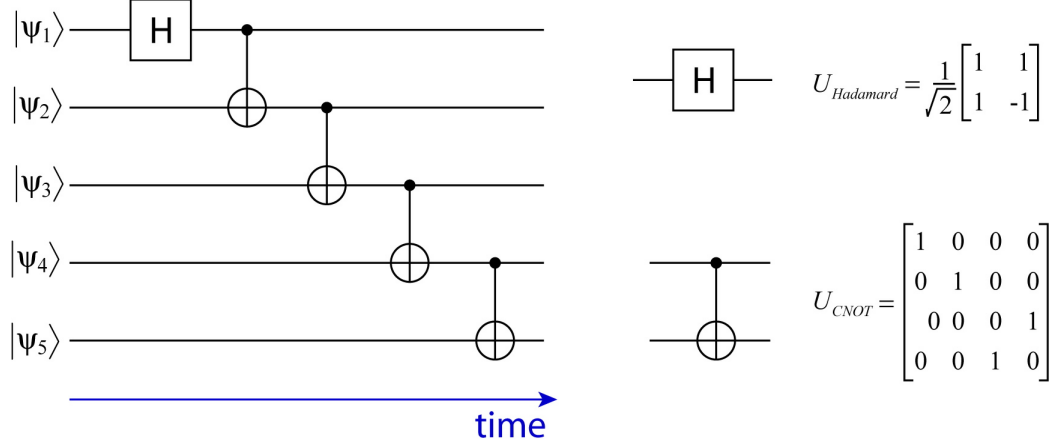


Figure 1.1: A quantum logic circuit to produce a five-qubit EPR type state. Individual qubits are represented as horizontal lines, quantum gates acting on the qubits are represented as boxes on or vertical connections between qubit lines.

of the full Hilbert space of the quantum register; or as a class of rotations over a continuous range of angles. Practically, the two-qubit rotations are much more challenging than the local ones, so it can be helpful to view the universal set as comprising a single, discrete two-qubit unitary and the set of continuous one-qubit transformations. Then, the requirement on the two-qubit gate in order that the set be universal is that it be a generator of the *Clifford group*, the largest discrete group of transformations of the n -qubit Hilbert space [13, 96]. (As a sort of shorthand, any two-qubit Clifford generator is itself termed universal, with the required one-qubit continuous control left implicit.)

Quantum gates are given a pictorial representation, allowing a computation to be represented as a quantum logic circuit, again by analogy with classical Boolean circuits, in a manner reminiscent of a musical score [7]. For example, a circuit to produce the generalization of an EPR pair to five qubits is shown in 1.1. The gates act in a defined way on arbitrary input states, allowing them to be faithfully deployed as building blocks of large scale computations.

One challenge facing the field lies in the identification of useful new algorithms and computational tasks that can be constructed from these blocks—a problem which naturally abstracts both the quantum logic states and their transformations. In this thesis we focus on the complementary problem of learning how to implement the gates themselves subject to practical experimental constraints. In other words, we aim to build the building blocks of a superconducting quantum computer.

Progress towards a quantum computer has come in waves. A great deal of excitement came early on, not long after Shor discovered his factoring algorithm, from results in liquid state NMR [16]. A seven-qubit quantum computer was used to factor ‘15’ using Shor’s algorithm in 2001 [35]. Progress with liquid NMR slowed, mostly due to problems scaling to larger molecules, and trapped ions [38] emerged as a serious competitor [39]. The third wave has emerged over the past few years using Josephson junction-based quantum circuits [30, 73, 26, 36, 46, 79, 97, 113, 141, 25, 31], to which we now turn.

1.3 Superconducting quantum circuits

1.3.1 The Josephson junction

In addition to being dissipationless, superconducting circuits can also be made non-linear by embedding in them Josephson junctions—thin insulating oxide barriers sandwiched by two superconducting electrodes. The Josephson junction may be modelled as a non-linear current-dependent inductance $L_J(I)$ (a pure *Josephson element*) in parallel with a capacitance C_J . The capacitance is geometric; it depends on the ratio of the junction area to the oxide thickness. The inductance L_J is more subtle, as it arises from the coherent tunneling of Cooper pairs across the oxide

barrier. The pure Josephson element has a current-voltage relation [98],

$$I(t) = I_o \sin(\phi(t)/\varphi_o), \quad (1.4a)$$

where,

$$\varphi_o = \frac{\hbar}{2e} \quad (1.5)$$

is the reduced flux quantum; $I_o = \frac{\varphi_o}{L_J(I=0)} = \frac{\hbar}{2eL_J(I=0)}$ is the junction critical current for switching to the resistive state; and $\phi(t)$ is the branch flux defined as in [21],

$$\phi(t) = \int_{-\infty}^t V(t') dt', \quad (1.6)$$

with the integral of the electric field taken along a line inside the element.

The ubiquity of the Josephson junction in superconducting qubit systems owes to it being the only known non-dissipative and nonlinear circuit element. Its nonlinear character allows us to create circuits with several required or desirable properties: anharmonic spectra – thus allowing reliable operation in an artificially truncated subspace of the system’s full Hilbert space; tunable interactions of the circuits with external control signals – allowing e.g. the qubit readout mechanism to be effectively switched off during state manipulation or free evolution; and tunable interactions between qubit subcircuits for implementing two- or multi-qubit gates.

Given these two properties, a variety of superconducting qubit systems can be envisioned, with creativity in circuit design typically limited only by the available fabrication processes. Though the systems are still evolving, we can simplify the discussion with some classifications. First, the circuits can be labeled as implementing qubits of the *charge*, *flux*, or *phase* variety depending on the circuit variable to which are coupled external signals for state manipulation. Qubits of each type have been

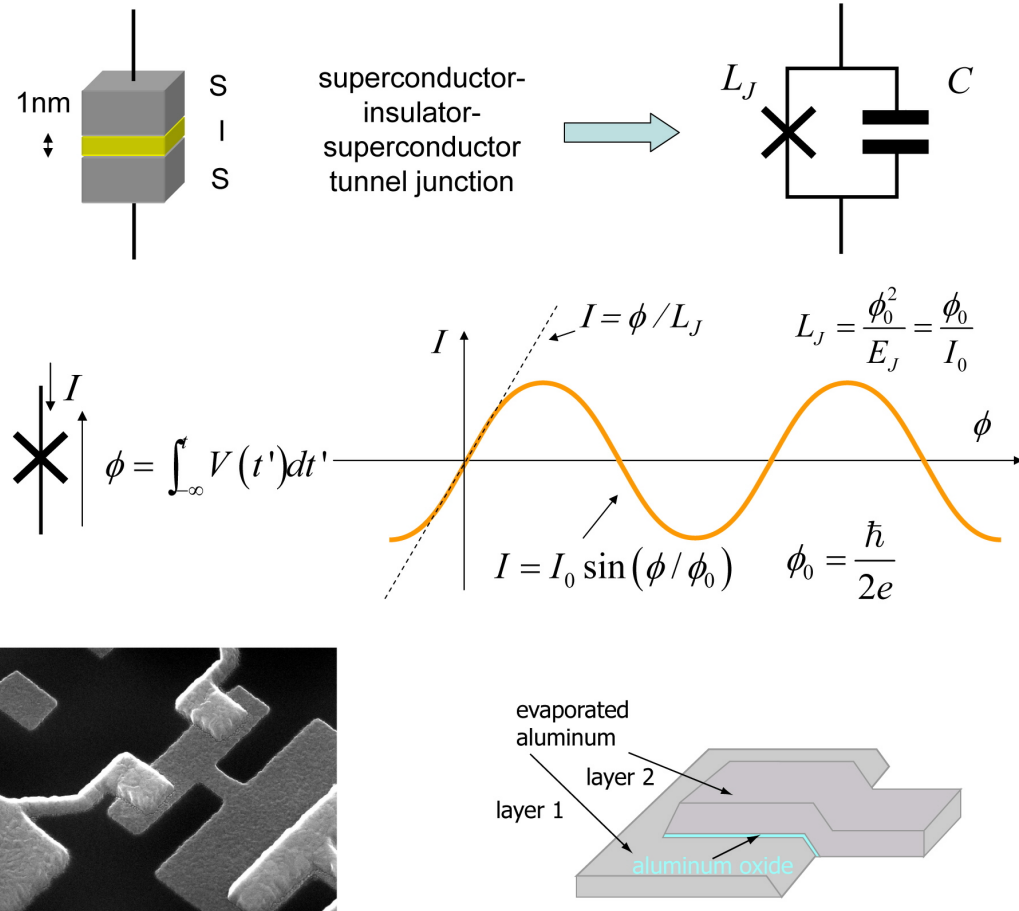


Figure 1.2: A Josephson junction is a thin layer of insulating oxide separating two superconducting electrodes. *Bottom:* Schematic and SEM of a junction formed by evaporation of superconducting material through a shadow mask at two different angles, with an oxidation between the two evaporation. A Josephson junction is formed where the two layers overlap. *Middle:* The non-linear current voltage relation of the Josephson junction. *Top:* Equivalent circuit diagram with the geometric capacitance C_J separated from the pure Josephson element characterized by L_J , the slope of the current-flux relation at $\phi = 0$.

implemented successfully. This work focuses primarily on qubits of the charge and flux type, discussed in more detail below.

1.3.2 Charge Qubits

The archetypal charge qubit, the *Cooper pair box*, consists of a superconducting island separated from a superconducting reservoir by a Josephson tunnel junction of characteristic energy E_J and raised to a potential U_g by placing charge on an effective gate capacitor C_g [29]. This circuit is described by the Hamiltonian

$$\hat{\mathcal{H}} = E_C(\hat{N} - N_g) - E_J \cos \hat{\theta}, \quad (1.7)$$

where E_J is the junction's Josephson energy and $E_C = (2e)^2 C_g / 2C_\Sigma$, where $C_\Sigma = C_J + C_g$ is the total capacitance to the island.

A closely related circuit is the *split* Cooper pair box, implemented by splitting the single junction into two nominally identical junctions, each of energy $E_J/2$, and connecting the reservoirs to form a loop. The two split junctions behave like a single junction with a variable Josephson energy $E_J^{eff} = E_J \cos(\pi \Phi_{ext}/\Phi_0)$, where Φ_{ext} is the externally applied flux through the loop. The Hamiltonian of the split CPB is the same as that of the CPB with $E_J \rightarrow E_J^{eff}$. The split box is thus a *dynamically tunable* Cooper pair box.

The extent to which the energy bands of the CPB deviate from the parabolic bands of a purely capacitive circuit is determined by the aspect ratio E_J/E_C . Increasing this ratio tends to flatten the bands, making the system's transition energies less strongly dependent on fluctuations in the external bias. However, it also reduces the systems anharmonicity, which is essential if the circuit is to behave as an effective two-level system.

The CPB may be manipulated by applying DC or radio-frequency voltage signals to the gate capacitor. When the CPB is biased at $N_g = 1/2$, its Hamiltonian may be written in the form

$$2\mathcal{H}/\hbar = \omega\sigma_z + 2\Omega \cos(\omega_{rf}t + \phi)\sigma_x, \quad (1.8)$$

where $\omega/2\pi$ is the qubit transition frequency, and Ω the amplitude of the applied AC signal at frequency $\omega_{rf}/2\pi$.

The split CPB has the advantage that it may be operated at a saddle point of the transition energy $\hbar\omega$ (N_g, Δ). When the system is DC biased at $N_g = 1/2$ and $\delta = 0$ and subject to exclusively AC control, the derivatives $\partial\omega/\partial N_g$ and $\partial\omega/\partial\delta$ both vanish, making the system immune, to first order, to fluctuations in both charge and phase. A qubit taking advantage of this property has been nicknamed the *quantronium* by Vion, *et al.* [26, 75], and we will look to it in more detail shortly.

1.3.3 Flux Qubits

The archetypal flux qubit, the radio-frequency superconducting quantum interference device, or RF SQUID, consists of a superconducting loop of inductance L interrupted by a Josephson junction of energy E_J and biased with an external flux Φ_{ext} [25, 28]. The Hamiltonian describing this circuit is

$$\mathcal{H} = \frac{q^2}{2C_J} + \frac{\phi^2}{2L} - E_J \cos\left(\frac{\phi - \Phi_{ext}}{\varphi_0}\right), \quad (1.9)$$

where q is the charge on the capacitance C_J , and ϕ is the flux through the loop. When the flux frustration $N_\phi = \Phi_{ext}/\Phi_o$ is half-integer, the potential landscape for the phase across the Josephson element is a symmetric double well, as shown

schematically in 1.3. The system's two lowest-lying states are then the symmetric and anti-symmetric linear combinations of the phase localized in either well. For $E_J \gg E_C$ and $L_J \approx L_{loop}$, the Hamiltonian of the RF SQUID may be written as

$$2\mathcal{H}/\hbar = \omega\sigma_z + 2\Omega \cos(\omega_{rf}t + \phi)\sigma_x, \quad (1.10)$$

the same form as that of the CPB.

1.3.4 Phase Qubits

A phase qubit is a large current biased Josephson junction. It is illustrated, along with its tilted washboard potential, in 1.3. A high impedance current source is obtained by using an inductively coupled flux bias. To increase the non-linearity of the phase qubit, the DC bias current is taken close to the junction critical current I_o . This system has the advantage of having a built-in readout mechanism. The excited state has a much higher probability of tunneling out of the well in the tilted washboard potential. This rate can be increased further by adiabatically decreasing the barrier height using a fast DC pulse. When the system tunnels, a measurable voltage of $2\Delta/e$ develops across the junction, where Δ is the superconducting energy gap. The first time resolved measurements were by Martinis et al. [27].

1.3.5 The Quantronium

The measurements presented in Chapter 7 have been made on quantronium-style superconducting qubits [129]. This circuit was the first superconducting qubit technology to demonstrate coherence properties that made extensions to multiqubit systems feasible. The quantronium circuit as implemented consists of a split Cooper pair box (see Appendix A) with aspect ratio $E_J/E_C \approx 1$ connected in parallel with a

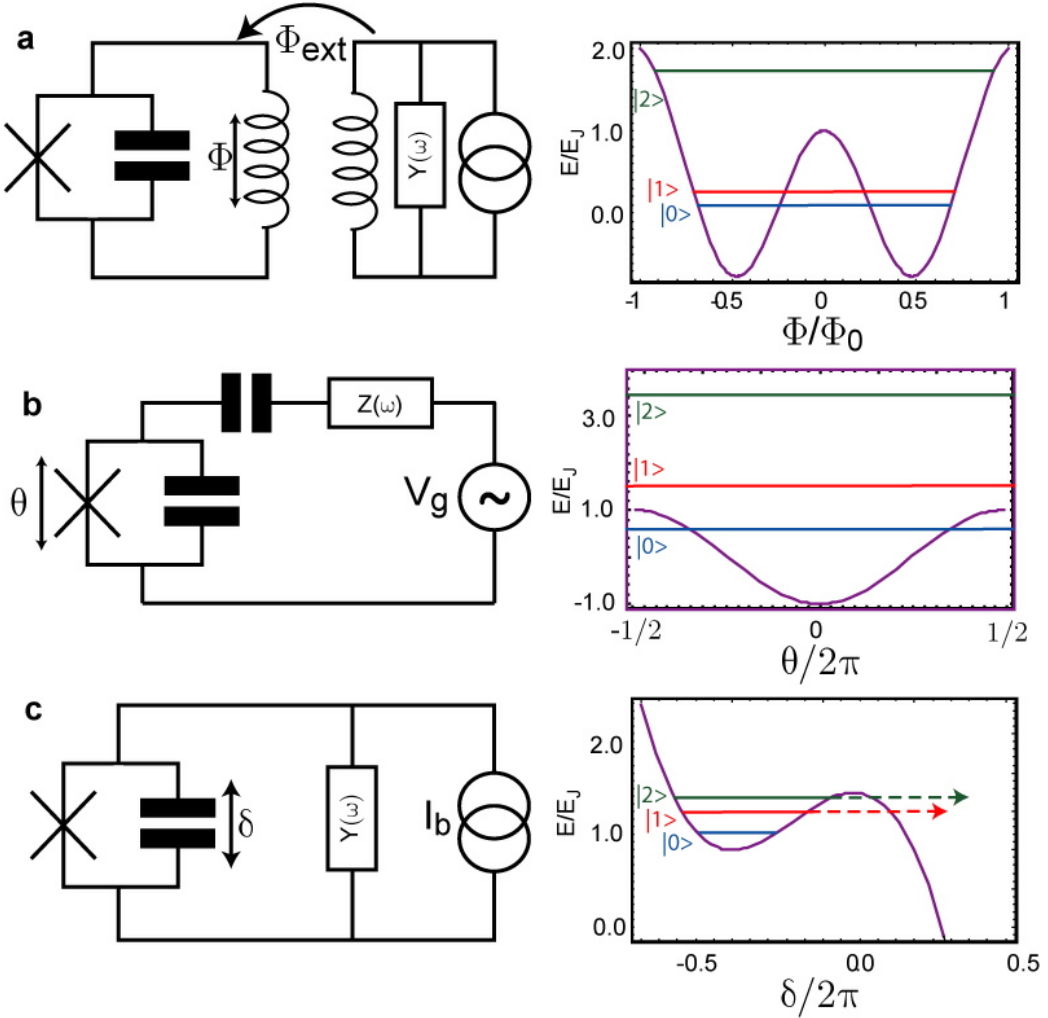


Figure 1.3: Three main types of superconducting qubit and their potential energy landscapes. **a.** Flux qubit with its double well potential. First two energy levels are symmetric and anti-symmetric superpositions of the persistent current states corresponding to the two minima of the potential energy. **b.** Cooper pair box with its cosine potential. The energy levels are superpositions of charge states of the superconducting island. **c.** Phase qubit and its tilted washboard potential. The system tunnels through the barrier with a much higher rate when excited, causing a voltage of $2\Delta/e$ to develop across the junction.

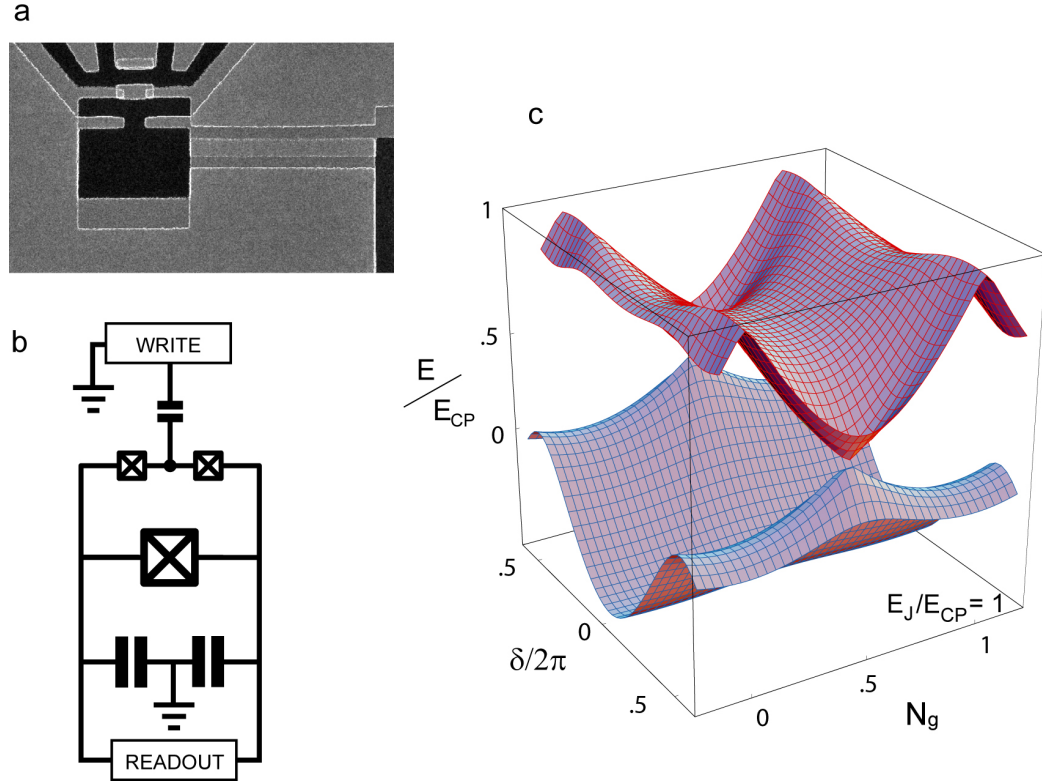


Figure 1.4: **a.** SEM image of quantronium qubit circuit implemented by Vion et al. **b.** Equivalent circuit diagram. **c.** Two lowest lying energy surfaces of the quantronium system as a function of the DC-controlled bias parameters N_g , the gate charge, and δ , the imposed phase difference across the circuit.

large Josephson junction used for reading the qubit state. The optimal working point of this circuit is at $N_g = 1/2$ and $\delta = 0$, where the two lowest eigenstates are the symmetric and antisymmetric combinations of zero and one excess Cooper pairs on the island. This point corresponds to a saddle point of the transition energy surface; the qubit is therefore immune to first-order to fluctuations in charge and flux. The first two energy surfaces are shown for $E_J/E_C = 1$.

One-qubit gates may be implemented in the quantronium system without moving away from optimal working point by applying purely radio frequency pulses at or near the qubits transition frequency $\omega/2\pi$. Working at this “sweet spot”, the times for longitudinal relaxation T_1 and pure dephasing T_φ have been measured to be $1.8\mu\text{s}$

and 500ns, respectively [26].

In addition to the first-order immunity to charge and flux noise when it is operated at the sweet spot, the success of the quantronium in achieving long coherence times can also be attributed to its low sensitivity to fluctuations in each junction's critical current I_o [30].

1.4 Coupling Schemes

There are several ways we could build up multi-qubit circuits from the core one-qubit technologies, and the body of work on this topic is already sufficiently rich to resist synopsis. Nonetheless, we can offer a rough taxonomy of the various proposals in 1.5 and 1.6. We emphasize that the appeal of a certain coupling strategy will be tied to the one-qubit technology being considered and the facilities and aims of the particular experimentalist.

First, we can characterize qubit–qubit coupling schemes by the signals used to control the qubit transition energies. They may be fixed, subject to DC control, or subject to AC control. The qubit–qubit coupling energy may be similarly classified. The nature of the coupling subcircuit provides a third point of distinction: it may be made either linear, comprising only simple inductances and capacitances, or non-linear through the inclusion of one or more Josephson junctions. Finally, we must also distinguish between two broad styles. Qubits that interact through an auxiliary quantum circuit that can transfer the delicate quantum information over distances that are large compared with the qubits themselves, or are comparable to the wavelength of the photons they couple between the qubits, can be thought of as interacting through a *quantum bus*, in analogy to the classical data bus that shuttles information around a classical processor [97, 79]. This classification is illustrated in

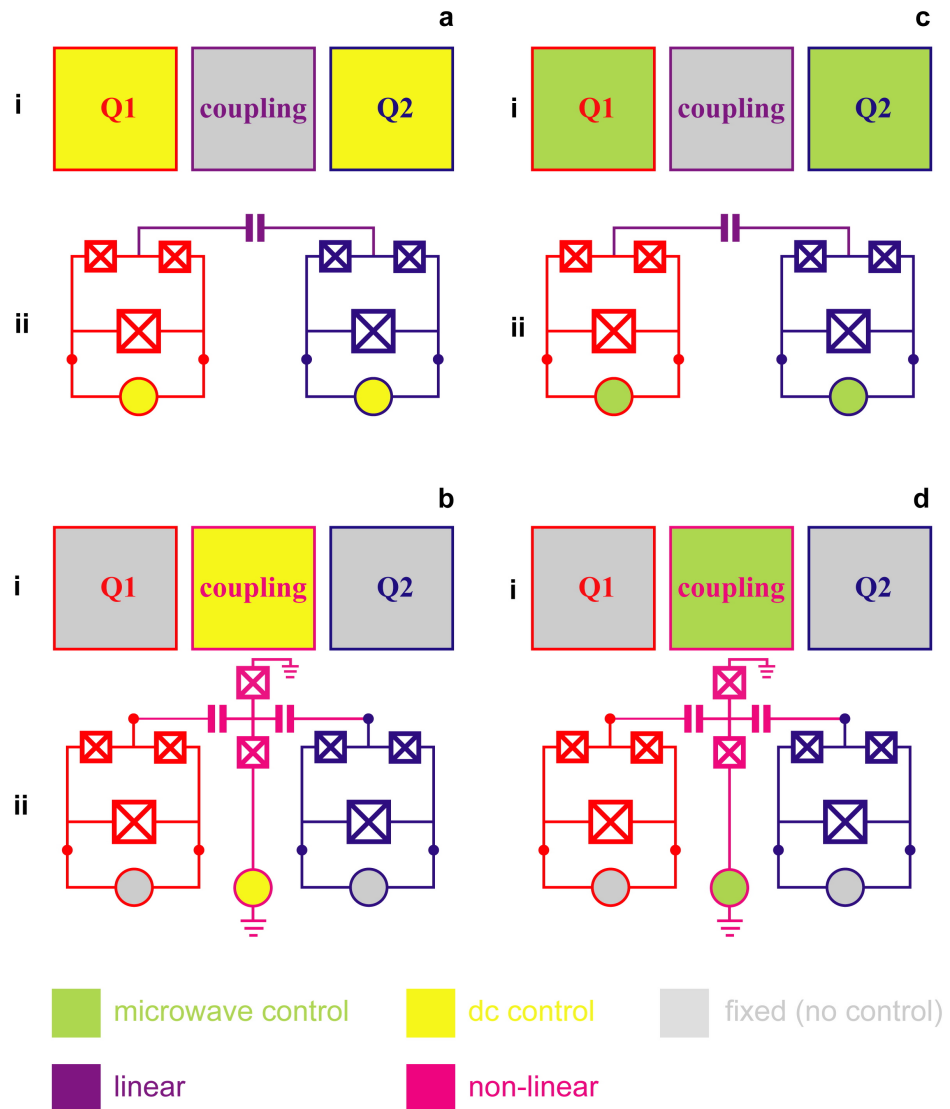


Figure 1.5: Coupling schemes for superconducting qubits. **i.** Schematic specifying qubit and coupling control (microwave (green), DC (yellow), fixed (gray)) and coupling type (linear (purple) or non-linear (magenta)). **ii.** Example circuit diagram based on quantronium charge/phase design. Many other incarnations are possible.

a. DC controlled qubits with fixed linear coupling. Qubits are DC-tuned into resonance for two-qubit gates. **b.** Fixed-frequency qubits with non-linear DC controlled coupling. The Cooper pair box coupling subcircuit acts as a tunable effective capacitance. **c.** Microwave controlled qubits with fixed linear coupling. Weak coupling capacitance gives rise to non-secular coupling Hamiltonian. Qubits are driven into resonance with microwave pulses **d.** Fixed-frequency qubits with microwave controlled non-linear coupling.

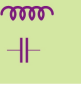
	Qubit Energies	Coupling Energy	Coupling Reactance	Coupling Subcircuit	Sample Reference
No Quantum Bus	DC CONTROL	FIXED	LINEAR		Shnirman, PRL 79 122373 (1997)
	FIXED	DC CONTROL	NON-LINEAR		Averin and Bruder, PRL 057003 (2003) Plourde, et al. PRB 70, 140501-R (2004)
	RF CONTROL	FIXED	LINEAR		Rigetti et al. PRL 94, 240502 (2005)
	FIXED	RF CONTROL	NON-LINEAR		Bertet et al., PRB 73, 064512 (2006)
Quantum Bus	FIXED	RF CONTROL	TUNABLE BUS		Blais et al., PRL 90, 127901 (2003).
	RF CONTROL	FIXED	FIXED BUS		Majer et al. Nature 449 (2007)

Figure 1.6: Taxonomy of proposals to couple superconducting qubits.

1.6; the various proposals are expounded below.

1.4.1 Fixed linear coupling, DC controlled qubits

The earliest work proposed coupling qubits together through a fixed linear circuit element such as a capacitor, and tuning the qubit transition energies into and out of resonance with DC control signals [79, 80, 40]. This minimal approach to the problem requires no additional control lines or nonlinear circuit elements beyond those required for the simultaneous operation of two uncoupled qubits, though fast tuning of the frequencies does require DC lines with very large relative bandwidth. The tuning, achieved by modulating loop fluxes or gate charges, necessarily moves the qubits away from their optimal DC bias points, and this will in most cases have a deleterious effect on the individual qubit coherence times [30].

1.4.2 DC controlled coupling, fixed qubits

Two superconducting qubits having fixed detuned transition frequencies may be coupled via a subcircuit containing one or more Josephson junctions [41, 53]. The strength of the interaction is tuned directly through external control lines. One-qubit gates are implemented as if the each qubit is the only one present, since the coupling is effectively off under typical conditions. Two-qubit gates are performed by applying DC pulses to the coupling subcircuit which exploit the non-linearity in the coupling to adjust the value of an effective capacitance (when coupled via a Cooper pair box) or inductance (coupled via a SQUID) that couples the individual qubit modes to one another. Once the coupling is ramped up, the system is left to evolve for a specified time. As above, rapid switching of the interaction requires large relative bandwidth of the DC control lines. This approach is powerful, yet also technically demanding.

In addition to two copies of a qubit circuit, it requires a non-linear subcircuit and extra control lines with bandwidth at DC that further expose the system to low frequency noise.

The essential advantage of this approach is the capability to statically tune the interaction to a precise zero. For both charge and flux qubits, there is a stray interaction due to the trivial on-chip proximity of the two circuits. The effective inductance or capacitance of the non-linear coupling subcircuit can be negative in each case, and this allows the cancellation of the stray direct couplings during one qubit gate operations [53].

1.4.3 Fixed linear coupling, RF controlled qubits

We proposed to circumvent the need for additional control lines *or* non-linear elements in the subcircuit by using exclusively microwave signals to drive detuned qubits into resonance [105]. This technique, here presented for completeness of the field overview, is discussed at length in Chapter Three. Our original strategy of this sort calls for resonant microwave pulses—as required for standard one-qubit gates—to be applied to the qubits simultaneously to perform two-qubit gates. When the drive powers match the condition $\Delta = |\omega_1 - \omega_2| = \Omega_1 + \Omega_2$ a strong effective interaction develops through the Rabi sidebands of the two driven qubits [121, 81]. The use of only linear coupling elements minimizes exposure to stray interaction with the environment, while the use of exclusively microwave signals allows the qubits to remain biased throughout the two-qubit gate at the optimal working point where coherence is maximized. The primary challenge of this approach derives from the practical limits on the drive amplitudes Ω in order that the state remain in the computational subspace and gate errors due to the Bloch-Siegert shift not be too large. The always-on interaction can be neglected up to order ω_{xx}^2/Δ^2 in the one-qubit gate

fidelity, and actively refocused using the techniques developed in NMR once higher fidelities are required [16, 99]. Also, the effective coupling strengths are limited in this particular irradiation protocol to 1/8th of the bare coupling, which itself must be small to satisfy the weak fixed coupling condition $\omega_{xx} \ll \Delta$ that allows it to be ignored during the implementation of one-qubit gates. The protocol achieves an on/off ratio of 20dB without any sophisticated efforts to cancel the coupling during one-qubit rotations, see Chapter Three. Alternative irradiation schemes simplify the protocol and can render the effective coupling tunable through the amplitude of the microwave drive, ultimately reaching a limiting strength of one-half of the bare coupling strength [116]. The sidebands employed in this scheme have been experimentally observed in a recent experiment by Baur, et al [54]. A very similar coupling was experimentally realized by Majer et al. [79]. They applied a single non-resonant microwave pulse simultaneously to both qubits, with pulse parameters chosen such that the AC Stark-shifted qubit transitions became resonant. The qubits were coupled through the effective LC circuit formed at that frequency by an on-chip superconducting resonator.

1.4.4 RF controlled coupling, fixed qubits

Bertet et al [42] and Niskanen et al [43] proposed the use of a microwave driven non-linear subcircuit to couple fixed off-resonant qubits. In their scheme the coupling subcircuit is driven through an added microwave control line—requiring only a small relative bandwidth—at the qubits’ difference or sum frequency $|\omega_1 \pm \omega_2|/2\pi$. Notably, this scheme leads to an effective interaction strength that increases linearly with microwave drive amplitude Ω , so the scheme can be applied to qubits with comparatively large detunings by simply increasing the applied signal level. Also, this proposal does not require DC excursions of any kind, so the qubits may remain

at their optimal working point. The protocol is very elegant, and has been experimentally tested in a series of measurements performed at NEC by Nakamura, *et al.* [113].

1.4.5 Quantum bus

The quantum bus described earlier can be implemented in one of two ways. The bus mode can be defined by a linear circuit of fixed frequency, or a tunable non-linear circuit. The first proposal came from Blais *et al* [78], who suggested coupling two fixed off-resonant qubits through an AC current biased Josephson junction. The bus is tuned into and out of resonance with each of the qubits in turn, entangling the first qubit and the bus mode, then transferring the entanglement to the second qubit. Later, Sillanpää *et al.* and Majer et al demonstrated coupling of superconducting qubits through a mode defined geometrically in a superconducting coplanar waveguide resonator [97, 79].

1.5 Summary of key results

We now summarize some key results of this work, beginning with tools we have developed to better understand quantum gates, entanglement, and gate protocols.

1.5.1 The discrete Hilbert space \mathfrak{H}_n

Quantum gates are rotations in Hilbert space. Though this continuity is perhaps the quintessential quantum property allowing exponential computational speedup for certain tasks, it is practically very troubling, as errors and imperfections in the rotations are themselves continuous [7, 12]. When combined with the basic properties

of quantum measurement, this makes it challenging to detect and debug small errors so as to achieve the gate fidelity required for quantum error correction schemes.

It is useful in this regard—be it conceptually or practically—to limit the state of the system to some discrete and finite collection of allowed states having well characterized observable properties. We have created a procedure for arriving at such a discrete n -qubit Hilbert space where the nearest-neighbor angular separation is $\pi/2$. The resulting set of states constitutes a uniform sampling of the underlying continuous space, implying that the figures formed by these sets are the Hilbert space equivalent of the Platonic solids. The states have the desirable property that they may be navigated with only Clifford group operations (see 2.36). They are the space in which a *digital* quantum computation takes place [88].

The n -qubit discrete Hilbert space is found by forming all the maximal Abelian (ie. mutually commuting) subsets of the n -qubit Pauli matrices, then retaining only states that are simultaneous eigenvectors of each element of the subset. The number of states in the discrete set, which we call a *uniform Hilbertian polyhedron* and denote \mathfrak{H}_n for n qubits, is shown below, along with the number of maximal Abelian subsets, each of which contributes one basis of 2^n states to the discrete set.

n	1	2	3	4	5	6	7
states in \mathfrak{H}_n	6	60	1080	36,720	2,423,520	315,057,600	81,284,860,800
bases in \mathfrak{H}_n	3	15	135	2,295	75,735	4,922,775	635,037,975
classical states	2	4	8	16	32	64	128

A system confined to the discrete Hilbert space has considerably simplified dynamics. The nearest neighbor distance of $\pi/2$ of course implies that we need not consider rotations of any finer angle. The discrete dynamics owing to individual

Hamiltonian terms proportional to a Pauli operator acting on the full Hilbert space can then be represented graphically, see 1.7.

1.5.2 Visual representation of two-qubit gates

We may go a step further and seek a graphical representation not of the relationship between the operators acting on the Hilbert space, but of the states themselves. For one qubit, this tool has already been developed, the Bloch sphere. Is there an equivalent for two-qubit states? The Bloch sphere provides a faithful depiction of one-qubit states in real space due to the rather coincidental isomorphism between $SU(2)$, the group of one-qubit rotations, and O_3 , the group mapping real three-dimensional space into itself. The group of two-qubit transformations, $SU(4)$, is isomorphic to O_7 , so a real space representation of two-qubit states must find a way to faithfully decompose O_7 into a visually interpretable useful composite of lower-dimensional real spaces. Ideally, we should like this decomposition to have the geometrically faithful attributes of the one-qubit Bloch sphere.

We arrive at such a representation through an avenue similar to the one taken in the above discretization. First, we classify the fifteen non-identity two-qubit Pauli matrices, operators that describe all possible measurements of a two-qubit system—as either local (having the identity occurring once in the direct product decomposition, e.g. $\sigma_x\sigma_w$) or non-local (identity doesn't occur in decomposition, e.g. $\sigma_x\sigma_x$). The six local operators are separated into the three acting on the first qubit and the three acting on the second qubit. The expectation values of these operators describe the reduced density operators ρ_1 and ρ_2 of the individual subsystems [7]. They are plotted on orthogonal x, y, z -axes, producing a Bloch sphere picture for the local dynamics of each individual qubit. It is essential to note that ρ_1 and ρ_2 vanish for pure maximally entangled states. In that case the information is contained in

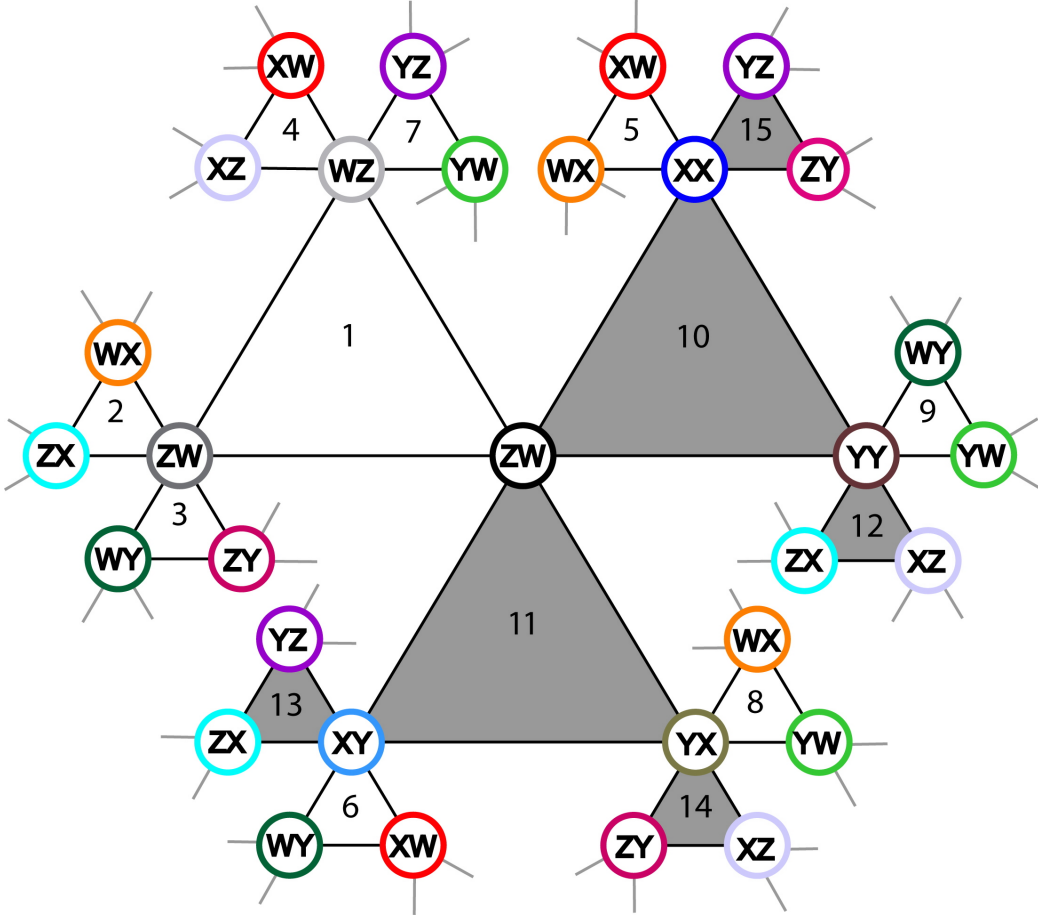


Figure 1.7: Graph of the set \mathcal{S}_2 of two-qubit generalized Pauli matrices Σ_j (circles bearing the subscript of the matrix in letter notation) and by the pseudostabilizers (triangles formed by three connected circles). The three Σ 's in a triangle share four common eigenvectors which form an orthonormal basis spanning the two-qubit Hilbert space. The fifteen triangles thus give fifteen sets of four basis vectors. Shaded triangles correspond to entangled states while non-shaded triangles correspond to product states. Neighbouring triangles have one (non-identity) Σ in common, and each (non-identity) Σ is shared by three triangles. The line segments joining the vertices of a triangle correspond to pairs $\{j, k\}$ of commuting matrices; each segment therefore specifies a $\pi/2$ rotation $X_{j,k} = (\Sigma_j + i\Sigma_k)/\sqrt{2}$ that transforms the eigenvectors of an adjacent triangle into its neighbour. The figure thus constitutes a “roadmap” for navigating the discrete set \mathfrak{H}_2 . Repeated circles indicate the closure of the graph.

the remaining nine (non-local) Pauli operators describing correlations of the local observables.

We represent these by collecting together those which mutually *anti*-commute, creating three ordered pairs of expectation values, e.g.

$$(r_{xx}, r_{xy}, r_{xz})$$

then subtracting from each component the product of the two corresponding local expectation values. This subtraction amounts to removing the trivial classical correlations. We obtain three entanglement vectors that fully describe the information stored non-locally in the system:

$$\mathbf{g}_1^x = (r_{xx} - r_{wx}r_{xw}, r_{yx} - r_{wx}r_{yw}, r_{zx} - r_{wx}r_{zw}) \quad (1.11)$$

$$\mathbf{g}_1^y = (r_{xy} - r_{wy}r_{xw}, r_{yy} - r_{wy}r_{yw}, r_{zy} - r_{wy}r_{zw}) \quad (1.12)$$

$$\mathbf{g}_1^z = (r_{xz} - r_{wz}r_{xw}, r_{yz} - r_{wz}r_{yw}, r_{zz} - r_{wz}r_{zw}) \quad (1.13)$$

These vectors can be simultaneously plotted on a single 3D coordinate system to give a full and succinct graphical representation of the entanglement of the two-qubit system. The details of this representation, and some examples of its utility, are presented in chapter 2.

1.5.3 Continuous two-qubit dynamics

The dynamics of a quantum system in the presence of non-unitary processes is described by a master equation. Most generally the time-evolution of the density

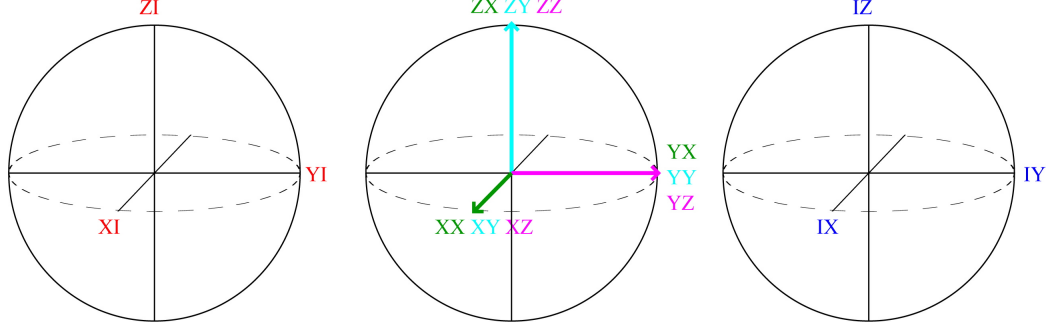


Figure 1.8: Representation of a two-qubit state in three real dimensions. The individual qubit state dynamics are plotted on Bloch spheres (red and blue). The non-local dynamics are plotted as a tri-vector on the *entanglement sphere*. The entanglement trivectors indicate the direction in Hilbert space along which the non-local quantum information is concentrated. For the state shown, measurement of the observables YX , ZX , XY , YY , XZ , ZZ will yield no information, while measurement of the set of commuting operators $\{XX, YZ, ZY\}$ will fully specify the two-qubit state. The entanglement trivector thus indicates which measurements will uncover the largest violation of a Bell type inequality for the given quantum state.

operator ρ may be written in the *Lindblad form* [37],

$$\frac{d\rho}{dt} = -i\hbar[\mathcal{H}, \rho] + \frac{1}{2} \sum_j \left([\mathcal{L}_j, \rho \mathcal{L}_j^\dagger] + [\mathcal{L}_j \rho, \mathcal{L}_j^\dagger] \right), \quad (1.14)$$

where \mathcal{H} is the system Hamiltonian and the \mathcal{L}_j 's are the Lindblad operators describing the effects of the environment. The one-qubit version of this equation is common. In this thesis we will make extensive use of the two-qubit version. A very useful form of this is derived by writing each of \mathcal{H} , ρ and the \mathcal{L}_j 's in the basis of n -qubit Pauli matrices (the \mathcal{L}_j 's describe non-unitary dynamics, so they take complex coefficients). Then, the dynamics of the system are structurally governed by the commutative and anti-commutative properties of the Σ 's. We obtain a set of $4^n - 1$ coupled first order linear differential that describe component-wise the $2^n \times 2^n$ density operator:

$$\frac{dr_i}{dt} = \sum_{k=1}^{4^n-1} \sum_{l=1}^{4^n-1} \sum_{j=1}^{4^n-1} (h_k r_l \mathbf{M}_{kli} + a_j r_l \mathbf{G}_{jli}), \quad (1.15)$$

where the h_k 's describe the Hamiltonian,

$$h_k = \frac{1}{2} \text{Tr}(\Sigma_k^\dagger \mathcal{H}), \quad (1.16)$$

and are directly interpretable as the transition energies of the two-qubit system. The r_l 's are the components of the two-qubit Bloch vector,

$$r_l = \frac{1}{2^n} \text{Tr}(\Sigma_l^\dagger \rho), \quad (1.17)$$

and the a_j 's are the Lindblad-Pauli coefficients that incorporate non-unitarity. The matrices \mathbf{M}_{kli} and \mathbf{G}_{jli} contain the (anti-) commutative structure of the two-qubit Pauli matrices:

$$\mathbf{M}_{kli} = \frac{1}{8i} \text{Tr}([\Sigma_k, \Sigma_l] \Sigma_i), \quad (1.18)$$

$$\mathbf{G}_{jli} = \frac{1}{8} \text{Tr}([\Sigma_j, \Sigma_l \Sigma_j] \Sigma_i). \quad (1.19)$$

These objects may be calculated once and for all, and Mathematica code to produce automatically is appended. This form of the master equation allows one to easily study the effects of various noise processes.

1.5.4 Two-qubit gates at optimal bias point

The **FLICFORQ** register

Early schemes for performing two-qubit gates relied on dynamic tuning of either the qubit transition frequencies [49, 80] or a subcircuit controlling the qubit–qubit interaction [78, 41, 53]. We proposed to use exclusively microwave control signals—and their limited relative bandwidth—with simple linear coupling reactances such

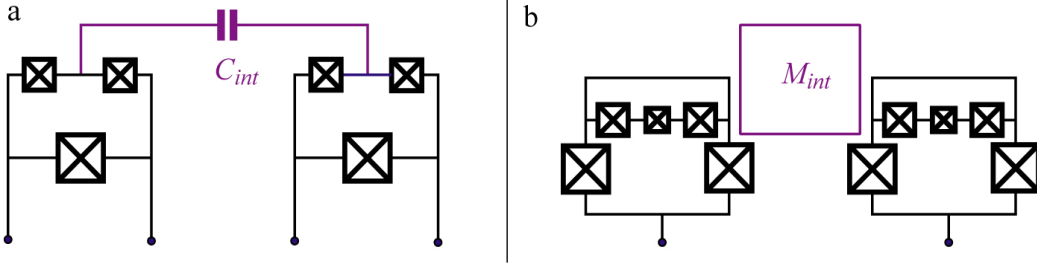


Figure 1.9: Superconducting two-qubit circuits for performing universal quantum gates at optimal bias point with linear fixed couplings. (a) Charge qubits coupled by capacitor. (b) Flux qubits coupled by mutual inductance.

capacitors or inductors that give rise to an always-on weak and off-diagonal coupling. Without the dependence on DC control signals of other earlier schemes, the qubit transition energies and the qubit–qubit coupling remain fixed throughout, while the non-secular coupling enters as a second order perturbative correction to the eigen energies, and can be neglected in the absence of certain special configurations of the microwave drive parameters up to errors proportional to $(\omega_{xx}/|\omega_1 - \omega_2|)^2$. We nicknamed this approach FLICFORQ for Fixed LInear Couplings between Fixed Off-Resonant Qubits. FLICFORQ, as such, is a style of quantum register, but it also implies a class of certain control signals. As the couplings are fixed, they are not subject to external control signals, and as the qubit frequencies are fixed, they may not be DC tuned to perform a two-qubit gate.

At optimal bias and in the two-level approximation, these two-qubit systems are described by the Hamiltonian

$$2\mathcal{H}/\hbar = \omega_1 \sigma_1^z + 2\Omega_1 \cos(\omega_1^{rf} t + \phi_1) \sigma_1^x + \omega_2 \sigma_2^z + 2\Omega_2 \cos(\omega_2^{rf} t + \phi_2) \sigma_2^x + \omega_{xx} \sigma_1^x \sigma_2^x, \quad (1.20)$$

where $\omega_j/2\pi$ is the transition frequency of qubit j ; Ω_j and $\omega_j^{rf}/2\pi$ are, respectively,

the amplitude and frequency of the microwave signal applied to the write port of qubit j ; and $\omega_{xx}/2\pi = (t^{ent})^{-1}$ is the coupling frequency (if only the $\sigma_1^x\sigma_2^x$ term were present in \mathcal{H} , the time needed to go from a computational basis state to a maximally entangled state would be $t^{ent}/4$). To ensure the qubits remain decoupled in the absence of control signals, FLICFORQ systems should satisfy the weak coupling constraint that the non-secular coupling ω_{xx} be much weaker than the inter-qubit detuning $\Delta = |\omega_2 - \omega_1|$.

Now, the task is to show how the weak off-diagonal inter-qubit coupling ω_{xx} may be used to perform two-qubit gates without adjusting ω_1 and ω_2 .

FLICFORQ with double-resonant irradiation

When the microwave field strengths Ω_1 and Ω_2 are tuned to satisfy [105],

$$\Omega_2 + \Omega_1 = |\omega_2 - \omega_1| \quad (1.21)$$

the upper Rabi sideband of the low frequency qubit overlaps the lower Rabi sideband of the high-frequency qubit, and the qubits develop a pure coupling Hamiltonian in the rotating frame given by

$$2\mathcal{H}^{eff}/\hbar = \omega_{xx}^{eff}[(\sigma_1^y\sigma_2^y + \sigma_1^z\sigma_2^z)\cos(\phi_1 - \phi_2) + (\sigma_1^z\sigma_2^y - \sigma_1^y\sigma_2^z)\sin(\phi_1 - \phi_2)], \quad (1.22)$$

of effective strength

$$\omega_{xx}^{eff} = \omega_{xx}/8. \quad (1.23)$$

This situation is depicted below in the dressed state picture [81].

As 1.22 is a universal Hamiltonian [56], this scheme allows us to perform any

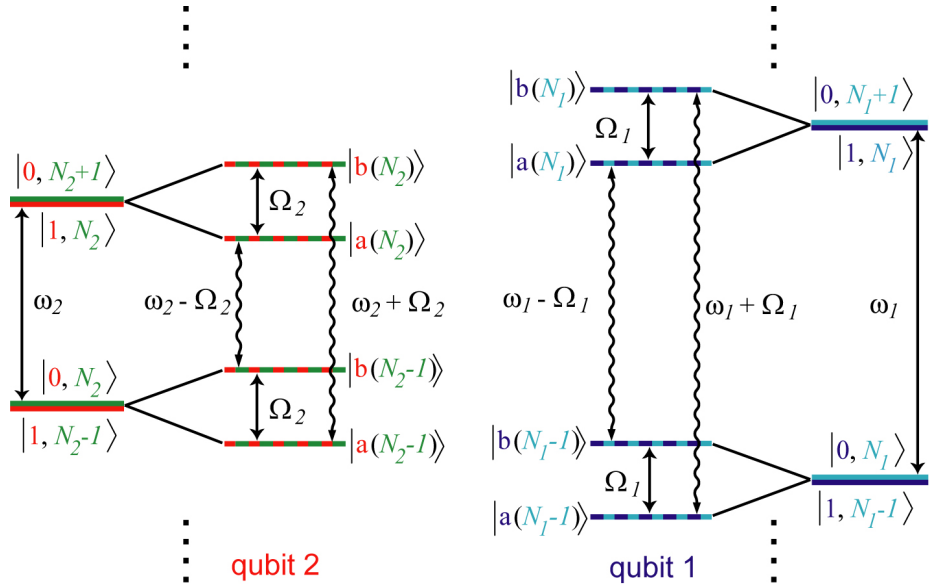


Figure 1.10: Energy levels of qubit + rf photons systems with (inner levels) and without (outer levels) qubit-photon coupling. *Outer*: systems have an infinite ladder of doubly-degenerate levels corresponding to products of a photon number state (green, orange) and a qubit state (red, blue). *Inner*: Photon–qubit coupling lifts degeneracy in each manifold by Rabi frequency $\Omega_{1,2}$. Transitions between adjacent manifolds (wavy arrows) correspond to absorption/emission of a photon from dressed qubit system. The off-resonant qubits can be put on speaking terms by adjusting Rabi frequencies such that $\Omega_1 + \Omega_2 = \omega_1 - \omega_2 \equiv \Delta$. Shown is the symmetric case where $\Omega_{1,2} = \Delta/2$

two-qubit gate with strictly no DC excursions from the optimal bias point of either qubit, and with no need for a tunable coupling between the two qubits. This scheme can produce an on/off ratio of approximately 20dB, see Chapter Three. Much higher on/off ratios are possible if the residual coupling during one-qubit gates is actively cancelled or refocused.

Generalization to off-resonant pulses The protocol can be generalized to the case of off-resonance microwave pulses [101]. The matching condition is analogous to 3.2 but then contains the generalized Rabi frequencies $\eta_j = \sqrt{\Omega_j^2 + \delta_j^2}$ in place of the drive strengths Ω_j . The off-resonant case allows one to make use of a *detuning field* of the microwave drives from the respective qubits, along with the drive strengths, to cover the spectral distance between ω_1 and ω_2 .

FLICFORQ with cross-resonance irradiation

The double-resonant irradiation scheme calls for Rabi drive amplitudes that are comparable to the inter-qubit detuning. This can lead to some difficulty, and practically limits the scheme to systems where the inter-qubit detuning is less than perhaps several hundred megahertz, and possibly up to a gigahertz or so with resonant pulses. But the gate speed decreases drastically if one moves too far towards detuned pulses, see 1.11 and ref. [101]. We developed an alternative irradiation protocol that relaxes these constraints and avails the FLICFORQ scheme to circuits having a broad range of parameters.

One needs to simply irradiate one qubit with a signal at the frequency of another. Then an effective interaction emerges,

$$2\mathcal{H}^{eff}/\hbar = \omega_{xx}^{eff}(\sigma_1^x\sigma_2^x \cos \phi_1 + \sigma_1^x\sigma_2^y \sin \phi_1)] \quad (1.24)$$

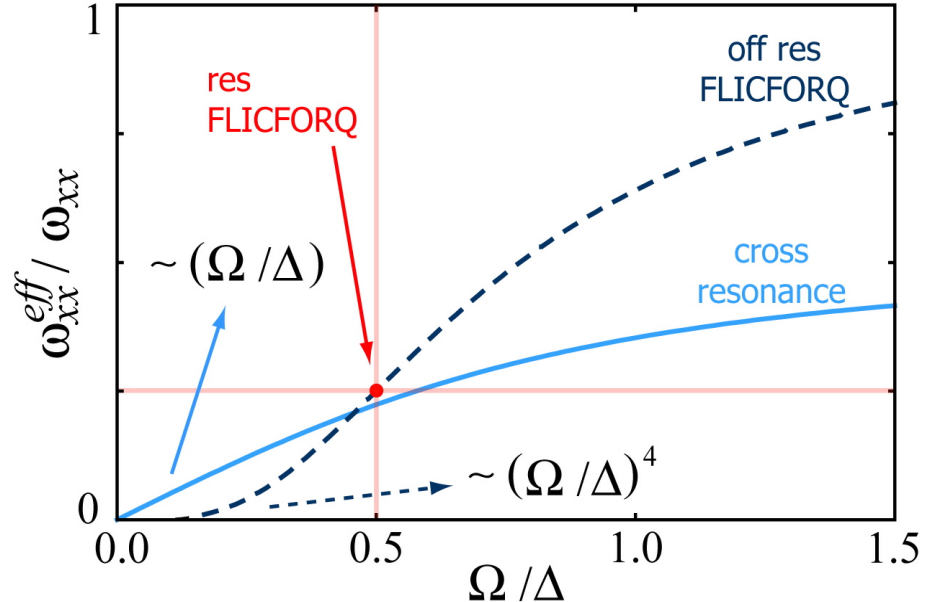


Figure 1.11: Effective interaction strength generated by cross-resonance irradiation as a function of drive strength : detuning ratio Ω/Δ (solid); generalized off-resonant FLICFORQ scheme of Ashhab and Nori (dashed); and original double-resonant driving of original FLICFORQ scheme (point at intersection of red lines). Equal drive amplitudes are assumed for the latter two. At small drive strengths the cross resonance effect is proportional to Ω/Δ , while off-resonant FLICFORQ coupling strength goes only as $(\Omega/\Delta)^4$. The horizontal and vertical red lines emphasize that satisfying the matching condition $\Omega_2 + \Omega_1 = \omega_2 - \omega_1$ with resonant pulses constrains all the available controls and thus does not admit tunability of the interaction strength.

whose strength,

$$\omega_{xx}^{eff} = \frac{\omega_{xx}}{2\sqrt{1 + (\Delta/\Omega)^2}},$$

increases linearly with the drive amplitude [116]. We call this gate scheme *cross resonance*. It is the minimal two qubit gate strategy: entangling two qubits requires only a single microwave tone applied to one of the qubits—the frequency ω_{rf} selects the target qubit, the amplitude Ω sets the gate speed, and the phase ϕ selects the principal axis in Hilbert space of the resulting two-qubit rotation. Like double resonance, this scheme produces an on/off ratio of approximately 20dB when the residual coupling is not refocused.

It may seem surprising that a dynamically tunable interaction strength is possible when the qubits are coupled only through a static linear reactance. But the qubits are themselves non-linear and mix the applied signals with virtual photons at their transition frequency. In essence, FLICFORQ with cross resonance irradiation achieves tunable coupling by exploiting these nonlinearities already present in the individual qubit subcircuits.

The effect can also be understood in the dressed atom picture. Whereas the above double resonance scheme makes use of the Rabi sidebands in the Mollow triplet of the driven quantum system, here we make use of the central peak [121]. The cross-resonance condition is precisely that which arranges this peak to overlap with the undriven qubit's bare transition.

1.5.5 Fourier approach to quantum gates

Though these two schemes address the key requirements, we can reasonably wonder what other drive signal configurations and effective interactions are possible.

More generally, we may broaden the question to include schemes where the qubits are subjected to DC control and where the coupling is not limited to be along $\sigma_1^x\sigma_2^x$ only. We emphasize that this question is important not only from the perspective of two-qubit gates, but also from the need to better understand the possible pitfalls when aiming to perform high fidelity one-qubit rotations. We had better, in other words, be aware of any strong effective interactions present in the system, whether we intend to exploit them when we wish to do two-qubit gates or simply to know to avoid them when we wish not to.

We have developed an approach to this problem based on Fourier analysis of the system Hamiltonian in a special rotating reference frame wherein the system dynamics are purely non-local. When applied to the two-qubit FLICFORQ-type

Hamiltonian the theory reveals other important configurations of the drive parameters which result in a significant inter-qubit interaction. Our general approach is sketched here, with a formalized presentation in Chapter Four.

We first transform the lab frame Hamiltonian to a special multiply rotating reference frame chosen to nullify the single-qubit terms in the Hamiltonian. In the case of two microwave-driven qubits, this frame rotates about four axes at four frequencies. Arriving to this quadruply rotating frame (i.e. the *quad frame*) requires two time-dependent and two time-independent rotations of each qubit. There, the full system dynamics are described by a purely non-local Hamiltonian. In the absence of any secular couplings, all terms are oscillatory at multiple frequencies, so under most conditions the effective Hamiltonian in this frame rapidly averages to zero.

However, we have seen above that there are some special configurations under which these time dependences cancel and the quad frame Hamiltonian (QFH) develops static terms. In general, we can identify all such configurations for an n -qubit system with the following technique.

The Hamiltonian is in general a non-linear function of the controls coupled to the system. We collectively denote these knobs by a control vector $\boldsymbol{\lambda}(t)$. We take the symbolic Fourier transform of the purely non-local Hamiltonian $\mathcal{H}(\boldsymbol{\lambda}(t))$, producing a Fourier decomposition of the form,

$$H(\omega; \boldsymbol{\lambda}) = \sum_j h_j(\boldsymbol{\lambda})\delta_j(\omega; \boldsymbol{\lambda}) \quad (1.25)$$

where h_j is an effective coupling Hamiltonian of $m \leq n$ qubits whose strength may depend on $\boldsymbol{\lambda}$; and $\delta_j(\omega; \boldsymbol{\lambda}) = \delta[g_j(\omega; \boldsymbol{\lambda})]$ is the Dirac delta function whose argument $g_j(\omega; \boldsymbol{\lambda})$ is a purely additive function of ω and the oscillation and drive frequencies in the problem. For example, in the two-qubit case, most generally

$g_j = f(\omega, \omega_1^{rf}, \omega_2^{rf}, \eta_1, \eta_2)$, where $\eta_j = \sqrt{(\omega_j^{rf} - \omega_j)^2 + \Omega_j^2}$ is the generalized Rabi frequency of qubit j . An effective inter-qubit coupling emerges whenever $\boldsymbol{\lambda}$ is adjusted such that one of $g_j = 0$.

The set of $\boldsymbol{\lambda}_k$'s defined according to:

$$\boldsymbol{\lambda} = \boldsymbol{\lambda}_k \Leftrightarrow g_k(0; \boldsymbol{\lambda}) = 0. \quad (1.26)$$

can be thought of as the *entanglement modes* of the system. Each is associated with a strength and a direction in Hilbert space, i.e. a particular combination of the possible couplings. When the strength of the effective Hamiltonian at an entanglement mode depends on a parameter in $\boldsymbol{\lambda}$ not appearing in the particular g_k , the effective Hamiltonian is dynamically tunable. In other words, certain controls can be used to turn on the effect while others are used to adjust its strength and direction. The Fourier approach is developed in more detail in chapter 4.

Two-qubit entanglement modes

A study of the two-qubit FLICFORQ-style Hamiltonian produces the associated entanglement modes:

$$\omega_1^{rf} \pm \omega_2^{rf} = 0 \quad (1.27a)$$

$$\eta_1 \pm \omega_1^{rf} \pm \omega_2^{rf} = 0 \quad (1.27b)$$

$$\eta_2 \pm \omega_1^{rf} \pm \omega_2^{rf} = 0 \quad (1.27c)$$

$$\eta_1 \pm \eta_2 \pm \omega_1^{rf} \pm \omega_2^{rf} = 0 \quad (1.27d)$$

The first of these is particularly interesting. On one hand, it implies that an effective coupling can be turned on by simply irradiating one qubit at the transition frequency

of the other, as we saw above with cross-resonance. But on the other hand, this entanglement mode could adversely affect the fidelity of one-qubit rotations performed with resonant control in the presence of crosstalk. The one-qubit errors resulting from this effect for some practical systems are discussed in chapter 5. A discussion of the other modes is also in Chapter Five.

1.5.6 GHZ state production

We have applied the Fourier approach to the study of the three-qubit systems, yielding strategies to produce tripartite entangled states.

DC control

For three-qubit Hamiltonians of the form

$$\begin{aligned} \mathcal{H} = & \frac{\hbar}{2} \sum_{k=1}^2 \left(\omega_k \sigma_k^z + 2\Omega_k \cos(\omega_k^{rf} t + \phi_k) \sigma_k^x \right) \\ & + \frac{\hbar}{2} \sum_{j,i=1; j \neq i}^3 \omega_{ji} \sigma_j^x \sigma_i^x + \omega_{123} \sigma_1^x \sigma_2^x \sigma_3^x. \end{aligned} \quad (1.28)$$

GHZ-type states can be produced with simple DC control of the qubit frequencies by tuning the qubit transition frequencies to satisfy,

$$\omega_1 + \omega_2 - \omega_3 = 0. \quad (1.29)$$

Then, an effective pure three-body interaction emerges

$$4\mathcal{H}^{eff}/\hbar = \omega_{123} (\sigma_1^x \sigma_2^x \sigma_3^x + \sigma_1^x \sigma_2^y \sigma_3^y + \sigma_1^y \sigma_2^x \sigma_3^y - \sigma_1^y \sigma_2^y \sigma_3^x) \quad (1.30)$$

that generates with high fidelity GHZ states directly without the need for pair-wise two-qubit gates, irradiation, or tuning the qubits into resonance. This surprising result takes advantage of the three-body secular point, where, in the presence of a weak three-body coupling term, any two of the qubits may conspire to exchange energy with the third [117].

AC control

We can also employ AC control over the qubit transition frequencies. There is an entanglement mode of the driven three qubit system at,

$$\omega_1^{rf} + \omega_2^{rf} - \omega_3^{rf} = 0, \quad (1.31)$$

whereat we find

$$8\mathcal{H}/\hbar \rightarrow \omega_{123}\sigma_1^x\sigma_2^x\sigma_3^x \cos\xi_1 \cos\xi_2 \cos\xi_3 \cos[\phi_1 + \phi_2 - \phi_3]. \quad (1.32)$$

Together, these AC and DC entanglement modes suggest an experimental strategy for directly exploiting a weak³ three-body interaction to generate GHZ states: aim the qubit frequencies (at optimal bias) to fall, through fabrication and circuit design, in the vicinity of the DC mode $\omega_1 + \omega_2 - \omega_3 = 0$; the natural scatter in fabrication parameters will of course prevent this from being rigorously satisfied. If possible, use DC tuning to make up for any discrepancies. Otherwise, simply apply irradiation to access the AC mode $\omega_1^{rf} + \omega_2^{rf} - \omega_3^{rf} = 0$. See chapter 5 for more details, including simulations of the three-qubit Bloch equations that confirm our analytical results from the Fourier approach.

³We haven't set any of the two-body couplings to zero. These modes just do not activate them.

1.5.7 Circuit design and fabrication

This work has employed some small innovations in the design and fabrication of superconducting circuits. First, we have designed and operated quantronium circuits with the readout mode defined by the odd mode of a coplanar stripline (CPS) superconducting resonator. The original microwave readout of the quantronium was performed by DC switching measurements of the readout junction [129, 26], and later at Yale with the Josephson Bifurcation Amplifier (JBA), where a lumped element on-chip shunt capacitance formed a non-linear resonator with the quantronium readout junction [139, 140, 131]. Size constraints, along with the need to limit stray inductances in the lines connecting the capacitance to the quantronium, necessitated the development of a more subtle approach for the simultaneous readout of multiple qubits. This type of readout has also been implemented using the geometrically defined modes of a coplanar waveguide (CPW) superconducting resonator, an implementation called the Cavity Bifurcation Amplifier (CBA). Yet, the CPW geometry is even more spatially extensive, and the particular geometry of the resonator and qubit system makes it rather tricky to realize coupled qubit circuits with independent control and readout. The CBA also does nothing to simplify the fabrication process compared to the JBA. Rather than a multi layer capacitor technology, it relies on a resonator defined through optical lithography, and quantronium circuits defined through one or more SEM lithography steps [132].

The CPS geometry was developed to address both of these shortcomings. Though the resonators are long, they are very narrow, and may be meandered to fit in a single SEM field of view, allowing the resonator and qubit circuits to be fabricated in a single SEM lithography and double-angle evaporation step. This short sample fabrication time is a considerable advantage for any circuits, but especially in regards

to multiqubit circuits, where our imperfect control over fabrication parameters is made more acute by the need for multiple copies to turn out with usable parameters simultaneously. Also, the CPS geometry couples rather elegantly to the quantronium circuits, as the parallel split Cooper pair box and readout junction can be placed as a termination at the end of the $\lambda/4$ resonator. This leaves the qubit islands exposed and free to be coupled to one another with whatever coupling subcircuit we wish to add, here a simple capacitor.

Furthermore, the CPS + quantronium has allowed us to address one of the rather subtle challenges in obtaining devices with reliable and predictable parameters. In the standard Dolan bridge lithography technique, both very small ($\sim 0.05\mu m^2$ qubit mode) junctions and very large ($\sim 10\mu m^2$ readout mode) junctions are made in the same step and each defined by depositing metal under a suspended bridge. Because the shift between the two images formed by the deposited metal in a double angle evaporation is practically limited by the resist thickness, large area junctions can only take on elongated geometries. This has two problems. First, the critical current density of a junction is set not only by the oxidation parameters, but also by edge effects that depend on the area-to-perimeter ratio. This leads to the practical observation that large and small junctions formed in the same double angle evaporation and oxidation will have very different critical current densities. And second, it requires long and narrow suspended bridges whose delicacy presents a common failure mode.

In an attempt to alleviate these issues, we made many of our circuits with a hybrid mask with Dolan bridges to define the small junctions and *ledges* that provide mechanical shielding of the substrate, but do not require deep trenches or suspended bridges, to define the large junctions. This allows better control the large and small junction critical current densities. as we have extricated ourselves from an awkward

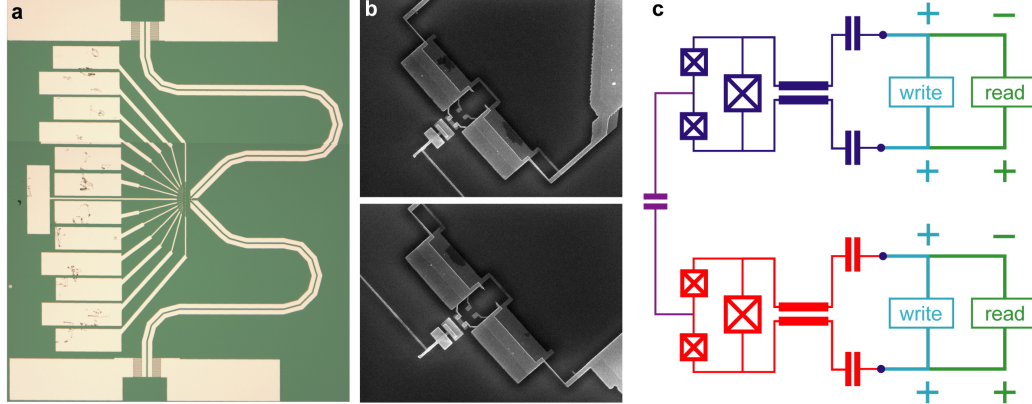


Figure 1.12: Superconducting circuit implementing coupled quantronia in coplanar stripline (CPS) geometry. **a.** Optical image of chip $\sim 3\text{mm}^2$ chip. Control signals are launched onto chip via large bonding pads (top and bottom rectangles), connected to interdigitated CPS resonator input capacitor. At left with scratches are probe pads for test quantronia. **b.** SEM images of the individual quantroniun subcircuits terminating the CPS resonators. Qubit islands are topologically exposed, making it easy to achieve inter-qubit capacitive coupling. **c.** Equivalent circuit diagram. All control signals are coupled to CPS even (WRITE) or odd (READ) mode.

reliance on long and often flimsy bridges for achieving the large area junctions.

Sample images of coupled coplanar stripline quantronium circuits and equivalent circuit diagrams are shown in 1.12.

1.5.8 Experimental results

We have carried out microwave measurements of these circuits in a dilution refrigerator at 20mK using the microwave measurement setup of 7.4.

Qubit readout Earlier results on the JBA + quantronium and CBA + quantronium have obtained maximum S-curve separation between the ground and first excited state of 35% and 50%, respectively [132, 131]. Our results, shown below, demonstrate an 80% separation.

We have not conclusively identified the source of this improved contrast, though

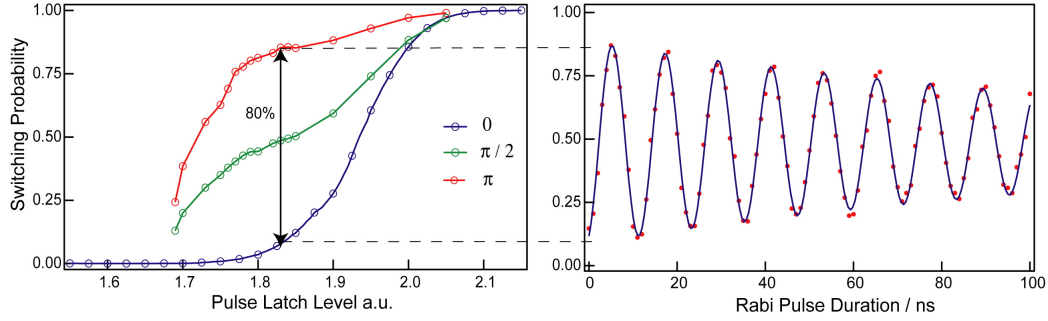


Figure 1.13: High raw visibility readout of coplanar stripline quantronium circuit. *Left:* Switching probability as a function of readout pulse latch level with no qubit control pulse (blue), $\pi/2$ -pulse (green), π -pulse (red). Location of maximum separation indicates optimal readout pulse height. *Right:* Sample Rabi oscillations. Points correspond to mean switching probability for 2000 events. Fit (blue) indicates raw visibility of 87%.

the differences between the 80% separation we have observed and the earlier observed values are too large to be due simply to decreased relaxation of the qubit being measured.

Qubit control We have carried out individual qubit Rabi oscillations experiments on two separate samples of capacitively coupled quantronium-style qubits with CPS resonator readouts. By performing synchronous Rabi experiments on each qubit of a coupled qubit sample, we have demonstrated simultaneous independent manipulation and read out of two interacting quantum circuits.

The data support the conclusion that we have achieved simultaneous independent control and readout of the quantum states of two interacting electrical circuits.

Qubit-qubit coupling We have obtained preliminary evidence to support our proposed cross-resonance irradiation scheme. The fixed non-secular coupling owing to the island-island coupling capacitance leads to a microwave power dependent effective coupling strength when one qubit is irradiated at the frequency of the other.

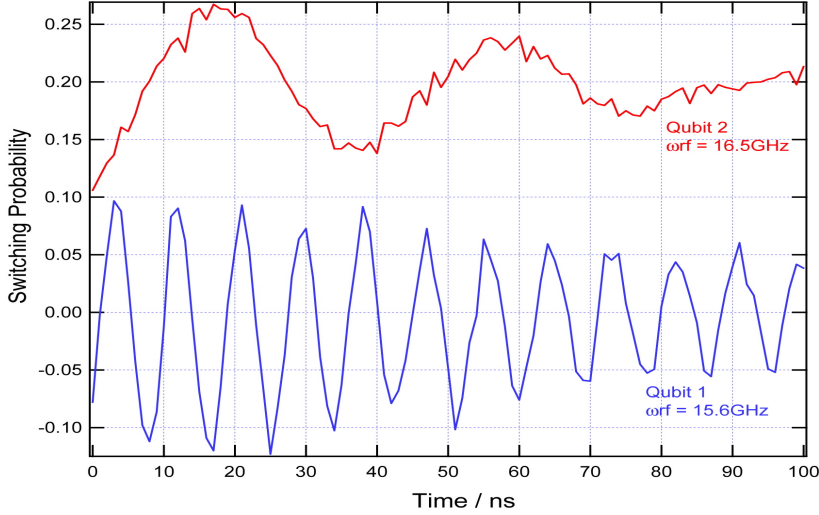


Figure 1.14: Simultaneous independent control and readout of two coupled superconducting qubits. A Rabi train of microwave pulses was applied to qubit 1 at 15.60GHz and to qubit 2 at 16.50GHz. Pulses were produced by splitting the output from a single Tektronix AWG channel and using each copy to drive a direct conversion mixing setup with an LO signal at the respective microwave frequency. Readout pulses are also synchronous, but originate from separate Agilent 80MHz AWG's, each enslaved to the master clock of the Tektronix AWG.

1.6 Conclusion

There are a selection of techniques available to the experimentalist by which to implement two-qubit gates in superconducting circuits. Individual qubit subcircuits may be tuned through either microwave or DC controls, or not at all. They can be linked together through fixed linear subcircuits, or through non-linear subcircuits subject, again, to either DC or microwave control. This thesis has focused on the case of fixed linear coupling of microwave controlled qubit subcircuits, an approach advantaged by its reliance on purely high-frequency signals requiring comparatively tiny relative bandwidth; by the simplicity of scaling from successful one-qubit experiments; by the lack of added control lines that would inevitably complicate system operation and add interactions with stray degrees of freedom in the electromagnetic environment; and by the relative ease with which the circuits themselves may be

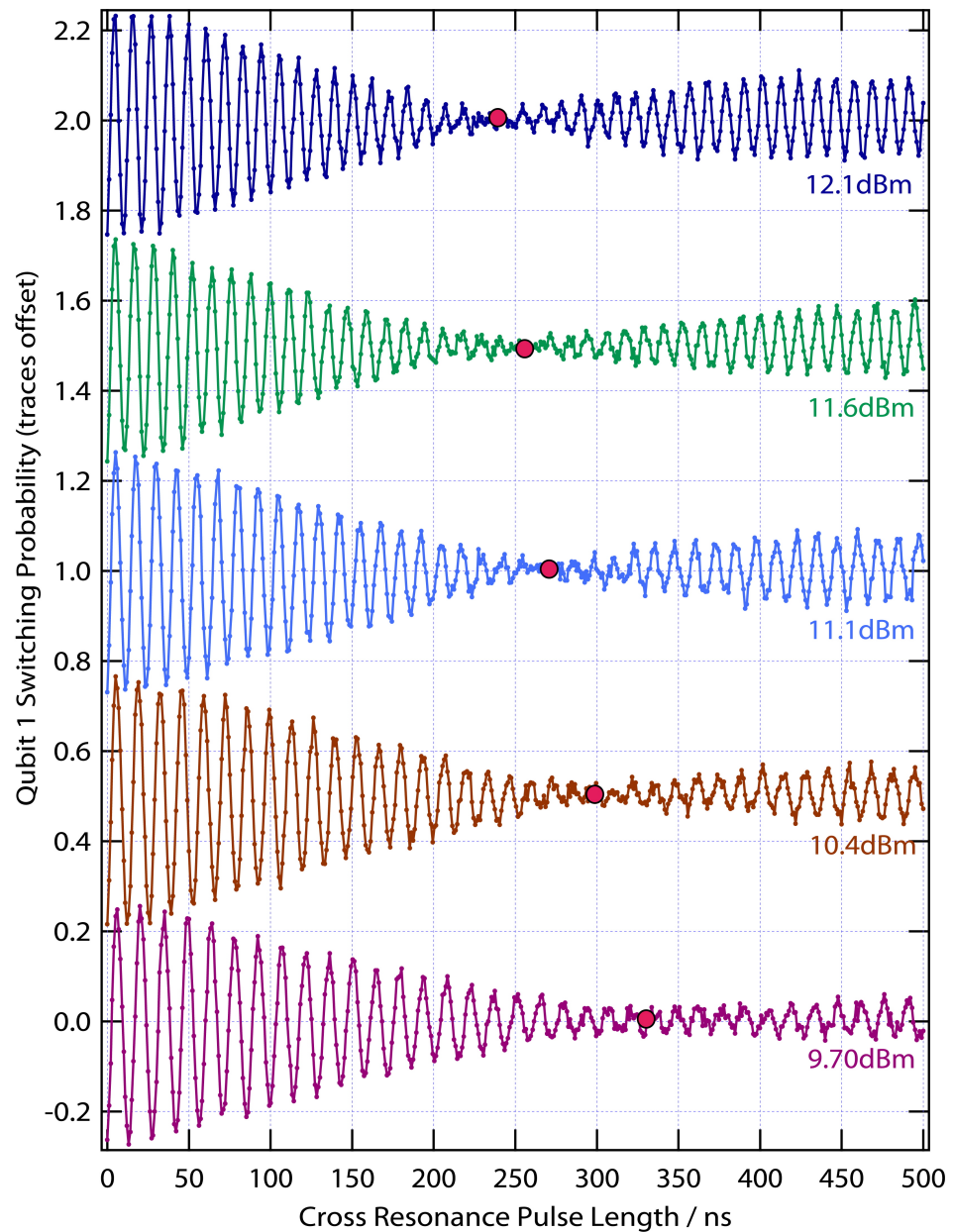


Figure 1.15: Rabi beating of two superconducting qubits subject to cross-resonance irradiation. Q1 is irradiated at the transition frequency of Q2 (16.331GHz), and the state of Q1 is read out. Different traces correspond to different drive powers; effective interaction strength increases with drive amplitude.

fabricated.

For qubit circuits in this FLICFORQ style, we have developed specific irradiation protocols and control sequences to exploit the tunabilities provided by the Hamiltonian to realize non-local rotations in the two-qubit Hilbert space. We have developed a general technique that can be applied to these and a broad class of other interacting qubit systems. Application of the technique has uncovered the possibility for several other irradiation schemes while also containing within it our earlier results and those of others. In particular, it reveals a truly minimal recipe for a fully tunable two-qubit gate in the FLICFORQ architecture. On the other hand, we have identified effects that will have to be accounted for, such as crosstalk-enhanced coupling, if high-fidelity one-qubit control is to be realized.

When applied to three-qubit systems, our Fourier approach leads to the prediction that a very weak and static off-diagonal three-body coupling term in a three-qubit Hamiltonian can be exploited to directly generate maximal tripartite entanglement, even when the three-body coupling is by far the weakest energy scale in the problem and the qubits are far detuned from one another, a finding which bears on the optimal design of superconducting quantum registers. Finally, we have designed and measured samples of capacitively coupled quantronium qubits, obtaining preliminary evidence to support the cross-resonance gate protocol.

Chapter 2

Two-Qubit Toolkit

2.1 Introduction

In this chapter we derive some useful tools for the quantum gate problem. First, we simplify the problem by deriving a discrete Hilbert space with a finite transformation group that nonetheless admits a description of a broad class of quantum gates. We show how the discrete rotations connecting states in the discrete space form a natural language for quantum gates and quantum logic. We then make connection back to the continuous Hilbert space wherein practical quantum gate protocols take place. We also give a representation of a two-qubit state in real space and show how it can be used to set the measurement axes in a Bell measurement. We will make use of the tools developed in this chapter throughout much of the thesis.

2.2 Discrete Hilbert space

The discrete nature of the configuration space for n classical bits is the key property allowing robustness of digital computation. The Hilbert space H_n for n qubits, on the other hand, is a *continuous* complex manifold. This continuity appears essen-

tial to the exponential speed-up of some quantum computing algorithms, such as Shor’s factoring algorithm [3], over their classical counterparts¹. But it also poses a challenging problem for the experimentalist: errors in quantum gates are themselves continuous, so even minute errors can accumulate throughout the execution of an algorithm and lead to its failure.

Yet, quantum error correction and fault-tolerant computation schemes have been developed to meet this challenge[89, 6, 90]. That reliable quantum computation is possible using both a noisy quantum register and noisy gates is a result of surpassing importance. However, such schemes still place stringent fidelity requirements on the basic quantum gates and the quantum register: estimates for the threshold error probability above which they fail are typically 10^{-5} – 10^{-6} [7].

Can universal control of a scalable quantum register with this level of fidelity be realized? If so, are there concepts we can borrow from digital computation that might facilitate the development of this technology? If not, are there intermediate computational paradigms that might relax these requirements, but still exploit “extra-classical” phenomena such as quantum parallelism and quantum entanglement? We note that these are still possible in a *discrete* Hilbert space.

Quantum gates are typically implemented by applying time-dependent fields to a qubit system. They correspond to rotations of a unit vector in H_n , with the angle of rotation usually determined by the duration and amplitude of the pulse which generates the field. In principle, such rotations are simple to implement, given an appropriate time-dependent Hamiltonian. But in practice, noise in both the qubit system and applied fields inevitably leads to errors. Sophisticated techniques that build up a desired gate from a sequence of rotations about successively orthogonal axes have been developed to mitigate the effects of noise. In the field of NMR,

¹As evinced by the Gottesman-Knill theorem, for example. See [86].

especially, techniques for performing high-fidelity rotations are now very mature[91]. Yet such techniques for protecting against noise are not directly generalizable to arbitrary angles and axes of rotation. As a result, most experimental protocols for quantum manipulations rely as heavily as possible on a small set of rotations, usually by an angle of $\pi/2$ or π , specifically optimized for the given qubit system. In the landmark experiment by Vandersypen, et al, in which an NMR-based quantum processor was used to factor the number fifteen via Shor’s algorithm, the protocol contained a single rotation by an angle less than $\pi/2$ —a conditional $\pi/4$ rotation[35].

Nonetheless, universal control of a quantum register requires in theory only a finite number of discrete gates, provided the gates form a universal set. Then an arbitrary “software-level” quantum gate can be constructed to a precision ϵ by concatenating $\mathcal{O}(\log^c(1/\epsilon))$ discrete gates from the universal set ($c \approx 2$)[7]. However, given that each discrete gate itself would likely comprise a sophisticated series of rotations, the prospect of concatenating $\mathcal{O}(\log^c(1/\epsilon))$ such gates to create each software-level operation—and doing so before the register decoheres—makes the fidelity requirements of fault-tolerant computing schemes all the more exacting.

Much of this difficulty in achieving high-fidelity control of a quantum register can be alleviated by limiting ourselves to *non* universal sets of quantum gates which generate only *finite* transformation groups. A finite transformation group implies a finite number of possible states, so this is equivalent to imposing a discretization on the underlying Hilbert space: the quantum register becomes “digital”. By suitably choosing the transformation group, the allowed states can be selected to have certain well-defined properties, such as known expectation values with respect to a set of measurement operators.

As an illustration of this idea, consider the task of testing the experimental protocol for generating one-qubit rotations, which can be represented on the Bloch sphere.

Suppose we wish to optimize the fidelity of a $\pi/2$ rotation about the y -axis in a given qubit system. Starting from the state $|0\rangle$, we perform a counter-clockwise $\pi/2$ rotation about the y -axis, yielding the target state $|+x\rangle = (|0\rangle + |1\rangle)/\sqrt{2}$, then we perform a measurement in the $\{|0\rangle, |1\rangle\}$ basis. By repeating this many times, we obtain the expectation value $\langle \sigma_z \rangle$ of the target state $|+x\rangle$. Assuming imperfections in the state preparation and readout have been accounted for, this expectation value would approach zero if our $\pi/2$ gate were perfect, since $\langle +x | \sigma_z | +x \rangle = 0$, while deviations from zero would imply an imperfect $\pi/2$ gate. Specifically, $\langle \sigma_z \rangle = \delta$ would imply that, on average, the gate has performed a rotation by an angle of $2 \arccos \sqrt{(\delta + 1)/2}$. With knowledge of other one-qubit discrete states and their expectation values $\langle \sigma_i \rangle$, we could also test rotations about the x - and z -axes. By direct generalization, this simple protocol can be used to test rotations on any number of qubits, provided we have an appropriate discrete set of target states.

Also, quantum feedback and bang-bang control techniques that *dynamically* correct or decouple quantum processes are often described by a finite set of operations and allowed states[92]. By performing continuous weak measurements on the quantum system, it is possible to control and correct quantum state evolution through feedback[93, 94]. Incorporating these techniques into quantum computing experiments could also be facilitated if the number of processes involved were reduced to include only a small class of rotations connecting states with well-defined properties.

Having explained why we wish to consider a discrete subset of the full continuous Hilbert space, we would now like to draw a geometrical analogy. Since we do not want to privilege any region of Hilbert space over any other, the set must comprise a uniform sampling of H_n . The structure of the finite sets we have in mind is exemplified in real space by the Platonic solids—geometrical figures such as the tetrahedron, cube and octahedron characterized by the geometric equivalence of their vertices—

which represent discrete subsets uniformly spanning a sphere in \mathbb{R}^3 . In short, we are seeking to generalize the Platonic solids to Hilbert space by selecting from H_n a finite set of states corresponding to the vertices of a 2^n -dimensional complex uniform polytope. We call such subsets *uniform Hilbertian polytopes*, and denote them by \mathfrak{H}_n .

In discretizing an n -qubit register, what extra-classical phenomena must be sacrificed? If we select the transformation group to include only π rotations—the quantum generalizations of the NOT gate—we generate only a discrete set of 2^n states, and fall back on a purely classical register, with no possibility for quantum entanglement. But, as we will show, the next level towards finer rotations, the transformation group based on $\pi/2$ rotations, is sufficient for rich extra-classical behavior: the number of discrete states in the set then grows as $2^{(n^2+3n)/2}$ [95], the majority of which are entangled for $n > 2$. Also, the super-extensive growth of the discrete set relative to the classical number of states 2^n implies that a great deal of the quantum parallelism possible in the full Hilbert space remains possible in the discrete set. Though such a digital quantum register would not allow algorithms which are exponentially faster than their classical counterparts (Gottesman-Knill theorem), a possible reduction of an algorithmic scaling speed from $O(n^2)$ to $O(n)$ could still be useful.

At the same time, within the framework of traditional quantum computation, a discrete set and its associated transformation group can provide a useful “roadmap” for navigation in the entire Hilbert space.

The notion of discrete sets of n -qubit states is not novel. Indeed, discrete sets have already been considered in quantum error-correcting codes. There, a special set of 2^k orthogonal states, to be used as codewords for the basis states of k encoded qubits, are selected from a higher-dimensional continuous space H_n . Gottesman’s stabilizer formalism provides a general framework for describing and producing quantum error-

correcting codes, and allows an analysis of a broad class of quantum networks in the Heisenberg picture[86, 96]. Powerful though it is, the stabilizer formalism approaches the problem of discretization algebraically; it does not address the geometric relationship between the discrete quantum states, nor the relationships among the various gates that connect these states.

The purpose of this section is thus to provide such a geometric approach to the uniform discretization of H_n , and to suggest the use of such discrete sets, either as an arena for exploring extra-classical behavior, or as a heuristic tool for the analysis of certain quantum information processing problems. We refer to these notions collectively as *digital quantum information*².

For simplicity, we focus here on the one- and two-qubit Hilbert spaces. However, most of our results are directly generalizable to higher-dimensional spaces. When possible, we use a language that makes this generalization straightforward, if tedious. In section 2, we treat the discretization problem using stabilizer theory and derive a class of generalized $\pi/2$ rotations belonging to the Clifford group that connect states in the discrete set. Later in section 3, we present an alternate, purely geometric approach to discretization based on shelling the high dimensional lattices.

2.2.1 Discretization based on stabilizer theory

Stabilizers and the generalized Pauli matrices

We begin this section with some essential results from stabilizer theory. First, define the n -qubit Pauli group \mathcal{G}_n as the set of all n -fold tensor products of 2×2 Pauli

²Later, we will use the phrase rigorously, in reference to the information content of the discrete Hilbert space.

matrices, with four possible overall phases to satisfy the closure requirement:

$$\mathcal{G}_n = \{\sigma_w, \sigma_x, \sigma_y, \sigma_z\}^{\otimes n} \otimes \{\pm 1, \pm i\}, \quad (2.1)$$

where³

$$\begin{aligned} \sigma_w = \sigma_0 &= \begin{bmatrix} 1 & 0 \\ 0 & 1 \end{bmatrix}, & \sigma_z = \sigma_1 &= \begin{bmatrix} 1 & 0 \\ 0 & -1 \end{bmatrix}, \\ \sigma_x = \sigma_2 &= \begin{bmatrix} 0 & 1 \\ 1 & 0 \end{bmatrix}, & \sigma_y = \sigma_3 &= \begin{bmatrix} 0 & -i \\ i & 0 \end{bmatrix}. \end{aligned}$$

Clearly, each element of \mathcal{G}_n acts on the n -qubit Hilbert space. \mathcal{G}_n has order 4^{n+1} , and is generated by a minimal set of $2n$ elements, i.e. two non-identity σ 's acting on each qubit. We refer to individual elements of \mathcal{G}_n as *generalized* Pauli matrices, and denote them $\Sigma_{\alpha\beta\dots\zeta} = \sigma_\alpha \otimes \sigma_\beta \otimes \dots \otimes \sigma_\zeta$. The generalized Pauli matrices share many of the properties of the 2×2 Pauli matrices. For example, they all either commute or anti-commute, and

$$\Sigma_j^\dagger = \Sigma_j \text{ (Hermitian)}, \quad (2.2)$$

$$\Sigma_j^2 = \text{id} \text{ (Square root of unity)}, \quad (2.3)$$

$$\text{Tr} \Sigma_j^\dagger \Sigma_k = 2^n \delta_{jk} \text{ (Orthogonal)}. \quad (2.4)$$

A stabilizer is an Abelian subgroup of the Pauli group. In the present work, we are predominantly concerned with the commutation properties of the generalized Pauli matrices, so we neglect the phases $\{\pm 1, \pm i\}$ required for closure of \mathcal{G}_n under multiplication. That is, we deal with the *set* \mathcal{S}_n of 4^n generalized Pauli matrices

³The present numbering scheme has been chosen to coincide with the binary vector space representation of stabilizer codes, as in [96].

rather than the group \mathcal{G}_n . To distinguish the Abelian subsets of \mathcal{S}_n from the Abelian subgroups of \mathcal{G}_n , we refer to the former as *pseudostabilizers*, a name which also highlights the close relationship between this work and stabilizer theory.

The largest possible subsets of \mathcal{S}_n whose elements all mutually commute have 2^n elements. These *maximal* pseudostabilizers will form the foundation of our discretization procedure.

The uniform Hilbertian polytope \mathfrak{H}_n

We are now in a position to discuss a formal definition for the uniform Hilbertian polytope for n qubits. First, we establish the desired properties the discrete sets must have. We seek to construct \mathfrak{H}_n , such that:

1. It contains all the states $|b_0 b_1 \dots b_{n-1}\rangle$ corresponding to the classical bit configurations.
2. Each state of \mathfrak{H}_n is geometrically equivalent to all the others (uniformity).
3. The distance between two normalized states Ψ_j and Ψ_k , defined as

$$d_{jk} = 2 \cos^{-1}(\langle \Psi_j | \Psi_k \rangle) \quad (2.5)$$

satisfies⁴

$$d_{jk} \geq \pi/2 \text{ for all } j, k. \quad (2.6)$$

4. It is the largest set of states which satisfies the above requirements.

Denote by s_n^a the maximal pseudostabilizers in \mathcal{S}_n . Then these desired properties are obtained if we adopt the following construction for the vertices of \mathfrak{H}_n :

Definition 1 *An n -qubit state vector is an element of \mathfrak{H}_n if and only if it is a*

⁴Discretizations with a finer minimum distance may be useful and would be interesting to explore. For one qubit this could correspond, for instance, to the icosahedral geometry.

common eigenvector of each element of a maximal pseudostabilizer s_n^a . That is, if Σ_j is a generalized Pauli matrix on n qubits belonging to s_n^a , $|\Psi_j\rangle$ is an n -qubit state vector, and λ_j is an eigenvalue of Σ_j belonging to the vector $|\Psi_j\rangle$,

$$|\Psi_j\rangle \in \mathfrak{H}_n \Leftrightarrow \Sigma_j |\Psi_j\rangle = \lambda_j |\Psi_j\rangle \text{ for all } \Sigma_j \in s_n^a. \quad (2.7)$$

As a consequence of this definition, and from the theory of stabilizers, we find:

- a) Each s_n^a , which has $2^n - 1$ elements different from the identity, generates 2^n different discrete states all separated by $d_{jk} = \pi$. Each state corresponds to a unique pattern of $\lambda_j = \pm 1$.
- b) Each s_n^a shares exactly half, or 2^{n-1} , of its elements with its nearest neighbors; 2^{n-2} with its second-nearest neighbors, etc. Any discrete state in \mathfrak{H}_n therefore has n “levels” of non-orthogonal neighboring states.
- c) For each s_n^a and each of its nearest neighbors s_n^b one can associate by a general algorithm a transformation from the common eigenvectors of s_n^a to those of s_n^b . That is, any two states of \mathfrak{H}_n are linked by a finite sequence of similarity transformations.
- d) The similarity transformations are formed from generalized orthogonal $\pi/2$ rotations of the form:

$$X_{kl}^a = \frac{1}{\sqrt{2}} (\Sigma_k + i\Sigma_l), \text{ where } \Sigma_k, \Sigma_l \in s_n^a. \quad (2.8)$$

The superscript a denotes a subset s_n^a to which both its Σ 's belong and the subscripts specify the Σ 's. The inverse operations are:

$$(X_{kl}^a)^{-1} = \frac{1}{\sqrt{2}} (\Sigma_k - i\Sigma_l) = -iX_{lk}^a. \quad (2.9)$$

This definition implies that for any X ,

$$X^\dagger X = \text{id} \quad (\text{Unitary}), \quad (2.10)$$

$$X^4 = -\text{id} \quad (\pi/2 \text{ Rotations}), \quad (2.11)$$

which is consistent with the property that a spin-1/2 acquires an overall phase of $e^{i\pi} = -1$ when rotated by 2π .

- e) The X 's generate the Clifford group \mathcal{C}_n , defined as the normalizer of the Pauli group[96], which has the property of leaving \mathfrak{H}_n invariant (proof to follow).
- f) The set \mathcal{S}_n of generalized Pauli matrices on n qubits contains

$$s = \prod_{k=0}^{n-1} (2^{n-k} + 1) \quad (2.12)$$

maximal pseudostabilizers s_n^a . Each has 2^n elements, and contributes 2^n simultaneous eigenvectors. The uniform Hilbertian polytope on n qubits \mathfrak{H}_n therefore contains

$$V_n = 2^n \prod_{k=0}^{n-1} (2^{n-k} + 1) \quad (2.13)$$

vertices, or states[95]. The following table gives the first values of V_n , along with the number of classical bit configurations for comparison.

n	1	2	3	4	5	6	7
V_n	6	60	1080	36,720	2,423,520	315,057,600	81,284,860,800
C_n	2	4	8	16	32	64	128

The digital quantum information in n qubits can be defined as the information content of \mathfrak{H}_n , i.e. as $\log_2 V_n$. It is easy to show that V_n grows as $2^{(n^2+3n)/2}$, so this information content is super-extensive in n . While it is insufficient for algorithms

which would be exponentially faster than classical ones, it is nonetheless a remarkable property for a discrete space.

We now turn to an explicit construction of the uniform Hilbertian polytope for the one- and two-qubit cases.

The one-qubit case, \mathfrak{H}_1

We show here that \mathfrak{H}_1 is isomorphic to an octahedron. For one qubit, the set \mathcal{S}_n is simply the Pauli matrices: $\mathcal{S}_1 = \{\sigma_w, \sigma_x, \sigma_y, \sigma_z\}$. The last three σ 's anti-commute with one another, while they all commute with the identity σ_w . So the three sets of mutually commuting matrices are trivial to construct: $s_1^1 = \{\sigma_w, \sigma_z\}$, $s_1^2 = \{\sigma_w, \sigma_x\}$ and $s_1^3 = \{\sigma_w, \sigma_y\}$.

When the elements of s_1^1 are diagonalized, we obtain the computational basis:

$$|+z\rangle = |0\rangle, \quad (2.14)$$

$$|-z\rangle = |1\rangle. \quad (2.15)$$

s_1^2 generates the pair

$$|+x\rangle = \frac{|0\rangle + |1\rangle}{\sqrt{2}}, \quad (2.16)$$

$$|-x\rangle = \frac{|0\rangle - |1\rangle}{\sqrt{2}}. \quad (2.17)$$

And s_1^3 generates

$$|+y\rangle = \frac{|0\rangle + i|1\rangle}{\sqrt{2}}, \quad (2.18)$$

$$|-y\rangle = \frac{|0\rangle - i|1\rangle}{\sqrt{2}}. \quad (2.19)$$

There are three orthogonal $\pi/2$ rotations, which form the *seed* of \mathfrak{H}_1 :

$$\begin{aligned} X_{01}^1 &= \frac{1}{\sqrt{2}} (\sigma_0 + i\sigma_1), \\ X_{02}^2 &= \frac{1}{\sqrt{2}} (\sigma_0 + i\sigma_2), \\ X_{03}^3 &= \frac{1}{\sqrt{2}} (\sigma_0 + i\sigma_3). \end{aligned} \quad (2.20)$$

The diagonalization of the seed elements leads directly to the six eigenstates, as summarized in the table below. The states are listed here as unnormalized row vectors for clarity, and are separated into columns according to their eigenvalues.

Set	$1+i$	$1-i$
1	(1, 0)	(0, 1)
2	(1, 1)	(1, -1)
3	(1, i)	(1, $-i$)

Each of the $\pi/2$ rotations has an inverse:

$$(X_{0k}^k)^{-1} = -iX_{k0}^k = \frac{1}{\sqrt{2}} (\sigma_0 - i\sigma_k). \quad (2.21)$$

It is easy to verify that

$$(X_{0k}^k)^2 = \frac{1}{2} (\sigma_0 + i\sigma_k)^2 = i\sigma_k \quad (2.22)$$

and that the X 's are mapped into one another by similarity transformation:

$$\begin{aligned}
X_{0j}^j X_{0i}^i (X_{0j}^j)^{-1} &= \frac{1}{2\sqrt{2}} (\sigma_0 + i\sigma_j) (\sigma_0 + i\sigma_i) (\sigma_0 - i\sigma_j) \\
&= \frac{1}{2\sqrt{2}} (2\sigma_0 + 2i \epsilon_{ijk} \sigma_k) \\
&= X_{0k}^k \quad \text{if } \epsilon_{ijk} = 1 \\
&= (X_{0k}^k)^{-1} \quad \text{if } \epsilon_{ijk} = -1
\end{aligned} \tag{2.23}$$

This implies that each X transforms a member of \mathfrak{H}_1 into its neighbor.

Proof. If

$$X^j |\Psi_j\rangle = \lambda_j |\Psi_j\rangle$$

and if

$$|\Psi_{i(j)}\rangle = X^i |\Psi_j\rangle,$$

then

$$\begin{aligned}
X^i X^j (X^i)^{-1} |\Psi_{i(j)}\rangle &= X^i X^j |\Psi_j\rangle \\
&= \lambda_j X^i |\Psi_j\rangle \\
&= \lambda_j |\Psi_{i(j)}\rangle
\end{aligned}$$

therefore $|\Psi_{i(j)}\rangle$ is an eigenvector of X^k . \blacksquare

The X 's with their inverse generate a twenty-four element group isomorphic to the octahedral group of pure rotations which leaves the octahedron invariant.

The two-qubit case, \mathfrak{H}_2

The set of generalized Pauli matrices for two qubits \mathcal{S}_2 comprises $4^2 = 16$, $2^2 \times 2^2$ matrices given by $\Sigma_{\lambda\mu} = \sigma_\lambda \otimes \sigma_\mu$, $\lambda, \mu = w, x, y, z$, as presented below. We write the

index on the σ' s in binary, then concatenate the two strings to form the new index for the Σ' s. For example, $\sigma_y \otimes \sigma_z = \sigma_3 \otimes \sigma_1 = \sigma_{11} = \sigma_{01} = \Sigma_{1101} = \Sigma_{13}$.

$$\Sigma_{ww} = \Sigma_0 = \begin{bmatrix} 1 & 0 & 0 & 0 \\ 0 & 1 & 0 & 0 \\ 0 & 0 & 1 & 0 \\ 0 & 0 & 0 & 1 \end{bmatrix} \quad \Sigma_{wz} = \Sigma_1 = \begin{bmatrix} 1 & 0 & 0 & 0 \\ 0 & -1 & 0 & 0 \\ 0 & 0 & 1 & 0 \\ 0 & 0 & 0 & -1 \end{bmatrix}$$

$$\Sigma_{wx} = \Sigma_2 = \begin{bmatrix} 0 & 1 & 0 & 0 \\ 1 & 0 & 0 & 0 \\ 0 & 0 & 0 & 1 \\ 0 & 0 & 1 & 0 \end{bmatrix} \quad \Sigma_{wy} = \Sigma_3 = \begin{bmatrix} 0 & -i & 0 & 0 \\ i & 0 & 0 & 0 \\ 0 & 0 & 0 & -i \\ 0 & 0 & i & 0 \end{bmatrix}$$

$$\Sigma_{zw} = \Sigma_4 = \begin{bmatrix} 1 & 0 & 0 & 0 \\ 0 & 1 & 0 & 0 \\ 0 & 0 & -1 & 0 \\ 0 & 0 & 0 & -1 \end{bmatrix} \quad \Sigma_{zz} = \Sigma_5 = \begin{bmatrix} 1 & 0 & 0 & 0 \\ 0 & -1 & 0 & 0 \\ 0 & 0 & -1 & 0 \\ 0 & 0 & 0 & 1 \end{bmatrix}$$

$$\Sigma_{zx} = \Sigma_6 = \begin{bmatrix} 0 & 1 & 0 & 0 \\ 1 & 0 & 0 & 0 \\ 0 & 0 & 0 & -1 \\ 0 & 0 & -1 & 0 \end{bmatrix} \quad \Sigma_{zy} = \Sigma_7 = \begin{bmatrix} 0 & -i & 0 & 0 \\ i & 0 & 0 & 0 \\ 0 & 0 & 0 & i \\ 0 & 0 & -i & 0 \end{bmatrix}$$

$$\Sigma_{xw} = \Sigma_8 = \begin{bmatrix} 0 & 0 & 1 & 0 \\ 0 & 0 & 0 & 1 \\ 1 & 0 & 0 & 0 \\ 0 & 1 & 0 & 0 \end{bmatrix} \quad \Sigma_{xz} = \Sigma_9 = \begin{bmatrix} 0 & 0 & 1 & 0 \\ 0 & 0 & 0 & -1 \\ 1 & 0 & 0 & 0 \\ 0 & -1 & 0 & 0 \end{bmatrix}$$

$$\Sigma_{xx} = \Sigma_{10} = \begin{bmatrix} 0 & 0 & 0 & 1 \\ 0 & 0 & 1 & 0 \\ 0 & 1 & 0 & 0 \\ 1 & 0 & 0 & 0 \end{bmatrix} \quad \Sigma_{xy} = \Sigma_{11} = \begin{bmatrix} 0 & 0 & 0 & -i \\ 0 & 0 & i & 0 \\ 0 & -i & 0 & 0 \\ i & 0 & 0 & 0 \end{bmatrix}$$

$$\Sigma_{yw} = \Sigma_{12} = \begin{bmatrix} 0 & 0 & -i & 0 \\ 0 & 0 & 0 & -i \\ i & 0 & 0 & 0 \\ 0 & i & 0 & 0 \end{bmatrix} \quad \Sigma_{yz} = \Sigma_{13} = \begin{bmatrix} 0 & 0 & -i & 0 \\ 0 & 0 & 0 & i \\ i & 0 & 0 & 0 \\ 0 & -i & 0 & 0 \end{bmatrix}$$

$$\Sigma_{yx} = \Sigma_{14} = \begin{bmatrix} 0 & 0 & 0 & -i \\ 0 & 0 & -i & 0 \\ 0 & i & 0 & 0 \\ i & 0 & 0 & 0 \end{bmatrix} \quad \Sigma_{yy} = \Sigma_{15} = \begin{bmatrix} 0 & 0 & 0 & -1 \\ 0 & 0 & 1 & 0 \\ 0 & 1 & 0 & 0 \\ -1 & 0 & 0 & 0 \end{bmatrix}$$

The products of these matrices can easily be found from

$$\Sigma_{\lambda\mu}\Sigma_{\eta\nu} = (\sigma_\lambda \otimes \sigma_\mu)(\sigma_\eta \otimes \sigma_\nu) = (\sigma_\lambda\sigma_\eta) \otimes (\sigma_\mu\sigma_\nu). \quad (2.24)$$

The maximal pseudostabilizers in \mathcal{S}_2 are presented below.⁵

Subset #	Letter notation	Number notation
1	$\{\Sigma_{ww}, \Sigma_{wz}, \Sigma_{zw}, \Sigma_{zz}\}$	$\{\Sigma_0, \Sigma_1, \Sigma_4, \Sigma_5\}$
2	$\{\Sigma_{ww}, \Sigma_{wx}, \Sigma_{zw}, \Sigma_{zx}\}$	$\{\Sigma_0, \Sigma_2, \Sigma_4, \Sigma_6\}$
3	$\{\Sigma_{ww}, \Sigma_{wy}, \Sigma_{zw}, \Sigma_{zy}\}$	$\{\Sigma_0, \Sigma_3, \Sigma_4, \Sigma_7\}$
4	$\{\Sigma_{ww}, \Sigma_{wz}, \Sigma_{xw}, \Sigma_{xz}\}$	$\{\Sigma_0, \Sigma_1, \Sigma_8, \Sigma_9\}$
5	$\{\Sigma_{ww}, \Sigma_{wx}, \Sigma_{xw}, \Sigma_{xx}\}$	$\{\Sigma_0, \Sigma_2, \Sigma_8, \Sigma_{10}\}$
6	$\{\Sigma_{ww}, \Sigma_{wy}, \Sigma_{xw}, \Sigma_{xy}\}$	$\{\Sigma_0, \Sigma_3, \Sigma_8, \Sigma_{11}\}$
7	$\{\Sigma_{ww}, \Sigma_{wz}, \Sigma_{yw}, \Sigma_{yz}\}$	$\{\Sigma_0, \Sigma_1, \Sigma_{12}, \Sigma_{13}\}$
8	$\{\Sigma_{ww}, \Sigma_{wx}, \Sigma_{yw}, \Sigma_{yx}\}$	$\{\Sigma_0, \Sigma_2, \Sigma_{12}, \Sigma_{14}\}$
9	$\{\Sigma_{ww}, \Sigma_{wy}, \Sigma_{yw}, \Sigma_{yy}\}$	$\{\Sigma_0, \Sigma_3, \Sigma_{12}, \Sigma_{15}\}$
10*	$\{\Sigma_{ww}, \Sigma_{zz}, \Sigma_{xx}, \Sigma_{yy}\}$	$\{\Sigma_0, \Sigma_5, \Sigma_{10}, \Sigma_{15}\}$
11*	$\{\Sigma_{ww}, \Sigma_{zz}, \Sigma_{xy}, \Sigma_{yx}\}$	$\{\Sigma_0, \Sigma_5, \Sigma_{11}, \Sigma_{14}\}$
12*	$\{\Sigma_{ww}, \Sigma_{zx}, \Sigma_{xz}, \Sigma_{yy}\}$	$\{\Sigma_0, \Sigma_6, \Sigma_9, \Sigma_{15}\}$
13*	$\{\Sigma_{ww}, \Sigma_{zx}, \Sigma_{xy}, \Sigma_{yz}\}$	$\{\Sigma_0, \Sigma_6, \Sigma_{11}, \Sigma_{13}\}$
14*	$\{\Sigma_{ww}, \Sigma_{zy}, \Sigma_{xz}, \Sigma_{yx}\}$	$\{\Sigma_0, \Sigma_7, \Sigma_9, \Sigma_{14}\}$
15*	$\{\Sigma_{ww}, \Sigma_{zy}, \Sigma_{xx}, \Sigma_{yz}\}$	$\{\Sigma_0, \Sigma_7, \Sigma_{10}, \Sigma_{13}\}$

Each of these fifteen sets, or pseudostabilizers, will yield four simultaneous eigenvectors, contributing four states to \mathfrak{H}_2 . We therefore recover the result that \mathfrak{H}_2 has sixty states.

These subsets can be classified as corresponding to entangled or product states by examining their generators. Note that each pseudostabilizer is generated by any two of its non-identity elements. The presence of the one-qubit identity σ_w when the

⁵Constructing the subsets of mutually commuting Pauli matrices can be done through a series of logical steps. The key is to note that $[\Sigma_{jk}, \Sigma_{lm}] = 0$ requires either $[\sigma_j, \sigma_l] = [\sigma_k, \sigma_m] = 0$ or $\{\sigma_j, \sigma_l\} = \{\sigma_k, \sigma_m\} = 0$

generators are decomposed into tensor products of one-qubit Pauli matrices implies that the states corresponding to that subset are product states. Conversely, the absence of the identity in this decomposition indicates that the states corresponding to that Abelian subset are fully entangled states. The subsets whose generators do not contain the one-qubit identity are denoted here and below by an asterisk(*)).

We can obtain all the states of \mathfrak{H}_2 directly by forming a mixed linear combination of the first two non-identity elements from within each set. For instance $X_{3,12} = \frac{1}{\sqrt{2}} (\Sigma_{wy} + i\Sigma_{yw})$, when diagonalized, gives four orthogonal eigenvectors with four different eigenvalues. (Note that other rotations from s_2^1 , such as $X_{12,15} = \frac{1}{\sqrt{2}} (\Sigma_{12} + i\Sigma_{15})$ and $X_{3,15} = \frac{1}{\sqrt{2}} (\Sigma_3 + i\Sigma_{15})$ will produce the same four eigenvectors, but with permuted eigenvalues.) We thus construct in this manner fifteen generalized X' s, each having a different principal axis, which form the seed of \mathfrak{H}_2 . Diagonalization of the seed X' s exhaustively gives the eigenvectors constituting \mathfrak{H}_2 . We list these eigenvectors below, separated into columns corresponding to the eigenvalues $(\pm 1 \pm i)$. For clarity, we list them as unnormalized row vectors. Again, entangled

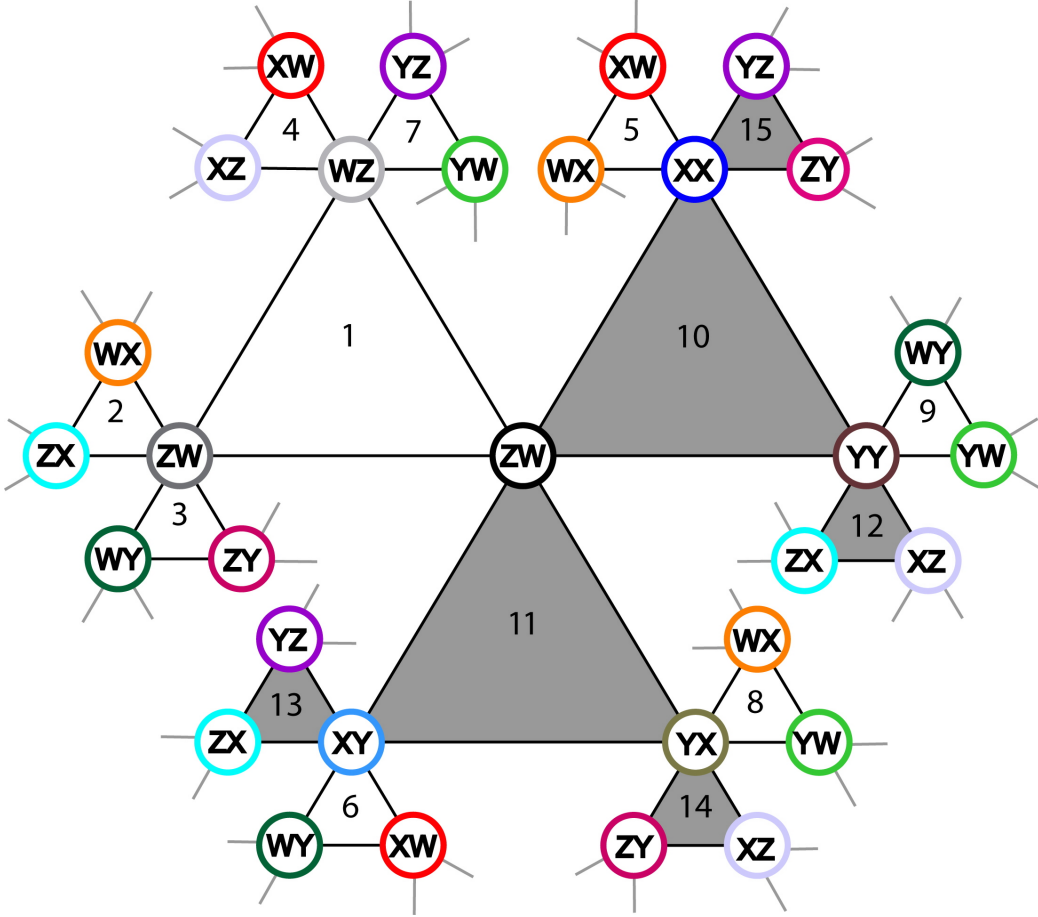


Figure 2.1: Graph of the set \mathcal{S}_2 of two-qubit generalized Pauli matrices Σ_j (circles bearing the subscript of the matrix in letter notation) and by the pseudostabilizers (triangles formed by three connected circles). The three Σ 's in a triangle share four common eigenvectors which form an orthonormal basis spanning the two-qubit Hilbert space. The fifteen triangles thus give fifteen sets of four basis vectors. Shaded triangles correspond to entangled states while non-shaded triangles correspond to product states. Neighbouring triangles have one (non-identity) Σ in common, and each (non-identity) Σ is shared by three triangles. The line segments joining the vertices of a triangle correspond to pairs $\{j, k\}$ of commuting matrices; each segment therefore specifies a $\pi/2$ rotation $X_{j,k} = (\Sigma_j + i\Sigma_k)/\sqrt{2}$ that transforms the eigenvectors of an adjacent triangle into its neighbour. The figure thus constitutes a “roadmap” for navigating the discrete set \mathfrak{H}_2 . Repeated circles indicate the closure of the graph.

states are denoted by an asterisk on the set label.

Set	$-1 - i$	$-1 + i$	$1 - i$	$1 + i$
1	(0, 0, 0, 1)	(0, 1, 0, 0)	(0, 0, 1, 0)	(1, 0, 0, 0)
2	(0, 0, -1, 1)	(-1, 1, 0, 0)	(0, 0, 1, 1)	(1, 1, 0, 0)
3	(0, 0, i , 1)	(i , 1, 0, 0)	(0, 0, - i , 1)	(- i , 1, 0, 0)
4	(0, -1, 0, 1)	(0, 1, 0, 1)	(-1, 0, 1, 0)	(1, 0, 1, 0)
5	(1, -1, -1, 1)	(-1, 1, -1, 1)	(-1, -1, 1, 1)	(1, 1, 1, 1)
6	(- i , -1, i , 1)	(i , 1, i , 1)	(i , -1, - i , 1)	(- i , 1, - i , 1)
7	(0, i , 0, 1)	(0, - i , 0, 1)	(i , 0, 1, 0)	(- i , 0, 1, 0)
8	(- i , i , -1, 1)	(i , - i , -1, 1)	(i , i , 1, 1)	(- i , - i , 1, 1)
9	(-1, i , i , 1)	(1, - i , i , 1)	(1, i , - i , 1)	(1, i , i , -1)
10*	(0, -1, 1, 0)	(-1, 0, 0, 1)	(1, 0, 0, 1)	(0, 1, 1, 0)
11*	(i , 0, 0, 1)	(0, - i , 1, 0)	(0, i , 1, 0)	(- i , 0, 0, 1)
12*	(1, 1, -1, 1)	(-1, 1, 1, 1)	(1, -1, 1, 1)	(1, 1, 1, -1)
13*	(i , - i , 1, 1)	(i , i , -1, 1)	(i , i , 1, -1)	(- i , i , 1, 1)
14*	(i , 1, - i , 1)	(- i , 1, i , 1)	(i , -1, i , 1)	(i , 1, i , -1)
15*	(-1, - i , i , 1)	(-1, i , - i , 1)	(1, - i , - i , 1)	(1, i , i , 1)

Note that the first stabilizer of the product sector corresponds to the computational basis, while the first stabilizer of the entangled sector corresponds to the Bell basis.

This method not only finds the states of \mathfrak{H}_2 in an exhaustive way. It also provides a road map for navigating the discrete set. To illustrate this, consider three pseudostabilizers which we call s^a , s^b and s^c . They have two generalized Pauli matrices in common, one of them being the trivial Σ_0 . We chose one of the two and call

it Σ_m . Consider three $\Sigma \neq \Sigma_m$,

$$\Sigma_j \in s^a, \quad \Sigma_k \in s^b, \quad \text{and} \quad \Sigma_l \in s^c \quad (2.25)$$

such that

$$\{\Sigma_j, \Sigma_k\} = \{\Sigma_k, \Sigma_l\} = \{\Sigma_l, \Sigma_j\} = 0. \quad (2.26)$$

Since all pairs of generalized Pauli matrices that do not commute must anti-commute, they also satisfy

$$[\Sigma_j, \Sigma_m] = [\Sigma_k, \Sigma_m] = [\Sigma_l, \Sigma_m] = 0. \quad (2.27)$$

Then it is easy to show by a direct calculation that

$$X_{m j}^a = \frac{1}{\sqrt{2}} (\Sigma_m + i\Sigma_j), \quad (2.28)$$

$$X_{m k}^b = \frac{1}{\sqrt{2}} (\Sigma_m + i\Sigma_k), \quad (2.29)$$

$$X_{m l}^c = \frac{1}{\sqrt{2}} (\Sigma_m + i\Sigma_l), \quad (2.30)$$

have one of the properties:

$$X_{m k}^b X_{m j}^a X_{k m}^b = X_{m l}^c \quad (2.31)$$

or

$$X_{m k}^b X_{m j}^a X_{k m}^b = (X_{m l}^c)^{-1} = -i X_{l m}^c \quad (2.32)$$

depending on whether the two anti-commuting σ' s in the decomposition of $\Sigma_j \Sigma_k$ appear in cyclic order or anti-cyclic order, respectively. This means, following the proof given for the one-qubit case, that all the eigenvectors of s^a are transformed into the eigenvectors of s^c by the transformation X^b .

All together, there are 120 different generalized two-qubit $\pi/2$ rotations generated by the scheme

$$X_{i,j} = \frac{1}{\sqrt{2}} (\Sigma_i + i\Sigma_j), \quad (2.33)$$

where Σ_i and Σ_j commute.

Among these X 's, there is a subset that plays an important practical role. These are $\pi/2$ rotations of the form

$$X_{0,j} = X_{0,\alpha\beta} = \frac{1}{\sqrt{2}} (\Sigma_0 + i\Sigma_j) \equiv (\alpha\beta)^{1/2}, \quad (2.34)$$

where $\alpha\beta \leftrightarrow j$ are the equivalent tags of the Pauli matrix in the letter and numeric notations, respectively. They correspond to the unitary time-evolution operator

$$U(t) = e^{i\Sigma_j \tau} \quad (2.35)$$

with $\tau = \pi/4$, and are thus directly implemented by a Hamiltonian proportional to Σ_j . These rotations constitute the practical means of navigating \mathfrak{H}_2 . They can be seen as the “primitives” of the Clifford group, as we show below.

But first, it is important to note that the generalized Pauli matrices in the above arguments are not limited to the two-qubit case, but can in fact be over any number of qubits. These results are therefore directly generalizable to larger Hilbert spaces H_n and larger discrete sets \mathfrak{H}_n . We duly conclude that our generalized $\pi/2$ rotations on n qubits, constructed from the pseudostabilizers s_n^a , leave \mathfrak{H}_n invariant.

2.2.2 The generalized $\pi/2$ rotations generate the n -qubit Clifford group

So far we have successfully discretized the continuous Hilbert space H_n , and in doing so we have described a class of generalized $\pi/2$ rotations that leave the \mathfrak{H}_n invariant. From the point of view of operators acting in H_n , this discretization means we have reduced the continuous transformation group $SU(2^n)$ to a finite group. Here we show that this finite group is the n -qubit Clifford group \mathcal{C}_n .

The Clifford group is defined as the normalizer of the Pauli group. That is, a unitary operator X is contained in \mathcal{C}_n if and only if

$$X\Sigma X^{-1} \in \mathcal{G}_n \quad \forall \Sigma \in \mathcal{G}_n. \quad (2.36)$$

First, let us show that our X' s are elements of \mathcal{C}_n . That is,

$$X_{j\ k} = \frac{1}{\sqrt{2}}(\Sigma_j + i\Sigma_k) \in \mathcal{C}_n \quad \text{if } [\Sigma_j, \Sigma_k] = 0. \quad (2.37)$$

We have

$$\Sigma_j \Sigma_l = \varepsilon_{jl} \Sigma_l \Sigma_j, \quad (2.38)$$

$$\Sigma_k \Sigma_l = \varepsilon_{kl} \Sigma_l \Sigma_k, \quad (2.39)$$

where $\varepsilon_{jl} = \pm 1$ and $\varepsilon_{kl} = \pm 1$. Thus,

$$X_{j\ k} \Sigma_l X_{j\ k}^{-1} = \frac{1}{2} (\Sigma_j + i\Sigma_k) \Sigma_l (\Sigma_j - i\Sigma_k) \quad (2.40)$$

$$= \frac{1}{2} \Sigma_l (\varepsilon_{jl} \Sigma_j + i\varepsilon_{kl} \Sigma_k) (\Sigma_j - i\Sigma_k) \quad (2.41)$$

$$= \frac{1}{2} \varepsilon_{jl} \Sigma_l (\Sigma_j + i\varepsilon_{kl} \varepsilon_{jl} \Sigma_k) (\Sigma_j - i\Sigma_k). \quad (2.42)$$

If $\varepsilon_{kl}\varepsilon_{jl} = 1$,

$$= \frac{1}{2}\varepsilon_{jl}\Sigma_l (2\Sigma_0 + i\Sigma_k\Sigma_j - i\Sigma_j\Sigma_k) \quad (2.43)$$

$$= \varepsilon_{jl}\Sigma_l \in \mathcal{G}_n. \quad (2.44)$$

If $\varepsilon_{kl}\varepsilon_{jl} = -1$,

$$= \frac{1}{2}\varepsilon_{jl}\Sigma_l (-i\Sigma_k\Sigma_j - i\Sigma_j\Sigma_k) \quad (2.45)$$

$$= -i\varepsilon_{jl}\Sigma_l\Sigma_j\Sigma_k \in \mathcal{G}_n. \quad (2.46)$$

So the generalized $\pi/2$ rotations on n qubits are elements of the Clifford group.

Now note that the Clifford group is generated by the Hadamard,

$$H = \frac{1}{\sqrt{2}} \begin{bmatrix} 1 & 1 \\ 1 & -1 \end{bmatrix} \quad (2.47)$$

phase,

$$S = \begin{bmatrix} 1+i & 0 \\ 0 & 1-i \end{bmatrix} \quad (2.48)$$

and CNOT,

$$CNOT = \begin{bmatrix} 1 & 0 & 0 & 0 \\ 0 & 1 & 0 & 0 \\ 0 & 0 & 0 & 1 \\ 0 & 0 & 1 & 0 \end{bmatrix} \quad (2.49)$$

gates[7]. The Hadamard gate may be composed from the one-qubit $\pi/2$ rotations

X_{02} and X_{01} :

$$\begin{aligned}
H &= X_{02}X_{01}(X_{20})^{-1} \\
&= -iX_{02}X_{01}X_{02} \\
&= \frac{-i}{2\sqrt{2}} \begin{bmatrix} 1 & i \\ i & 1 \end{bmatrix} \begin{bmatrix} 1+i & 0 \\ 0 & 1-i \end{bmatrix} \begin{bmatrix} 1 & i \\ i & 1 \end{bmatrix} \\
&= \frac{1}{\sqrt{2}} \begin{bmatrix} 1 & 1 \\ 1 & -1 \end{bmatrix}. \tag{2.50}
\end{aligned}$$

The phase gate may be trivially constructed from a single one-qubit $\pi/2$ rotation:

$$\begin{aligned}
S &= X_{01} \\
&= \begin{bmatrix} 1+i & 0 \\ 0 & 1-i \end{bmatrix}, \tag{2.51}
\end{aligned}$$

while the CNOT is simply the product of three X 's:

$$\begin{aligned}
CNOT &= (X_{02})^{-1} X_{06} (X_{04})^{-1} \\
&= -X_{20} X_{06} X_{40} \\
&= \frac{-1}{2\sqrt{2}} \begin{bmatrix} i & 1 & 0 & 0 \\ 1 & i & 0 & 0 \\ 0 & 0 & i & 1 \\ 0 & 0 & 1 & i \end{bmatrix} \begin{bmatrix} 1 & i & 0 & 0 \\ i & 1 & 0 & 0 \\ 0 & 0 & 1 & -i \\ 0 & 0 & -i & 1 \end{bmatrix} \begin{bmatrix} 1+i & 0 & 0 & 0 \\ 0 & 1+i & 0 & 0 \\ 0 & 0 & -1+i & 0 \\ 0 & 0 & 0 & -1+i \end{bmatrix} \\
&= \frac{1}{\sqrt{2}} \begin{bmatrix} 1-i & 0 & 0 & 0 \\ 0 & 1-i & 0 & 0 \\ 0 & 0 & 0 & 1-i \\ 0 & 0 & 1-i & 0 \end{bmatrix}. \tag{2.52}
\end{aligned}$$

So our generalized $\pi/2$ rotations allow a direct construction of a gate set that generates the Clifford group. The finite transformation group leaving \mathfrak{H}_n invariant, generated by the generalized $\pi/2$ rotations on n qubits, is thus the n -qubit Clifford group \mathcal{C}_n .

One of the motives we presented for this work was the difficulty we anticipate in achieving the reliability requisite for fault-tolerant quantum computation. Clearly, limiting the register to a finite number of possible states must alleviate this difficulty, but by how much?

It can be derived from the properties of the Pauli group that each pseudostabilizer s_n^a has n levels of non-orthogonal neighbors. Since the eigenstates of neighboring pseudostabilizers are connected by a single $\pi/2$ rotation, any state on \mathfrak{H}_n can be reached from any other in at most $n + 1$ such rotations. This is to be compared with the result that an arbitrary state in the full Hilbert space can be reached to

within an error ϵ by concatenating $\mathcal{O}(\log^c(1/\epsilon))$ rotations from a universal set, with $c \approx 2$. In addition, note that the CNOT and H gates are not directly implemented by a physical Hamiltonian, but must be built up from $\pi/2$ rotations which are naturally realized with accessible field variations, so there is a second simplification from working with the $\pi/2$ rotations rather than standard universal gate sets such as $\{\text{H}, \text{S}, \text{T}, \text{CNOT}\}$.

From an experimentalist's point of view, therefore, the X 's form a very natural language for building quantum gates. A rotation of the form $X_{0j} = (\Sigma_0 + i\Sigma_j)/\sqrt{2}$ is directly implemented by a term in the Hamiltonian proportional to Σ_j . And as shown above, this class of rotations generates \mathcal{C}_n . The X 's are thus the basic instructions for a sort of "machine language" for quantum processors. The following section shows a simple example of their calculus.

2.2.3 Sample application of digital quantum information: Gottesman tables and synonyms for CNOT

The Hamiltonian describing a given physical system determines which of the generalized $\pi/2$ rotations will be directly realizable in that system. Implementing CNOT according to the decomposition in section 2.5 requires a physical system with a Hamiltonian proportional to Σ_{zx} in order to realize the entangling operation $X_{06} = (\Sigma_{ww} + i\Sigma_{zx})/\sqrt{2}$. Though this type of inter-qubit interaction is possible⁶, most qubit systems rely on a less exotic interaction, such as one proportional to Σ_{zz} or Σ_{xx} . How can we implement the CNOT gate in one of these more standard registers? Specifically, suppose the system is described by an effective two-qubit

⁶and indeed, in Chapter Five we will give a rather simple prescription for generating it from a fixed non-secular interaction when one qubit is irradiated at the transition frequency of the other.

Hamiltonian of the form

$$H = a(t)\Sigma_{wz} + b(t)\Sigma_{wx} + c(t)\Sigma_{zw} + d(t)\Sigma_{xw} + e(t)\Sigma_{xx}, \quad (2.53)$$

where the tuning parameters a, b, c, d, e allow the relative strengths of the terms to be adjusted during an experiment.

Any n -qubit gate is fully specified by giving its induced transformation of some minimal set of $2n$ generators of the n -qubit Pauli group. For gates in the Clifford group \mathcal{C}_n , this action by definition maps Pauli group elements into one another. It is thus very helpful when addressing questions of this sort to construct a table to track the image of the $2n$ generators under some concatenated string of the available rotations. For example, the CNOT gate is described by[86],

	CNOT
WX	WX
XW	XX
WZ	ZZ
ZW	ZW

(2.54a)

This table can be generalized to a string of rotations. In the left-most column is some initial set of $2n$ independent generators – typically X and Z on each qubit, though any two independent generators per qubit would do. Clifford group rotations are written along the top row. Moving across the table, each successive column contains the image of the previous column under the transformation denoted at the top of that column.

The task of implementing CNOT from a naturally realizable set of gates thus comes down to constructing a table whose first and last columns are identical to

2.54a but along the top of which are only the naturally available gates. In the example at hand, it is straightforward to construct

	$(\mathbf{Z}\mathbf{W})^{1/2}$	$(\mathbf{X}\mathbf{W})^{1/2}$	$(\mathbf{Z}\mathbf{W})^{-1/2}$	$(\mathbf{X}\mathbf{X})^{1/2}$	$(\mathbf{Z}\mathbf{W})^{1/2}$	$(\mathbf{X}\mathbf{W})^{1/2}$	$(\mathbf{W}\mathbf{X})^{-1/2}$
WX	WX	WX	WX	WX	WX	WX	WX
XW	$-YW$	ZW	ZW	YX	XX	XX	XX
WZ	WZ	WZ	WZ	XY	$-YY$	ZY	ZZ
ZW	ZW	YW	XW	XW	$-YW$	ZW	ZW

(2.55)

Because the first and last columns of 2.54a and 2.55 are identical, the words written across the top of the table that connect the columns have the same action. We refer to such pairs as *synonyms*, and to the construction as a whole as a *Gottesman table*. While the gate CNOT is a completely general quantum logic transformation, the sequence of rotations appearing in 2.55 is tailored to the example system described by 2.53. And of course CNOT is not a special case; a synonym suitable for a particular implementation could likewise be calculated for *any* gate in \mathcal{C}_2 .

We will make use of these tools in a very practical context in Chapters Three and Five, where we derive microwave pulse sequences to implement universal gates.

2.2.4 Conclusion

In this section we have presented a geometric method for producing from the continuous Hilbert space H_n a discrete, uniform sampling \mathfrak{H}_n . Because all the states in the discrete set are geometrically equivalent, \mathfrak{H}_n represents a generalized Platonic solid in H_n . This method is closely related to the stabilizer formalism of quantum error-correcting codes. Inherent in our construction is a description of how different

elements of \mathfrak{H}_n are related by transformations generated by physical Hamiltonians expressed in the basis of generalized Pauli matrices. This has been demonstrated in detail for \mathfrak{H}_1 and \mathfrak{H}_2 , and is obtainable by direct analogy for higher-dimensional spaces. These ideas provide a useful tool for analyzing problems in traditional quantum computation, as the example above illustrates. And though computation over the discrete set \mathfrak{H}_n is clearly less powerful than computation in the full H_n , it is potentially more powerful than classical computation. The results of this discretization appeared in ref. [88].

2.3 Generalized Bloch equations

Classical information processing can be performed using only two basic boolean operations: the NOT and AND gates. Likewise, any unitary operation in quantum information processing can be decomposed into a sequence of one-qubit and two-qubit operations called quantum gates. The one-qubit gates can be viewed as finite rotations of an effective spin-1/2 representing the qubit under the influence of a magnetic-like field. The two-qubit operations are more complicated unitary transformations of the two-qubit Hilbert space into itself involving an interaction between the quantum bits. While quantum information theory treats a quantum algorithm as a sequence of discrete gate operations, the gates themselves are in fact continuous rotations performed in practice by applying time-dependent fields to the qubit systems. Therefore even tiny errors – due to noise in the applied fields or stray deterministic fields, for example – can accumulate, leading to full bit-flip or phase flip errors in the qubits’ state.

For one-qubit gates, the qubit’s continuous evolution can be studied using the Bloch equations: a set of three linear, first order, coupled differential equations

describing the expectation values of the effective spin-1/2 along the x -, y -, and z -axes. While the Bloch equations' solution is in general numerical if the time dependence of the field is arbitrary, the equations are exact in the sense that they make no assumptions whatsoever about the strength of the field or its direction. They are therefore essential to the study of one-qubit systems and ensembles of non-interacting qubits.

Two-qubit gate operations require an interaction between the two qubits. When qubit-qubit interactions are present, quantum information will in general flow from 'local' degrees of freedom involving individual qubits into 'non-local' ones involving correlations between qubits – a phenomenon known as quantum entanglement. Any complete description of the continuous time evolution of an interacting qubit system must therefore describe both its local *and* non-local degrees of freedom. In this article, we present a direct generalization of the Bloch equations that provides such a description without making any assumptions whatsoever about the fields or the qubit-qubit interaction.

It is worth noting that the study of systems with many interacting spins is commonplace in the field of NMR. There, interacting spins are treated by decomposing the total spin into multiplets and by using the notion of tensorial spin operators [14]. In quantum information processing, where each spin is a priori addressable separately in both 'write' and 'read' operations, and where qubit-qubit interactions do not a priori have any symmetry, these notions are of limited interest. We are thus following an alternative approach, where all components of the density matrix and all possible interactions are treated on the same footing.

2.3.1 One-qubit dynamics: Bloch equations

The Bloch equations describing the evolution of a spin-1/2 particle – or more generally any two level quantum system – in an external, time-dependent magnetic field are derived by first considering the Pauli spin matrices as a basis for both the spin-1/2 Hamiltonian and the spin-1/2 density operator. We can then write the time-dependent Hamiltonian \mathcal{H} and the density operator ρ as linear combinations of these four basis matrices:

$$\mathcal{H} = \sum_{j=0}^3 \sigma_j \text{Tr}(\sigma_j^\dagger \mathcal{H}) \quad (2.56)$$

$$= \sum_{j=0}^3 h_j \sigma_j \quad (2.57)$$

$$= h_0 \sigma_0 + \vec{h} \cdot \vec{\sigma}, \quad (2.58)$$

$$\rho = \frac{1}{2} \sum_{k=0}^3 \sigma_k \text{Tr}(\sigma_k^\dagger \rho) \quad (2.59)$$

$$= \frac{1}{2} \sum_{k=0}^3 r_k \sigma_k \quad (2.60)$$

$$= \frac{1}{2} (r_0 \sigma_0 + \vec{r} \cdot \vec{\sigma}), \quad (2.61)$$

where we have separated out the trivial σ_0 dependence of both \mathcal{H} and ρ , which will not contribute to the dynamics, and written the remaining terms as three-component vectors \vec{h} and \vec{r} , respectively. Note that $|\vec{r}|=1$ while $|\vec{h}|$ can take any value. The time-dependence of ρ under the influence of \mathcal{H} is given by the Heisenberg equation of motion:

$$\frac{d}{dt} \rho = \frac{1}{i\hbar} [\rho, \mathcal{H}]. \quad (2.62)$$

With the above linear expansions, this becomes

$$\frac{d}{dt} \sum_{k=1}^3 r_k \sigma_k = \frac{1}{i\hbar} \left[\frac{1}{2} \sum_{k=1}^3 r_k \sigma_k, \sum_{j=1}^3 h_j \sigma_j \right] \quad (2.63)$$

$$= \frac{1}{2i\hbar} \sum_{k=1}^3 \sum_{j=1}^3 r_k h_j [\sigma_k, \sigma_j]. \quad (2.64)$$

By taking the scalar product of the last equation with a basis matrix σ_i , we obtain an equation for each component dr_i/dt of the vector derivative:

$$\frac{d}{dt} \sum_{k=1}^3 r_k \text{Tr}(\sigma_k \sigma_i) = \frac{1}{2i\hbar} \sum_{k=1}^3 \sum_{j=1}^3 r_k h_j \text{Tr}([\sigma_k, \sigma_j] \sigma_i) \quad (2.65)$$

$$\frac{d}{dt} r_i = \frac{1}{\hbar} \sum_{k=1}^3 \sum_{j=1}^3 h_j m_{kji} r_k, \quad (2.66)$$

where $m_{kji} = \frac{1}{2i} \text{Tr}([\sigma_k, \sigma_j] \sigma_i)$ is the $(kji)^{th}$ component of a $3 \times 3 \times 3$ tensor which here coincides with the fully antisymmetric tensor ε_{ijk}^{123} . In vector notation, the last set of equations can be written

$$\frac{d}{dt} \vec{r} = \frac{1}{\hbar} \sum_{i=1}^3 \sum_{k=1}^3 \sum_{j=1}^3 h_j m_{kji} r_k \hat{x}_i = \bar{\bar{\mathbf{h}}} \cdot \vec{r}. \quad (2.67)$$

The matrix $\bar{\bar{\mathbf{h}}}$ is the *super-operator* associated with the one-qubit Hamiltonian \mathcal{H} ; it is a 3×3 antisymmetric matrix with a priori time-dependent entries. It reads

$$\bar{\bar{\mathbf{h}}} = \begin{bmatrix} 0 & h_3 & -h_2 \\ -h_3 & 0 & h_1 \\ h_2 & -h_1 & 0 \end{bmatrix}. \quad (2.68)$$

The vector $\vec{r}(t)$ is often called the Bloch vector, while the equations for its three

components r_x, r_y and r_z are often called the Bloch equations. They can be put into the more familiar form

$$\frac{d}{dt}\vec{r} = \frac{1}{\hbar}(\vec{h} \times \vec{r}). \quad (2.69)$$

The solution $\vec{r}(t)$ gives the motion of a unit vector in three real dimensions. Since $r_i = \text{Tr}(\sigma_i^\dagger \rho)$ is the expectation value of the operator σ_i in the state ρ , the vector $\vec{r}(t)$ represents the time-dependent expectation values of the measurement operators associated with σ_1, σ_2 and σ_3 .

2.3.2 General two-qubit dynamics

We now examine a two-qubit system. We will use as a basis for operators in the two-qubit Hilbert space the sixteen linearly independent 4×4 matrices of the Pauli set \mathcal{S}_2 , as introduced earlier. That is, we will use the set

$$\{\sigma_w, \sigma_z, \sigma_x, \sigma_y\}^{\otimes 2} = \begin{array}{|c|c|c|c|} \hline & \sigma_w \otimes \sigma_w & \sigma_x \otimes \sigma_w & \sigma_y \otimes \sigma_w & \sigma_z \otimes \sigma_w \\ \hline \sigma_w \otimes \sigma_x & \sigma_w \otimes \sigma_x & \sigma_x \otimes \sigma_x & \sigma_y \otimes \sigma_x & \sigma_z \otimes \sigma_x \\ \hline \sigma_w \otimes \sigma_y & \sigma_x \otimes \sigma_y & \sigma_y \otimes \sigma_y & \sigma_z \otimes \sigma_y & \\ \hline \sigma_w \otimes \sigma_z & \sigma_x \otimes \sigma_z & \sigma_y \otimes \sigma_z & \sigma_z \otimes \sigma_z & \\ \hline \end{array} = \Sigma_0 \cdots \Sigma_{15} \quad (2.70)$$

as defined in the Notation section preceding the body of the thesis. We will refer to the subset of these matrices which act non-trivially just one of the two qubits as the *local* two-qubit Pauli matrices. These elements appear in the first row and in the first column above. Similarly, those which act non-trivially on both of the qubits will be referred to as *non-local* two-qubit Pauli matrices (ie. the other nine above, $\sigma_i \otimes \sigma_j, i, j = x, y, z$).

As a reminder, these matrices retain many of the properties of the one-qubit Pauli matrices. They all either commute or anti-commute, and they are all linearly

independent and orthogonal:

$$\frac{1}{4}\text{Tr}(\Sigma_j^\dagger \Sigma_k) = \delta_{jk} \quad \text{for all } j, k \quad (2.71)$$

and therefore form a basis for 4×4 matrices (note that non-hermitian operators will take complex coefficients). As in the one-qubit case, we can thus write any two-qubit Hamiltonian and the density operator of any two-qubit system as linear combinations of these basis elements:

$$\mathcal{H} = \frac{1}{2} \sum_{j=0}^{15} \Sigma_j \text{Tr}(\Sigma_j^\dagger \mathcal{H}) \quad (2.72)$$

$$= \frac{1}{2} \sum_{j=0}^{15} \Sigma_j \quad (2.73)$$

$$= \frac{1}{2} (\mathcal{H}_0 \Sigma_0 + \vec{\mathcal{H}} \cdot \vec{\Sigma}), \quad (2.74)$$

$$\rho = \frac{1}{4} \sum_{k=0}^{15} \Sigma_k \text{Tr}(\Sigma_k^\dagger \rho) \quad (2.75)$$

$$= \frac{1}{4} \sum_{k=0}^{15} r_k \Sigma_k \quad (2.76)$$

$$= \frac{1}{4} (r_0 \Sigma_0 + \vec{r} \cdot \vec{\Sigma}), \quad (2.77)$$

where we have again separated out the Σ_0 -dependence of \mathcal{H} and ρ . The time-evolution of the state ρ is described by the Heisenberg equation:

$$\frac{d}{dt} \rho = \frac{1}{i\hbar} [\rho, \mathcal{H}] \quad (2.78)$$

which becomes

$$\frac{d}{dt} \sum_{k=1}^{15} r_k \Sigma_k = \frac{1}{i\hbar} \left[\frac{1}{4} \sum_{k=1}^{15} r_k \Sigma_k, \frac{1}{2} \sum_{j=1}^{15} \mathcal{H}_j \Sigma_j \right] \quad (2.79)$$

$$= \frac{1}{8i\hbar} \sum_{k=1}^{15} \sum_{j=1}^{15} r_k \mathcal{H}_j [\Sigma_k, \Sigma_j] \quad (2.80)$$

Projecting onto the set formed by the Σ' s, we get

$$\begin{aligned} \frac{d}{dt} R_i &= \frac{1}{8i\hbar} \text{Tr} \left(\sum_{k=1}^{15} \sum_{j=1}^{15} r_k \mathcal{H}_j [\Sigma_k, \Sigma_j] \Sigma_i \right) \\ &= \frac{1}{8i\hbar} \sum_{k=1}^{15} \sum_{j=1}^{15} r_k \mathcal{H}_j \text{Tr}([\Sigma_k, \Sigma_j] \Sigma_i) \\ &= \frac{1}{\hbar} \sum_{k=1}^{15} \sum_{j=1}^{15} r_k \mathcal{H}_j M_{kji}, \end{aligned} \quad (2.81)$$

where $M_{kji} = \frac{1}{8i} \text{Tr}([\Sigma_k, \Sigma_j] \Sigma_i)$ is the $(kji)^{th}$ component of a $15 \times 15 \times 15$ tensor we call the *two-qubit super-commutator*. Evaluating the entries in the two-qubit super-commutator is facilitated by noting that

$$(\sigma_i \otimes \sigma_j)(\sigma_k \otimes \sigma_l) = \sigma_i \sigma_k \otimes \sigma_j \sigma_l. \quad (2.82)$$

Carrying out this calculation allows us to write the two-qubit analog of the Bloch equations:

$$\frac{d}{dt} \vec{r} = \frac{1}{\hbar} \sum_{i=1}^{15} \sum_{k=1}^{15} \sum_{j=1}^{15} r_k \mathcal{H}_j M_{kji} \hat{x}_i = \bar{\bar{\mathbf{H}}} \cdot \vec{r} \quad (2.83)$$

We call $\bar{\bar{\mathbf{H}}}$ the *two-qubit super-operator*. It is a 15×15 matrix with a priori time-dependent entries which, in its structure, contains all the commutation and anti-commutation properties of the two-qubit Pauli matrices. Explicitly, the dynamics of a two-qubit system with any Hamiltonian is described by the fifteen coupled, linear,

first-order differential equations generated by the super-operator $\bar{\bar{H}}$, presented below.

The solution to this set of differential equations is a fifteen-component time-dependent vector $\vec{r}(t)$ analogous to the Bloch vector of a single qubit. It constitutes a complete description of the continuous time evolution of the two-qubit system. Since $r_i(t) = \text{Tr}(\Sigma_i^\dagger \rho(t))$ is the expectation value of the two-qubit measurement operator Σ_i for the state $\rho(t)$, the solution is given completely in terms of observable quantities. Such a solution is easily obtained by numerical integration on any standard personal computer.

2.3.3 Graphical representation of the dynamical equations

The structure of the super-operators \bar{h} and $\bar{\bar{H}}$ governing one- and two-qubit dynamics can be represented graphically. We will introduce our graphic conventions by first examining the simple one-qubit case. Recall that each component dr_x/dt , dr_y/dt and dr_z/dt of the time-derivative of the Bloch vector $\vec{r}(t)$ depends on the two products of a Bloch vector component r_k ($k = x, y, z$) and a field component h_j ($j = x, y, z$) for which their corresponding basis matrices satisfy $[\sigma_k, \sigma_j] = \pm 2i\sigma_i$. A map of all the directed threesomes $\{k, j, i\}$ satisfying $[\sigma_k, \sigma_j] = \pm 2i\sigma_i$ therefore fully describes the equations. This simple map is shown below.

Likewise, each differential component dR_i/dt in the differential equations governing two qubits depends on all the products of a density operator coefficient R_k and a Hamiltonian coefficient H_j for which their corresponding basis matrices satisfy $[\Sigma_k, \Sigma_j] = \pm 2i\Sigma_i$. Since any two generalized Pauli matrices anti-commute if they do not commute, each threesome $dR_i/dt, H_j, R_k$ of a non-zero matrix element of $\bar{\bar{H}}$ corresponds to a set of three mutually anti-commuting Σ 's, i.e. an *anti*-Abelian subset of the set of two-qubit Pauli matrices. In addition, because each two-qubit Pauli ma-

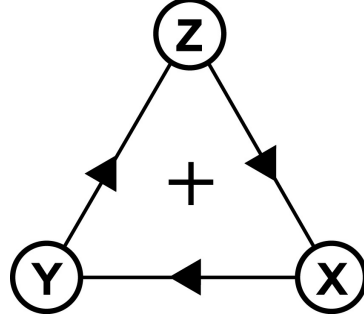


Figure 2.2: Graphical representation of general one-qubit dynamics. The triangle is to be read as $dr_x/dt = r_y h_z - r_z h_y$, etc. Terms corresponding to cyclic permutations are positive, as indicated by the arrows on the triangle. The action of a Hamiltonian h_z along Z is thus to perform a rotation on the projection of $\vec{r}(t)$ into the plane specified by the side of the triangle opposite Z , the XY -plane. The rotation performed by h_z transfers amplitude from X (Y) to Y (X) at the rate $\frac{1}{\hbar} h_z r_x$ ($\frac{1}{\hbar} h_z r_y$).

trix (excluding the identity) anti-commutes with exactly half of the complete set of sixteen, each will be shared between four anti-Abelian subsets. The structure of the matrix $\bar{\bar{H}}$ can therefore be represented by a map of the twenty anti-Abelian subsets. This map is shown in Figure 2.

2.3.4 n -qubit dynamics

As we might expect, these equations can be extended to provide a complete continuous time-dependent representation of the dynamical evolution of any number of qubits. We now make this generalization.

As above, write the Hamiltonian in the form:

$$\begin{aligned}\mathcal{H} &= \frac{\omega_0}{2} \Sigma_0 + \frac{\omega_1}{2} \Sigma_1 + \frac{\omega_2}{2} \Sigma_2 + \cdots + \frac{\omega_{4^n}}{2} \Sigma_{4^n} \\ \mathcal{H} &= \frac{1}{2} \sum_{j=0}^{4^n-1} \omega_j \Sigma_j.\end{aligned}\tag{2.84}$$

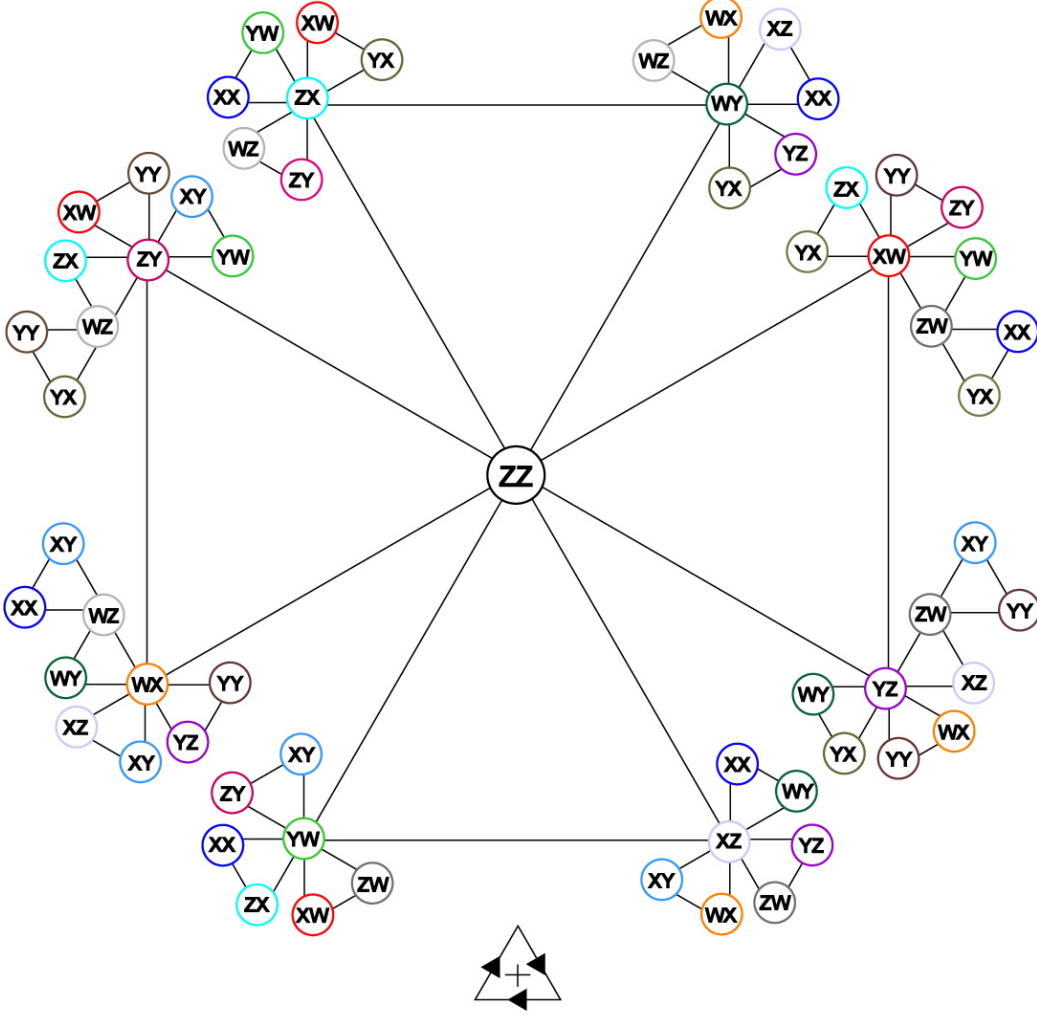


Figure 2.3: Graphical representation of continuous two-qubit dynamics. The structure of the equations governing two-qubit systems follows directly from the anti-Abelian subsets of the two-qubit Pauli matrices. Each subset is represented as a triangle whose vertices are two-qubit Pauli matrices (e.g. $ZZ = \sigma_z \otimes \sigma_z$). As in the one-qubit case, each side of a triangle specifies a plane of rotation, but here the underlying space is fifteen-dimensional rather than three-dimensional. For illustration, consider the triangle with vertices ZZ, WX, ZY . This triangle is to be read as $dR_{zy}/dt = H_{zz}R_{wx} - H_{wx}R_{zz}$, along with all other permutations. Clockwise cycles are positive, while counterclockwise cycles require a negative sign (as indicated by the small triangle at the bottom). The action of a two-qubit Hamiltonian H_{zz} is to perform simultaneous rotations on the projection of $\vec{R}(t)$ into the four planes $WX-ZY$, $ZX-WY$, $XW-YZ$, $XZ-YW$, as specified by the sides appearing opposite ZZ in the above triangles. The rotation performed by H_{zz} in the $WX-ZY$ plane transfers amplitude into $R_{zy}(R_{wx})$ at the rate $\frac{1}{\hbar}H_{zz}R_{wx}(\frac{1}{\hbar}H_{zz}R_{zy})$. The other rotations have analogous rates.

Now define the generalized fields H_j as

$$H_j = \frac{1}{2^{n-1}} \text{Tr}(\Sigma_j^\dagger \mathcal{H}), \quad (2.85)$$

which are thus just the ω'_j s. This allows us to write the Hamiltonian as

$$\mathcal{H} = \frac{1}{2} \sum_{j=0}^{4^n-1} H_j \Sigma_j \quad (2.86)$$

$$= \frac{1}{2} (H_0 \Sigma_0 + \vec{H} \cdot \vec{\Sigma}). \quad (2.87)$$

The n -qubit density operator can be written

$$\rho = \frac{1}{2^n} \sum_{k=0}^{4^n-1} \Sigma_k \text{Tr}(\Sigma_k^\dagger \rho) \quad (2.88)$$

$$= \frac{1}{2^n} \sum_{k=0}^{4^n-1} R_k \Sigma_k \quad (2.89)$$

$$= \frac{1}{2^n} (R_0 \Sigma_0 + \vec{R} \cdot \vec{\Sigma}), \quad (2.90)$$

where we have again separated out the Σ_0 -dependence of \mathcal{H} and ρ . The time-evolution of the state ρ is described by the Heisenberg equation 2.78 which becomes

$$\frac{d}{dt} \sum_{k=1}^{4^n-1} R_k \Sigma_k = \frac{1}{i\hbar} \left[\frac{1}{2^n} \sum_{k=1}^{4^n-1} R_k \Sigma_k, \frac{1}{2} \sum_{j=1}^{4^n-1} H_j \Sigma_j \right] \quad (2.91)$$

$$= \frac{1}{2^{n+1} i\hbar} \sum_{k=1}^{4^n-1} \sum_{j=1}^{4^n-1} R_k H_j [\Sigma_k, \Sigma_j] \quad (2.92)$$

Projecting onto the set formed by the Σ' s, we get

$$\begin{aligned}
\frac{d}{dt}R_i &= \frac{1}{2^{n+1}i\hbar}\text{Tr}\left(\sum_{k=1}^{4^n-1}\sum_{j=1}^{4^n-1}R_kH_j[\Sigma_k,\Sigma_j]\Sigma_i\right) \\
&= \frac{1}{2^{n+1}i\hbar}\sum_{k=1}^{4^n-1}\sum_{j=1}^{4^n-1}R_kH_j\text{Tr}([\Sigma_k,\Sigma_j]\Sigma_i) \\
&= \frac{1}{\hbar}\sum_{k=1}^{4^n-1}\sum_{j=1}^{4^n-1}R_kH_jM_{kji},
\end{aligned} \tag{2.93}$$

where $M_{kji} = \frac{1}{2^{n+1}i}\text{Tr}([\Sigma_k,\Sigma_j]\Sigma_i)$ is the $(kji)^{th}$ component of a $(4^n - 1) \times (4^n - 1) \times (4^n - 1)$ tensor we call the *N-qubit super-commutator*. With these definitions, all the entries in the super-commutator are ± 1 or 0. Evaluating these entries is facilitated by noting that

$$(\sigma_i \otimes \sigma_j \otimes \cdots)(\sigma_k \otimes \sigma_l \otimes \cdots) = \sigma_i\sigma_k \otimes \sigma_j\sigma_l \otimes \cdots \tag{2.94}$$

Carrying out this calculation allows us to write the n -qubit analog of the Bloch equations:

$$\frac{d}{dt}\vec{R} = \frac{1}{\hbar}\sum_{i=1}^{4^n-1}\sum_{k=1}^{4^n-1}\sum_{j=1}^{4^n-1}R_kH_jM_{kji}\hat{x}_i = \bar{\bar{\mathsf{H}}}_n \cdot \vec{R}. \tag{2.95}$$

This requires the calculation of $\bar{\bar{\mathsf{H}}}_n$ once and for all for each dimensionality of interest. This best carried out with a math engine such as *Mathematica* for $n > 2$.

2.3.5 Lindblad form

The last piece of the puzzle connecting the discrete and continuous Heisenberg pictures involves treating dissipation. While projective measurements of the Pauli operators can be described within Gottesman's Heisenberg representation [86], weak continuous measurement and dissipative processes cannot. To do so we account for

couplings to the environment, which give rise to non-unitary processes, by adding, in the appropriate form, the dissipation terms, yielding a (Markovian) master equation. The time-evolution of the density operator ρ may be written in the *Lindblad form* [37],

$$\frac{d\rho}{dt} = -i\hbar[\mathcal{H}, \rho] + \frac{1}{2} \sum_j \left([\mathcal{L}_j, \rho \mathcal{L}_j^\dagger] + [\mathcal{L}_j \rho, \mathcal{L}_j^\dagger] \right), \quad (2.96)$$

where \mathcal{H} is again the system Hamiltonian and the \mathcal{L}_j 's are the Lindblad operators describing the effects of the environment. The one-qubit version are the common Bloch equations. We may proceed as above, writing each of \mathcal{H} , ρ and the \mathcal{L}_j 's in the basis of two-qubit Pauli matrices (as the \mathcal{L}_j 's describe non-unitary dynamics, they will take complex coefficients in the Pauli expansion). We obtain again a set of fifteen coupled first order linear differential equations:

$$\frac{dr_i}{dt} = \sum_{k=1}^{4^n-1} \sum_{l=1}^{4^n-1} \sum_{j=1}^{4^n-1} (h_k r_l \mathbf{M}_{kli} + a_j r_l \mathbf{G}_{jli}), \quad (2.97)$$

where,

$$h_k = \frac{1}{2} \text{Tr}(\Sigma_k^\dagger \mathcal{H}), \quad (2.98)$$

the r_l 's are the components of the two-qubit Bloch vector,

$$R_l = \frac{1}{4} \text{Tr}(\Sigma_l^\dagger \rho), \quad (2.99)$$

and the a_j 's are the *Lindblad-Pauli coefficients*. The key to writing down or encoding these equations for simulations lies in calculating the matrices \mathbf{M}_{kli} and \mathbf{G}_{jli} that contain the commutative and anti-commutative structure of the two-qubit Pauli

matrices:

$$\mathbf{M}_{kli} = \frac{1}{8i} \text{Tr} ([\Sigma_k, \Sigma_l] \Sigma_i), \quad (2.100)$$

$$\mathbf{G}_{jli} = \frac{1}{8} \text{Tr} ([\Sigma_j, \Sigma_l \Sigma_j] \Sigma_i). \quad (2.101)$$

These objects may be calculated once and for all, and Mathematica code to produce automatically is in Appendix B. This form of the master equation allows one to easily study the effects of various noise processes.

This master equation is the final bridge from the crisp and conceptually powerful description of the system according to the discrete Heisenberg representation, and the subtle continuous dynamics, both dissipative and coherent, required to fully understand and study the dynamics of practical systems. Ultimately, we can use the continuous picture to study and optimize protocols which then would be able to be deployed as black-box type quantum gate operations.

2.3.6 Conclusion

We have presented a framework for the numerical study of arbitrary n -qubit dynamics. By writing both the Hamiltonian and density operator in a basis of n -qubit Pauli matrices, we arrive at a $(4^n - 1) \times (4^n - 1)$ super-operator that generates a set of fifteen coupled differential equations easily solved by numerical integration. Although the structure of these equations cannot be directly interpreted geometrically as a cross-product between the Bloch vector and the field vector like in the one-qubit Bloch equations, the two-qubit case at least can be represented in graphical form as a map of the twenty anti-Abelian subsets of the two-qubit Pauli matrices.

Our equations remain fully general; they can treat all the possible types of noise and all the possible stray interactions between the two qubits which may degrade

the fidelity of a gate operation. This generality, combined with the ease of numerical integration of a large but linear system, makes this technique immediately useful for the study and implementation of real two-qubit systems.

2.4 Visual representation of two-qubit states

There is only one road to follow, that of analysis of the basic elements in order to arrive ultimately at an adequate graphic expression.

- Wassily Kandinsky

2.4.1 Bloch sphere revisited

The Bloch sphere is used in many branches of physics, but nowhere is it so crucial as in quantum computing and its precursory fields such as NMR and quantum optics. This common tool is a manner of representing in the Euclidean space \mathbf{R}^3 the state of any two-level quantum system. Most generally, the wave function $|\psi\rangle$ of a two-level quantum system may be written as a complex linear combination of the basis states associated with the two energy levels

$$|\psi\rangle = \alpha|0\rangle + \beta|1\rangle \quad (2.102)$$

subject to the normalization constraint that ensures the coefficients describe probabilities:

$$\alpha^2 + \beta^2 = 1. \quad (2.103)$$

Since the overall phase of a quantum state is not observable, we may without loss of generality take the coefficient of $|0\rangle$ to be real and non-negative and rewrite $|\psi\rangle$ as

$$|\psi\rangle = \cos\theta|0\rangle + e^{i\phi}\sin\theta|1\rangle. \quad (2.104)$$

The pure two-level system is thus characterized by two real numbers, and this is the key property allowing it to be represented \mathbf{R}^3 .

At a deeper level, the group of unit-determinant transformations of the Hilbert space of a two-level quantum system, $SU(2)$, is isomorphic to the group of rotations in three real dimensions $O(3)$, allowing the Bloch sphere to provide a geometrically faithful real-space representation of the quantum state.

It may be graphically phrased in either the Heisenberg picture, where the operators representing observables are dynamical quantities, or in the Schrödinger picture, where the states contain the system's time dependence. In the latter, the dynamical state is represented as a point on a Cartesian sphere in \mathbf{R}^3 whose coordinates are

$$\begin{aligned} x &= \sin 2\theta \cos \phi \\ y &= \sin 2\theta \sin \phi \\ z &= \cos 2\theta. \end{aligned} \quad (2.105)$$

Rotations of the state in Hilbert space manifest as rotations of the sphere.

In the former, the Bloch sphere is a Cartesian sphere in \mathbf{R}^3 whose axes correspond to the expectation values of the standard spin-1/2 measurement operators σ_x , σ_y , and σ_z . In this case, the Bloch vector may represent also impure states, or even, as we shall see, the product portion of a partially entangled two-qubit state. Indeed, it is this Heisenberg version of the Bloch sphere that we will make the most use

of. Also, note that one advantage of the Heisenberg version is that it makes the relationships between the measurement operators explicit. Just as the x, y, z -axes are mutually orthogonal, so are the matrices $\sigma_x, \sigma_y, \sigma_z$, so a rotation about e.g. σ_z transforms the component of the state aligned along σ_x to σ_y .

We can make these ideas quantitative with the following prescription. As in the previous section, form the density operator ρ associated with the state $|\psi\rangle$ then write ρ as a linear combination of the Pauli matrices

$$\rho = \frac{1}{2} \sum_{k=0}^1 \sigma_k \text{Tr}(\sigma_k^\dagger \rho) \quad (2.106)$$

$$= \frac{1}{2}(r_0 \sigma_0 + \vec{r} \cdot \vec{\sigma}). \quad (2.107)$$

The projection of ρ onto the identity doesn't contain any relevant information, so we need only focus on the components r_x, r_y, r_z of \vec{r} . This triplet of real expectation values form precisely the components of the Bloch vector in the Heisenberg picture.

2.4.2 Two-qubit representation

We have developed a generalization of this Heisenberg-picture one-qubit Bloch sphere. The two qubit state may be written as a linear combination of four basis functions:

$$|\psi\rangle = \alpha|00\rangle + \beta|01\rangle + \gamma|10\rangle + \delta|11\rangle \quad (2.108)$$

subject to the normalization constraint

$$\alpha^2 + \beta^2 + \gamma^2 + \delta^2 = 1 \quad (2.109)$$

and again, the overall phase is meaningless. This amounts to six real parameters, and indeed, it is well known that $SU(4)$, the transformation group for two qubits, is isomorphic to $O(6)$. The general two-qubit state may thus be represented in terms of six angles; this formulation was recently given by Havel and Doran [107].

In terms of a graphical representation, it would also be desirable to have a picture which would represent explicitly the expectation values of measurement operators, like the one-qubit Bloch sphere in the Heisenberg picture. To this end, we offer the following prescription.

As in the one-qubit case, project the two-qubit density operator onto the basis of Pauli matrices, here the Σ s:

$$\rho = \frac{1}{4} \sum_{k=0}^{15} \Sigma_k \text{Tr}(\Sigma_k^\dagger \rho) \quad (2.110)$$

$$= \frac{1}{2^n} (R_0 \Sigma_0 + \mathbf{R} \cdot \boldsymbol{\Sigma}), \quad (2.111)$$

where \mathbf{R} is the fifteen-component vector of expectation values of the Σ s, and $\boldsymbol{\Sigma}$ is the vector of Σ s, identified, as usual, by the numbering system of section 2.1.1. There are nine non-local and six local components of \mathbf{R} . We separate the local components, in two sets of three, one set pertaining to each qubit, and represent them in two copies of the familiar one-qubit Heisenberg picture Bloch sphere. In this case, however, these two local vectors,

$$\mathbf{R}_{q1} = (r_{wx}, r_{wy}, r_{wz}) = (r_1, r_2, r_3) \quad (2.112)$$

and

$$\mathbf{R}_{q2} = (r_{xw}, r_{yw}, r_{zw}) = (r_4, r_8, r_{12}) \quad (2.113)$$

need not be of unit length, and indeed may vanish altogether when the state at hand

is a fully entangled one. If the two qubit system forms but a subspace of a larger many-qubit register, their magnitudes may vary independently, as one may become entangled with another qubit not in the subspace, but if these are the only two qubits present, then the magnitudes are constrained to be equal.

We must now represent the nine non-local components of \mathbf{R} , those which contain the non-classical correlations present in the system. In so doing it is desirable to isolate the purely non-local quantum information from the local quantum information by subtracting from each of the nine components the trivial classical correlations. Then, we may arrange the nine components into the entanglement matrix: \mathcal{E} :

$$\mathcal{E} = \begin{pmatrix} r_{xx} - r_{wx}r_{xw} & r_{xy} - r_{wy}r_{xw} & r_{xz} - r_{wz}r_{xw} \\ r_{yx} - r_{wx}r_{yw} & r_{yy} - r_{wy}r_{yw} & r_{yz} - r_{wz}r_{yw} \\ r_{zx} - r_{wx}r_{zw} & r_{zy} - r_{wy}r_{zw} & r_{zz} - r_{wz}r_{zw} \end{pmatrix} \quad (2.114)$$

or, with the definitions

$$\begin{aligned} \mathbf{g}_1^x &= \begin{pmatrix} r_{xx} - r_{wx}r_{xw} \\ r_{yx} - r_{wx}r_{yw} \\ r_{zx} - r_{wx}r_{zw} \end{pmatrix} & \mathbf{g}_2^x &= \begin{pmatrix} r_{xx} - r_{wx}r_{xw} \\ r_{xy} - r_{wy}r_{xw} \\ r_{xz} - r_{wz}r_{xw} \end{pmatrix} \\ \mathbf{g}_1^y &= \begin{pmatrix} r_{xy} - r_{wy}r_{xw} \\ r_{yy} - r_{wy}r_{yw} \\ r_{zy} - r_{wy}r_{zw} \end{pmatrix} & \mathbf{g}_2^y &= \begin{pmatrix} r_{yx} - r_{wx}r_{yw} \\ r_{yy} - r_{wy}r_{yw} \\ r_{yz} - r_{wz}r_{yw} \end{pmatrix} \\ \mathbf{g}_1^z &= \begin{pmatrix} r_{xz} - r_{wz}r_{xw} \\ r_{yz} - r_{wz}r_{yw} \\ r_{zz} - r_{wz}r_{zw} \end{pmatrix} & \mathbf{g}_2^z &= \begin{pmatrix} r_{zx} - r_{wx}r_{zw} \\ r_{zy} - r_{wy}r_{zw} \\ r_{zz} - r_{wz}r_{zw} \end{pmatrix} \end{aligned} \quad (2.115)$$

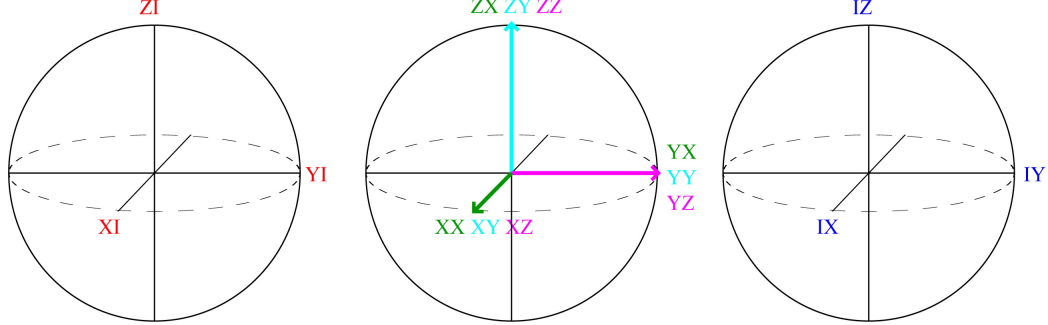


Figure 2.4: Representation of a two-qubit state in three real dimensions. The individual qubit state dynamics are plotted on Bloch spheres (red and blue). The non-local dynamics are plotted as a tri-vector on the *entanglement sphere*. The entanglement trivectors indicate the direction in Hilbert space along which the non-local quantum information is concentrated. For the state shown, measurement of the observables YX, ZX, XY, YY, XZ, ZZ will yield no information, while measurement of the set of commuting operators $\{XX, YZ, ZY\}$ will fully specify the two-qubit state. The entanglement trivector thus indicates which measurements will uncover the largest violation of a Bell type inequality for the given quantum state.

we can write it more succinctly as

$$\mathcal{E} = \begin{pmatrix} \mathbf{g}_1^x & \mathbf{g}_1^y & \mathbf{g}_1^z \end{pmatrix} = \begin{pmatrix} \mathbf{g}_2^x & \mathbf{g}_2^y & \mathbf{g}_2^z \end{pmatrix}^t. \quad (2.116)$$

This entity⁷ characterizes both the magnitude and the direction in Hilbert space of the two-qubit entanglement. The magnitude may be defined as the norm of \mathcal{E} ,

$$|\mathcal{E}| = \frac{1}{3}\text{Tr}(\mathcal{E}^t \mathcal{E}), \quad (2.117)$$

which is a valid entanglement monotone for all pure states [134]. As such, $\mathcal{E}=1$ for a maximally entangled two-qubit state, while $\mathcal{E}=0$ for a fully factorable product state; and single qubit rotations leave \mathcal{E} invariant.

The \mathbf{g}_a^α 's make up an *entanglement trivector* whose three components may be

⁷The two possible decompositions, in terms of the \mathbf{g}_1^α 's or the \mathbf{g}_2^α 's, are informationally equivalent.

simultaneously plotted on a single \mathbf{R}^3 Cartesian coordinate system, see figure 2.4. They indicate which two-qubit observables contain the non-local quantum information stored in the system. Since two-qubit observables must be built up from correlative measurements of the one-qubit operators, this representation thus visually indicates which Bell-type measurement protocol would reveal the largest correlations *for the given two-qubit state*. See figure 2.5.

For two-qubit states in the discrete set \mathfrak{H}_2 , the vectors \mathbf{g}_a^α are each of unit length and mutually orthogonal

$$\mathbf{g}_a^x \cdot \mathbf{g}_a^y = \mathbf{g}_a^x \cdot \mathbf{g}_a^z = \mathbf{g}_a^y \cdot \mathbf{g}_a^z = 0 \quad (2.118)$$

with

$$\mathbf{g}_a^x = \mathbf{g}_a^y \times \mathbf{g}_a^z. \quad (2.119)$$

2.4.3 Applications of the two-qubit representation: illustration of cnot gate

The action of the CNOT gate is typically understood as flipping the state of the target qubit if the control qubit is in state one, otherwise leaving it alone. This is a caricature phrased in the language of classical computing; the gate is of course a continuous rotation, and it is necessarily more complex. This is made evident by viewing it through our representation. The CNOT gate also induces a phase rotation on the control qubit when the target is not flipped. This crucial effect has been called the *phase kickback* and has no classical analog.

With the tools of this chapter squared away in our quantum toolbox, I now turn to the main topic of this thesis: providing solutions to the quantum gate problem that allow us to generate entanglement in superconducting qubits.

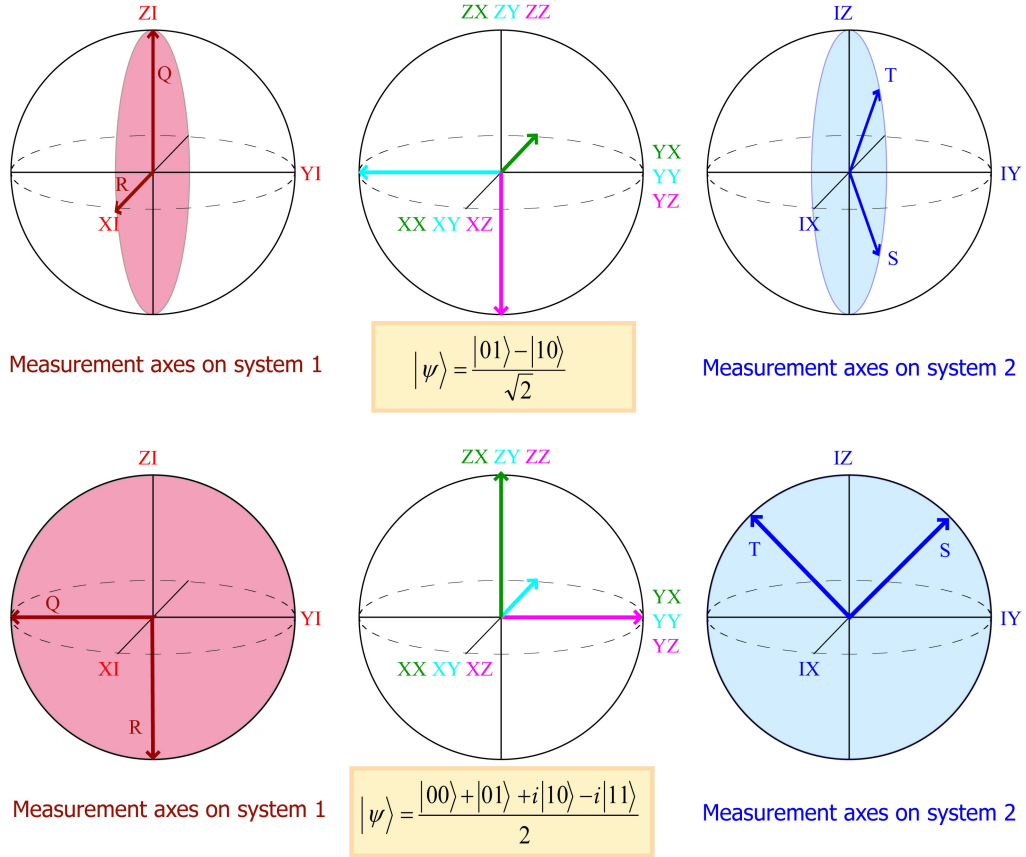


Figure 2.5: Representation of two-qubit maximally entangled states in real space, with associated measurement axes for one-qubit observables. The representation allows one to easily identify the measurements that will reveal the maximal Bell inequality violation. A rotation of the two-qubit state in the entangled subspace must be accompanied by a rotation of the measurement apparatus in real space in order to observe maximal violation. *Top:* singlet state $(|01\rangle - |10\rangle)/\sqrt{2}$, with measurement axes oriented in xz plane. *Bottom:* maximally entangled two-qubit state, $(|00\rangle + |01\rangle + i|10\rangle - i|11\rangle)/2$, with measurement axes oriented in yz plane. In each case, the system will show maximal violation of the Bell inequality $\langle QS \rangle + \langle RS \rangle + \langle RT \rangle - \langle QT \rangle \leq 2$ for the observables Q, R, S, T shown on the one-qubit spheres.

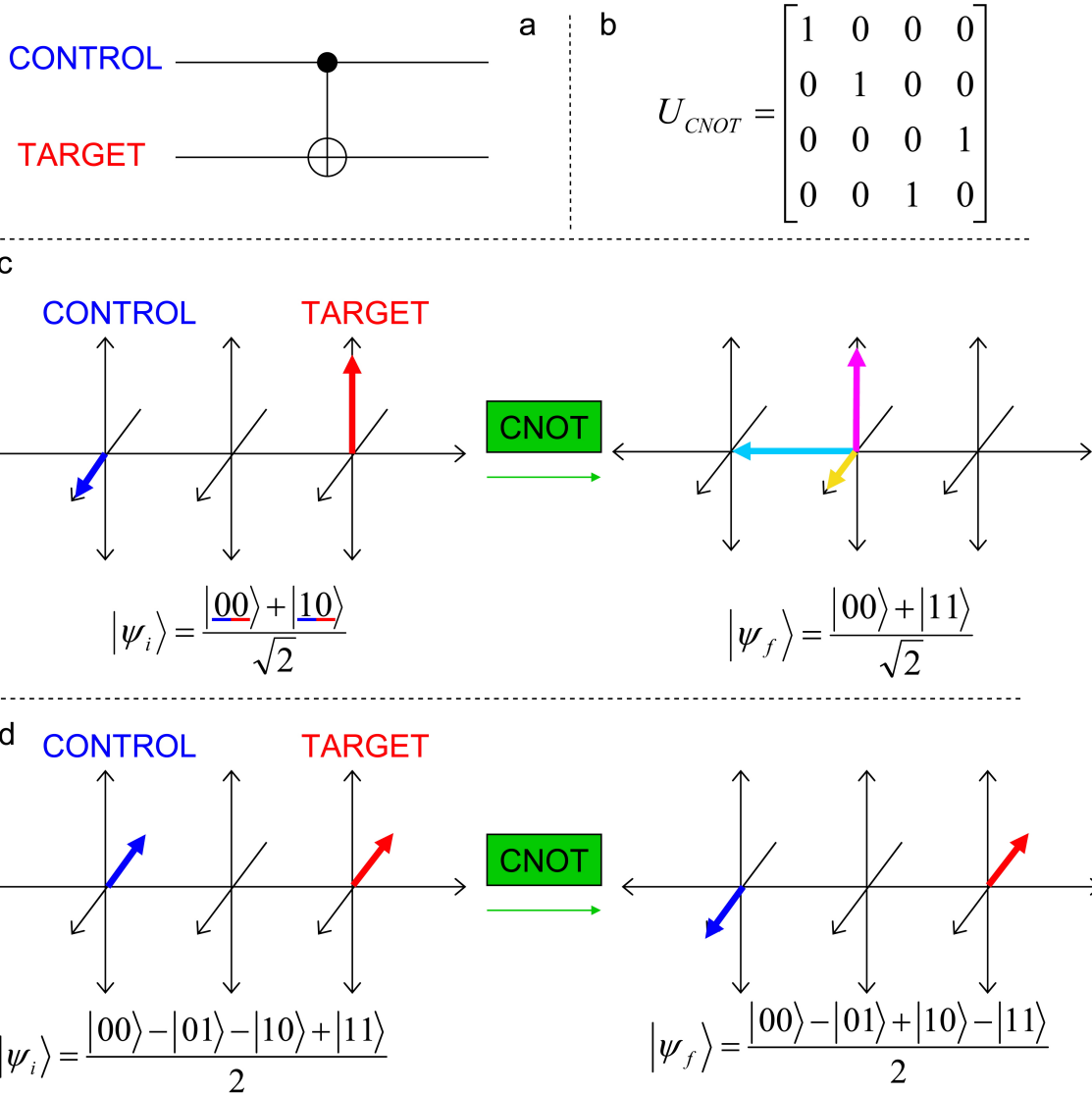


Figure 2.6: Illustration of the CNOT gate. **a.** The standard quantum logic or “musical score” representation, largely in analogy with classical logic. **b.** The corresponding unitary transformation. **c.** Illustration of CNOT in our representation by its action on an input state where the control qubit is prepared in a superposition state $\sqrt{2}|\psi\rangle_{\text{control}}=|0\rangle-|1\rangle$ and the target is $|\psi\rangle_{\text{target}}=|1\rangle$. The result is the EPR pair. **d.** Action of CNOT when both qubits are prepared in the superposition $\sqrt{2}|\psi\rangle_{\text{control}}=\sqrt{2}|\psi\rangle_{\text{target}}=|0\rangle-|1\rangle$. The control gate performs a π rotation of the control. This phase kickback of the CNOT is not captured by the standard representation.

2.5 Conclusion

We have presented a method of discretizing the n -qubit Hilbert space with a technique very closely related to the stabilizer theory of quantum error correcting codes. This discretization provides a map of the underlying Hilbert space. It provides some of the benefits and extra-classical behavior associated with quantum mechanics, such as maximally entangled multi-qubit states, without the headaches inherent in the full continuous space. Interestingly, its information content does not grow exponentially in the number of qubits, placing it as an intermediate paradigm for computation between the classical and full quantum cases.

The discrete Hilbert space and the rotations that navigate it form a discrete Heisenberg-picture machine language for quantum computation, one that we have found to be much more natural and powerful than the standard language constructed by analogy with classical computation.

This discrete Heisenberg picture can be extended to capture the full continuous dynamics with the n -qubit Bloch equations. We started with the quantum Liouville equation, and by making use of the family of n -qubit Pauli operators, derived the $4^n - 1$ coupled first order linear differential equations that describe the system.

Our representation of two-qubit gates allows one to envision in 3D the action of particular gate.

Taken together, these tools for a sort of alternative approach to practical problems in quantum computing, one we think is both more powerful and more adapted to practical concerns of actually building operational systems than the familiar standard language.

Chapter 3

Two-Qubit Gates at Optimal Bias Point

3.1 Introduction

In this chapter we present a family of solutions to the two-qubit quantum gate problem for the case of superconducting qubits sharing a static, weak and linear non-secular interaction and each independently controlled by exclusively microwave-frequency electric fields.

I begin with a discussion of the circuits themselves before moving on to the irradiation strategies.

3.2 The FLICFORQ system

The design of a two-qubit system involves a series of trade-offs and optimizations. Early schemes for performing two-qubit gates relied on dynamical tuning of either the qubit transition frequencies [49, 80] or a subcircuit controlling the qubit–qubit

interaction [78, 41, 53]. The former requires DC pulses that move the qubits away from their optimal bias points for coherence, while the latter requires additional control lines and non-linear elements that inevitably introduce additional couplings to uncontrolled degrees of freedom in the environment.

We first sought to develop a coupling scheme that would improve the chances of experimental success by both minimizing the required complexity in fabrication and measurement, and maximizing the expected qubit performance.

The need to minimize fabrication and measurement complexity naturally leads to the use of simple fixed linear coupling elements, such as capacitors and inductors, that do not require dynamical tuning through external control lines. The need to maximize qubit coherence times leads to the use of exclusively microwave signals so the qubits may remain at their optimal DC bias points throughout the gate operation.

This strategy was also motivated by the success of liquid NMR quantum computing, where the nuclear spins making up the quantum register have fixed detuned Larmor frequencies (set by the static polarizing magnetic field) and share exchange couplings that are determined, once and for all, by the molecular structure [16].

We are, in essence, constructing sort of *artificial molecules* – qubit circuits having fixed, detuned Larmor frequencies and fixed coupling strengths – and, like in NMR, using AC fields to perform one and two-qubit gate operations [16, 135]. The essential difference between our molecules and those of NMR resides in the qubit–qubit couplings and the way they are exploited. In NMR, the secular terms in the coupling Hamiltonian (those that commute with the Zeeman Hamiltonian and thus act to first order) dominate the spin–spin interaction. Two-qubit gates are realized as the spins precess freely, while refocusing pulses are applied in order to do nothing [99]. In our scheme, the coupling is purely *non*-secular, and acts only to second order. So with respect to the AC control signals, we are in rather the opposite case of NMR:

here, the coupling may be neglected during the one-qubit gates and free evolution, but must be enhanced through irradiation pulses to perform two-qubit gates.

I will refer to this gate scheme by the nickname *FLICFORQ*: *Fixed LInear Couplings between Fixed Off-Resonant Qubits*. FLICFORQ, as such, is a style of quantum register, but it also implies a class of certain control signals. As the couplings are fixed, they are not subject to external control signals, and as the qubit frequencies are fixed, they may not be DC tuned. Our task, then, comes down to constructing microwave control sequences that enhance the non-secular coupling and give rise to a strong enough qubit–qubit interaction to entangle the qubits.

A FLICFORQ register could be implemented using most any quantum computing technology, but it is particularly applicable to superconducting qubits of the charge or flux variety. We focus here on two-qubit registers (sample circuits shown in figure 3.1), the simplest that allow the realization of a universal set of quantum gates; comments on extensions to larger systems will follow. The optimal bias conditions for the circuits shown are with half a Cooper pair worth of charge on the effective gate capacitance (not shown), e.g. $N_{g1} = N_{g2} = 1/2$ for charge qubits, where $N_g = C_g U / 2e$ is the dimensionless gate charge; or $N_{\phi 1} = N_{\phi 2} = 1/2$ for flux qubits, where $N_\phi = \Phi_{ext} / \Phi_o$ is the flux frustration in the qubit loops. Under these conditions, the systems are immune, to first order, to variations in the control parameters, such as $1/f$ charge noise in the Josephson junctions or substrate or noise due to the motion of trapped flux [30].

At optimal bias and in the two-level approximation, these two-qubit systems are described by the Hamiltonian

$$2\mathcal{H}/\hbar = \omega_1 \sigma_1^z + 2\Omega_1 \cos(\omega_1^{rf} t + \phi_1) \sigma_1^x + \omega_2 \sigma_2^z + 2\Omega_2 \cos(\omega_2^{rf} t + \phi_2) \sigma_2^x + \omega_{xx} \sigma_1^x \sigma_2^x, \quad (3.1)$$

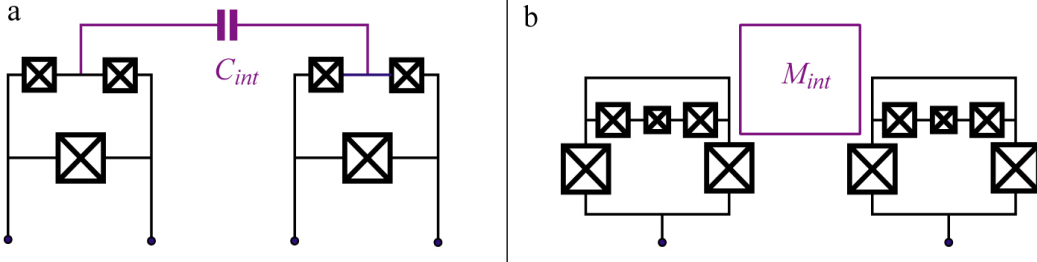


Figure 3.1: Superconducting two-qubit circuits for performing universal quantum gates at optimal bias point with linear fixed couplings. (a) Charge qubits coupled by capacitor. (b) Flux qubits coupled by mutual inductance.

where $\omega_j/2\pi$ is the transition frequency of qubit j ; Ω_j and $\omega_j^{rf}/2\pi$ are, respectively, the amplitude and frequency of the microwave signal applied to the write port of qubit j ; and $\omega_{xx}/2\pi = (t_{ent})^{-1}$ is the coupling frequency (if only the $\sigma_1^x \sigma_2^x$ term were present in \mathcal{H} , the time needed to go from a computational basis state to a maximally entangled state would be $t_{ent}/4$). To ensure the qubits remain decoupled in the absence of control signals, we impose the weak coupling constraint that the non-secular coupling ω_{xx} be much weaker than the interqubit detuning $\Delta = |\omega_2 - \omega_1|$.

3.3 Entanglement by double-resonant irradiation

An analysis of this problem using the dressed state formalism of quantum optics [81] can point the way to one possible solution, as it allows us to understand how the very weak non-secular interqubit coupling ω_{xx} may be used to produce maximally entangled two-qubit states, see figure 3.1. For the moment, consider only resonant microwave pulses applied to each qubit simultaneously.

When the AC drive fields and qubits are uncoupled, each qubit + field system has an infinite discrete ladder of doubly-degenerate energy levels, labelled by the qubit state $|1\rangle$ or $|0\rangle$ and the photon number $|N\rangle$, and separated by $\omega_{1,2}^{rf} = \omega_{1,2}$. Taking the

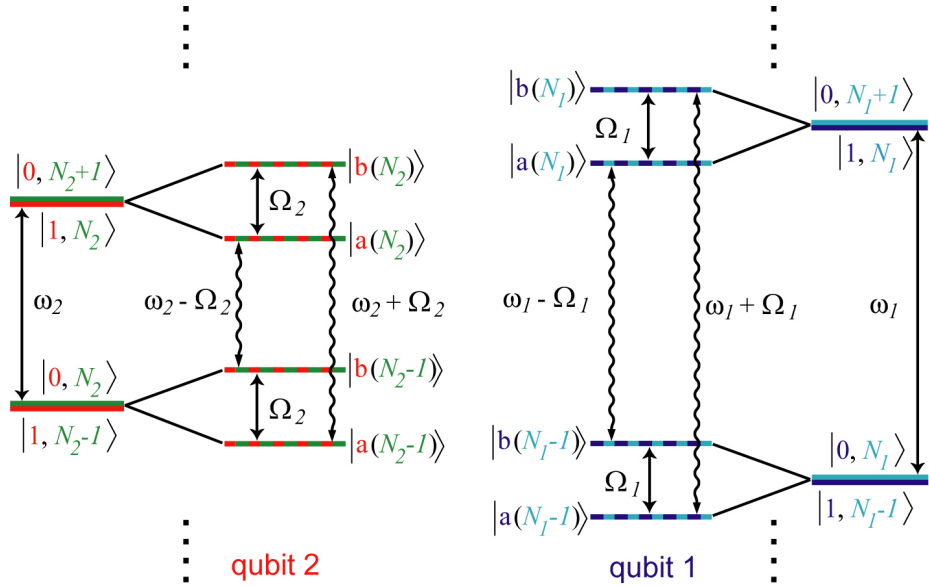


Figure 3.2: Energy levels of qubit + rf photons systems with (inner levels) and without (outer levels) qubit-photon coupling. *Outer*: systems have an infinite ladder of doubly-degenerate levels corresponding to products of a photon number state (green, orange) and a qubit state (red, blue). *Inner*: Photon–qubit coupling lifts degeneracy in each manifold by Rabi frequency $\Omega_{1,2}$. Transitions between adjacent manifolds (wavy arrows) correspond to absorption/emission of a photon from dressed qubit system. The off-resonant qubits can be put on speaking terms by adjusting Rabi frequencies such that $\Omega_1 + \Omega_2 = \omega_1 - \omega_2 \equiv \Delta$. Shown is the symmetric case where $\Omega_{1,2} = \Delta/2$

qubit–field coupling into account lifts the degeneracy, splitting the two states in each manifold by the field strength (Rabi frequency) $\Omega_{1,2}$. The two dressed qubits may then absorb and emit energy at frequencies $\omega_1 \pm \Omega_1$ and $\omega_2 \pm \Omega_2$, respectively. The irradiation thus splits the single-mode qubit spectra into two sidebands. Choosing

$$\Omega_1 + \Omega_2 = \Delta \quad (3.2)$$

causes the upper sideband of one qubit to overlap the lower sideband of the other, and they can then exchange photons of energy $\hbar(\omega_1 - \Omega_1) = \hbar(\omega_2 + \Omega_2)$ through the coupling reactance.

A more quantitative picture of the qubit–qubit interaction follows from an analysis using rotating reference frames. First, note that measurement in the computational basis commutes with the $\sigma_{1,2}^z$ terms in \mathcal{H} , and that one-qubit RF pulses perform pure σ^x and σ^y rotations in the doubly Larmor-precessing frame $\mathfrak{R}^{(2)}$ rotating at $\omega_{1,2}$ about $\sigma_{1,2}^z$, respectively. This allows us to define all gates in $\mathfrak{R}^{(2)}$, where the qubits are static in the absence of irradiation pulses.

Then an effective Hamiltonian for a FLICFORQ system under doubly-resonant irradiation may be obtained by moving from $\mathfrak{R}^{(2)}$ to a quadruply-rotating frame $\mathfrak{R}^{(4)}$ which, in addition, rotates at $\Omega_{1,2}$ about $\sigma_{1,2}^x$, respectively [55]. We now focus on the case where $\Omega_{1,2} = \Delta/2$, as depicted in fig. 2, for which one obtains in $\mathfrak{R}^{(4)}$ in the rotating wave approximation,¹

$$2\mathcal{H}'/\hbar = \frac{\omega^{xx}}{8} \{ (\sigma_1^y \sigma_2^y + \sigma_1^z \sigma_2^z) \cos(\phi_1 - \phi_2) + (\sigma_1^z \sigma_2^y + \sigma_1^y \sigma_2^z) \sin(\phi_1 - \phi_2) \}. \quad (3.3)$$

¹All other terms in \mathcal{H}' oscillate rapidly and average to zero.

This Hamiltonian can be used as the sole non-local generator of arbitrary two-qubit gates [56, 57, 58, 59, 60, 61]. Noting the established capability for arbitrary local unitaries with the same microwave control hardware we have assumed here [26, 71], this FLICFORQ scheme is thus a simple and practical implementation of a universal quantum register with only local microwave control.

In general, the extraction of some desired effective interaction from a naturally available interaction calls for the interleaving of one qubit rotations with periods of evolution under the available interaction². Regarding 3.3 as the available interaction in the present case, we now show how the primitive $\pi/2$ rotation (defined as in 2.33),

$$R_{yy} = \frac{1}{\sqrt{2}} (\mathbf{1} - i\sigma_1^y\sigma_2^y),$$

which we demonstrated in Chapter One to be generator of the Clifford group, can be extracted by simply adjusting the phase of the resonant tone applied to one of the qubits.

Choosing the microwave frequencies to be resonant and the amplitudes $\Omega_{1,2}$ to satisfy 3.2 switches the interaction from being only a second order effect proportional to $(\omega_{xx}/\Delta)^2$, where it can be ignored or actively cancelled [135, 82, 62], to a strength of $\omega_{xx}/8$ where it has a strong effect on the system's evolution. However, as the Hamiltonian 3.3 contains multiple terms, some of which do not commute, the engendered gate will be rather complicated. The most straightforward case is when the microwave phases are either the same, e.g. $\phi_1 = \phi_2 = 0$, or different by $\pi/2$, e.g. $\phi_1 - \phi_2 = \pi/2$. As any of the individual terms in 3.3 would suffice for universal control, we can consider the former case without loss of generality. Then the two terms present, directed along $\sigma_1^y\sigma_2^y$ and $\sigma_1^z\sigma_2^z$, commute and the unitary evolution of

²There has been a great deal of work studying methods and costs of simulating one Hamiltonian with another. The references [56, 57, 58, 59, 60, 61] are all relevant, especially [59] and refs. therein.

the system proceeds according to

$$\begin{aligned}
U(t_o, t) &\equiv \exp[-i\mathcal{H}'(t - t_o)/\hbar] \\
&= \exp[-i\omega^{xx}(t - t_o)(\sigma_1^y\sigma_2^y + \sigma_1^z\sigma_2^z)/16] \\
&= \exp[-i\frac{\varphi}{2}\sigma_1^y\sigma_2^y]\exp[-i\frac{\varphi}{2}\sigma_1^z\sigma_2^z],
\end{aligned} \tag{3.4}$$

where,

$$\varphi = \frac{(t - t_o)\omega_{xx}}{8}. \tag{3.5}$$

The gate naturally implemented in the FLICFORQ system irradiated according to 3.2 with $\phi_{1,2} = 0$ is thus,

$$D(\varphi) = \{\cos \frac{\varphi}{2}I - i \sin \frac{\varphi}{2}\sigma_1^y\sigma_2^y\} \tag{3.6}$$

$$\times \{\cos \frac{\varphi}{2}I - i \sin \frac{\varphi}{2}\sigma_1^z\sigma_2^z\} \tag{3.7}$$

$$= R_{yy}(\varphi)R_{zz}(\varphi), \tag{3.8}$$

where I have used standard definitions of rotation operators $R(\varphi)$ [7]. Note that under these conditions, shifting the relative phase $\phi_1 - \phi_2$ of the irradiation signals by π allows one to generate the inverse operation $D(-\varphi)$. Applying the irradiation for a duration $t - t_o = 4\pi/\omega_{xx}$ corresponding to $\varphi = \pi/2$ generates the two-qubit $\pi/2$ rotation,

$$\begin{aligned}
D &= R_{yy}(\pi/2)R_{zz}(\pi/2) \\
&= (\mathbf{1} - i\sigma_1^y\sigma_2^y)(\mathbf{1} - i\sigma_1^z\sigma_2^z)/2,
\end{aligned} \tag{3.9}$$

where I have used the bare 'D' to denote this particular discrete black-box unitary transformation. The D gate and its inverse are generators of the Clifford group

and are thus universal when augmented with local unitaries. They have Gottesman tables:

	D		D^{-1}	
WX	XW		XW	
XW	WX		WX	
WZ	YX		$-YX$	
ZW	XY		$-XY$	

and

WX	XW
XW	WX
WZ	$-YX$
ZW	$-XY$

(3.10)

To demonstrate the universality of D and D^{-1} , we explicitly construct a synonym for the canonical two-qubit gate CNOT, in the spirit of 2.55:

	D^{-1}	$(WY)^{1/2}$	D	$(WX)^{1/2}$	$(ZW)^{1/2}$	
WX	XW	XW	WX	WX	WX	
XW	WX	WZ	YX	YX	XX	
WZ	$-YX$	$-YZ$	$-ZY$	ZZ	ZZ	
ZW	$-XY$	$-XY$	ZW	ZW	ZW	

(3.11)

A comment is in order. We have asked only for the minimal and simplest hardware – fixed linear coupling circuit elements. We have restricted ourselves to exclusively microwave control of static and detuned qubits, meaning there is no reliance on fast tuning of the qubit transition frequencies and the implied large relative bandwidth of the control lines. We have restricted the available microwave control signals themselves to those typically used to perform individual one-qubit rotations, namely signals resonant with the (uncoupled) qubits' transition frequencies. And under these restrictions, made with an eye towards maximizing both qubit coherence and experimental feasibility, we have shown how control of the four experimental knobs $\Omega_1(t)$, $\Omega_2(t)$, $\phi_1(t)$ and $\phi_2(t)$ allows one to implement any rotation of the two-qubit Hilbert

space.

We now turn to the issue of timing. Note that the evolution operator \mathcal{U} in $\mathfrak{R}^{(2)}$ is related to the evolution operator \mathcal{U}' in $\mathfrak{R}^{(4)}$ according to

$$\mathcal{U} = \mathcal{R}(t)\mathcal{U}'(t - t_o)\mathcal{R}^{-1}(t_o), \quad (3.12)$$

where

$$\mathcal{R}(t) = \exp\{it(\omega_1^R\sigma_1^x + \omega_2^R\sigma_2^x)\} \quad (3.13)$$

is the one-qubit rotation operator connecting $\mathfrak{R}^{(2)}$ and $\mathfrak{R}^{(4)}$, so in general a two-qubit gate must be accompanied by the appropriate one-qubit rotations. However, for $\Omega_{1,2} = \Delta/2$, $\mathcal{R}(t)$ reduces to the identity operation at times $t_m^{sync} = 4\pi m/\Delta$ when the two frames $\mathfrak{R}^{(2)}$ and $\mathfrak{R}^{(4)}$ coincide. So one can always do away with the initial one-qubit rotation $\mathcal{R}^{-1}(t_o)$ by choosing to initiate two-qubit gates only at times $t_o = t_m^{sync}$.

Also, the CNOT synonym 3.11 requires two applications of D, a trait the emerges from the presence of two commuting non-local terms in the effective Hamiltonian under the conditions at hand. A protocol to construct a more efficient generator of the Clifford group can be obtained by applying the notion of refocusing as in NMR [135, 82, 62, 15]. Here, we refocus the $\sigma_1^z\sigma_2^z$ term in 3.3 by adjusting the phase of the irradiation on one of the two qubits by π . The effective Hamiltonian acquires an overall sign due to

$$\cos(\phi_1 - \phi_2) \rightarrow \cos(\phi_1 - \phi_2 - \pi) = -\cos(\phi_1 - \phi_2), \quad (3.14)$$

but the term $\sigma_1^y\sigma_2^y$ acquires also a second sign change because the phase flip, when translated back to the laboratory frame, amounts to an instantaneous σ_z rotation

by π on the affected qubit, resulting in $\sigma_1^y \sigma_2^y \rightarrow -\sigma_1^y \sigma_2^y$. The result is an inversion of only the $\sigma_1^z \sigma_2^z$ term in 3.3. As in NMR, letting the system evolve for equal durations under the two inverse Hamiltonians refocuses any dynamics owing to the inverted term.

We have verified the efficacy of this phase flip numerically. The result is a protocol to produce the rotation $(YY)^{1/2}$, which is a minimal generator of the Clifford group and need only be deployed a single time to produce CNOT, as the following Gottesman table verifies,

	$(WZ)^{1/2}$	$(ZW)^{1/2}$	$(YY)^{1/2}$	$(XW)^{1/2}$	$(WY)^{1/2}$	$(WZ)^{-1/2}$	$(ZW)^{-1/2}$
WX	$-WY$	$-WY$	$-WY$	$-WY$	$-WY$	WX	WX
XW	XW	XW	ZY	YY	YY	$-YX$	XX
WZ	WZ	WZ	$-YX$	ZX	ZZ	ZZ	ZZ
ZW	ZW	$-YW$	$-YW$	ZW	ZW	ZW	ZW

(3.15)

Figure 3.3 explicitly depicts the pulse sequence that uses this refocusing scheme to implement $(Y_1 Y_2)^{1/2}$. The phases are initially chosen $\phi_{1,2} = 0$, and after t_{ent} , the phase ϕ_2 of the signal applied to qubit 2 is adjusted by π . After another t_{ent} the $\sigma_1^z \sigma_2^z$ term in \mathcal{H}' is refocused, and the universal gate $(1 + i\sigma_1^y \sigma_2^y)/\sqrt{2} = (Y_1 Y_2)^{1/2}$ has been implemented.

We have performed simulations of the protocol generating $(YY)^{1/2}$ as shown in 3.3 by solving the two-qubit Bloch equations as developed in Chapter Two. The simulations do not rely on the rotating wave approximations leading to the effective Hamiltonian 3.3, nor on a perturbative expansion of the time-dependent Hamiltonian. However, we did use a two-level approximation and square RF pulses for the simulation results presented.

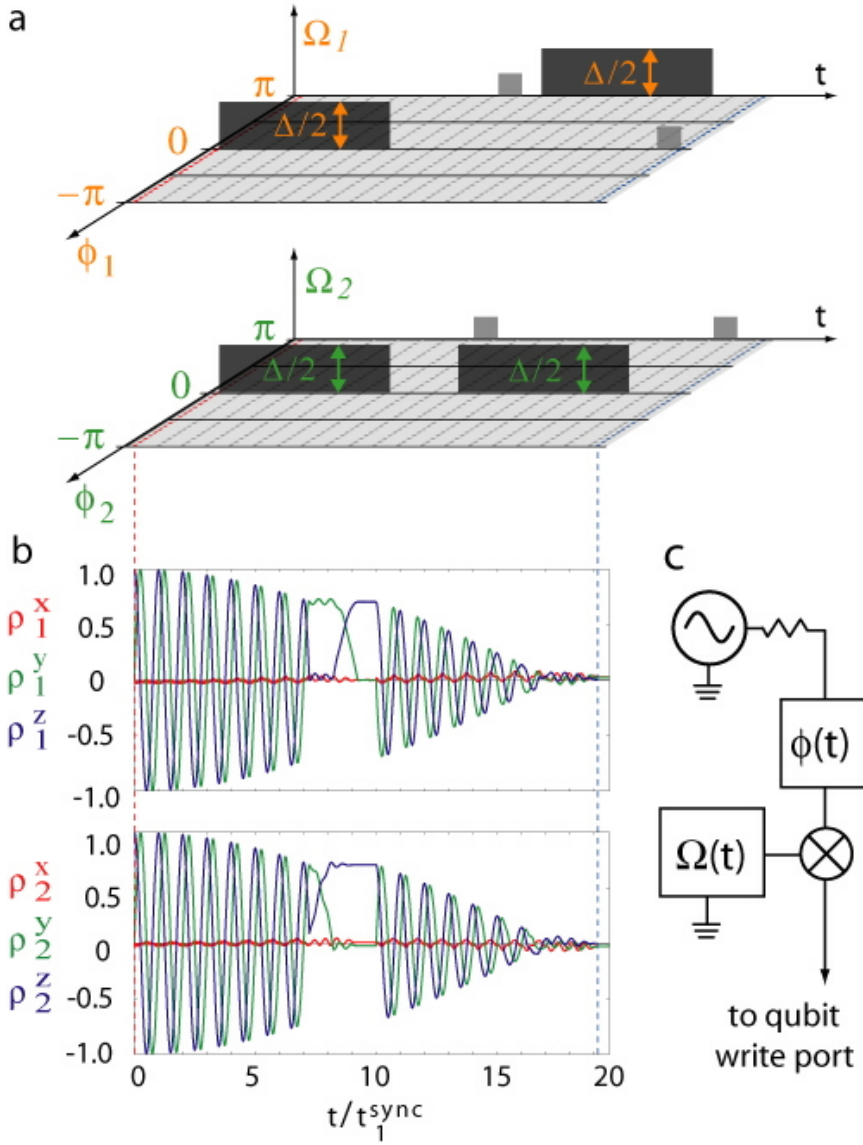


Figure 3.3: (a) Polar representation of pulse sequence for the universal two-qubit gate $(YY)^{1/2}$ at optimal bias using FLICFORQ. Two-qubit pulses (black) have amplitude $\Delta/2$ and duration t^{ent} , and are initiated only at times $t_m^{\text{sync}} = 4\pi m/\Delta$ (grey dashed lines) when the doubly- and quadruply-rotating frames coincide. One-qubit pulses (grey) have amplitude $(\frac{\Delta\pi}{\omega^{xx}} \bmod 2\pi)/t^{\text{sync}}$ and duration t^{sync} . (b) Sample simulation of pulse sequence using the full time-dependent Hamiltonian (1) and parameters $\omega_1^L = 1.1060$, $\omega_2^L = 1.0527$, $\omega^{xx} = .003679$. Initial state is $|00\rangle$. Simultaneous vanishing of each reduced density operator indicates generation of maximally entangled state. Final state is $(|00\rangle - i|11\rangle)/\sqrt{2}$; gate fidelity is $> .99$, with errors due to Bloch-Seigert shift. Plotted are the components of each reduced density operator ($\rho_i^\alpha = \langle \sigma_i^\alpha \rangle$). (c) Schematic experimental set-up for producing pulses to implement universal gates with FLICFORQ.

3.4 Gate fidelity under double-resonant irradiation

3.4.1 Errors in one-qubit rotations due to fixed coupling

The presence of the always-on coupling will cause some degree of error in the single qubit rotations. How large will these effects be? The coupling Hamiltonian \mathcal{H}_{xx} and the Larmor terms \mathcal{H}_z do not commute,

$$[\mathcal{H}_{xx}, \mathcal{H}_z] \neq 0, \quad (3.16)$$

so the first order corrections to the energy levels will vanish,

$$E_{00}^{(1)} = E_{01}^{(1)} = E_{10}^{(1)} = E_{11}^{(1)} = 0. \quad (3.17)$$

To second order, the energies will shift according to

$$\begin{aligned} E_{00}^{(2)} &= -\frac{\omega_{xx}^2}{\omega_1 + \omega_2} \\ E_{01}^{(2)} &= -\frac{\omega_{xx}^2}{\Delta} \\ E_{10}^{(2)} &= \frac{\omega_{xx}^2}{\Delta} \\ E_{11}^{(2)} &= \frac{\omega_{xx}^2}{\omega_1 + \omega_2}. \end{aligned} \quad (3.18)$$

By assumption we are in the weak coupling regime where $\omega_{xx} \ll |\omega_1 - \omega_2| \ll \omega_{1,2}$ so the energy shifts will lead to an error rate in the one-qubit rotations of approximately 10^{-3} . Note that these errors are due to the very slight residual entanglement of the qubits in the absence of driving, so they can be corrected by performing brief two-qubit rotations using any of the schemes presented in this thesis.

3.4.2 Leakage due to strong driving

What will be the dominant sources of fidelity loss in this gate scheme? As with other gate schemes for superconducting qubits, there will be errors due to leakage to states outside the computational subspace. The fast Rabi flopping used here to bring two detuned qubits into resonance – the essential new “technology” this scheme requires – may make this more significant. Rabi frequencies up to approximately 150MHZ are commonly achieved in a broad range of technologies, with frequencies as high as several hundred MHZ reported [63]. The leakage will depend strongly on the anharmonicity of the qubit systems, which is typically set by fabrication and bias parameters. For example, for charge qubits at optimal bias our simulations indicate that the ratio of the effective Josephson energy E_J to the Cooper pair charging energy E_C should satisfy $E_J/E_C \lesssim 2$ if the leakage probability due to strong driving ($\Omega_j \approx .1\omega_j$) is to be $\lesssim 1\%$. These simulations assume a constant driving level integrated over the duration of a typical two-qubit gate pulse. They do not account for imperfect pulses, where bandwidth effects or dispersion can cause leading or trailing edge distortion that could be more efficient at generating excitations outside the computational subspace. However, these effects can largely be managed by careful engineering of the microwave pulse amplitudes [64, 65]

3.4.3 The rotating wave approximation

The above derivation of the effective Hamiltonian 3.3 required a rotating wave approximation for the drive signal on each qubit. (The rotating wave approximation regards the oscillatory fields applied to each qubit along σ_x as a superposition of two fields rotating in opposite directions in the xz plane, their σ_y components always equal and opposite; in a frame rotating about σ_z at the respective drive frequency

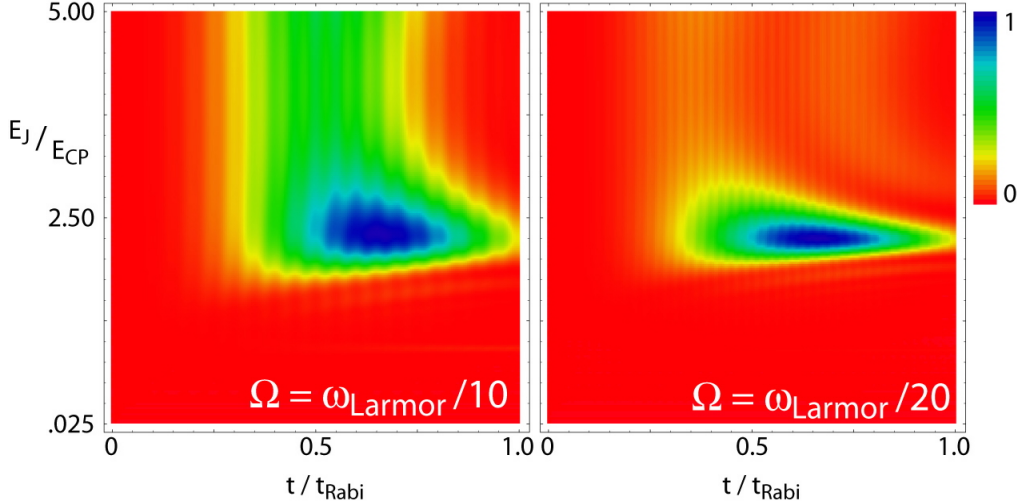


Figure 3.4: Leakage probability for charge qubits under strong resonant driving as a function of E_J/E_{CP} . Simulations are performed by keeping the lowest seven energy levels and driving system at a constant driving level $\Omega = \omega/10$ (*Left panel*) and $\Omega = \omega/20$ (*Right panel*). The strong leakage as the aspect ratio passes through the harmonic point whereat $\omega_{01} = \omega_{12}$ is as expected. As the gate scheme is applicable when $\Gamma_{1,2} \ll \omega_{xx} \ll \Omega$, we have not included finite lifetime effects.

one of these is thus static while the other oscillates at twice the drive frequency. The RWA is to discard this counter-rotating term.) The effect of the term is to slightly renormalize the qubit frequency, an effect known as the Bloch-Siegert shift [69]. Analytical results can be obtained for the leading order corrections with a perturbative analysis [70]. For the purposes of quantum gates it can be viewed as leading to oscillations in the qubit state at frequency $2\omega_{rf}$ and of amplitude of order Ω/ω_{rf} [128]. These effects will have minimal impact on one-qubit rotations, since Ω can be chosen to be small. For the two-qubit gates, however, $\Omega_{1,2}$ are set by Δ , which is constrained by $\Delta \gg \omega_{xx}$, so the effect could be more troublesome. There is thus a trade-off in selecting system parameters for optimal gate fidelity – to reduce the two-qubit errors in one qubit gates, we should like to make ω_{xx}/Δ as small as possible. To avoid errors due to Bloch-Siegert shift during the two-qubit gates, though, we would like to keep Δ and thus $\Omega_{1,2}$ small compared with $\omega_{1,2}$. Parameters in

the general range of those used in our simulations approximately balance these two effects. We emphasize that these errors are all deterministic in nature and can be accounted for in a straightforward manner.

3.4.4 Other sources of error

In practice, there will also be gate errors due to imperfect microwave pulses. Since one-qubit rotations are sensitive to the integrated applied irradiation power, constructing pulses to perform high-fidelity one-qubit gates should be straightforward. Producing the two-qubit pulses, however, will be more difficult: the strength of the effective qubit–qubit interaction depends strongly on the amplitude of both RF signals, so the gates will be very sensitive to variations in the pulse amplitudes. For the parameters used in simulations and a qubit linewidth $\approx 2\text{MHz}$, the uncertainty in the pulse amplitudes should not be more than about 0.5%. Though challenging, this level of stability is possible with commercially available electronics.

Finally, the cross-coupling of write signals between two qubits will also lead to gate errors. In practice, this can be actively compensated with supplementary pulses.

We note that these effects leading to gate errors are predominantly systematic and can thus, in principle, be reduced or eliminated. Also, as we will see later, there are configurations of the drive parameters that can lead to spurious effective coupling terms during one-qubit rotations. But we note that the situation is at least as hopeful as in NMR, where there is also a *secular* coupling term to be nullified, in addition to the non-secular term we have here [135]. It is our hope that some of the techniques for combatting gate errors that have been developed in NMR quantum computing can be adapted or extended to suit FLICFORQ systems. For example, the error rate due to the always-on coupling could be largely reduced by dynamically decoupling the qubits with refocusing pulses [15, 16], or with short cross-resonant

pulses of appropriate phase to take advantage of the effect described by 5.10 and 5.1. Here, this would be achieved by performing appropriately timed π rotations about σ_y , which anticommutes with the coupling term $\sigma_1^x\sigma_2^x$. The techniques of composite pulses, pulse shaping, and phase ramping could prove similarly useful. For one-qubit gates, some early steps have been taken in this direction [71].

3.4.5 Entanglement modulation depth and bandwidth

Gate schemes can be quantitatively compared by defining the following characteristics. The *entanglement bandwidth* Υ is the maximal rate of entanglement generation allowed by the scheme³. Here we have simply,

$$\Upsilon = \frac{1}{8} \frac{\omega_{xx}}{2\pi} \quad (3.19)$$

as the effective interaction strength is set once the effect is switched on by satisfying 3.2 with the resonant drive amplitudes.

The error rate can be discussed by defining the *entanglement modulation depth* Λ as,

$$\Lambda = \frac{F_{2q}}{1 - F_{1q}}, \quad (3.20)$$

where F_{1q} and F_{2q} stands for some fidelity measure of the one and two-qubit gates – we will use the trace fidelity $F = 2^{-n}Tr[\mathcal{U}_{ideal}^\dagger \mathcal{U}_{actual}]$ where \mathcal{U} is the evolution operator. As the one-qubit rotations are, collectively, limited in fidelity by the residual entanglement introduced through the two-qubit gate hardware unless we perform refocusing or otherwise actively compensate for the weak coupling, this measure identifies the modulation depth of the entanglement in the system.

³For experimental systems, this number can be compared to the dephasing time T_φ to give a quality factor of the two-qubit control.

In the fixed coupling scheme, the energy eigenstates will pick up some entangled character proportional to $(\omega_{xx}/\Delta)^2$, and this limits the fidelity of one-qubit rotations when the coupling is uncompensated, while the two-qubit rotations will likely be limited in fidelity by the Bloch-Siegert oscillations when $E_J/E_C \lesssim 1.5$. We find,

$$\begin{aligned}\Lambda &\simeq \frac{1 - \Delta^2/\bar{\omega}^2}{\omega_{xx}^2/\Delta^2} \\ &= \frac{\Delta^2}{\omega_{xx}^2} - \frac{\Delta^4}{\omega_{xx}^2 \bar{\omega}^2}\end{aligned}\quad (3.21)$$

where $\bar{\omega}$ is average of the qubit frequencies. In the weak coupling regime $\omega_{xx} \ll |\omega_1 - \omega_2| \ll \omega_{1,2}$ these characteristics evaluate to,

$$\Lambda \approx 100 = 20\text{dB},$$

and

$$\Upsilon = \frac{\pi}{4\omega_{xx}} \quad (3.22)$$

with larger modulation depths possible by actively cancelling the residual couplings.

3.5 Other protocols for gates at optimal bias

3.5.1 Generalization to off-resonant drive

The above protocol was the first proposal for generating entanglement in two-qubit superconducting circuits while keeping both qubits biased at their respective optimal bias points in both charge and flux throughout the entire gate protocol. The idea was supplemented by ideas from other groups, a few of which are now described. First, the above dressed state picture can be rather directly extended to include the more gen-

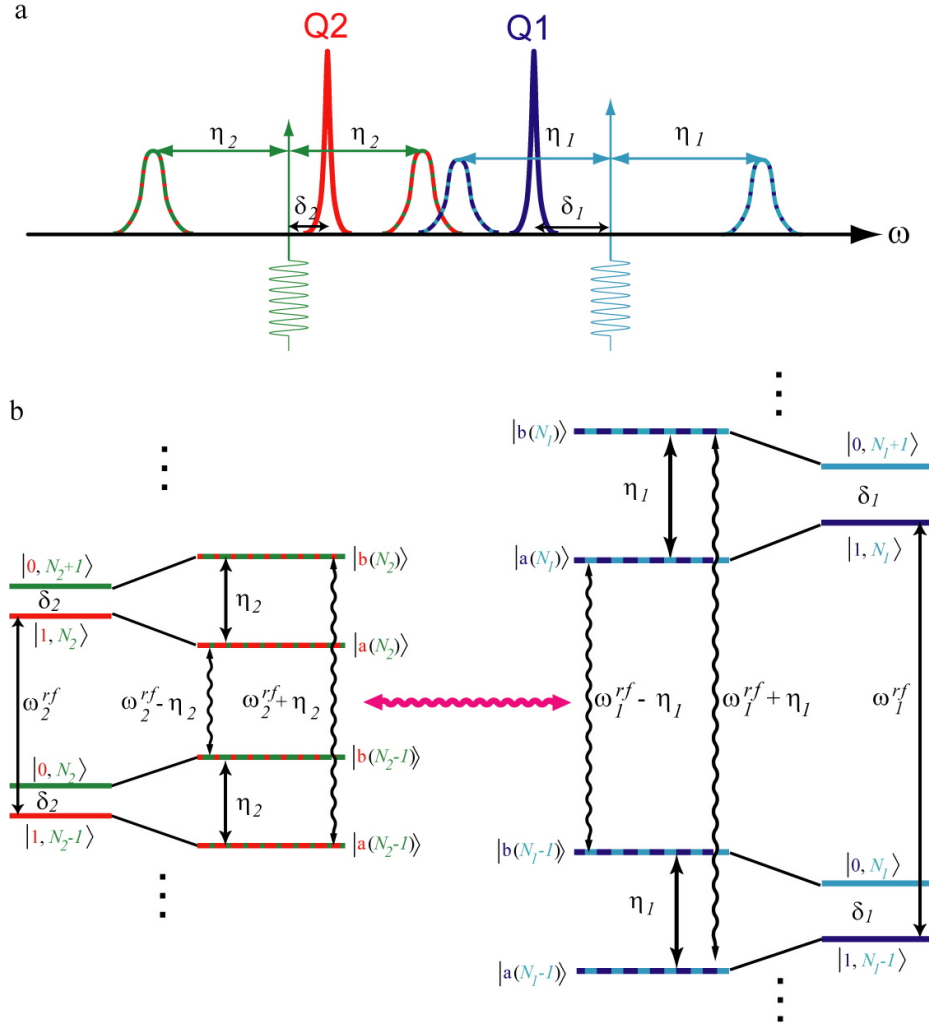


Figure 3.5: Schematic of sidebands of the doubly driven two-qubit system generalized to case of off-resonant microwave signals. (a) When the signals are detuned by $\delta_j = |\omega_j - \omega_j^{rf}|$ the effective precessional frequencies are $\eta_j = \sqrt{\Omega_j^2 + \delta_j^2}$ and sidebands of the driven systems emerge at $\omega_j^{rf} \pm \eta_j$. The sidebands closer to the undriven qubit frequencies contain a large portion of qubit eigenstate and less photon number state, and vice versa (depicted through the weight of color-dashed lines). (b) dressed state picture.

eral case of dual off-resonant driving, a task carried out by Ashhab *et. al*[101]. This extension partially addresses one complaint about the original FLICFORQ proposal - namely the requirement for strong driving signals in order to bridge the spectral gap between the two qubits⁴. By driving the qubits away from their respective transition frequencies, the matching condition contains the generalized precessional frequencies $\eta_j = \sqrt{\Omega_j^2 + \delta_j^2}$ rather than simply the drive strengths Ω_j . In other words, it allows one to make use of a *detuning field* of the microwave drives from the respective qubits, along with the drive strengths, rather than the drive strengths alone. This case is depicted below.

The effective coupling strength obtained in this case is, from Ashhab *et al*,

$$\frac{\omega_{xx}^{eff}}{\omega_{xx}} = \frac{1}{4} \left[1 + \frac{x - \frac{1}{4x}}{\sqrt{1 + (x - \frac{1}{4x})^2}} \right]^2, \quad (3.23)$$

where $x = \Omega/\Delta$, and the drive amplitudes applied to each qubit are assumed to be equal. This case is discussed further when we turn to the cross-resonance irradiation protocol.

3.5.2 Driven non-linear coupling

Though the above generalization to off-resonant driving somewhat relaxes the requirements for large driving fields, the protocol nonetheless requires qubits that are relatively close in frequency to be useful⁵. In charge qubits, this is a problem one can approach with confidence, as the qubit frequencies depend only linearly on the junction critical currents, the parameter in which the natural scatter in the fabri-

⁴It is worth noting that the limits on drive strengths in a given system have nothing to do with the available microwave power, but rather the desire to remain in the artificially truncated computational portion of the quantum circuits' full Hilbert space.

⁵Note that the effective coupling goes as Ω^4 for weak driving.

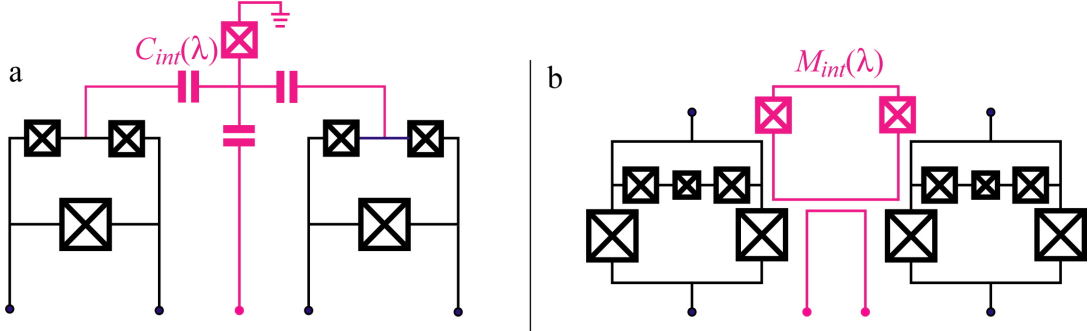


Figure 3.6: Schematic circuits for implementing two-qubit gates at optimal bias with parametric driving of a non-linear coupling subcircuit. Adding a non-linear element to the coupling allows the effective interaction strength to be tuned by varying some external control parameter λ , which for charge qubits (a) would be a voltage bias and for flux qubits (b) a current bias. When the coupling is modulated at one of $\omega_1 \pm \omega_2$ the interaction strength increases linearly with the drive strength.

cation process is manifest. With flux qubits, however, the situation is less hopeful: there, transition frequencies are exponentially sensitive to junction critical currents.

It should also be noted that the risk of generating excitations outside the truncated computational portion of the quantum circuits subspace depends, for a given ratio of the drive strength to the qubit transition frequency, strongly on the anharmonicity of the system's spectrum of transitions. In more recent experiments involving only weakly anharmonic systems, these constraints on drive strengths are also very important.

Bertet *et al* proposed a solution to the problem that allows the qubits to remain at optimal bias but also allow one to entangle broadly detuned qubits without the need of strong driving fields. This elegant solution was also studied by Niskanen et al [43]. The solution calls for a non-linear coupling subcircuit, specifically a third flux qubit with larger energy splitting than the other two, to be driven at the sum or difference frequency of the two targeted qubits. Idealized circuits implementing this system are shown below.

These systems implement an effective Jaynes-Cummings interaction between the target qubits with a strength linearly dependent on the drive. This makes it possible to use microwave power (but not applied to the qubits themselves!) to overcome the interqubit detuning and generate entanglement. The effective Hamiltonian when the coupling strength is varied harmonically with amplitude $\delta\omega_{xx}$ at the difference frequency $\omega_{xx}^{rf} = |\omega_1 - \omega_2|$ is,

$$2\mathcal{H}_{(-)}^{eff}/\hbar = \delta\omega_{xx} (\sigma_1^- \sigma_2^+ + \sigma_1^+ \sigma_2^-)$$

One could enact an anti-Jaynes-Cummings interaction by instead modulating the coupling at the sum of the qubit frequencies, i.e $\omega_{xx}^{rf} = \omega_1 + \omega_2$, which leads to

$$\begin{aligned} 2\mathcal{H}_{(+)}^{eff}/\hbar &= \delta\omega_{xx} (\sigma_1^- \sigma_2^- + \sigma_1^+ \sigma_2^+) \\ &= 2\delta\omega_{xx} (\sigma_x^1 \sigma_x^2 - \sigma_y^1 \sigma_y^2). \end{aligned} \quad (3.24)$$

This style of coupling, and its linear dependence on the drive strength, has been experimentally verified by the NEC group[113].

3.6 Limitations

We have presented a few solutions to the two-qubit quantum gate problem for superconducting charge and flux qubits. Since we studied the dual-resonant driving case presented in [105], we have realized – and our colleagues gently pointed out – some of the limitations of the protocol. In searching for other, perhaps better procedures, we ran into a different problem: the techniques we were using to develop solutions were not particularly powerful.

The main problem is that they did not allow us to identify with confidence a

certain scheme as being optimal. Guided by our own or others' intuition, or by previous results from other quantum computing fields such as ion traps or NMR, we proceeded by a sort of trial and error, testing ideas and protocols through simulations of the two-qubit master equation. Of course, after identifying a potential solution, calculating the corresponding effective Hamiltonian was another task in itself. To do so, we relied, as we did in the FLICFORQ paper, on rotating frames and the identification of static terms in a special frame once certain constraints had been imposed⁶.

Though fruitful, this technique didn't address the main issue of drawing general conclusions about a solution, or to identify new solutions. To do so, we would need a tool that could encapsulate a broad range of schemes and place them all on the same footing.

⁶This technique was originally brought to our attention by Daniel Esteve, though we later found it in an early paper by Hartman and Hahn[55].

Chapter 4

Fourier Approach to The Quantum Gate Problem

...and one should fight for the form only insofar as it can serve as a means of expression of the inner resonance.- Wassily Kandinsky, from Der Blaue Reiter (1912)

First, let me phrase the problem clearly. Consider the (idealized) Hamiltonian of a two-qubit system coupled to classical control fields,

$$\begin{aligned}\mathcal{H} \equiv \mathcal{H}(\boldsymbol{\lambda}) = & \sum_{k=1}^n \left(\omega_k \sigma_k^z + 2\Omega_k \cos(\omega_k^{rf} t + \phi_k) \sigma_k^x \right), \\ & + \frac{\hbar}{2} \sum_{j,i=\{x,y,z\}} \omega_{ji} \sigma_1^j \sigma_2^i,\end{aligned}\tag{4.1}$$

where ω_k are the qubit transition frequencies; Ω_k are the drive strengths; ω_k^{rf} the drive frequencies; ϕ_k the drive phases; ω_{ji} is the effective coupling strength directed along $\sigma_1^j \sigma_2^i$, and $\boldsymbol{\lambda}$ is the vector of parameters $\boldsymbol{\lambda} = \{\omega_{ji}[t], \omega_k[t] \dots \phi_k[t]\}$. The quantum gate problem may be stated as follows:

Problem 2 Idealized Quantum Gate Problem: Given the Hamiltonian (3.1) with some or all of the parameters $\{\omega_{ji}, \omega_k, \omega_k^{rf}, \Omega_k, \phi_k\}$ dynamically controlled by lab-level knobs and others controlled through circuit design and fabrication¹, derive a control sequence, i.e. specify a trajectory of $\boldsymbol{\lambda}(t) = \{\omega_{ji}[t], \omega_k[t] \dots \phi_k[t]\}$ over the interval $\{t_o, t\}$ which implements in time $t - t_o$ a particular transformation \mathcal{U} of the two-qubit Hilbert space.

The problem may be extended to address non-idealized systems by including in the Hamiltonian a description of their particular noise and decoherence properties, and it may be phrased in terms of a bound on the fidelity of the realized transformation.

In essence, the quantum gate problem is difficult because it involves inverting the Schrödinger equation. Given a time-dependent Hamiltonian acting over time $t - t_o$, quantum mechanics tells us the resultant unitary transformation of the underlying Hilbert space:

$$\mathcal{U}(t_o, t) = \mathcal{T} \exp \left\{ -\frac{i}{\hbar} \int_{t_o}^t dt' \mathcal{H}(t') \right\} \quad (4.2)$$

where \mathcal{T} is the time-ordering operator, and numerical integration provides a solution when an analytic form is not obvious.

I now describe our approach to the quantum gate problem. We will use a Fourier decomposition of the Hamiltonian in a special rotating reference frame to identify all the modes of the qubit system. Carrying this out without *a priori* restrictions on $\boldsymbol{\lambda}(t)$ allows us to identify all the entanglement modes of the two qubit system. These modes are associated with a direction in the underlying Hilbert space, and are navigable via the control vector $\boldsymbol{\lambda}(t)$.

Before that, we comment briefly on a related problem, which incorporates the

¹We do not make any particular assumptions about the degree and speed of control of any of these parameters for the time being.

non-idealities of the quantum register. When the noise and decoherence properties of the system are built into \mathcal{H} , the problem may be extended to include the study of methods by which we may not only engender a desired coherent evolution of the state of the system, but also how the trajectory of the control vector may be selected to minimize the influence of the noise, relaxation, and dephasing terms in \mathcal{H} . Ultimately, this more realistic quantum gate problem is one of the most important challenges facing experimentalists and theorists working towards the implementation of quantum computer [48].

While this problem currently defines an exciting field of research², the focus of this thesis is largely on the idealized quantum gate problem.

4.1 Fourier Analysis of the Transformed Hamiltonian

We now show how to identify these modes, using the two-qubit FLICFORQ Hamiltonian in equation 3.1 as an example.

4.1.1 Multiply-rotating references frames

We begin by taking the lab frame Hamiltonian through a series of time-independent and time-dependent transformations that, one by one, nullify and simplify the one-qubit dynamics and transfer that complexity to the qubit–qubit interaction term, ultimately arriving to a special frame wherein the Hamiltonian is purely non-local. The nullification of the individual one-qubit terms is depicted below.

²Recent results have been very encouraging, c.f. [119]

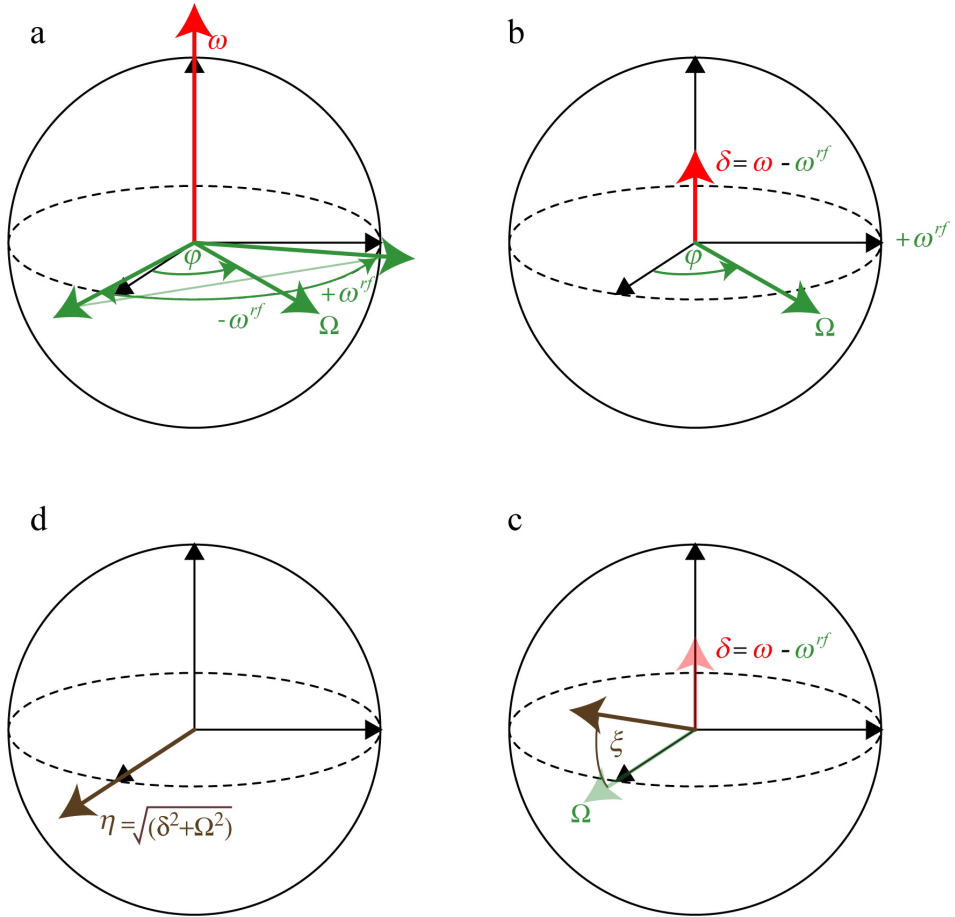


Figure 4.1: Illustration of the transformations to null out one-qubit dynamics. **a** Move to a frame rotating about σ_z at the drive frequency ω_{rf} . **b** Perform a time-independent rotation about σ_z to account for the microwave signal phase and bring the effective field into the laboratory xz-plane. **c** Tilt the remaining field by the mixing angle ξ with a time independent rotation about σ_y . **d** Move now to a rotating frame that precesses also with the generalized Rabi oscillations of frequency $\eta = \sqrt{\delta^2 + \Omega^2}$ with a time-dependent rotation about σ_x . No local terms remain in the Hamiltonian. For finite drive amplitudes Ω one RWA is made per qubit after each of **a** and **d**.

Starting from the Schrödinger equation,

$$\dot{\psi} = -\frac{i}{\hbar} \mathcal{H} \psi \quad (4.3)$$

make the substitution

$$\psi \rightarrow U \psi_o, \quad (4.4)$$

where U is the rotation operator connecting two reference frames where the state is described by ψ and ψ_o , to obtain

$$\dot{U} \psi_o + U \dot{\psi}_o = -\frac{i}{\hbar} \mathcal{H} U \psi_o. \quad (4.5)$$

Multiply on the left by U^{-1} , solve for $\dot{\psi}_o$, and the Schrödinger equation in the new frame is seen to be

$$\dot{\psi}_o = -\left(\frac{i}{\hbar} U^{-1} \mathcal{H} U + U^{-1} \dot{U}\right) \psi_o, \quad (4.6)$$

implying a Hamiltonian \mathcal{H}' in the new frame of

$$\mathcal{H}' = U^{-1} \mathcal{H} U - i \hbar U^{-1} \dot{U}. \quad (4.7)$$

We will make use of the unitary operators

$$U_j^\alpha(\theta) = \exp(-i\theta \sigma_j^\alpha / 2) \quad (4.8)$$

where σ is a Pauli matrix, $\alpha = \{x, y, z\}$ and $j = \{1, 2\}$. The action of these operators

by conjugation according to $U^{-1}\sigma U$ may be summarized as:

	$U^x(\theta)$	$U^y(\theta)$	$U^z(\theta)$
σ^x	σ^x	$\sigma^x \cos \theta + \sigma^z \sin \theta$	$\sigma^x \cos \theta - \sigma^y \sin \theta$
σ^y	$\sigma^y \cos \theta - \sigma^z \sin \theta$	σ^y	$\sigma^y \cos \theta + \sigma^x \sin \theta$
σ^z	$\sigma^z \cos \theta + \sigma^y \sin \theta$	$\sigma^z \cos \theta - \sigma^x \sin \theta$	σ^z

(4.9)

First, we transform the FLICFORQ Hamiltonian to a frame that precesses with the drive on each qubit, i.e. at ω_1^{rf} about σ_1^z and ω_2^{rf} about σ_2^z , with

$$\begin{aligned} U_{(1)} &= U_1^z(\omega_1^{rf}t) + U_2^z(\omega_2^{rf}t) \\ &= \exp(-it(\omega_1^{rf}\sigma_1^z + \omega_2^{rf}\sigma_2^z)/2). \end{aligned} \quad (4.10)$$

With the definition

$$\delta_j \equiv \omega_j - \omega_j^{rf}, \quad (4.11)$$

the Hamiltonian in this doubly rotating frame becomes:

$$\begin{aligned} 2\mathcal{H}_A &= \delta_1\sigma_1^z + \Omega_1\sigma_1^x \cos \phi_1 + \Omega_1\sigma_1^y \sin \phi_1 \\ &\quad + \delta_2\sigma_2^z + \Omega_2\sigma_2^x \cos \phi_2 + \Omega_2\sigma_2^y \sin \phi_2 \\ &\quad + \omega_{xx}[\sigma_1^x \cos(\omega^{rf}t) - \sigma_1^y \sin(\omega^{rf}t)] \\ &\quad \times [\sigma_2^x \cos(\omega^{rf}t) - \sigma_2^y \sin(\omega^{rf}t)], \end{aligned} \quad (4.12a)$$

where I have performed a rotating wave approximation[100] by ignoring the terms on each qubit that precess in this new frame at twice the drive frequency.

The driving fields, oscillatory in the lab frame, are static here, their time-dependence

having been transferred to the coupling term.

Next, we perform time-independent rotations by angles $\phi_{1,2}$ about $\sigma_{1,2}^z$, respectively, to transfer the irradiation phase dependences also to the non-local term. Applying

$$\begin{aligned} U_{(2)} &= U_1^z(\phi_1) + U_2^z(\phi_2) \\ &= \exp(-i(\phi_1\sigma_1^z + \phi_2\sigma_2^z)/2), \end{aligned} \quad (4.13)$$

we obtain

$$\begin{aligned} 2\mathcal{H}_{(2)} &= \delta_1\sigma_1^z + \Omega_1\sigma_1^x \\ &\quad + \delta_2\sigma_2^z + \Omega_2\sigma_2^x \\ &\quad + \omega_{xx}[\sigma_1^x \cos(\omega_1^{rf}t + \phi_1) - \sigma_1^y \sin(\omega_1^{rf}t + \phi_1)] \\ &\quad \times [\sigma_2^x \cos(\omega_2^{rf}t + \phi_2) - \sigma_2^y \sin(\omega_2^{rf}t + \phi_2)], \end{aligned} \quad (4.14a)$$

and the static irradiation fields are now aligned directly along the $\sigma_{1,2}^x$ -axes. The detuning fields are directed along $\sigma_{1,2}^z$, respectively, so the total effective one-qubit fields in this frame are of magnitudes

$$\eta_j = \sqrt{\delta_j^2 + \Omega_j^2}. \quad (4.15)$$

They are located in the qubits σ_1^x, σ_2^y -planes and form angles

$$\xi_j = \arctan(\delta j / \Omega_j)$$

with the $\sigma_{1,2}^x$ -axes.

In the last step, we will null out these remaining one-qubit dynamics, but first

we tilt the effective fields into direct alignment with the $\sigma_{1,2}^x$ -axes with another time-independent rotation, this time about $\sigma_{1,2}^y$. We apply

$$\begin{aligned} U_{(3)} &= U_1^y(\xi_1) + U_2^y(\xi_2) \\ &= \exp(-i(\xi_1\sigma_1^y + \xi_2\sigma_2^y)/2), \end{aligned} \quad (4.16)$$

and obtain

$$\begin{aligned} 2\mathcal{H}_{(3)} &= \eta_1\sigma_1^x + \eta_2\sigma_2^x \\ &+ \omega_{xx}[\cos(\omega_1^{rf}t + \phi_1)(\sigma_1^x \cos \xi_1 - \sigma_1^z \cos \xi_1) - \sigma_1^y \sin(\omega_1^{rf}t + \phi_1)] \\ &\times [\cos(\omega_2^{rf}t + \phi_2)(\sigma_2^x \cos \xi_2 - \sigma_2^z \cos \xi_2) - \sigma_2^y \sin(\omega_2^{rf}t + \phi_2)]. \end{aligned} \quad (4.17a)$$

Again, we note the transferal of the system's complexity from local to non-local terms.

Finally, we perform the second set of time-dependent transformations by moving to a frame rotating at the residual precessional frequencies $\eta_{1,2}$ about $\sigma_{1,2}^x$ with the unitary

$$\begin{aligned} U_{(4)} &= U_1^x(\eta_1 t) + U_2^x(\eta_2 t) \\ &= \exp(-it(\eta_1\sigma_1^x + \eta_2\sigma_2^x)/2), \end{aligned} \quad (4.18)$$

and this brings us to a quadruply rotating frame wherein the Hamiltonian is purely

non-local:

$$\begin{aligned}
2\mathcal{H}_{(4)} = & + \omega_{xx} [\cos(\omega_1^{rf}t + \phi_1)(\sigma_1^x \cos \xi_1 - (\sigma_1^z \cos(\eta_1 t) + \sigma_1^y \sin(\eta_1 t)) \sin \xi_1) \\
& - (\sigma_1^y \cos(\eta_1 t) - \sigma_1^z \sin(\eta_1 t)) \sin(\omega_1^{rf}t + \phi_1)] \\
& \times [\cos(\omega_2^{rf}t + \phi_2)(\sigma_2^x \cos \xi_2 - (\sigma_2^z \cos(\eta_2 t) + \sigma_2^y \sin(\eta_2 t)) \sin \xi_2) \\
& - (\sigma_2^y \cos(\eta_2 t) - \sigma_2^z \sin(\eta_2 t)) \sin(\omega_2^{rf}t + \phi_2)]
\end{aligned} \tag{4.19a}$$

This is the quad frame FLICFORQ Hamiltonian (QFH). It contains all the dynamics of the original FLICFORQ system. In essence, we have moved to a special frame that precesses with the driven dynamics of each qubit, and in so doing have imbued the once static coupling term with multiple time dependences.

Our task is now to find a set or sets of parameters – all of which have been left fully general thus far – that cause the coupling to become static in this frame so that its effect will be accumulated over time rather than averaged out. .

We note that the a priori time dependent nature of all terms in the QFH is a manifestation of the non-secular nature of the coupling, as this allows it to be neglected under typical conditions.

4.1.2 The coupling matrix

We may expand the QFH and project it onto the basis of two-qubit Pauli matrices according to

$$\mathcal{H}_{\alpha\beta} = \frac{1}{4} \text{Tr}(\sigma_1^\alpha \sigma_2^\beta \mathcal{H}_{(4)}), \tag{4.20}$$

and represent it as the 3×3 matrix of coefficients

$$\mathcal{M}(t) = \begin{pmatrix} m_{xx} & m_{xy} & m_{xz} \\ m_{yx} & m_{yy} & m_{yz} \\ m_{zx} & m_{zy} & m_{zz} \end{pmatrix}. \quad (4.21)$$

This matrix representation organizes the various terms and allows us to treat the linearly independent elements individually.

4.1.3 Fourier analysis

The QFH Hamiltonian derived above is still highly complex, and one might wonder what we have gained with all this work. Indeed, we have merely transferred the complexity of the two individual driven one-qubit dynamics into the qubit–qubit interaction term.

However, with a purely non-local description of the system dynamics, we can identify possible solutions to a given two-qubit quantum gate problem by looking for static terms in \mathcal{M} that arise when we impose certain constraints on $\boldsymbol{\lambda} = \{\omega_{xx}, \omega_1, \omega_2, \omega_1^{rf}, \omega_2^{rf}, \Omega_1, \Omega_2, \phi_1, \phi_2\}$.

To do so, we transform the QFH into Fourier space. The matrix \mathcal{M} is useful in this regard, as the Fourier transform, denoted

$$\frac{1}{\sqrt{2\pi}} \int_{-\infty}^{\infty} \mathcal{H}_{\alpha\beta}(t; \boldsymbol{\lambda}(s)) e^{-i\omega t} dt \equiv \mathcal{F}_{\alpha\beta}[\omega; \boldsymbol{\lambda}(s)],$$

may be calculated termwise, yielding the Fourier space quad frame Hamiltonian,

denoted $\mathcal{G}[\omega]$:

$$\mathcal{G}[\omega; \boldsymbol{\lambda}] = \begin{pmatrix} \mathcal{F}_{xx} & \mathcal{F}_{xy} & \mathcal{F}_{xz} \\ \mathcal{F}_{yx} & \mathcal{F}_{yy} & \mathcal{F}_{yz} \\ \mathcal{F}_{zx} & \mathcal{F}_{zy} & \mathcal{F}_{zz} \end{pmatrix}. \quad (4.22)$$

The components are each of the general form

$$\mathcal{F}_{\alpha\beta} = \omega_{xx} \sum_k A_k^{(\alpha\beta)}(\phi_1, \phi_2, \xi_1, \xi_2) G_k^{(\alpha\beta)}(\omega; \omega_1^{rf}, \omega_2^{rf}, \eta_1, \eta_2), \quad (4.23)$$

where

$$A_k^{(\alpha\beta)}[\boldsymbol{\lambda}(s)] = a_k^{(\alpha\beta)} \exp[i f_k^{(\alpha\beta)}(\phi_1, \phi_2, \xi_1, \xi_2)] \quad (4.24)$$

$$a_k^{(\alpha\beta)} \exp[i f_k^{(\alpha\beta)}(\boldsymbol{\lambda}(s))] \quad (4.25)$$

is a functional of a purely additive real function f_k of the microwave phases and the mixing angles; and

$$G_k^{(\alpha\beta)}[\omega; \boldsymbol{\lambda}(s)] = \delta[g_k^{(\alpha\beta)}(\omega, \omega_1^{rf}, \omega_2^{rf}, \eta_1, \eta_2)] \quad (4.26)$$

$$= \delta[g_k^{(\alpha\beta)}(\omega; \boldsymbol{\lambda}(s))] \quad (4.27)$$

denotes the Dirac delta function whose argument g_k is a purely additive real function of the frequencies in the problem.

Now we identify the modes of the system as the $\boldsymbol{\lambda}_k$'s, where

$$\boldsymbol{\lambda}^{(\alpha\beta)} = \boldsymbol{\lambda}_k^{(\alpha\beta)} \Leftrightarrow g_k^{(\alpha\beta)}(0; \boldsymbol{\lambda}) = 0. \quad (4.28)$$

Each mode is associated with a strength,

$$\frac{1}{\sqrt{2\pi}} \int_{-\infty}^{\infty} A_k[\boldsymbol{\lambda}_k] \delta[\omega] e^{i\omega t} d\omega, \quad (4.29)$$

and a direction $\alpha\beta$ in Hilbert space³, as setting $\boldsymbol{\lambda} = \boldsymbol{\lambda}_k$ will turn on one or more effective coupling terms in \mathcal{H} .

4.1.4 Extraction of the effective Hamiltonian

Once we have identified the modes, the effective Hamiltonian prevailing in the system at $\boldsymbol{\lambda} = \boldsymbol{\lambda}_k$ is obtained by inverse Fourier transform:

$$\mathcal{H}(\cdot; \boldsymbol{\lambda}_k) = \frac{1}{\sqrt{2\pi}} \int_{-\infty}^{\infty} \mathcal{G}[\omega; \boldsymbol{\lambda}_k] e^{i\omega t} d\omega. \quad (4.30)$$

where $\mathcal{H}(\cdot; \boldsymbol{\lambda}_k)$ denotes a time-independent Hamiltonian. We have

$$\mathcal{H}_{\alpha\beta}(\cdot; \boldsymbol{\lambda}_k) = \frac{1}{\sqrt{2\pi}} \int_{-\infty}^{\infty} \mathcal{F}_{\alpha\beta} e^{i\omega t} d\omega \quad (4.31)$$

$$= \frac{\omega_{xx}}{\sqrt{2\pi}} \int_{-\infty}^{\infty} \sum_{k'} A_{k'}^{(\alpha\beta)}(\phi_1, \phi_2, \xi_1, \xi_2) G_{k'}^{(\alpha\beta)}(0; \omega_1^{rf}, \omega_2^{rf}, \eta_1, \eta_2) e^{i\omega t} d\omega \quad (4.32)$$

$$= \frac{\omega_{xx}}{\sqrt{2\pi}} \int_{-\infty}^{\infty} \delta[\omega] \sum_{k'} A_{k'}^{(\alpha\beta)}[\boldsymbol{\lambda}_k] \delta[g_k - g_{k'}] e^{i\omega t} d\omega \quad (4.33)$$

$$\mathcal{H}_{\alpha\beta}(\cdot; \boldsymbol{\lambda}_k) = \frac{\omega_{xx}}{\sqrt{2\pi}} \sum_{k'} A_{k'}^{(\alpha\beta)}[\boldsymbol{\lambda}_k] \delta[g_k - g_{k'}]. \quad (4.34)$$

The last step is to return the effective Hamiltonian from the special rotating frame to the lab frame by inverting the original transformations outlined above.

³Note that a mode $\boldsymbol{\lambda}_k^{(\alpha\beta)}$ is not necessarily unique to $G_k^{(\alpha\beta)}$. In other words, each mode may turn on different coupling types. The original FLIFORQ paper found the mode sampled under the constraint $\omega_1 - \omega_2 = \Omega_1 + \Omega_2$ was associated with G^{yz} , G^{zy} , G^{yy} , and G^{zz} .

Finally, we note that as this approach in principle identifies all the modes, it makes it possible to make a quantitative comparison of the different possible configurations and say with some degree of confidence which approach is best suited to a particular experiment. We now have a general constructive theory with which to approach our problem. Indeed, most of the difficult work is now done. The last step is to apply it to some practical systems while taking account of the experimentally imposed constraints.

Chapter 5

Application of Fourier Approach

In the previous chapter we developed a strategy to help us find solutions to the quantum gate problem. In this chapter, we apply the entanglement mode theory to the study of practical qubit systems. We first use the formalism to reproduce earlier results, both our own and others', then delve into some new insights the theory has brought. In particular, the theory easily adapts to describe the parametrically driven coupling protocols described earlier, as well as indicating a new protocol we've called *cross-resonance* that has several advantages compared to earlier work. Finally, we apply the theory to the study of three qubit systems, demonstrating how to exploit a weak effective three-qubit interaction to generate a pure GHZ type Hamiltonian.

5.1 Two-Qubit Gates

5.1.1 Generalized FLICFORQ Protocols

The dual-resonant drive protocol applied to a system of qubits with fixed linear non-secular couplings established the practical possibility of entangling qubits without the need for external control over the qubit frequencies nor their coupling strength.

Though technologies have morphed since that original proposal, many practical benefits of not requiring DC control and using linear couplings remain. As a first application, we study the FLICFORQ Hamiltonian, with the aim of testing the theory against earlier results, and perhaps shedding new light on the quantum gate problem in such systems.

We will apply the methods of the previous chapter to the Hamiltonian of (3.1),

$$2\mathcal{H}/\hbar = \omega_1 \sigma_1^z + 2\Omega_1 \cos(\omega_1^{rf} t + \phi_1) \sigma_1^x \\ + \omega_2 \sigma_2^z + 2\Omega_2 \cos(\omega_2^{rf} t + \phi_2) \sigma_2^x + \omega_{xx} \sigma_1^x \sigma_2^x.$$

After transforming to the special quadruply rotating frame, we find

$$2\mathcal{H}_{(4)} = +\omega_{xx} [\cos(\omega_1^{rf} t + \phi_1) (\sigma_1^x \cos \xi_1 - (\sigma_1^z \cos(\eta_1 t) + \sigma_1^y \sin(\eta_1 t)) \sin \xi_1) \\ - (\sigma_1^y \cos(\eta_1 t) - \sigma_1^z \sin(\eta_1 t)) \sin(\omega_1^{rf} t + \phi_1)] \\ \times [\cos(\omega_2^{rf} t + \phi_2) (\sigma_2^x \cos \xi_2 - (\sigma_2^z \cos(\eta_2 t) + \sigma_2^y \sin(\eta_2 t)) \sin \xi_2) \\ - (\sigma_2^y \cos(\eta_2 t) - \sigma_2^z \sin(\eta_2 t)) \sin(\omega_2^{rf} t + \phi_2)] \quad (5.1a)$$

The components of the coupling matrix \mathcal{M} are,

$$2m_{xx} = \hbar\omega_{xx} \cos \xi_1 \cos \xi_2 \cos(\omega_1^{rf}t + \phi_1) \cos(\omega_2^{rf}t + \phi_2),$$

$$2m_{xy} = \hbar\omega_{xx} \cos \xi_1 \cos(\omega_1^{rf}t + \phi_1) \left(-\cos(\omega_2^{rf}t + \phi_2) \sin(\eta_2 t) \sin \xi_2 - \cos(\eta_2 t) \sin(\omega_2^{rf}t + \phi_2) \right),$$

$$2m_{xz} = \hbar\omega_{xx} \cos \xi_1 \cos(\omega_1^{rf}t + \phi_1) \left(-\cos(\eta_2 t) \cos(\omega_2^{rf}t + \phi_2) \sin \xi_2 + \sin(\eta_2 t) \sin(\omega_2^{rf}t + \phi_2) \right),$$

$$2m_{yx} = \hbar\omega_{xx} \cos \xi_2 \cos(\omega_2^{rf}t + \phi_2) \left(-\cos(\omega_1^{rf}t + \phi_1) \sin(\eta_1 t) \sin \xi_1 - \cos(\eta_1 t) \sin(\omega_1^{rf}t + \phi_1) \right),$$

$$\begin{aligned} 2m_{yy} &= \hbar\omega_{xx} \left(\cos(\omega_1^{rf}t + \phi_1) \sin(\eta_1 t) \sin \xi_1 + \cos(\eta_1 t) \sin(\omega_1^{rf}t + \phi_1) \right) \\ &\times \left(\cos(\omega_2^{rf}t + \phi_2) \sin(\eta_2 t) \sin \xi_2 + \cos(\eta_2 t) \sin(\omega_2^{rf}t + \phi_2) \right), \end{aligned}$$

$$\begin{aligned} 2m_{yz} &= \hbar\omega_{xx} \left(-\cos(\omega_1^{rf}t + \phi_1) \sin(\eta_1 t) \sin \xi_1 - \cos(\eta_1 t) \sin(\omega_1^{rf}t + \phi_1) \right) \\ &\times \left(\cos(\eta_2 t) \cos(\omega_2^{rf}t + \phi_2) \sin \xi_2 - \sin(\eta_2 t) \sin(\omega_2^{rf}t + \phi_2) \right), \end{aligned}$$

$$2m_{zx} = \hbar\omega_{xx} \cos \xi_2 \cos(\omega_2^{rf}t + \phi_2) \left(-\cos(\omega_1^{rf}t + \phi_1) \cos(\eta_1 t) \sin \xi_1 + \sin(\eta_1 t) \sin(\omega_1^{rf}t + \phi_1) \right)$$

$$\begin{aligned} 2m_{zy} &= \hbar\omega_{xx} \left(-\cos(\omega_1^{rf}t + \phi_1) \cos(\eta_1 t) \sin \xi_1 + \sin(\eta_1 t) \sin(\omega_1^{rf}t + \phi_1) \right) \\ &\times \left(-\cos(\omega_2^{rf}t + \phi_2) \sin(\eta_2 t) \sin \xi_2 - \cos(\eta_2 t) \sin(\omega_2^{rf}t + \phi_2) \right), \end{aligned}$$

$$\begin{aligned} 2m_{zz} &= \hbar\omega_{xx} \left(-\cos(\omega_1^{rf}t + \phi_1) \cos(\eta_1 t) \sin \xi_1 + \sin(\eta_1 t) \sin(\omega_1^{rf}t + \phi_1) \right) \\ &\times \left(-\cos(\omega_2^{rf}t + \phi_2) \cos(\eta_2 t) \sin \xi_2 + \sin(\eta_2 t) \sin(\omega_2^{rf}t + \phi_2) \right). \end{aligned}$$

(5.2)

We Fourier transform each element and identify the entanglement modes of the

system,

$$\omega_1^{rf} \pm \omega_2^{rf} = 0, \quad (5.3a)$$

$$\eta_1 \pm \omega_1^{rf} \pm \omega_2^{rf} = 0, \quad (5.3b)$$

$$\eta_2 \pm \omega_1^{rf} \pm \omega_2^{rf} = 0, \quad (5.3c)$$

$$\eta_1 \pm \eta_2 \pm \omega_1^{rf} \pm \omega_2^{rf} = 0. \quad (5.3d)$$

with

$$\eta_j = \sqrt{\delta_j^2 + \Omega_j^2} \quad (5.4)$$

where

$$\delta_j = |\omega_j - \omega_j^{rf}|. \quad (5.5)$$

We have placed no constraints on 3.1 beyond the assumption of a weak non-secular coupling $\omega_{xx} \ll |\omega_1 - \omega_2|$ and have arrived to an exhaustive enumeration of the system configurations that create from the weak non-secular coupling a strong effective interaction.

When we impose the constraints $\omega_j^{rf} \rightarrow \omega_j$ and $\eta_j \rightarrow \Omega_j$ describing resonant driving of each qubit the modes become,

$$\omega_1 \pm \omega_2 = 0, \quad (5.6a)$$

$$\Omega_1 \pm \omega_1 \pm \omega_2 = 0, \quad (5.6b)$$

$$\Omega_2 \pm \omega_1 \pm \omega_2 = 0, \quad (5.6c)$$

$$\Omega_1 \pm \Omega_2 \pm \omega_1 \pm \omega_2 = 0. \quad (5.6d)$$

With the drive amplitudes satisfying $\Omega_1 + \Omega_2 = \omega_1 - \omega_2$ we find the effective rotating

frame Fourier Hamiltonian,

$$\mathcal{G} = \frac{\omega_{xx}}{8} \sqrt{\frac{\pi}{2}} \begin{pmatrix} 0 & 0 & 0 \\ 0 & \cos(\phi_1 - \phi_2) & -\sin(\phi_1 - \phi_2) \\ 0 & \sin(\phi_1 - \phi_2) & \cos(\phi_1 - \phi_2) \end{pmatrix} \quad (5.7)$$

corresponding to

$$\begin{aligned} \mathcal{H}/\hbar &= \frac{\omega_{xx}}{16} (\sigma_y^1 \sigma_y^2 + \sigma_z^1 \sigma_z^2) \cos(\phi_1 - \phi_2) \\ &\quad + (\sigma_y^1 \sigma_z^2 - \sigma_z^1 \sigma_y^2) \sin(\phi_1 - \phi_2) \end{aligned}$$

This is the original result.

We now study these modes under the practical constraints emerging from various experimental configurations.

Single-tone experiment

The simplest implementation of a FLICFORQ system would involve the application of a single microwave tone to one of the two qubits. In this section, we apply to this simple experiment the results of the prior sections, first in the limit of zero microwave crosstalk, and then for arbitrary crosstalk.

Zero Crosstalk Consider the two-qubit experiment where the first qubit is irradiated and the second is left alone. To adapt our above results to this case we need only let the signal frequency on the unirradiated qubit $\omega_2^{rf} \rightarrow \omega_2$ and let the amplitude vanish by imposing $\Omega_2 \rightarrow 0$. Imposing both these limits simultaneously implies that

the mixing angle $\xi_2 \rightarrow 0$. With these conditions, the ERCs reduce to

$$\omega_1^{rf} \pm \omega_2 = 0, \quad (5.8a)$$

$$\eta_1 \pm \omega_1^{rf} \pm \omega_2 = 0. \quad (5.8b)$$

The first of these indicates that simply by irradiating one qubit at the transition frequency of the other we may generate a strong effective interaction, while the second describes the case where one Rabi sideband of the driven qubit is in resonance with the undriven qubit.

Single tone cross resonance I will refer to the case where $\omega_1^{rf} = \omega_2$ as *cross resonance*. When we impose the set of constraints

$$\{\omega_1^{rf} \rightarrow \omega_2, \xi_2 \rightarrow 0, \eta_2 \rightarrow 0, \phi_2 \rightarrow 0\}, \quad (5.9)$$

the Hamiltonian prevailing in the system becomes

$$\mathcal{M} = \frac{\omega_{xx}}{4} \cos \xi_1 \begin{pmatrix} \cos \phi_1 & \sin \phi_1 & 0 \\ 0 & 0 & 0 \\ 0 & 0 & 0 \end{pmatrix}, \quad (5.10)$$

where the mixing angle ξ_1 is still given by

$$\cos \xi_1 = \frac{1}{\sqrt{1 + (\Delta/\Omega_1)^2}}. \quad (5.11)$$

For fixed circuit parameters ω_{xx} , ω_1 and ω_2 , the interaction strength increases with the drive amplitude Ω_1 . And critically, the effect turns on linearly in the ratio Ω_1/Δ , allowing it to be used to perform two-qubit gates between broadly detuned qubits

with only comparatively weak driving fields.

That this is possible at all, and that a dynamically tunable interaction strength can emerge when the qubits are coupled only through a static linear reactance, may at first seem surprising. The presence of the interaction can be understood in the dressed state picture, as we will see shortly. And we note that the individual qubit subcircuits are themselves non-linear. In essence, cross resonance exploits these already present non-linearities to achieve tunable coupling, thus circumventing the need for non-linear elements in the coupling subcircuit.

As with the original FLICFORQ proposal [105], cross-resonance can be understood also in the dressed state picture of quantum optics, see figure 5.1. Whereas the matching condition 3.2 ensured that the upper and lower Rabi sidebands of the lower and higher frequency qubits, resp., overlapped, here the condition 5.8a ensures that the central transition at the irradiation frequency of the driven qubit + photon system matches the bare transition of the undriven qubit. We are thus creating a resonance between the central feature of the Mollow triplet [121] on qubit two with bare transition at ω_1 of qubit one¹.

It is instructive to look at the effective Hamiltonian 5.10 in the doubly Larmor-precessing frame wherein most practical measurements of qubit observables are performed. To do so, we invert (in this order) the time-dependent rotations by angles $\eta_{1,2}t$ and the time-independent rotations by angles $\xi_{1,2}$ on each qubit. In that frame we have,

¹The effect can also be derived in second order perturbation theory [122]. But one must of course know first to look for it. Here, the Fourier approach identified the effect when we did not have any prior knowledge of it, an important demonstration of why the technique is so useful.

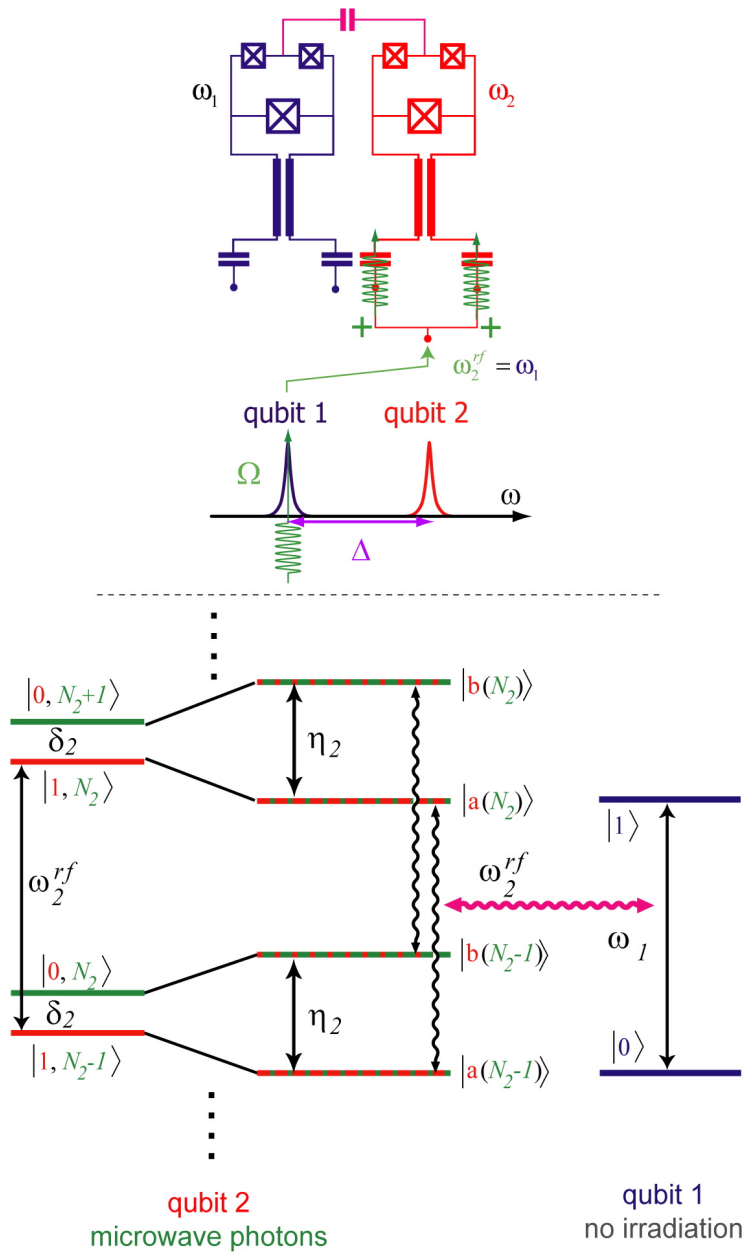


Figure 5.1: The cross-resonance effect in dressed state picture. When qubit 2 (red) is irradiated with photons (green) at the transition frequency of qubit 1 (blue), transitions between neighbouring dressed state manifolds, occurring at ω_2^{rf} , become resonant with ω_1 . These form the center peak of the Mollow triplet. Note the location of the center peak is set entirely by the microwave frequency and is independent of the microwave amplitude. The makeup of the dressed states connected by the transitions at ω_2^{rf} changes as Ω_2 increases, and this changing weight of the bare qubit transition is responsible for the amplitude-tunability of the effective interaction strength. Where cross-talk is introduced, the effect is "always on" but of frequency and amplitude-dependent strength, as the two Mollow center peaks always line up.

$$2\mathcal{H}/\hbar = \frac{\omega_{xx}}{2} \begin{pmatrix} \cos^2 \xi_1 \cos \phi_1 & \cos^2 \xi_1 \sin \phi_1 & 0 \\ 0 & 0 & 0 \\ \cos \xi_1 \cos \phi_1 & \cos \xi_1 \sin \phi_1 & 0 \end{pmatrix}, \quad (5.12)$$

which, in terms of the inter-qubit detuning Δ and drive strength Ω_1 , is

$$2\mathcal{H}/\hbar = \frac{\omega_{xx}}{2} \frac{1}{1 + \Delta^2/\Omega_1^2} \begin{pmatrix} \cos \phi_1 & \sin \phi_1 & 0 \\ 0 & 0 & 0 \\ \frac{\Delta}{\Omega_1} \cos \phi_1 & \frac{\Delta}{\Omega_1} \sin \phi_1 & 0 \end{pmatrix}. \quad (5.13)$$

Perhaps the most important attribute of this cross-resonance protocol is that the effect turns on linearly in the ratio Ω_1/Δ , a stark contrast to the case in off-resonant FLICFORQ where the effect turns on as $(\Omega/\Delta)^4$ [101]. For most practical implementations of this protocol the driving will satisfy $\Omega_1 \ll \Delta$, and only the ZX and ZY terms are important. We thus have,

$$2\mathcal{H}/\hbar \approx \frac{\Omega_1 \omega_{xx}}{2\Delta} (\cos \phi_1 \sigma_1^z \sigma_2^x + \sin \phi_1 \sigma_1^z \sigma_2^y). \quad (5.14)$$

With $\phi_1 = 0$, this simple scheme naturally implements the most direct Clifford group generator of CNOT, the sort of exotic ZX coupling mentioned in Chapter Two. The associated Gottesman table for CNOT has only three columns,

	$(WX)^{-1/2}$	$(ZX)^{1/2}$	$(ZW)^{-1/2}$
WX	WX	WX	WX
XW	XW	$-YX$	XX
WZ	$-WY$	ZZ	ZZ
ZW	ZW	ZW	ZW

(5.15)

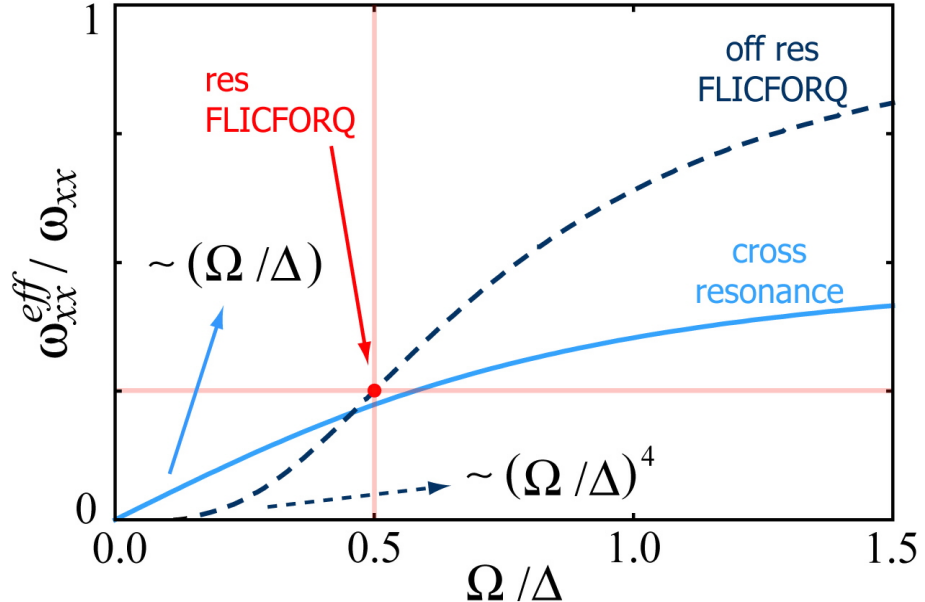


Figure 5.2: Effective interaction strength generated by cross-resonance irradiation as a function of drive strength : detuning ratio Ω/Δ (solid); generalized off-resonant FLICFORQ scheme of Ashhab and Nori (dashed); and original double-resonant driving of original FLICFORQ scheme (point at intersection of red lines). Equal drive amplitudes are assumed for the latter two. At small drive strengths the cross resonance effect is proportional to Ω/Δ , while off-resonant FLICFORQ coupling strength goes only as $(\Omega/\Delta)^4$. The horizontal and vertical red lines emphasize that satisfying the matching condition $\Omega_2 + \Omega_1 = \omega_2 - \omega_1$ with resonant pulses constrains all the available controls and thus does not admit tunability of the interaction strength.

We have therefore found a protocol with several advantages relative to our first proposal in Chapter Three. The advantages as discussed there all apply. But now, we need only control a single tone; the effect is fully tunable and is switched on by a frequency-only matching condition, a strong advantage given the ease with which signal frequencies can be precisely controlled compared to signal amplitudes.

We have compared the effective coupling strength found here to those obtained in earlier proposals involving two driving tones, see figure 5.2. Notably, cross-resonance opens up the possibility of entangling pairs of broadly detuned, fixed-coupling qubits. When the detuning is large, absolute limits on the drive strength-imposed by the ap-

plicability of the RWA and the requirement to remain in the computational subspace—necessarily place us in the regime of small Ω/Δ . There, the only previous applicable proposal, the off-resonant dual driving of Nori and Ashhab, gives rise to an effective interaction strength that vanishes as $(\Omega/\Delta)^4$ [101], whereas cross-resonance effects an interaction that is linear in this parameter.

Working with larger detunings in turn makes it possible to use larger fixed couplings while ensuring the separability constraint $\omega_{xx} \ll \Delta$ is satisfied, so any downward adjustment in the interaction strength from the limits on Ω may be compensated with an increased bare coupling. The applicability of cross-resonance to broadly detuned qubits bears on the fabrication process, as well. There, the challenge of overcoming the natural spread in circuit parameters is greatly reduced when our gate scheme can accommodate a large range of detunings.

In addition to the tunable coupling *strength*, cross-resonance also allows the coupling *direction* to be tuned via the microwave signal. Each of the microwave signal parameters thus plays an important role: the *frequency switches on the coupling* to the target qubit; the *amplitude controls the gate speed*; and the *phase determines the two-qubit gate*.

We have verified the analytic derivation of cross-resonance with simulations of the full laboratory frame Hamiltonian master equation. The only approximation we have made is the commonplace restriction of the qubit circuits to their two lowest-lying states. We have, in particular, not made the rotating wave approximation(s) as we did in the analytical treatment, nor have we kept only the DC terms in the spectral decomposition of the Hamiltonian under the cross-resonance condition, as we did in arriving to the effective rotating frame Hamiltonian 5.10. Care must be taken to interpret the results for the range of drive strengths where the two-level approximation would be valid for the particular superconducting qubit circuit with

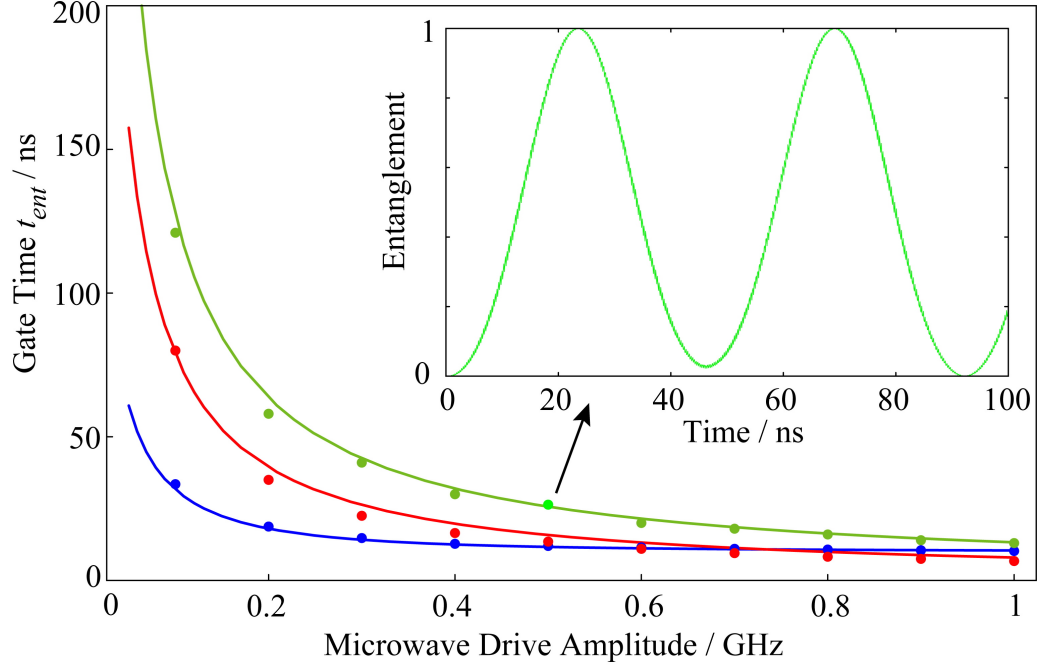


Figure 5.3: Cross-resonance two-qubit gate time (time required to generate fully entangled state from product state, and vice-versa) for three practical parameter sets as function of absolute drive amplitude $\Omega/2\pi$. System parameters for the three sets of simulations are shown in corresponding colors green, red and blue below graph. Solid lines are from analytics ($t_{ent}=\pi/2\omega_{xx}^{eff}$) and the Fourier approach; points are extracted from explicit simulation of full lab frame Hamiltonian master equation. *Inset:* entanglement vs. time for point indicated by arrow at $\Omega=0.5$ GHz.

which you'd like to implement the cross-resonance scheme. An analysis of state leakage outside the computational subspace should otherwise be performed.

From the simulations, we may extract the two-qubit entanglement as measured by the concurrence [85] as a function of time, and in turn the two-qubit gate speed under cross-resonance. We find excellent agreement with the analytical results over the broad and practical range of parameters tested.

Modulation depth and bandwidth The discussion of errors in Chapter three applies also here, as all the hardware is nominally the same. The entanglement bandwidth is now,

$$\begin{aligned} \Upsilon &= \frac{\omega_{xx}}{4\pi\sqrt{1 + (\Delta/\Omega_1)^2}} \\ &\approx \frac{\omega_{xx}\Omega_1}{4\pi\Delta} \end{aligned} \quad (5.16)$$

and the modulation depth is,

$$\begin{aligned} \Lambda &\simeq \frac{1 - \Omega^2/\omega^2}{\omega_{xx}^2/\Delta^2} \\ &\approx 100 = 20\text{dB}. \end{aligned} \quad (5.17)$$

Single tone sideband resonance The second entanglement resonance available in the single-tone experiment describes a Rabi sideband resonance. This type of resonance has been exploited by us [105] and others [101] for two-qubit gates, but only in the two-tone case. The one-tone case found here is a straightforward simplification, and like the two-tone instance it may be understood in the dressed state picture.

The quad frame formalism is again useful to deduce the prevailing effective Hamil-

tonian under single-tone sideband resonance. Note that the relevant constraint equation is an implicit relation between the drive frequency and amplitude. Solving for ω_1^{rf} the constraint becomes

$$\omega_1^{rf} \rightarrow \frac{\omega_1^2 + \Omega_1^2 - \omega_2^2}{2(\omega_1 \pm \omega_2)} \quad (5.18)$$

which, along with the constraints imposing the single-tone situation (with the tone applied to qubit 1),

$$\{\omega_2^{rf} \rightarrow \omega_2, \xi_2 \rightarrow 0, \eta_2 \rightarrow 0, \phi_2 \rightarrow 0\}, \quad (5.19)$$

yields the quad frame coupling matrix

$$\mathcal{M} = \frac{\omega_{xx}}{4} \begin{pmatrix} 0 & 0 & 0 \\ -\sin \phi_1 & -\cos \phi_1 & 0 \\ -\cos \phi_1 \sin \xi_1 & \sin \phi_1 \sin \xi_1 & 0 \end{pmatrix}. \quad (5.20)$$

This situation is also sufficient for universal two-qubit gates. It is interesting to note that this case naturally incorporates the two extreme configurations we might consider. The purpose of the drive, of course, is to push the qubits into some form of resonance. Here, the spectral distance to be covered, Δ , may be made up of either pure Rabi flopping when the tone is resonant ($\delta_1 \rightarrow 0, \eta_1 \rightarrow \Omega_1$); or of an AC Stark shift of the driven qubit when the tone is far detuned ($\Omega_1 \rightarrow 0, \eta_1 \rightarrow \delta_1$). The presence of the mixing angle ξ_1 in the sideband resonance effective Hamiltonian smoothly accounts for this entire range.

Finite crosstalk Any electrical circuit for implementing quantum bits will have channels through which the microwave signals applied to one qubit will leak onto the

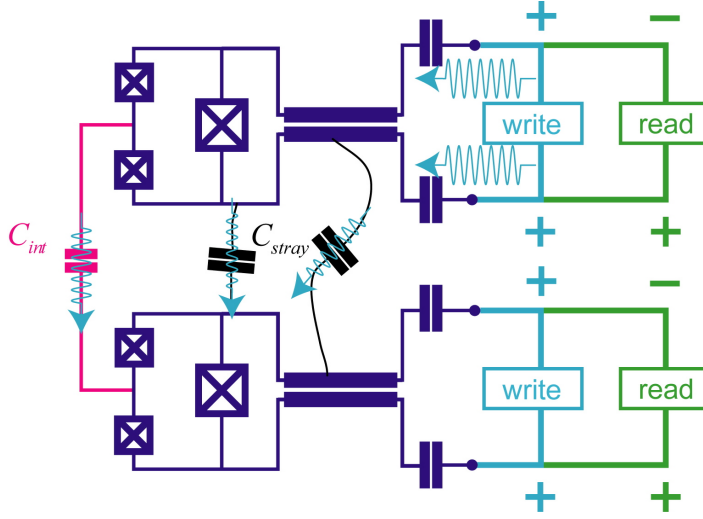


Figure 5.4: Practical superconducting quantum circuits will always involve some intrinsic crosstalk between signals applied to the individual qubit subcircuits. Crosstalk can occur through the intentional couplings exploited for quantum gates, or through stray effective elements.

unirradiated qubits. This *microwave crosstalk* may occur through either intended coupling channels – in the FLICFORQ case the capacitive or inductive elements used to realize the weak non-secular couplings – or through stray elements unintended in the circuit design. As FLICFORQ implies intended couplings in the regime where $\omega_{xx} \ll \Delta$, the crosstalk through these channels will also be weak, but we cannot necessarily say the same of the unintended crosstalk channels. They may emerge from stray on-chip capacitances and inductances; from box modes of the sample holder; from imperfections in the passive devices through which we couple signals to chip, such as a hybrid or directional coupler. Indeed, they are notoriously difficult to pin down, and even harder to predict. For these reasons, it is important to consider the possibility of crosstalk of the write signals.

Our preceding analysis is well suited to this task, as it lets us incorporate an arbitrary level of crosstalk, with possible phase shifting of the crosstalk signal, into the QFH of the single-tone experiment: we simply retrofit the general QFH results

with a set of constraints that impose the crosstalk conditions. (With no loss of generality, I will take qubit 1 as being intentionally irradiated, with qubit 2 feeling only the crosstalk signal.) The microwave frequencies are set equal ($\omega_1^{rf} \rightarrow \omega_2^{rf} \rightarrow \omega_{rf}$). The microwave amplitude of the unirradiated qubit becomes some fraction $\alpha \in [0, 1]$, the *crosstalk coefficient*, of the amplitude on the irradiated qubit ($\Omega_2 \rightarrow \alpha\Omega_1$). And the phases are equal but for the *crosstalk phase shift* v ($\phi_2 \rightarrow \phi_1 + v$).

With these relations imposed on the QFH, something seemingly magical happens: the QFH develops, without further restrictions, a static term whose strength is determined by α and the drive amplitude and frequency relative to the qubit frequencies. This effect derives from the same ERC that gave us cross-resonance. As the crosstalk parameter α is increased from zero, the cross-resonance condition loses its delta function nature and becomes a broad effect; the peak intensity moves slowly from that of the cross-resonance without crosstalk case (peak at $\omega_1^{rf} = \omega_2$) to the intermediate frequency $(\omega_1 + \omega_2)/2$ when the crosstalk is 100% ($\alpha = 1$) and the system becomes symmetric. This crosstalk resonance has been alluded to in earlier work by Ashhab and Nori [106]. Our theory indicates that the Hamiltonian prevailing under the crosstalk condition is

$$\mathcal{M} = \frac{\omega_{xx}}{4} \begin{pmatrix} \cos \xi_1 \cos \xi_2 \cos v & 0 & 0 \\ 0 & 0 & 0 \\ 0 & 0 & 0 \end{pmatrix}. \quad (5.21)$$

This effect may be made use of to entangle qubits. It is unique in that it does not arise only through the satisfaction of a delta function matching condition. Instead, the effect is broadened by both the microwave drive level and crosstalk coefficient. At the same time, even if this is not the configuration by which the experimentalist is intending to couple the qubits, the crosstalk-induced coupling must be accounted

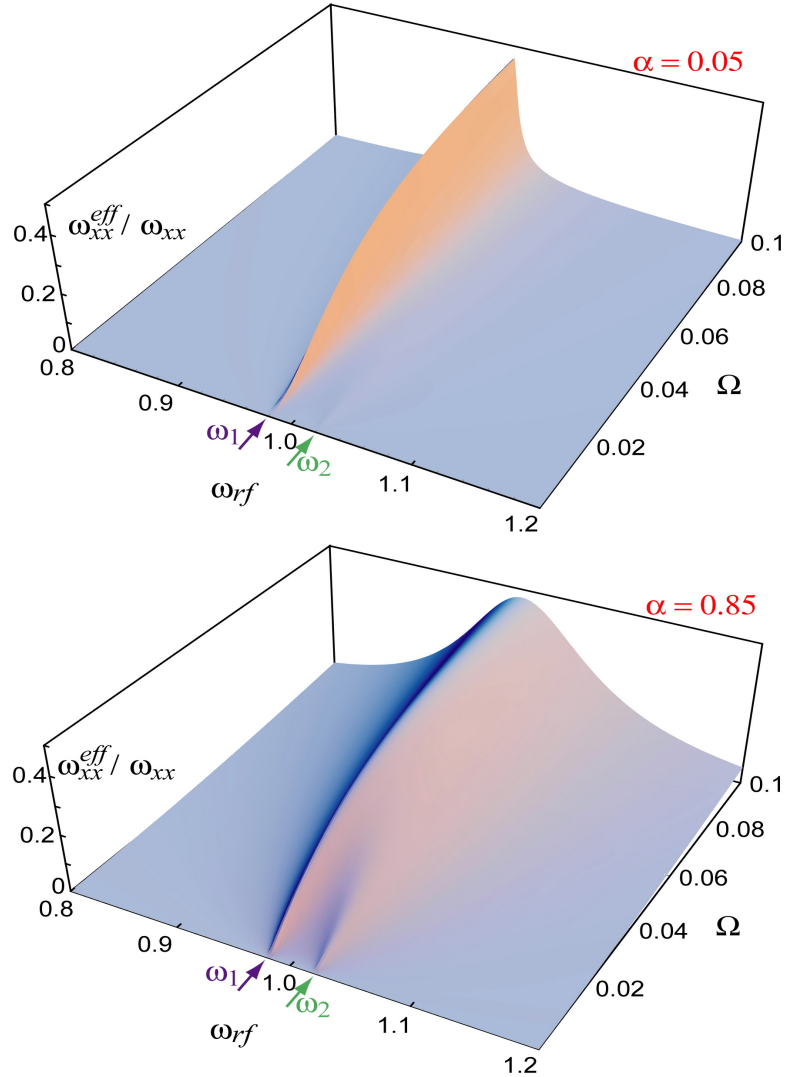


Figure 5.5: Effective coupling strength under cross resonance in presence of microwave control signal crosstalk as function of drive frequency ω_{rf} and drive amplitude Ω for two different levels of signal crosstalk. Qubit frequencies are indicated by purple (Q1) and green (Q2) arrows. At zero crosstalk the cross-resonance effect is broadened by fluctuations in the drive signal photon number. The effect broadens as crosstalk is tuned on. *Top:* $\alpha=0.05$; *Bottom:* $\alpha=0.85$. At $\alpha=0.85$, the range of drive frequencies effective at generating entanglement is dramatically broadened by the presence of crosstalk. When $a = 1$ (not shown) the effective coupling strength is symmetric about $(\omega_1 + \omega_2)/2$.

for when interpreting experimental results.

Two-tone experiment

Constraints $\eta_1 \pm \omega_1^{rf} \pm \omega_2^{rf} = 0$ The constraints

$$\eta_1 \pm \omega_1^{rf} \pm \omega_2^{rf} = 0, \quad (5.22)$$

$$\eta_2 \pm \omega_1^{rf} \pm \omega_2^{rf} = 0, \quad (5.23)$$

are the symmetric pairs associated with the condition where one of the drive tones is fixed in both frequency and amplitude, while the other traces a path in the two-dimensional control space $\{\omega_a^{rf}, \Omega_a\}$. In these cases there is no dependence on one of the drive amplitudes, so the matching condition is a constraint on three of the four microwave knobs. The second entanglement resonance available in the single-tone experiment describes a Rabi sideband resonance.

Solving the above we obtain

$$\omega_1^{rf} \rightarrow \frac{\omega_1^2 + \Omega_1^2 - (\omega_2^{rf})^2}{2(\omega_1 \pm \omega_2^{rf})} \quad (5.24)$$

which yields the quad frame coupling matrix

$$\mathcal{M} = -\frac{\omega_{xx}}{4} \cos \xi_2 \begin{pmatrix} 0 & 0 & 0 \\ \sin(\phi_1 + \phi_2) & 0 & 0 \\ \cos(\phi_1 + \phi_2) \sin \xi_1 & 0 & 0 \end{pmatrix}. \quad (5.25)$$

This situation is also sufficient for universal two-qubit gates. The drive strength Ω_2 doesn't appear in the constraint equation, leaving it free to adjust the gate speed, again giving tunability of the coupling Hamiltonian.

Constraints $\pm\eta_1 \pm \eta_2 \pm \omega_1^{rf} \pm \omega_2^{rf} = 0$ Last, and most complex are the twelve constraints

$$\pm\eta_1 \pm \eta_2 \pm \omega_1^{rf} \pm \omega_2^{rf} = 0. \quad (5.26)$$

Satisfying them involves tracing a path in the full four-dimensional microwave control space $\{\omega_1^{rf}, \Omega_1, \omega_2^{rf}, \Omega_2\}$.

Solving the above we obtain solutions

$$\omega_1^{rf} \rightarrow \frac{1}{2}(\omega_1 \pm \sqrt{\Omega_2^2 + (\omega_2 - \omega_2^{rf})^2} \pm \omega_2^{rf}) \quad (5.27)$$

$$\pm \frac{\Omega_1^2 \sqrt{\Omega_2^2 + (\omega_2 - \omega_2^{rf})^2}}{-\omega_1^2 + \omega_2^2 + \Omega_2^2 - 2\omega_2^{rf}(\omega_2 \pm \omega_1)} \quad (5.28)$$

$$+ \frac{\Omega_1^2(\omega_1 \pm \omega_2^{rf})}{\omega_1^2 - \omega_2^2 - \Omega_2^2 + 2\omega_2^{rf}(\omega_2 \pm \omega_1)} \quad (5.29)$$

which yields the quad frame coupling matrix

$$\mathcal{M} = \frac{\omega_{xx}}{8} (\sin \xi_2 \pm 1) \begin{pmatrix} 0 & 0 & 0 \\ 0 & \pm \cos(\phi_1 \pm \phi_2) & \sin(\phi_1 \pm \phi_2) \\ 0 & \pm \sin(\phi_1 \pm \phi_2) \sin \xi_1 & \cos(\phi_1 \pm \phi_2) \sin \xi_1 \end{pmatrix}. \quad (5.30)$$

5.1.2 Protocols involving DC control of transition frequencies

The earliest proposals for quantum gates involved DC control over the qubit frequencies[40]. With the constraints,

$$\{\omega_1^{rf} \rightarrow \omega_1, \omega_2^{rf} \rightarrow \omega_2, \eta_1 \rightarrow 0, \eta_2 \rightarrow 0\} \quad (5.31)$$

the modes are located only at

$$\omega_1 = \omega_2. \quad (5.32a)$$

as we expect. The situation is trivial except for the instance where 3.1 is modified to include a secular coupling term. In that case, we obtain instead at mode present for all λ . This is the case in liquid state NMR, where the spins should be dynamically decoupled in order to avoid entangling them under free evolution.

5.1.3 Protocols involving AC control of transition frequencies

Another interesting case is when the qubit transition frequencies are harmonically varied [87]. Here, we address the case where the rates and amplitudes satisfy $\omega_j^{zrf}, \delta\omega_j \ll \omega_j$. The Hamiltonian is,

$$\begin{aligned} 2\mathcal{H}/\hbar &= (\omega_1^z + 2\delta\omega_1 \cos(\omega_1^{zrf}t + \phi_1^z))\sigma_1^z \\ &\quad + (\omega_2^z + 2\delta\omega_2^z \cos(\omega_2^{zrf}t + \phi_2^z))\sigma_2^z \\ &\quad + \omega_{xx}\sigma_1^x\sigma_2^x, \end{aligned} \quad (5.33)$$

The Fourier technique can be applied to this case. We find entanglement resonances at

$$\omega_j^{zrf} \pm \omega_1^z \pm \omega_2^z = 0.$$

That is, the qubits can entangled by modulating the transition frequency of one qubit at the difference or sum frequency $|\omega_1^z \pm \omega_2^z|$ with respect to the target qubit. When this condition is met the effective coupling strength again increases with the drive strength $\delta\omega_j$.

This entanglement resonance could be relevant to the systems recently used for

two-qubit cQED experiments at Yale [144], where the modulation of ω^z could be implemented through the flux bias lines that address the qubits individually.

5.1.4 Protocols involving harmonic variation of the coupling

Many practical systems place the qubit–qubit coupling strength under experimental control. The DC tuning case is straightforward. We turn in this section to systems where one can harmonically vary the interaction strength ω_{xx} , as carried out experimentally by Niskanen, et al[113]. The Hamiltonian is very very similar to 3.1, with the substitution,

$$\omega_{xx} \rightarrow \omega_{xx}^o + \delta\omega_{xx} \cos[\omega_{xx}^{rf}t] \quad (5.34)$$

which we make prior to taking the Fourier transform of the Hamiltonian. There are entanglement modes at

$$\omega_1 \pm \omega_2 - \omega_{xx}^{rf} = 0. \quad (5.35)$$

whereat the effective Hamiltonian is

$$2\mathcal{H}/\hbar = 2\delta\omega_{xx}(\sigma_x^1\sigma_x^2 \pm \sigma_y^1\sigma_y^2) \quad (5.36)$$

identical to the results of Bertet, et al obtained by different methods.

Crosstalk in the parametric pumping scheme

Of practical interest, there are also modes of the harmonically-varied coupling system at

$$a\eta_1 + b\eta_2 + c\omega_1^{rf} + d\omega_2^{rf} + f\omega_{xx}^{rf} = 0 \quad (5.37)$$

where

$$\{a, b, c, d, f\} = \{0, \pm 1\}. \quad (5.38)$$

These can be used, with some care, to identify how the resonance condition is modified in the presence of crosstalk of the pumping signal onto the two qubits. When the signal at ω_{xx}^{rf} is the only one present but leaks onto each of the qubits, we have modes at

$$\begin{aligned}\omega_{xx}^{rf} &= \eta_1 \pm \eta_2 \\ &= \sqrt{(\alpha_1 \Omega_{xx})^2 + (\omega_{xx}^{rf} - \omega_1)^2} \pm \sqrt{(\alpha_2 \Omega_{xx})^2 + (\omega_{xx}^{rf} - \omega_2)^2}\end{aligned}\quad (5.39)$$

where α_j is the crosstalk of signal applied to the coupling subcircuit onto qubit j . When the crosstalk coefficients become very small the condition reduces to the results we found earlier in 5.36 and confirmed by ref. [113, 42]. There are many other modes to be investigated for this very interesting case. The results presented here are incomplete, as a thorough examination of all the entanglement modes for the various physical systems we have considered is beyond the scope of this work. What we have presented should serve to demonstrate the utility of the Fourier approach, and also to convey the richness of the space of possible solutions to the quantum gate problem for even simple and idealized systems.

5.2 Three-Qubit Gates

The capability to perform two-qubit gates between at least all nearest neighbor qubits in a quantum register is sufficient to generate an arbitrary transformation of the system's full computational Hilbert space. In principle, then, everything can be done by addressing the qubits pairwise. However, the capability to perform quantum gates that *directly* entangle $n > 2$ qubits greatly reduces the number of operations needed to implement a computational task over a large Hilbert space [142]. Further,

the correlations between observables on individual subsystems contain ever more sophistication as the degree of communal entanglement grows. While Bell states of the form,

$$|\psi\rangle = \frac{|00\rangle + |11\rangle}{\sqrt{2}} \quad (5.40)$$

can be used to *statistically* rule out local hidden variables theories, the three-qubit analog known as the Greenberger-Horne-Zeilinger (GHZ) state [72],

$$|GHZ\rangle = \frac{|000\rangle + |111\rangle}{\sqrt{2}} \quad (5.41)$$

can in principle rule out such theories in a *single* measurement. In the case of another well known three-qubit state,

$$|W\rangle = \frac{|001\rangle + |010\rangle + |100\rangle}{\sqrt{3}}, \quad (5.42)$$

wherein – though the system contains some information in the two- and three-body correlations – the individual qubits retain some independent character, such an *eigenvalue violation* of Bell-type inequalities is impossible.

States of the GHZ form can of course be generated by cascaded application of entangling gates between pairs in the three-qubit system. Here, we apply the Fourier analysis technique to study the three-qubit quantum gate problem. We report protocols to directly generate GHZ-type states in a single step, both in the presence and absence of a weak effective three-qubit coupling in the system Hamiltonian.

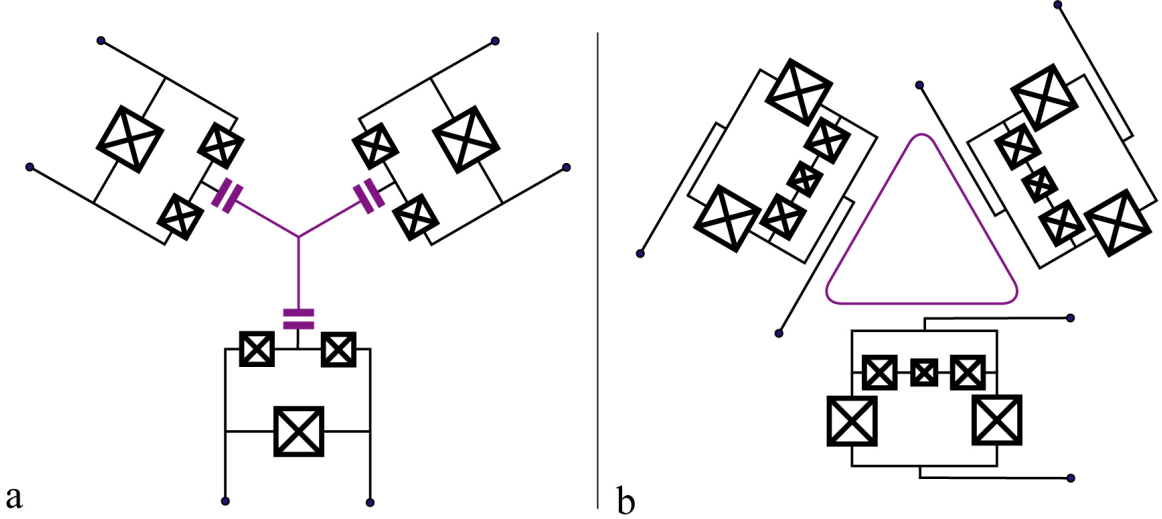


Figure 5.6: Equivalent circuit diagrams for systems implementing the three qubit Hamiltonian. Qubits shown are of (a) quantronium variety or (b) Delft-style flux qubits. In each case, a fixed linear coupling is implemented between each pair of qubits that is off-diagonal in the computational basis.

5.2.1 GHZ state production with DC control

We now turn to the study of three-qubit FLICFORQ style Hamiltonians

$$\begin{aligned} \mathcal{H} = & \frac{\hbar}{2} \sum_{k=1}^2 \left(\omega_k \sigma_k^z + 2\Omega_k \cos(\omega_k^{rf} t + \phi_k) \sigma_k^x \right) \\ & + \frac{\hbar}{2} \sum_{j,i=1; j \neq i}^3 \omega_{ji} \sigma_j^x \sigma_i^x + \omega_{123} \sigma_1^x \sigma_2^x \sigma_3^x. \end{aligned} \quad (5.43)$$

There is now the possibility of realizing an effective three-body interaction of the sort $\omega_{123} \sigma_1^x \sigma_2^x \sigma_3^x$. Circuits described by this Hamiltonian could be implemented by direct extension of the two-qubit circuits discussed earlier; two possible designs are in 5.6. A three-body interaction will emerge, for example, if three quantronium circuits in the intermediate E_J/E_C regime where neither charge nor phase are good quantum numbers are coupled to a common superconducting island. Effective three-body couplings in a superconducting circuit have been exploited in the Josephson ring

modulator [143], and systems have been proposed using optical lattices [126].

We now discuss how we exploit such a term under the weak coupling assumption,

$$\omega_{123}, \omega_{ji} \ll |\omega_j - \omega_i|. \quad (5.44)$$

In the two qubit case, the restriction to coupling strengths far weaker than the inter-qubit detuning allowed us to safely ignore the second-order effects of the coupling unless the qubits were otherwise brought into resonance. This is not so in the presence of an effective three-body interaction, as we now show.

We again move to a special frame where the system dynamics are purely non-local, then analyze the Hamiltonian in Fourier space to identify the entanglement modes associated to 5.43².

We begin by analyzing the system in the absence of any irradiation. In that case, we find an entanglement mode when the three qubit frequencies are matched,

$$\omega_1 = \omega_2 = \omega_3 \quad (5.45)$$

as we expect. The effective Hamiltonian is purely non-local

$$4\mathcal{H}/\hbar \rightarrow \omega_{12}(\sigma_1^x\sigma_2^x + \sigma_1^y\sigma_2^y) + \omega_{13}(\sigma_1^x\sigma_3^x + \sigma_1^y\sigma_3^y) + \omega_{23}(\sigma_2^x\sigma_3^x + \sigma_2^y\sigma_3^y), \quad (5.46)$$

This trigonal resonance may certainly be of use, as it generates directly maximally entangled states of the GHZ type in 5.41 up to asymmetries in the pairwise couplings. When the trigonal symmetry is broken the Hamiltonian will produce states comprising a portion of tripartite entanglement of the GHZ-type and a portion of partial

²There is a great deal of information present in the various entanglement modes, and a thorough study of all of them is beyond the scope of this thesis. We limit the discussion here to those of obvious interest.

pairwise entanglement of the W type in 5.42. Note that – perhaps surprisingly – even though the effective Hamiltonian is symmetric it does not contain the three-coupling term. This might lead one to the conclusion that the three-body interaction, especially if it is weak, has little influence over the dynamics of the systems.

However, the effective three-coupling term, even when it is much weaker than all the other energy scales in the system³ can in appropriate conditions be the dominant driver of the system’s dynamical evolution.

Searching for entanglement resonances that contain the three-coupling term ω_{123} immediately identifies a mode, in the absence of irradiation, located at

$$\omega_1 + \omega_2 = \omega_3 \quad (5.47)$$

There, an effective pure three-body interaction emerges in the rotating frame:

$$8\mathcal{H}/\hbar \rightarrow \omega_{123}(\sigma_1^x\sigma_2^x\sigma_3^x + \sigma_1^x\sigma_2^y\sigma_3^y + \sigma_1^y\sigma_2^x\sigma_3^y - \sigma_1^y\sigma_2^y\sigma_3^x). \quad (5.48)$$

This surprising result is emphasized. Even when the system is not irradiated and with the individual qubits parked at frequencies such that ω_{123} is the smallest energy in the problem, i.e. $\omega_{123} \ll \omega_{ji} \ll |\omega_j - \omega_i| \ll \omega_i$, one can extract an effective pure three-body interaction Hamiltonian with this very simple prescription. Needless to say, this Hamiltonian generates GHZ-type states from product states⁴. How can we understand the existence of such an effect? The condition $\omega_1 + \omega_2 = \omega_3$ implies that any two qubits can conspire to jointly exchange energy with the third. It is thus a sort of *three-body secular point*, the equivalent of the point $\omega_1 = \omega_2$ in a two-qubit

³And it is of course off diagonal in the computational basis.

⁴We note in passing its resemblance to the well known Mermin operator[118]

system that allows the two systems to freely exchange energy.

As with cross resonance, this effect must also be considered when trying to implement high-fidelity one-qubit rotations in the presence of an off-diagonal coupling, as it could lead to unwanted residual entanglement if not properly managed.

Simulations

We have verified these analytical results with numerical simulations. In the case where $\omega_1 = \omega_2 = \omega_3$ we expect a three-qubit entangled state to emerge once initializing the system to the computational basis state $|000\rangle$ and letting the effective Hamiltonian act for time

$$T_{GHZ} = \frac{2\pi}{\omega_{ij}} \times 2 \times \frac{1}{4} = \frac{\pi}{\omega_{ij}}, \quad (5.49)$$

where the factor of two comes from the strength of the effective Hamiltonian and the 1/4 corresponds to the time for a $\pi/2$ -rotation. For the test parameters (all units GHz),

$$\omega_i/2\pi = 7.3; \Omega_i = 0; \omega_{ij}/2\pi = 0.1; \omega_{123}/2\pi = 0.01 \quad (5.50)$$

the system indeed evolves from a fully factorable product state to a GHZ state in time,

$$T_{GHZ} = \frac{\pi}{2\pi \times 0.1\text{GHz}} = 5\text{ns},$$

as shown in 5.7.

For the case where $\omega_1 + \omega_2 = \omega_3$ and,

$$\omega_1/2\pi = 5.00, \omega_2/2\pi = 6.30; \omega_3/2\pi = 11.30, \quad (5.51)$$

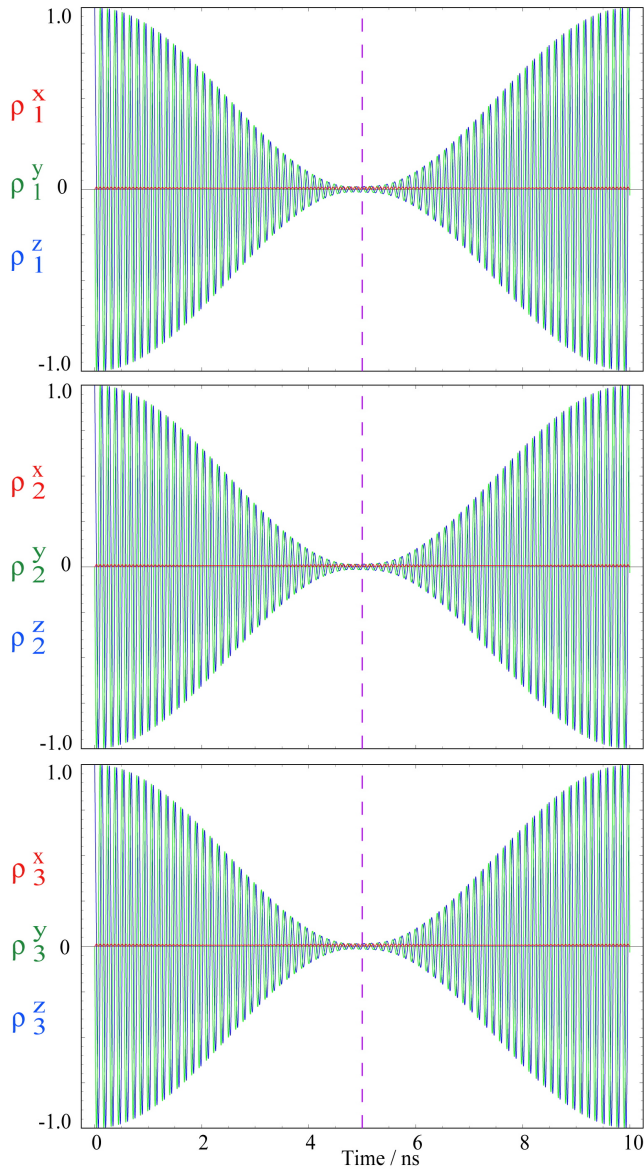


Figure 5.7: Generation of entangled three-qubit states by tuning to $\omega_1 = \omega_2 = \omega_3$. Qubits are not irradiated. The interaction is due to the three two-body coupling terms $\sigma_1^x \sigma_2^x, \sigma_1^x \sigma_3^x$ and $\sigma_2^x \sigma_3^x$, which are energy conserving when the qubits are resonant. The three-qubit coupling term $\sigma_1^x \sigma_2^x \sigma_3^x$ is present but not effective. The vertical dashed line is the three-body entanglement time predicted from Fourier analysis of the purely non-local Hamiltonian.

with couplings

$$\omega_{12}/2\pi = 0.13; \omega_{12}/2\pi = 0.10; \omega_{12}/2\pi = 0.11; \quad (5.52)$$

$$\omega_{123}/2\pi = 0.04 \quad (5.53)$$

we expect $T_{GHZ} = 25\text{ns}$, in agreement with the simulations of 5.8.

5.2.2 GHZ state production with AC control

We can also employ AC control over the qubit transition frequencies. In fact, the most recent result can be adapted even if it is impossible to DC tune the qubits to the three-body secular point, as there is an entanglement mode of the driven three qubit system at,

$$\omega_1^{rf} + \omega_2^{rf} = \omega_3^{rf}, \quad (5.54)$$

whereat we find

$$8\mathcal{H}/\hbar \rightarrow \omega_{123}\sigma_1^x\sigma_2^x\sigma_3^x \cos\xi_1 \cos\xi_2 \cos\xi_3 \cos[\phi_1 + \phi_2 - \phi_3]. \quad (5.55)$$

The effective three-coupling strength is maximized when each of the tones are nearly resonant, though in the limit of that case the qubits will entangle in the absence of irradiation.

Together, these AC and DC pure three-coupling entanglement resonances suggest an experimental strategy for exploiting a weak⁵ three-body interaction to generate GHZ states: through fabrication and circuit design aim the qubit frequencies to fall (at optimal bias, if applicable) in the vicinity of the DC mode $\omega_1 + \omega_2 = \omega_3$; the

⁵We emphasize that the pairwise two-body couplings are still present in the lab frame Hamiltonian. These modes just do not activate them.

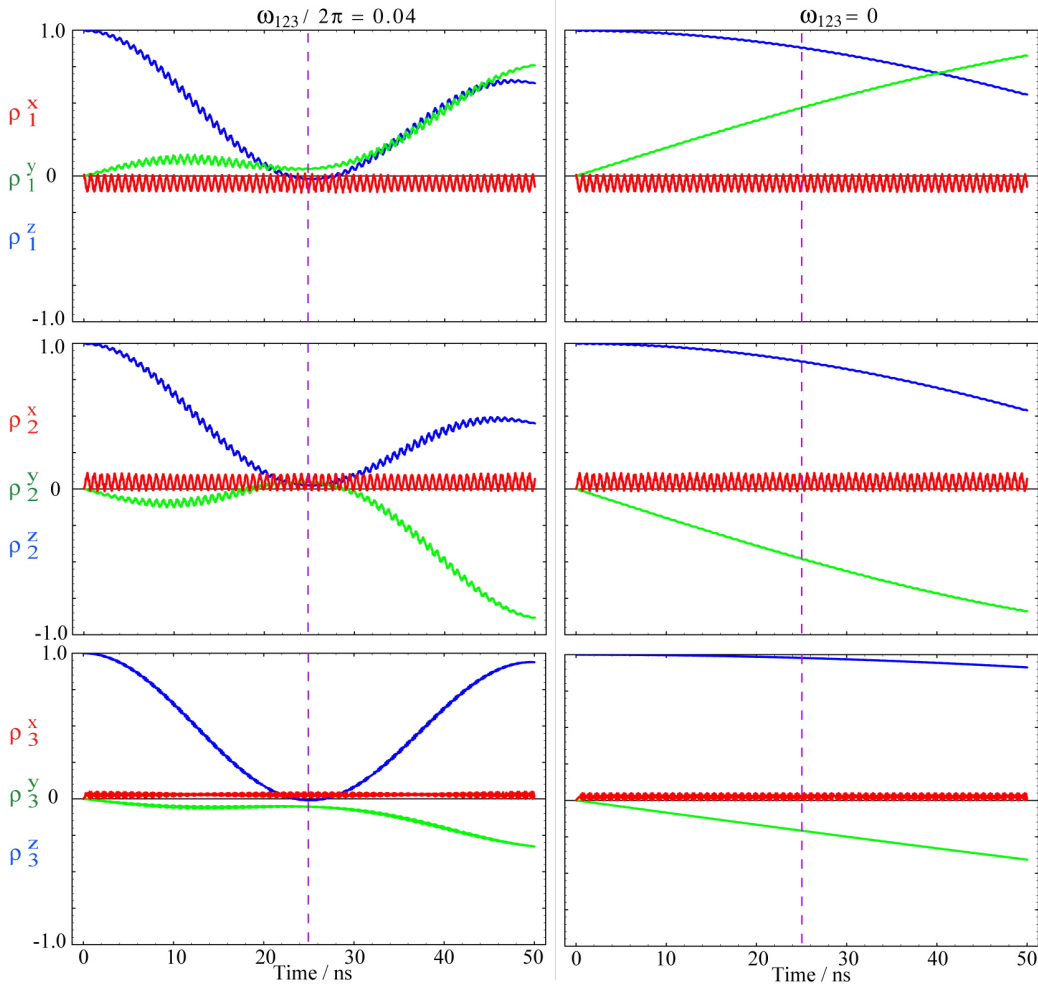


Figure 5.8: Generation of maximally entangled three-qubit states by exploiting a weak three-body coupling term $\sigma_1^x \sigma_2^x \sigma_3^x$ with DC tuning to the three-body secular point $\omega_1 + \omega_2 = \omega_3$. Qubits are not irradiated, and reduced density operator components are rendered in their respective Larmor-precessing frames. GHZ-type state emerges in 25ns, in agreement with the analytical predictions. *Left:* $\omega_{123}/2\pi = 0.04$. *Right:* Verification that the entanglement is due to the three-body interaction by setting $\omega_{123}/2\pi = 0$. With other parameters identical, the effect disappears.

natural scatter in fabrication parameters will prevent this from occurring exactly. If possible, use fast DC tuning to access the three-body secular point. Otherwise, apply irradiation to access the AC entanglement mode $\omega_1^{rf} + \omega_2^{rf} = \omega_3^{rf}$.

Simulations

For qubits of frequency

$$\omega_1/2\pi = 3.85, \omega_2/2\pi = 7.95, \omega_3/2\pi = 12.30, \quad (5.56)$$

with two-body couplings

$$\omega_{12}/2\pi = 0.13; \omega_{12}/2\pi = 0.10; \omega_{12}/2\pi = 0.11; \quad (5.57)$$

and a three body coupling much weaker,

$$\omega_{123}/2\pi = 0.04 \quad (5.58)$$

irradiated with drives tones,

$$\omega_1^{rf}/2\pi = 4.00, \omega_2^{rf}/2\pi = 8.00, \omega_3^{rf}/2\pi = 12.00, \quad (5.59)$$

of amplitude

$$\Omega_1/2\pi = 0.19; \Omega_2/2\pi = 0.13; \Omega_3/2\pi = 0.21, \quad (5.60)$$

the analytical result,

$$\begin{aligned}\omega_{123}^{eff} &= \frac{\omega_{123}}{4} \cos \xi_1 \cos \xi_2 \cos \xi_3 \cos[\phi_1 + \phi_2 - \phi_3] \\ &= \frac{\omega_{123}}{4} \frac{\cos[\phi_1 + \phi_2 - \phi_3]}{\sqrt{1 + \delta_1^2/\Omega_1^2} \sqrt{1 + \delta_2^2/\Omega_2^2} \sqrt{1 + \delta_3^2/\Omega_3^2}}\end{aligned}$$

predicts a GHZ state will be produced from the computational basis state $|000\rangle$ in

$$T_{GHZ} = 59.51\text{ns}.$$

Numerical simulations of the full three-qubit microwave driven Hamiltonian are in excellent agreement with this analytic result. Also shown are simulations for the identical system and input state, but with $\omega_{123} \equiv 0$. The effect disappears as we would expect from the theory.

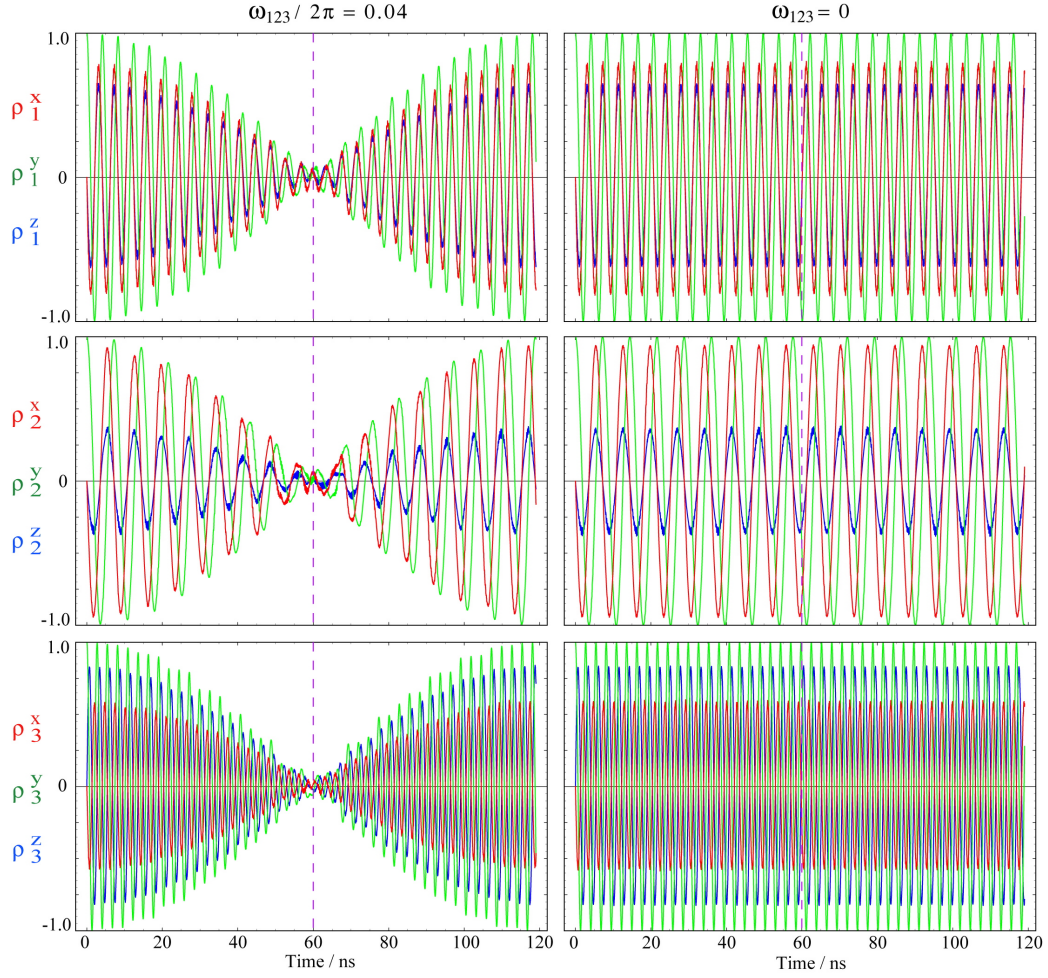


Figure 5.9: Generation of maximally entangled three qubit states by exploiting a weak three-body coupling term $\sigma_1^x \sigma_2^x \sigma_3^x$. The qubits are detuned from one another and from the three-body secular point $\omega_1 + \omega_2 = \omega_3$, but irradiated with tones satisfying the related condition $\omega_1^{rf} + \omega_2^{rf} = \omega_3^{rf}$. The simultaneous vanishing of all nine components of the three reduced density operators indicates a maximally entangled three-qubit state. *Left:* $\omega_{123}/2\pi = 0.04$. Vertical magenta line indicates the point at which a maximally entangled three-qubit state emerges as predicted from the Fourier approach. *Right:* Verification that the entanglement is due to the three-body interaction by setting $\omega_{123}/2\pi = 0$. With other parameters identical, the effect disappears.

Chapter 6

Device fabrication

6.1 Overview

Mesoscopic electrical circuits typically have features ranging from about 50 nanometers to 5 millimeters. As such, their construction places strong demands on the resolution and dynamic range of the equipment and techniques used in the fabrication process. The standard techniques used to produce them involve optical and electron beam lithography for pattern definition; sputtering, electron beam evaporation, and various chemical vapor deposition techniques for thin film deposition; and a host of chemical etching processes. In this work we have made efforts to limit our reliance on all but the most accessible of these tools, e-beam lithography and e-beam evaporation. Even so, doing fab is a complex and complicated procedure, neither pure science nor pure art, perhaps somewhat akin to baking. Details are important, though it's often difficult to say just which ones matter and which ones don't. This chapter describes some design considerations and standard fab techniques we have relied upon to make our qubit circuits.

Our aim is to fabricate two-qubit circuits to implement and test the microwave

controlled coupling schemes derived in Chapter 3 and Chapter 5, specifically the minimal and straightforward cross-resonance scheme. The circuits will comprise two copies of a quantronium style qubit, with a capacitance added between the two qubit islands to realize the non-secular coupling.

6.2 Standard fabrication techniques

The workhorse of our fabrication efforts is electron beam lithography with shadow mask evaporation. These procedures are established, flexible, straightforward, and offer very fast turnaround from design to room temperature testing. In what follows I describe the fabrication of a typical device employing these workhorse techniques. I then comment on how other key procedures complement them and expand the fabrication toolbox.

6.2.1 Typical device fabrication by e-beam lithography and shadow mask evaporation

Substrate preparation

Our standard fabrication typically begins with a high resistivity (typically $\rho > 20,000\Omega\cdot\text{cm}$) $300\mu\text{m}$ -thick two-inch wafer of Boron-doped silicon with only naturally occurring oxide. Devices can be fabricated directly on the weakly conducting silicon substrate, or we can add an insulating layer to facilitate the simple measurement of room temperature circuit resistances. We have used both silicon nitride¹ and thermally grown silicon oxide as an insulator.

The wafer must then be prepared with a bilayer resist. The bottom layer of the bilayer resist is chosen to be more sensitive to exposure to an electron beam,

¹Deposited by Plasma-Enhanced Chemical Vapor Depostion.

allowing the it to removed from underneath an intact top layer in certain regions. This undercut is an essential part of the shadow mask technique.

The wafer is cleaned in a sonic bath of isopropanol then methanol and dried with nitrogen, then spun at approximately 3000rpm with a resist of methyl methacrylate/methacrylic acid copolymer dissolved in ethyl lactate. We have used the MMA(8.5)MAA Copolymer Series Resists from the MicroChem Corporation, with the particular resist and the spinning speed chosen to generate a layer thickness tailored to the particular device and fab procedure. Our devices have used a first layer thickness ranging from 650nm to 1.2 μ m. For thicknesses at the top extreme of this range two layers of MMA are typically required.

After spinning the wafer is baked for 5min at 170°C; cooled for 1min; then spun at approximately 4400rpm with a resist of polymethyl methacrylate in ethyl lactate (we have used primarily the PMMA 950k series). The device is then baked under a ventilated petri dish for 30min at 170°C.

The wafer with bilayer resist is at this point either diced into chips suitable for one or a few devices, or, if required, an entire wafer of SEM alignment marks is written and deposited in Au and Ti before applying a second bilayer for the actual device fabrication.

Electron beam lithography

Chips of approximately (3-5mm)² are mounted in the FEI Scanning Electron Microscope for patterning with the electron beam. A layered pattern is composed using a computer aided design program (we have used primarily AutoCAD, though there are far better alternatives. Layers are assigned an electron beam spot size, and individual elements are assigned current doses. Once the chip is aligned, the SEM beam is focused and the stigmatism is corrected, the system automatically executes the

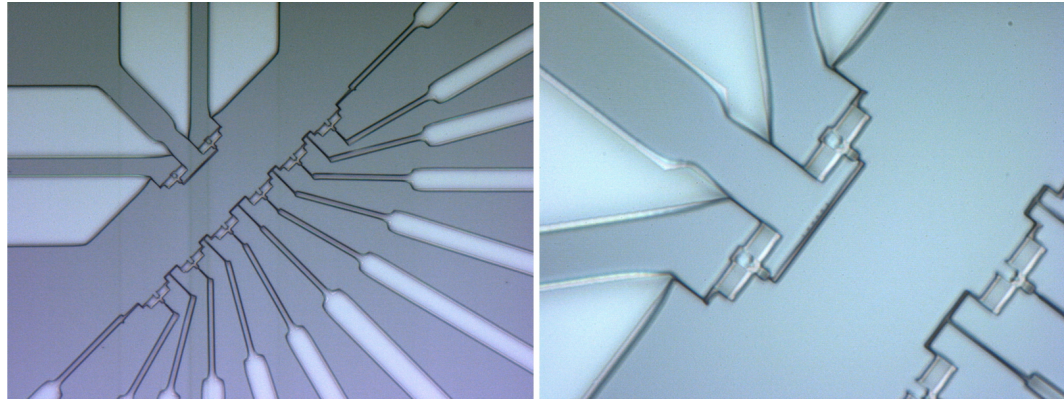


Figure 6.1: Optical image of a shadow mask for a coupled qubit device. Qubits are located at the ends of $\lambda/4$ coplanar stripline resonators, and coupled with a capacitor between their islands.

defined pattern of current doses.

The patterning by electron beam breaks chemical bonds in the resist, introducing a differing solubility of the exposed vs unexposed regions and between the top and bottom layer of the resist in certain solvents. We use the solvent methyl isobutyl ketone in a 1:3 ratio with isopropanol to develop the pattern for 60s, followed by 10s in pure isopropanol to remove the MIBK and stop the solving.

The chip has now been patterned with a lithographically defined shadow mask. Where both layers of resist have been removed, the substrate is exposed; where only the bottom layer is removed, there is a region of *undercut* accessible through an angled exposure to the evaporated metal. We now view the pattern under an optical microscope to check for obvious defects and signatures of successfully defined features smaller than the diffraction limit. Some typical images of successful devices are shown below.

Double angle evaporation

The patterned chip is mounted in an electron beam evaporator for metal deposition. The loadlocked system is pumped down to a pressure of approximately few $x10^{-7}\text{T}$ in the loadlock and $5 \times 10^{-8}\text{T}$ in the main chamber near the metal target. Aluminum is deposited at a rate of 1nm/s to a predetermined thickness, usually in the 30-60nm range at an angle. A mixture of Argon and Oxygen is introduced into the loadlocked portion of the machine bringing the pressure up to the 10^{-4} to 10^{-2}T range, and the device is left to oxidize for a duration of 5-20minutes. The pressure and duration of this oxidation step are the main parameters we adjust to generate Josephson junctions having the desired critical current densities.

After the oxidation step, the argon/oxygen mixture is pumped out of the system and a second evaporation is performed at a different angle. The angles are chosen such that they produce a shift between the two pattern images commensurate with the device design. In order to realize a particular circuit topology, it may be necessary to choose the angles and doses such that certain portions of the pattern are not deposited on the substrate but rather on the wall of resist, ensuring it will not be removed in the subsequent liftoff step.

After the second evaporation the chip is removed and the resist along with the metal deposited on it are lifted off by dissolving the resist in acetone at 65°C .

6.2.2 Bridge/ledge hybrid

The above procedure is powerful and flexible, but it is not without limitations. One limitation is the size constraints on features imposed by the strength of the resist. Making large junctions typically requires some combination of a large image shift (sharp evaporation angles, thick resist) and a long suspended PMMA bridge. But

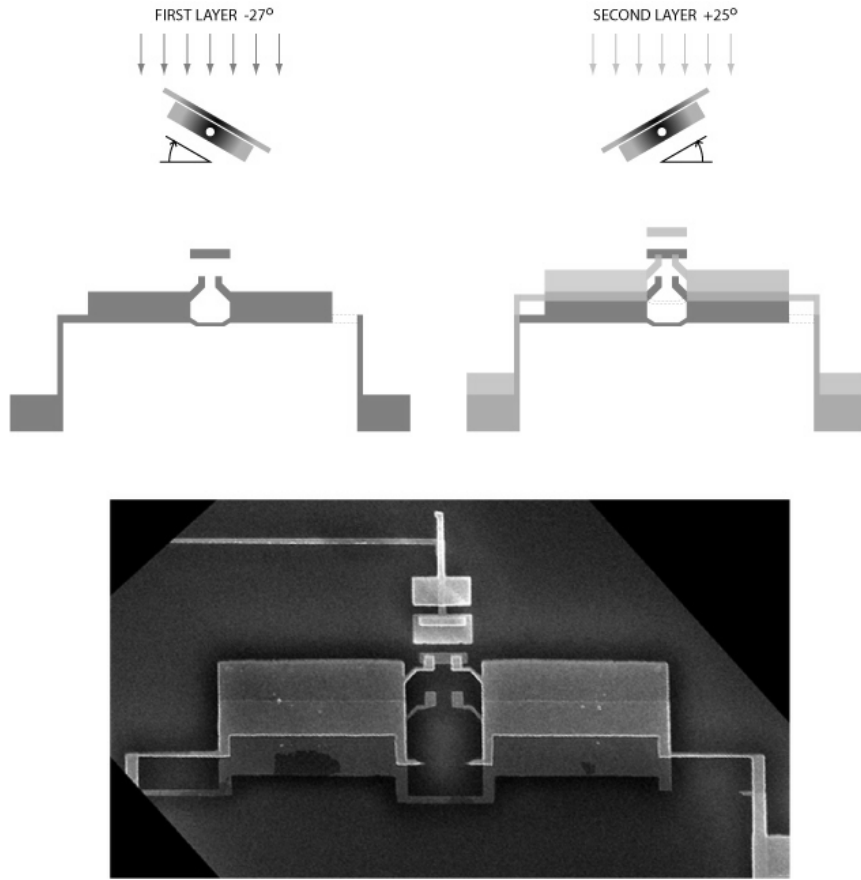


Figure 6.2: Double angle evaporation using a bridge/ledge hybrid shadow mask. The large junction is not formed by deposition under a bridge, while the small junctions are.

it is challenging to fully remove a thick underlayer of MMA from beneath a PMMA bridge without weakening it to the point of sagging or collapse. Furthermore, the thick resist, heavy current doses to remove large regions of the bilayer, and large shifts are conditions that make it very challenging to produce reliable, repeatable, and symmetric pairs of small junctions, as required for our typical quantronium style qubit devices.

To address these issues I have used a shadow mask design that combines Dolan bridges, where the evaporated metal travels under a bridge, for the small junctions with simple ledge shielding, where the metal travels in part under a ledge but mostly

has a clear path to the substrate, for the large junctions. In this case the required resist thickness is reduced, and the sensitive dose settings under and near the large bridge are done away with, generally making the shadow mask more robust.

This hybrid shadow mask technique has made it possible to reduce the asymmetry of two small junctions to better than 1%.

Chapter 7

Experiments

7.1 Introduction

We have carried out microwave measurements of coupled qunatronium circuits in the CPS geometry in a dilution refrigerator at 20mK.

7.1.1 Previous Measurements

Readout of Superconducting Qubits via a Dynamical Bifurcation

Earlier measurements in Prof. Devoret's group at Yale have established first the *Josephson Bifurcation Amplifier* (JBA) [139, 140, 131] and later the closely related *Cavity Bifurcation Amplifier* (CBA) [132] as single-shot readouts for superconducting qubits. Though they differ in the details of their implementations, these two technologies exploit the current-dependent inductance of an added Josephson junction in the quantum circuit to construct a non-linear oscillator which, when the readout is switched on, is coupled to the mode storing the logical state of the qubit. Very generally, a non-linear oscillator displays a dynamical bifurcation. Here, its coupling to the qubit mode means the onset of the bifurcation depends on the logical state of

the qubit. The switching of the non-linear oscillator between one of two meta-stable oscillation states is then detected in the phase of the microwave signal reflected off the device.

The JBA + Quantronium Early measurements of quantum bits implemented in superconducting circuits measured the logical state with a DC switching measurement[26]. There, an added Josephson junction was again coupled to the qubit mode, making the effective critical current of the readout junction dependent on the logical state of the qubit. By ramping the current through the junction to a midpoint between the two state-dependent critical currents, the state could be inferred from the observation of a voltage pulse indicative of a switching of the readout junction to the resistive regime.

The JBA was developed as an alternative to this DC switching method that allows faster repetition rates¹, less backaction of the readout onto the qubit mode, and a greater sensitivity. Its operation involves driving the readout junction with an RF current pulse rather than a DC pulse. The dynamics of the driven oscillator is described by

$$C_S \varphi_0 \frac{d^2\delta(t)}{dt^2} + \frac{\varphi_0}{R} \frac{d\delta(t)}{dt} + I_0 \sin(\delta(t)) = I_{RF} \cos(\omega_d t) \quad (7.1)$$

Here δ is the gauge-invariant phase difference across the junction, I_0 is the critical current of the junction, C_S is the shunt capacitance, R is the source impedance of the current drive and provides damping, ω_d is the drive frequency and $\varphi_0 = \hbar/2e$ is the reduced flux quantum. The sine term whose origin is the current phase relation of the Josephson junction[137], is the source of non-linearity in the oscillator. Under

¹In the DC current pulse technique, quasiparticles flood the circuit when the readout junction switches to the resistive state, a problem which ultimately limited the repetition rate for the experiment of Vion et al.

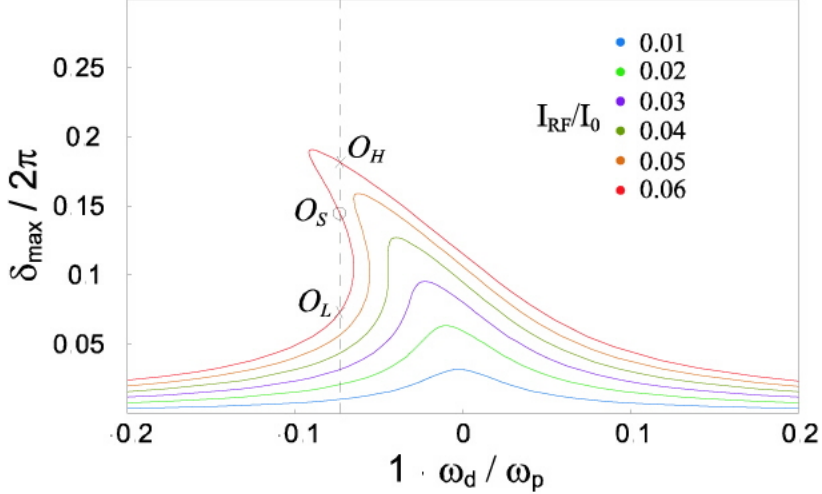


Figure 7.1: Non-linear resonance curves in a driven Josephson oscillator as a function of relative detuning $1 - \omega_d/\omega_p$ and drive amplitude I_{RF}/I_0 . ω_p is known as the plasma frequency and is the frequency for small oscillations. The resonance curves bend over as the drive amplitude is increased and become multi-valued for certain parameters. In this regime, for a given drive frequency and amplitude, there are two stable solutions (\times) separated by an unstable saddle point (\circ). Maximum response for small amplitude oscillations occurs at $\omega_d = \omega_p$. For higher drive amplitudes, maximum response occurs at frequencies below ω_p . The sign of the first non-linear term, which is negative in our case, determines the direction of this shift.

appropriate driving conditions, this non-linear oscillator can have two steady driven states differing in amplitude and phase[138, 139]. We will call these two states as the low amplitude state (O_L) and the high amplitude state (O_H) respectively. Fig. 7.1 shows the non-linear resonance curves for such a system. The figure shows a plot of the normalized oscillation amplitude ($\delta_{\max}/2\pi$) as a function of detuning ($1 - \omega_d/\omega_p$) for different drive current amplitudes.

For small drive amplitudes the response is the familiar Lorentzian response we would expect of a linear system. But as the drive current is increased, the oscillation amplitude increases, and the dynamics begin to sense the underlying non-linearity. The resonance curves start to bend towards lower frequencies², a tell-tale sign of the

²The direction of bending of the resonance curves is determined by the sign of the non-linear term; here, we have $\sin(\delta) \simeq \delta - \delta^3/6$ and hence the resonance curves bend towards lower frequencies.

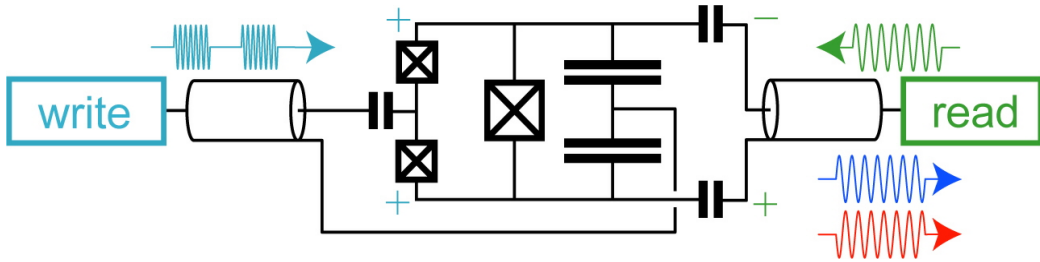


Figure 7.2: Schematic of a JBA coupled to a Quantronium qubit. The non-linear readout oscillator formed by large junction in parallel with shunt capacitance is energized through differential mode RF signals (green) applied across the circuit. The readout is coupled to the even qubit mode (blue) through the shared large junction. The readout is turned on by sending to the read port an RF pulse; the phase of the reflected signal encodes the result of the measurement of the (spin-1/2) qubit operator σ_z on the qubit mode.

non-linear behavior. For larger drive amplitudes, the solution becomes multi-valued. The two stable solutions are indicated with crosses for the curve with the largest drive amplitude (red) while the unstable solution is marked with a circle.

For a given drive frequency, the onset of bistable behavior depends on the ratio of the drive amplitude I_{RF} to the readout junction's critical current I_o . By coupling the qubit mode to the readout mode through a shared large readout junction, I_o may be made to depend on the qubit state when the RF drive is applied across the readout junction [140]. The JBA allows single-shot readout of a superconducting qubit with no on-chip dissipation and thus very fast repetition rates.

The shunt capacitors in the quantronium + JBA setup are employed to lower the plasma oscillation frequency from the bare value in the 40GHz range a dressed value in the 1-2GHz range, where the circuit is well described by a lumped element model. Fabrication of the large, typically 30pF, capacitors is straightforward, but their large dimensions have two undesirable effects. First, it is not easy to fabricate a pure capacitance at microwave frequencies, and stray effective elements – namely a stray inductance – can dilute or even destroy the bifurcation phenomena within the range

of interest. Second, the sheer size of the capacitors make scaling to multiqubit circuits challenging. In the original JBA work we used capacitors measuring $300\mu\text{m} \times 300\mu\text{m}$, and one can immediately see the problem in building multiple copies of such devices in close enough proximity to realize a useful coupling between the two qubit modes. See R. Vijay’s Yale Ph.D. thesis [131] for a complete study of the JBA and its application to reading out superconducting qubits.

These factors, in addition to the goal of pushing the limits of the JBA by operating it at higher frequencies, prompted a new incarnation of the bifurcation amplifier wherein the Josephson junction whose inductance contributes the essential non-linearity to the readout scheme is embedded in a *geometrically defined* transmission line resonator.

The CBA + Quantronium Geometrically defined coplanar waveguide (CPW) transmission line resonators can easily be built in the range of typical qubit frequencies of 5–20 GHz and with internal quality factors into the 10^6 ’s [123]. The CPW is a planar cross-section of a coaxial cable, comprising two large ground planes symmetrically separated from a narrow center conductor. By interrupting the center conductor of such a transmission line resonator with a large Josephson junction, the resonator can be made non-linear and employed again as a bifurcation amplifier.

In this version, coined the *Cavity Bifurcation Amplifier* (CBA), operating frequencies can be controlled through geometry without the risk of introducing stray elements. They may be fabricated in a planar lithographic process with optical lithography for the resonator preceding electron beam lithography for the junction. The resonance frequency of the CPW resonator is determined, for a given substrate and enclosure, by its length. The center conductor is interrupted in two places to define input and output capacitances, C_{in} and C_{out} . These capacitances determine the rate

at which energy may be added to and extracted from the resonator mode, as required to both energize the non-linear oscillator and then to measure its oscillation state to readout the measurement result.

The CBA resonance displays similar behavior to the JBA, and is operated in an equivalent manner. It has been used by Metcalfe et al[145] to measure the state of a quantronium style qubit embedded in the CPW.

Though it nicely solves the problems of operation at higher frequencies, the CBA still leaves complications when it comes to implementing multi-qubit circuits. The readout in this in-line geometry is coupled to the current in the center conductor of the CPW, the readout cannot be placed too near the end of the resonator, where the current is zero. If the qubit is to accompany the readout in a quantronium style circuit, this means the qubits themselves will be physically far apart. Adding additional lines to couple charges or fluxes from one qubit to another is troublesome in the presence of the all-over ground planes. One solution is to place a few qubits in each resonator, though this necessarily reduces the extent to which each qubit may be individually manipulated and measured.

Coplanar Stripline Resonator These problems have been addressed by fabricating the geometric resonator rather from a coplanar stripline resonator. Coplanar striplines consist of two microstrips of width W separated by distance S atop a conductor-backed dielectric of thickness D , with the resonator defined by a symmetric input capacitor on of the lines. This geometry is better suited to multiqubit devices. The striplines do not call for an all-over ground plane as with the CPW, and the readout junction and qubit circuit may be fabricated at the open end of a $\lambda/4$ resonator.

As we saw in the description of the JBA coupled to a quantronium style qubit,

the readout mode is the differential or odd mode that drives current through the large readout junction, while the qubit mode corresponds to the even mode that drives symmetric current through each of the small junctions of the SET.

In the CPS version of the Josephson bifurcation amplifier, the even and odd mode are each launched onto the chip through the same line and (nominally symmetric) input capacitances, and are separated outside the sample box with a 180° hybrid. Odd mode signals launched into the resonator drive current through the large readout junction and thus energize the readout, while even mode signals symmetrically raise and lower the potential of the small SET island and thus drive symmetric currents through the SET junctions. In an ideal device these modes are orthogonal, though in reality they can mix both on- and off-chip through broken circuits symmetries originating from device imperfections (e.g. the two SET junctions aren't identical), imperfect bias conditions, or imperfect mode isolation in the 180° hybrid, among other sources.

There are two central benefits of the CPS with read/write signal multiplexing arrangement. First, the CPS resonators require only comparatively small regions of the chip to be metallized. This makes it much easier to bring two nominally independent qubits close enough to one another to couple them with a simple capacitance. And it allows the fabrication to be done using a one-step all electron beam lithography process³. Second, it allows us to do away with the gate line previously used in the experiments on the JBA + quantronium to control the qubit mode, again facilitating the coupling of the SET islands of respective qubits to one another via a simple and small capacitance.

The CPS incarnation of the JBA/CBA is shown below.

³In trying to realize now two qubit circuits with the right parameters, the faster turnaround time all e-beam process affords is more than welcome.

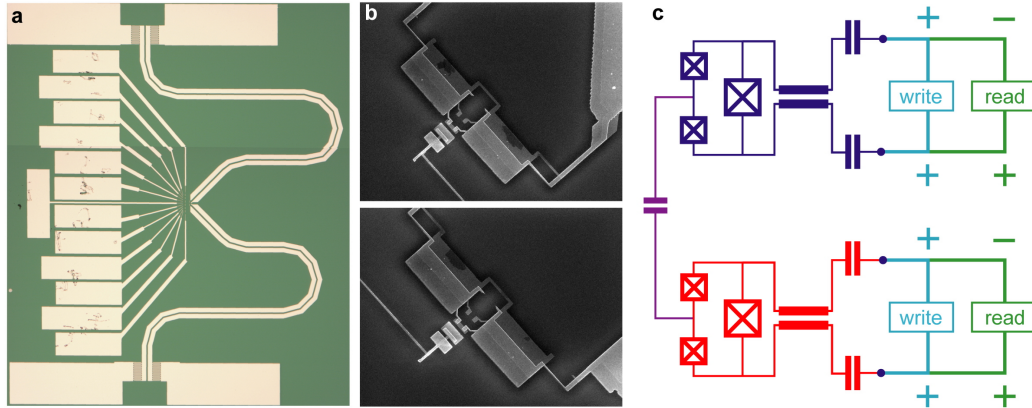


Figure 7.3: Superconducting circuit implementing coupled quantronium in coplanar stripline (CPS) geometry. **a.** Optical image of chip $\sim 3\text{mm}^2$ chip. Control signals are launched onto chip via large bonding pads (top and bottom rectangles), connected to interdigitated CPS resonator input capacitor. At left with scratches are probe pads for test quantronium. **b.** SEM images of the individual quantroniun subcircuits terminating the CPS resonators. Qubit islands are topologically exposed, making it easy to achieve inter-qubit capacitive coupling. **c.** Equivalent circuit diagram. All control signals are coupled to CPS even (WRITE) or odd (READ) mode.

7.1.2 Aims

Our aim in our measurements was to test the microwave protocols for performing two qubit gates we developed in chapters 3 and 5. To facilitate the extension to two and possibly more qubits, we have adapted the design and operation procedures of the CBA + quantronium and JBA + quantronium experiments to an implementation where it is possible to retain full read and write control over each qubit independently as additional qubits are added to the circuit.

With that in mind, the first aim of our measurements was to establish the coplanar stripline geometry as a functional incarnation of the JBA. The second aim was to demonstrate the simultaneous independent operation (i.e. both independent control and readout *at the same time*) of two superconducting qubits on the same chip. Our third aim was to demonstrate that a fixed weak non-secular coupling could be used to deterministically entangle superconducting qubits, and to test some of the coupling

protocols developed in chapter 3 and chapter 5.

7.2 Experiment design

The samples we have measured comprise two capacitively coupled coplanar stripline quantronria (cCSQ) fabricated on a high resistivity silicon chip. A mounted sample is shown figure 8.5. Microwaves are launched onto the chip through a Southwest Microwave edgemount connector that is secured directly to the printed circuit board and substrate that carry the signals to the edge of the silicon chip. Each qubit requires two signal-carrying lines. At the sample holder these correspond to one line per arm of the CPS resonator; above the hybrid, they correspond to one line for each of the readout and control microwave signals. We now describe the details of this microwave measurement setup.

7.2.1 Measurement setup

Experiments were performed in a dilution refrigerator from CryoConcept at an operational base temperature of 20–30mK. The measurement setup is shown in 7.4.

Microwave readout setup

Readout excitation Microwave pulses at the readout frequency are sent to the Δ -port of a Krytar 6–20GHz 180° hybrid[127] through a -13dB directional coupler, also from Krytar. The hybrid splits the pulse into a differential signal across its two output ports, which in turn are connected to the arms of the CPS resonators through input capacitors. The microwave readout pulses were created by direct conversion through a two-level mixing chain. Mixers are from Marki Microwave. DC-going

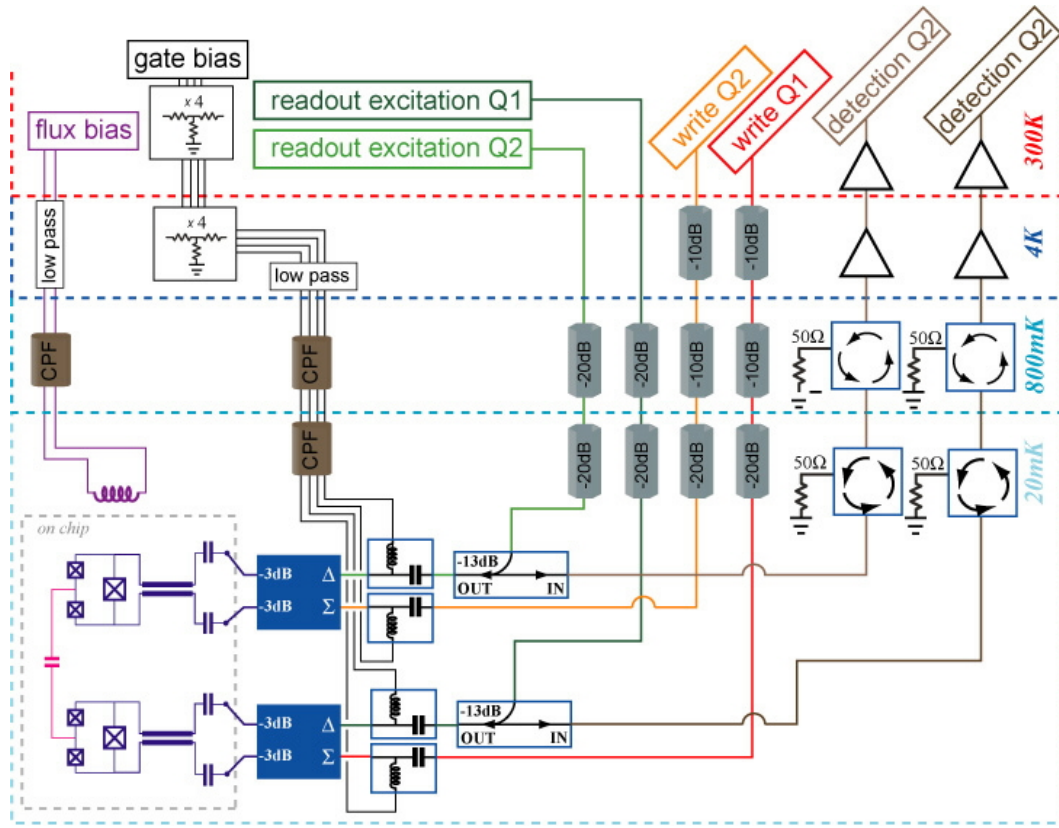


Figure 7.4: Cryogenic microwave measurement setup for our experiments on capacitively coupled qubits.

pulses to drive the IF ports of the mixing chain were created in Burst and Arb mode of an Agilent 33250A 80 MHz Arbitrary Waveform Generator.

Readout detection The reflected readout signal, which contains encoded in its phase the state of the qubit mode, is recombined into a symmetric signal with respect to ground on its return path through the 180° hybrid. The signal travels through the directional coupler and two cryogenic circulators to a HEMT amplifier operated at 4k, then an additional microwave amplifier at room temperature. The signal is transformed to DC by mixing it with a copy of the original excitation signal, then again amplified with a Stanford Research Systems SR445A DC–350 MHz preamplifier.

The voltage signal is filtered and sampled by an Acqiris digital sampling card. Statistics are accumulated by repeating the measurement approximately 10^4 times. When histogrammed, the voltage levels show a well separated bimodal distribution corresponding to the two oscillation states of the non-linear oscillator. The amplitude of the readout excitation pulse is adjusted to control the weight in each mode of the histogram.

Microwave 'write' setup

Microwave pulses are produced by driving the internal IQ modulator of an Agilent E8251A source with pulses from a Tektronix 1GS/s Arbitrary Waveform Generator. The pulses are sent to the Σ -port of the 180° hybrid which splits the signal into two symmetric copies relative to ground before passing to the qubit through the CPS resonator. As the SET islands have capacitance to ground, these even mode signals symmetrically drive currents through each junction of the SET.

DC biases

Flux A cold coil mounted approximately 5mm from the sample is connected through lossy copper powder and epoxy filters to a Yokogawa voltage source. The voltage applied to the coil allows the control of a *global* flux bias for both qubits, but not of each independently.

Charge The qubit circuits are charge biased with either a Yokogawa 7651 Programmable DC Supply, or, when performing charge sweeps, with an Agilent 33250A Arbitrary Waveform Generator. The DC control signals are resistively divided and passed through reflective low-pass filters and lossy low-pass filters, once at room temperature and again at 4k. The signals are then applied symmetrically to each arm of the resonator through bias T's at both the Δ and Σ ports of the 180 hybrid.

7.3 Measurement Results

We have measured two samples of capacitively coupled superconducting qubits. The samples are fabricated in the quantronium style using a bridge/ledge hybrid shadow mask and coupled to CPS versions of the JBA / CBA. We now highlight the results of these measurements.

7.3.1 Qubit Readout

Phase diagrams

We have verified the non-linear behavior of our CPS readout resonators by measuring the phase of the reflected differential mode signal. For a series of discrete frequency steps near the linear resonance point we ramp the power adiabatically with respect to the switching dynamics of the non-linear and monitor the reflected signal [131,

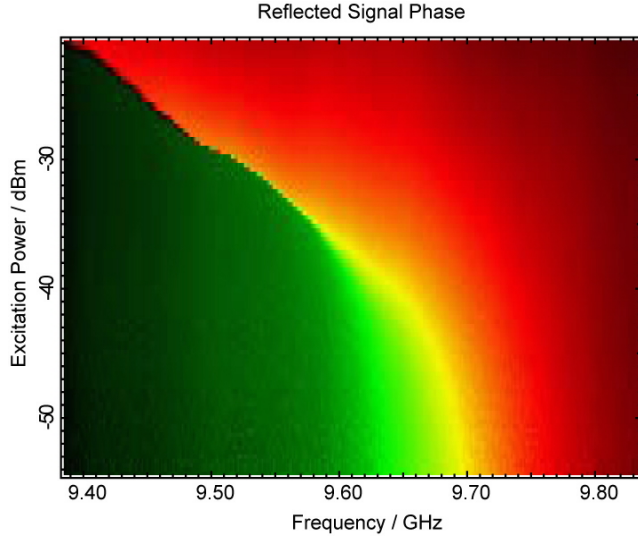


Figure 7.5: Characteristic phase diagram for a CPS resonator implementation of the JBA/CBA. The linear resonance displays a quality factor of 80, and a bistable region appears around 9.50GHz. Data were taken on Qubit 1 of sample CSQNOV07.

[139, 140]. A plot of these data show the signal phase as a function of power and frequency, and should demonstrate a characteristic bending of the linear resonance to lower frequency as the power is increased. A characteristic phase diagram is shown below. The extracted resonator Q for the linear resonance is 80.

Readout performance

Readout protocol To readout the state of the qubit mode we follow the procedure developed by Siddiqi et al [131, 139, 140]. A differential mode microwave pulse at a drive frequency ω_d slightly detuned below the resonance frequency ω_p is applied to the quantum circuit. The readout pulse has a ‘latching’ shape as shown below. The return signal is mixed to DC, digitized, and sampled. The sampled voltages are histogrammed as the experiment is repeated many times with a minimal time separation of a few T_1 to ensure the qubit is in its ground state. The parameters of the readout may be adjusted to maximize the separation of the two peaks in the

bimodal histogram.

Tuning the readout protocol The power is ramped, at a rate limited by the quality factor of the linear resonance, to a point P_{latch} , to be optimized in what follows, near to the critical point where switching to the higher of the two bistable states occurs with probability P_{switch} . A histogram of the phase, encoding the switching events, is created for a range of values of P_{latch} . As this latch power increases so does P_{switch} , and the weight of the histograms in the switched state maps out a sigmoidal curve nicknamed an s-curve.

To optimize the readout, the procedure is repeated with the qubit now in the excited state. The excited state s-curve will be displaced and stretched relative to the ground state s-curve. The optimal operation point of the readout, i.e. the latch level P_{latch} and the frequency ω_d , are those at which the spread between the ground and excited state s-curves show the largest separation, a number called the *contrast* of the readout.

S-curves Earlier results on the JBA + quantronium and CBA + quantronium have obtained maximum s-curve separation between the ground and first excited state of 35% and 50%, respectively [131, 132]. Our results, shown below, demonstrate an 80% separation.

We have not conclusively identified the source of this improved contrast, though the differences between the 80% separation we have observed and the earlier observed values are too large to be due simply to decreased relaxation of the qubit being measured.

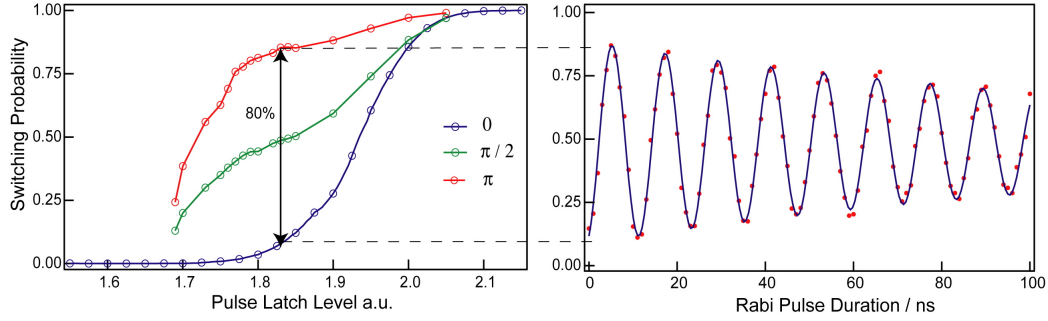


Figure 7.6: High raw visibility of coplanar stripline quantronium circuit. *Left:* S-curves: switching probability as a function of readout pulse latch level with no qubit control pulse (blue), $\pi/2$ -pulse (green), π -pulse (red). Location of maximum separation indicates optimal readout pulse height. A perfect projective quantum measurement would have a separation of 100% between the red and blue curves, with the green curve always midway between the two. *middle:* Sample Rabi oscillations. Points correspond to mean switching probability for 2000 individual measurements. Fit (blue) indicates raw visibility of 87% in the Rabi trace.

7.3.2 Qubit Control

DC Modulations

The JBA readout is sensitive to the curvature of the energy surface, and this allows us to characterize the properties of the ground state of the quantum circuit by measuring the switching probability as a function of the circuit bias point in charge and flux. In addition to measuring the energy surface, this technique can spectroscopically probe the systems transitions, see figure.

Rabi oscillations

We have carried out individual qubit Rabi oscillations experiments on two separate samples of capacitively coupled quantronium-style qubits with CPS resonator readouts. By performing synchronous Rabi experiments on each qubit of the coupled qubit sample, we have demonstrated simultaneous independent manipulation and read out of two interacting quantum circuits. The Rabi oscillations protocol, and

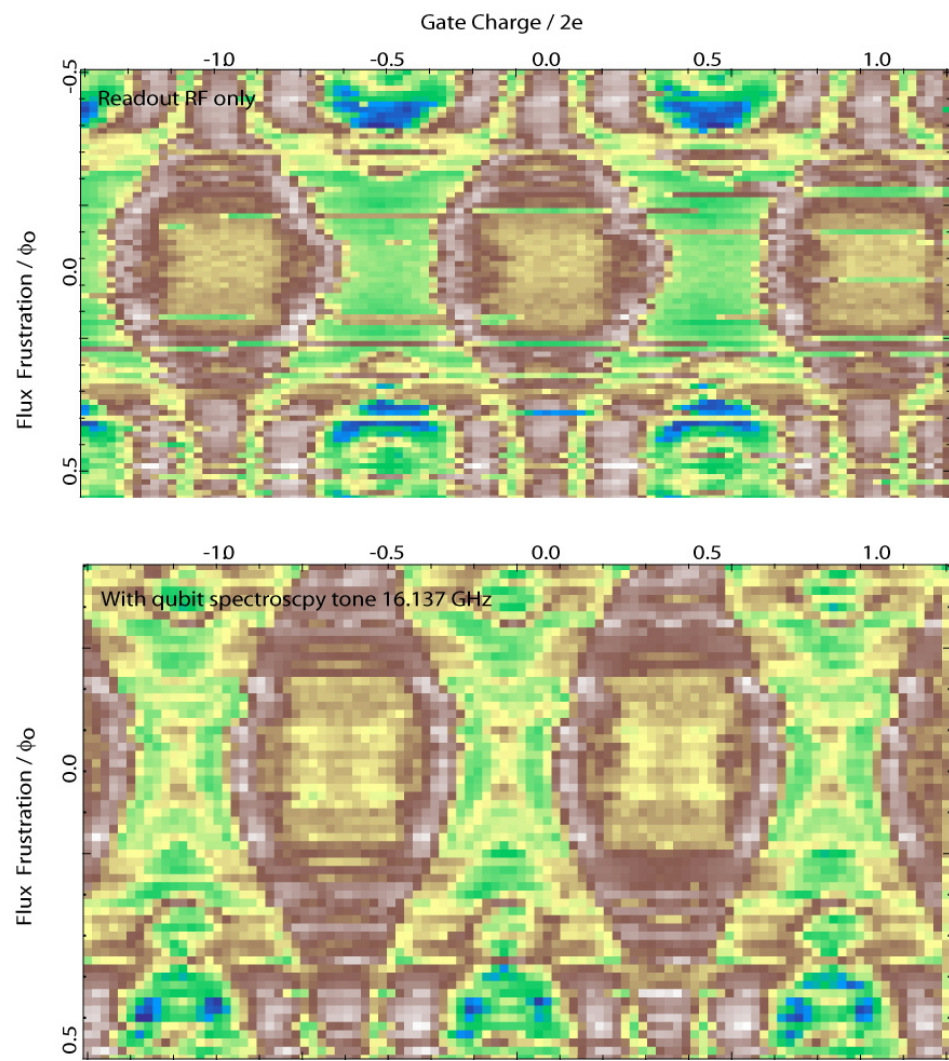


Figure 7.7: Gate and flux modulations of a quantronium circuit with CPS readout resonator. In the bottom data we have added a spectroscopic tone to the even mode at 16.137GHz, and additional features corresponding to the qubit $0 \rightarrow 1$ transition are visible.

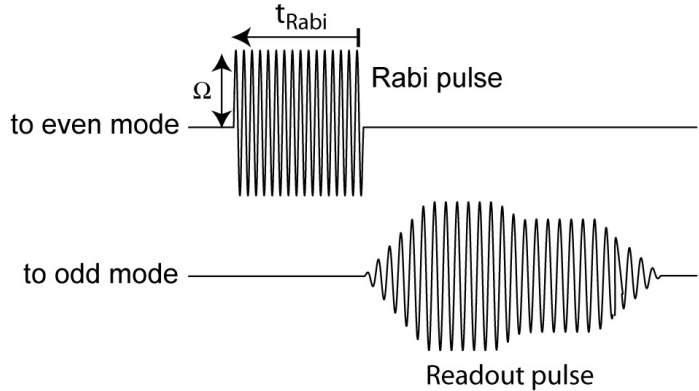


Figure 7.8: Pulse protocol for Rabi oscillations experiment. A qubit control pulse of amplitude Ω and duration t_{Rabi} is applied to the circuit's even mode, followed immediately by a latching readout pulse applied to the odd mode. The duration t_{Rabi} is increased in 1ns steps, then the procedure repeated $\sim 10^3$ times, and switching histograms are constructed for each t_{Rabi} .

resulting data, are depicted below.

In the Rabi oscillation experiment, an even-mode microwave pulse at the qubit transition frequency and lasting t_{Rabi} is applied to the circuit, inducing a rotation about σ_x whose angle is determined by the integrated pulse angle. By limiting to flat top pulses, we can drive the system continuously between the states $|0\rangle$ and $|1\rangle$. Immediately after the Rabi pulse an odd-mode readout pulse is applied to the system to readout the state of the qubit. By building up switching probability histograms for each time duration t_{Rabi} we can map out a sinusoidal variation corresponding to the state's driven precession. The data support the conclusion that we have fabricated and controlled two quantum bits each having independent read and write capability.

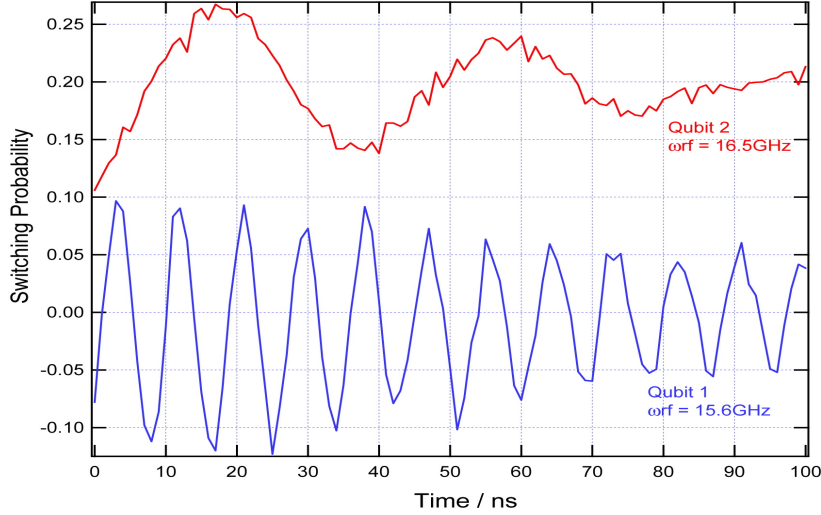


Figure 7.9: Simultaneous independent control and readout of two coupled superconducting qubits. A Rabi train of microwave pulses was applied to qubit 1 at 15.60GHz and to qubit 2 at 16.50GHz. Pulses were produced by splitting the output from a single Tektronix AWG channel and using each copy to drive a direct conversion mixing setup with an LO signal at the respective microwave frequency. Readout pulses are also synchronous, but originate from separate Agilent 80MHz AWG's, each enslaved to the master clock of the Tektronix AWG.

7.3.3 Qubit–qubit Coupling

Cross-resonance irradiation

We have obtained preliminary evidence to support our proposed cross-resonance irradiation scheme of Chapter Five. We performed the following experiment in an attempt to observe a signature of this effect. First, we perform a Rabi oscillations experiment on Q2 over a range of frequencies to locate its transition. Once Q2 is located, we switch the Rabi pulse train that was resonant with Q2 to Q1, and measure Q1. Note that the presence of the cross-resonant effect doesn't depend on the frequency of Q1. However, the observed oscillation frequency on Q1 as a result of the drive will increase with the $\delta = \Delta = |\omega_1 - \omega_2|$, while the effective coupling strength ω_{xx}^{eff} will decrease with δ .

During a cross-resonant pulse on qubit 1 of amplitude Ω and phase $\phi = 0$ the

effective rotating frame Hamiltonian is

$$\mathcal{H} = \frac{\omega_{xx}}{4} \cos \xi \sigma_1^x \sigma_2^x \quad (7.2)$$

where the angle ξ is given by

$$\cos \xi = \frac{1}{\sqrt{1 + (\Delta/\Omega)^2}}. \quad (7.3)$$

The measurement of the switching probability of Q1 should reveal oscillations at the frequency $\eta = \sqrt{\Delta^2 + \Omega^2}$ with nodes or beats at a frequency

$$\omega_{xx}^{eff} = \frac{\omega_{xx}}{2} \frac{1}{\sqrt{1 + (\Delta/\Omega)^2}}$$

where the amplitude of oscillations goes to zero provided the microwave pulse is properly tuned to $\omega_{rf} = \omega_2$. The beats correspond to a reduction of the expectation values of the local measurement operators $\langle \sigma_z \rangle$ due to the generation of entanglement, and occur every $t_{ent} = \pi/(2\omega_{xx}^{eff})$. Unfortunately, our measurement was hampered by a rather unstable bias point of qubit 1, and to a lesser extent of qubit 2. Also, I did not have the microwave equipment required to simultaneously drive and measure both qubits at the time these data were taken, as would be required to conclusively identify both qubits' transition frequencies under the bias conditions of the measurement.

We can, however, get a qualitative estimate of the bare coupling strength ω_{xx} by taking into account the *amplitude* of the induced Rabi oscillations of the measured qubit 1 due to the drive at ω_2 , as this amplitude gives an approximate indication of the ratio Ω/Δ . This leads to the estimate that $\omega_{xx}/2\pi \approx 7MHz$.

A more complete measurement would identify conclusively the transition frequency of each qubit under the operating conditions. This could be done most easily

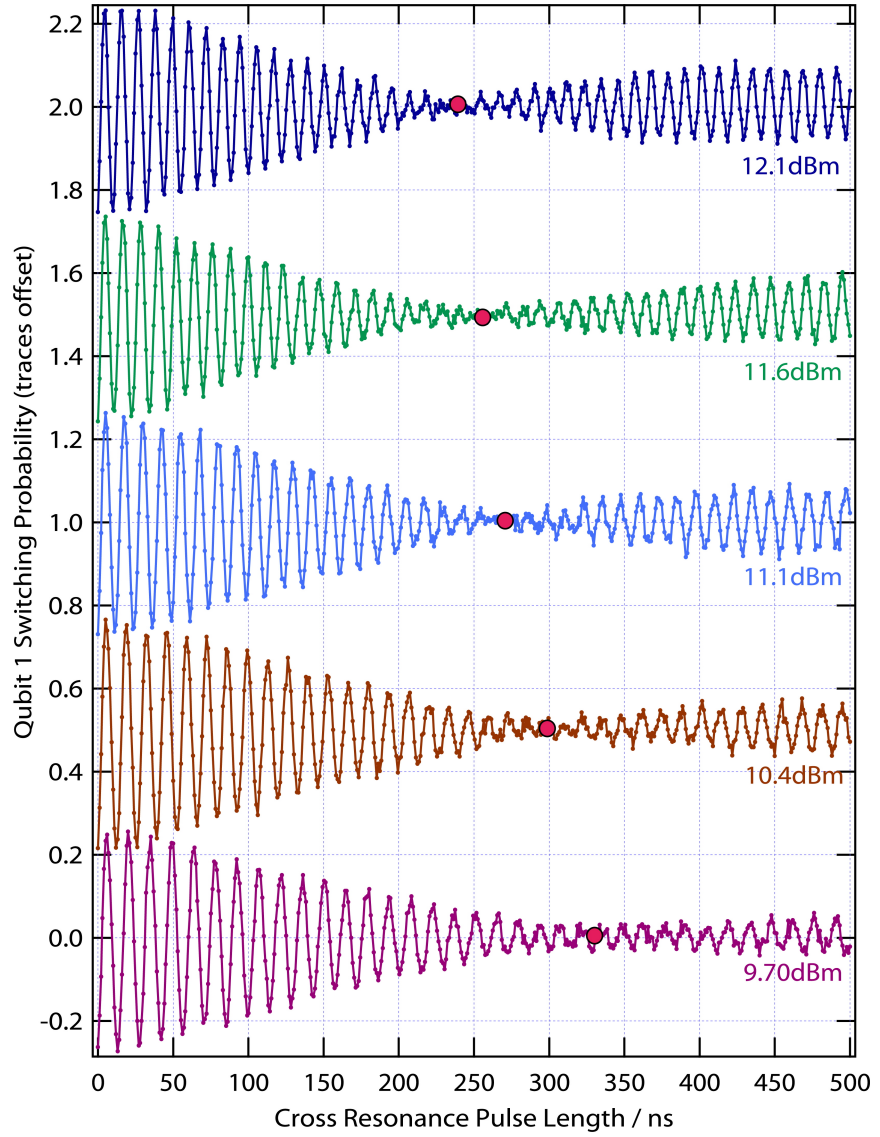


Figure 7.10: Rabi beating of two superconducting qubits subject to cross-resonance irradiation. Q1 is irradiated at the transition frequency of Q2 (16.331GHz), and the state of Q1 is read out. Different traces correspond to different drive powers. The effective coupling strength ω_{xx}^{eff} depends on the drive amplitude Ω and the detuning $\Delta = |\omega_1 - \omega_2|$, and has a maximum value of $\omega_{xx}/4$. A node in the oscillations appears every $t_{ent} = \pi/2\omega_{xx}^{eff}$. The complete cancellation of the oscillations at the node occurs when $\omega_1^{rf} = \omega_2$.

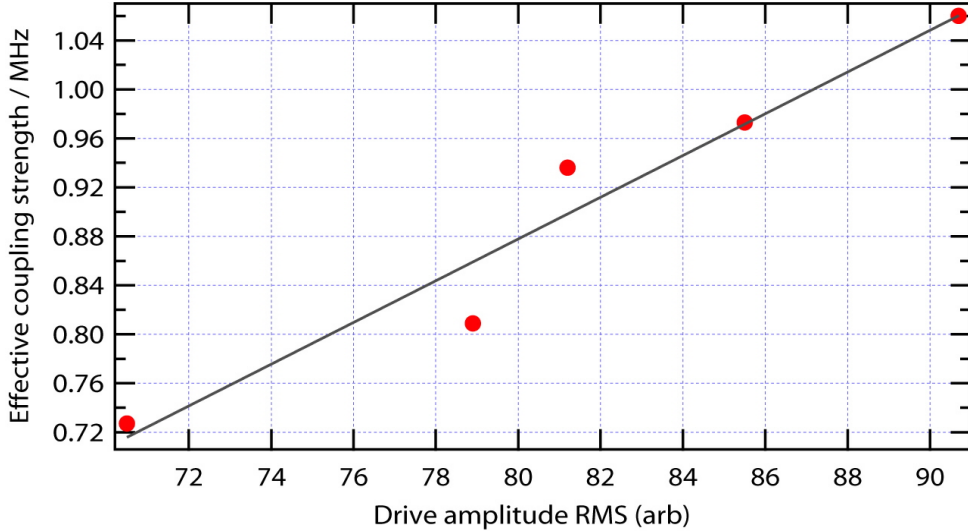


Figure 7.11: Observed effective coupling strength as a function of the rms drive signal voltage. The data does not cover a large enough range to distinguish linear vs. quadratic dependence. The red points are extracted from the above beating data and the grey line is a linear fit.

by stepping the drive signal frequency of the Rabi tone through a range covering both the irradiated qubit's transition frequency and unirradiated qubit's transition. The irradiated qubit should then develop a beating in its Rabi signal when the tone becomes cross resonant. Repeating this procedure for a large range of drive amplitudes would allow a more conclusive observation of the cross resonance effect.

Chapter 8

Conclusion

8.1 Conclusions

The central results of this work are the strategies we have developed for entangling superconducting quantum bits and some of the techniques we have adapted to the task. We began by formalizing some tools of general utility in quantum computation and particularly in solving the quantum gate problem, including the discretized Hilbert space and the n -qubit generalization of the familiar Bloch equations.

Our results on discretization of the two-qubit Hilbert space – and the straightforward extension to larger systems – suggest that the continuity of Hilbert space, and not merely the existence of entangled states within it, is the essential property allowing the exponential speed up of certain quantum algorithms over their classical counterparts. Maximally entangled states emerge in a computational paradigm where such a speed up would be impossible. It is worth noting that this conclusion is contrary to the beliefs of many researchers in quantum information and quantum computation, who tend to overemphasize the power of entanglement alone as a computational resource.

We proposed several schemes for performing two-qubit gates in superconducting qubits. Our FLICFORQ scheme demonstrates that a switchable qubit-qubit coupling can be achieved without tuning the qubit frequencies nor the coupling subcircuit, allowing two-qubit gates to be performed at the optimal bias point, an operating condition that can dramatically improve qubit performance. Our cross-resonance gate scheme complements and improves upon this result. It requires a single tone applied to one of the two qubits to be entangled, and results in a coupling strength that increases with the amplitude strength of the tone. In other words, the non-linearity of the qubit circuits themselves can be used to achieve a tunable interaction. These schemes achieve a two-qubit gate on/off ratio of 20dB, with limits set by residual entanglement during one-qubit gates when the fixed couplings are not refocused or otherwise compensated, and doing so would allow much larger ratios. The emergent theme is clear: there is no fundamental need for complicated tunable sub-circuits to couple our qubits. Simple linear couplings are sufficient.

The cross-resonance protocol emerged from a powerful (and to our knowledge original) approach to the quantum gate problem: Fourier analysis of the qubits' Hamiltonian in a special multiply-rotating reference frame where the system dynamics are purely non-local. The technique can be applied to a broad class of quantum computing systems. It can identify gate protocols that use DC or microwave control over the qubits or the couplings, or a combination thereof. Importantly, the approach is comprehensive: it identifies *all* the configurations of available controls under which a desired effective Hamiltonian emerges.

A study of the three qubit case with the Fourier approach has led us to the following prediction: with simple DC control over one of the qubit frequencies, a very weak three-body coupling term present in the Hamiltonian can be made to

dominate the full system dynamics even when the qubits are mutually far detuned from another. This effect opens up the possibility for *direct* generation of GHZ-type states.

We have designed, fabricated and measured two-qubit circuits with the aim of implementing two-qubit gates with our proposed protocols. The measurements, though inconclusive, offer strong support for the validity of the cross-resonance scheme. We have observed the anticipated beating in the Rabi oscillations of the cross-driven qubit. The beat frequency was observed to increase with the amplitude of the drive over a range of about 1.5. Our data are consistent with the cross-resonance theoretical result, but they don't allow us to draw conclusions with any certainty as to the validity of the scheme for reliably performing two-qubit gates.

8.2 Future work

8.2.1 Gate strategies for cQED with flux bias lines

Recent results have demonstrated independent control over two transmon qubits in the cQED architecture. A common criticism of the scaling prospects of this architecture is that the presence of just a single microwave port means two-qubit gates can be done just one at a time. For a cavity containing several qubits, the following control strategy would overcome this. By adding a few GHz of bandwidth to the existing flux lines, one can achieve couplings to spectrally distant qubits by applying to the flux bias line a signal at the difference frequency of the two. That is, modulate the frequency ω_1 at $\omega_{rf} = |\omega_1 - \omega_2|$, where ω_2 is the frequency of the targeted qubit. This protocol is very similar to the parametric pumping scheme of Bertet, et al. The effective coupling strength increases with the amplitude of the drive signal.

Though it requires a some microwave engineering of the flux bias lines, we believe this represents a good trade-off, as it opens up the possibility to entangle any pair of qubits in the cavity, and to do so simultaneously.

8.2.2 Active cancellation of fixed coupling

One of the most useful features of a non-linear coupling subcircuit is that the tunable coupling strength can be used to set the effective interaction strength to a true zero during one-qubit rotations. The full qubit-qubit coupling Hamiltonian contains two contributions: the intended tunable interaction and the unintended stray interaction owing to the trivial proximity of the two circuits on the chip. As the non-linear coupling can typically be adjusted to give rise to both positive and negative effective couplings, any stray interaction can in principle be identically cancelled with the tunable portion of the interaction [53]. With steady progress of the state-of-the-art fidelities of one- and two-qubit gates (cf. [146]), it will be important for fixed coupling proposals to demonstrate that similar tunability is possible with microwave control.

The Fourier approach is a powerful way to address this problem. Indeed, it can be seen immediately from 5.14 that a weak ($\Omega \ll \Delta$) cross-resonant drive tone with small-excursion phase modulations on time scales slow compared to $2\pi/\omega_{rf}$ but fast relative to the induced effective coupling strength $\omega_{xx}\Omega/\Delta$ will continuously refocus the second order interaction due to the fixed coupling. Performing this in the background during one qubit operations would allow one to microwave tune the interaction to a true zero in the same manner as [53]. A very interesting project would formalize, extend and study the limits to this idea, and optimize the specific protocol for some practical systems.

8.2.3 Architectures for direct multi-qubit gates

Our prediction that weak multi-qubit effective interactions can dominate the dynamics of even mutually detuned multi-qubit systems is suggestive. While most quantum algorithms are decomposed in the standard picture into one- and two- or sometimes one- and three-qubit gates, this decomposition is costly in terms of the number of operations required. One would be better off constructing the called for $2^n \times 2^n$ unitary transformation of n qubits directly, rather than in 4×4 blocks as resulting from two-qubit gates, for example. In terms of the study of entanglement or testing quantum error correcting codes, generating entanglement across n qubits directly would greatly simplify certain procedures.

Three-body effects can arise in superconducting qubit circuits when the qubits are operated in the intermediate regime where neither charge nor phase are good quantum numbers. And a three-body mixing has been exploited for quantum measurements with the Josephson ring modulator. Further, it is known that effective three-body interactions can be strong when polar molecules are trapped in optical lattices, for example [126]. An analysis of potential architectures for realizing the effective multi-qubit interactions in superconducting qubits would shed light on this interesting option. One candidate interaction would be the two-qubit gate scheme employed by Di Carlo in recent cQED measurements at Yale, where a transition outside the computational subspace is used to realize an effective $\sigma_z\sigma_z$ interaction within it, the generalization of which, making use of e.g. the $0 \rightarrow 3$ transition of a transmon qubit, would allow the exciting possibility to realize a *tunable* three-body interaction.

8.2.4 Quantum gates in a dynamically decoupled subspace

An emerging topic of interest is the notion of dynamically decoupled subspaces for quantum computing [119, 11]. By performing a specialized sequence of rotations on individual qubits, they may be dynamically decoupled from interactions with the environment that cause dephasing and relaxation, subject to limitations on the modes present in the environment and the control we can exert over the qubits. An interesting practical project would seek to combine the control required to remain in such a decoupled subspace, and the various trade-offs in the system design, with those required to realize multi-qubit gates with microwave control.

Appendix A

The Quantronium qubit

A.1 Cooper pair box (CPB)

A Cooper pair box (CPB) is a small superconducting island connected to a voltage source V_g through a capacitance C_g and to a superconducting reservoir through a Josephson junction with capacitance C_J and characteristic energy E_J . The circuit has one degree of freedom: the excess number of Cooper pairs of the island, N . Charges may tunnel onto the island through the junction at an energy cost of E_J per Cooper pair.

The Hamiltonian of the CPB contains two parts,

$$\hat{\mathcal{H}} = \hat{\mathcal{H}}_{el} + \hat{\mathcal{H}}_J, \quad (\text{A.1})$$

describing (respectively) the electrostatic energy associated with the charge stored on the sum of all island capacitances C_Σ ; and the energy stored in the non-linear inductance of the Josephson junction. The electrostatic portion \mathcal{H}_{el} is,

$$\hat{\mathcal{H}}_{el} = 4E_C(\hat{N} - N_g)^2,$$

where the energy scale $E_C = \frac{(2e)^2}{2C_\Sigma}$; $N_g = \frac{C_g V_g}{2e}$ is the dimensionless gate charge in units of Cooper pairs, and $\hat{N} = \frac{\hat{Q}_{island}}{2e}$ is the dimensionless operator associated with the charge on the island. The eigenstates of the charge operator are written $|\psi_N\rangle$, where $\hat{N}|\psi_N\rangle = N|\psi_N\rangle$, i.e. states of an integer number of excess Cooper pairs on the island.

The Josephson term describes the tunneling of Cooper pairs through the junction, and thus couples neighboring charge states:

$$\hat{\mathcal{H}}_J = -\frac{E_J}{2} \sum_{N \in Z} (|\psi_N\rangle\langle\psi_{N+1}| + |\psi_{N+1}\rangle\langle\psi_N|). \quad (\text{A.2})$$

In this basis of charge states the CPB is thus described by,

$$\hat{\mathcal{H}} = \sum_{N \in Z} \left\{ 4E_C(N - N_g)^2 |\psi_N\rangle\langle\psi_N| - \frac{E_J}{2} (|\psi_N\rangle\langle\psi_{N+1}| + |\psi_{N+1}\rangle\langle\psi_N|) \right\} \quad (\text{A.3})$$

The energy eigenstates of the CPB can be found numerically by truncating the summation in A.3 to a handful of charge states, with the particular number chosen based upon the aspect ratio E_J/E_C , which determines the charge-state makeup of the energy states.

A.1.1 Phase basis

The energy eigenstates of the system may be found analytically by instead writing A.3 in a basis of eigenstates $|\theta\rangle$ of the operator $\hat{\theta}$ associated with the phase of the superconducting condensate on the island. The phase and charge operators are canonical conjugate variables in the sense,

$$\hat{N} = -i \frac{\partial}{\partial \theta}, \quad (\text{A.4})$$

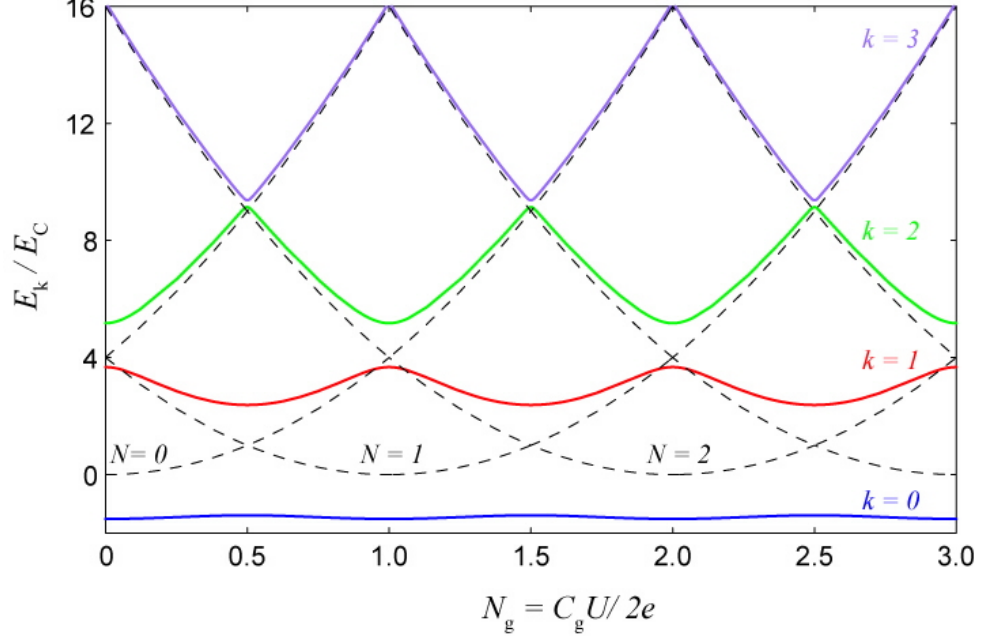


Figure A.1: Energy levels of the Cooper pair box.

and

$$\hat{\theta} = i \frac{\partial}{\partial N}. \quad (\text{A.5})$$

While the spectrum of eigenvalues of \hat{N} is discrete, the eigenvalues of $\hat{\theta}$ are circular, i.e. defined only mod[2π]. The operator $\exp[\pm i\hat{\theta}]$ acts to shift the charge by one Cooper pair,

$$\exp[\pm i\hat{\theta}]|\psi_N\rangle = |\psi_{N\pm 1}\rangle. \quad (\text{A.6})$$

while the operator $\exp[\pm i\tau\hat{N}]$ correspondingly shifts the phase by τ ,

$$\exp[\pm i\tau\hat{N}]|\psi_\theta\rangle = |\psi_{\theta\pm\tau}\rangle. \quad (\text{A.7})$$

In the phase basis the CPB Hamiltonian is,

$$\hat{\mathcal{H}} = -4E_C(i\frac{\partial}{\partial\theta} + N_g)^2|\psi_\theta\rangle\langle\psi_\theta| - \frac{E_J}{2} \left(e^{-i\hat{\theta}} + e^{i\hat{\theta}} \right) |\psi_\theta\rangle\langle\psi_\theta|. \quad (\text{A.8})$$

The time-independent Schrödinger equation becomes,

$$-4E_C(i\frac{\partial}{\partial\theta} + N_g)^2|\psi_k\rangle - E_J \cos \hat{\theta}|\psi_k\rangle = E_k|\psi_k\rangle. \quad (\text{A.9})$$

This equation can be solved analytically in terms of Mathieu functions, see [129] for a detailed derivation.

A.2 Split Cooper pair box (sCPB)

A closely related device splits the Josephson junction into two junctions in parallel to create a loop through which flux may be passed in order to tune the effective Josephson energy. If the two junctions have characteristic energies $E_{J1} = E_J(1+d)/2$ and $E_{J2} = E_J(1-d)/2$ and we make the identifications,

$$\theta_+ \rightarrow (\theta_1 + \theta_2)/2,$$

and

$$\hat{\theta}_- \rightarrow (\hat{\theta}_1 - \hat{\theta}_2)/2,$$

where $\hat{\theta}_i$ is the phase across junction i , the sCPB is described by

$$\begin{aligned} \hat{\mathcal{H}} = & \sum_{N \in Z} (4E_C(N - N_g)^2 |\psi_N\rangle\langle\psi_N| \\ & - \frac{E_J}{2}(\cos\theta_+ - id\sin\theta_+) |\psi_N\rangle\langle\psi_{N+1}| - \frac{E_J}{2}(\cos\theta_+ + id\sin\theta_+) |\psi_{N+1}\rangle\langle\psi_N|) \end{aligned}$$

where we take the total phase across the junctions θ_+ to be a classical parameter and the difference of the phases θ_- to retain its quantum character [129]. For the sCPB with no asymmetry, i.e. $d = 0$, the Hamiltonian reduces to that of the original

simpler device with an externally tunable Josephson energy,

$$\mathcal{E}_J = E_J \cos \theta_+,$$

as the total phase drop across the two junctions may be tuned with the application of a magnetic flux through the loop of the sCPB.

A.3 Energy Surfaces of the sCPB

The Mathieu functions used to solve the CPB case can be directly adapted to the sCPB with the identifications

$$\tan[\gamma(d, \theta_+)] = -d \tan \theta_+$$

and

$$\mathcal{E}_J(d, \theta_+) = E_J \sqrt{\frac{1 + d^2 - (d^2 - 1) \cos(2\theta_+)}{2}}$$

with which we obtain the sCPB time-independent Schrödinger equation in the phase representation,

$$-4E_C(i \frac{\partial}{\partial \hat{\theta}_-} + N_g)^2 |\psi_k\rangle - \mathcal{E}_J \cos(\hat{\theta}_- + \gamma) |\psi_k\rangle = E_k |\psi_k\rangle. \quad (\text{A.11})$$

The energy surfaces for the three lowest lying states are shown below for $E_J/E_C = 1$.

$\omega_{01} = E_1 - E_0$ is at a saddle point and thus first order insensitive to noise in both θ_+ and N_g .

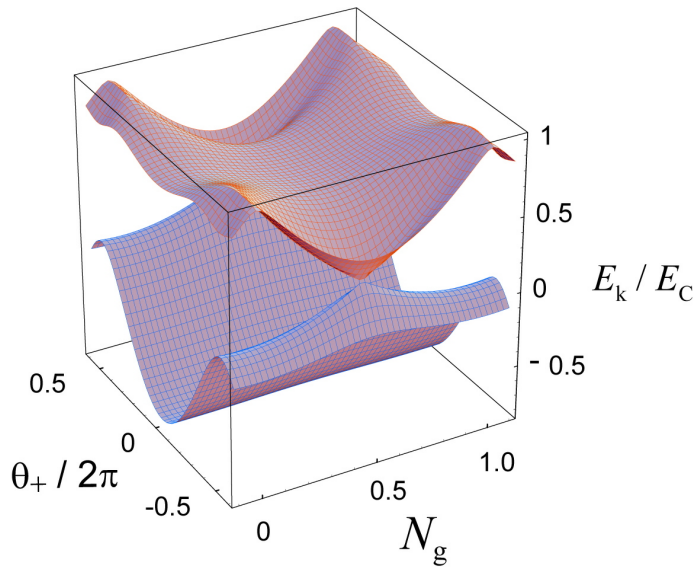


Figure A.2: Energy surfaces $E_k(\theta_+, N_g)$ for two lowest-lying states $k = 0, 1$ of the split Cooper pair box. When the circuit is biased at 1 electron ($N_g = 0.5$) and zero loop flux ($\theta_+ = 0$) the transition energy $\hbar\omega_{01} = E_1 - E_0$ is at a saddle point and thus first order insensitive to noise in both θ_+ and N_g .

Appendix B

Mathematica code

B.1 The n-qubit Pauli matrices

In Mathematica 5.2, the two-qubit Pauli matrices can be generated and numbered automatically with the function g2,

```
g2[a_, b_] := BlockMatrix[Outer[Times, a, b]]
```

called in the following manner

```
Table[ $\Sigma_n$  = Apply[g2, Take[Tuples[{w, x, y, z}, 2], {n+1, n+1}]], {n, 0, 15}].
```

The matrices are explicitly displayed with

```
Table[sn//MatrixForm], {n, 0, 15}].
```

The protocol can be extended to any number of qubits with a recursive definition

of g. For example, the three-qubit Pauli matrices are equivalently generated and numbered with the function g3,

```
g3[a_, b_, c_] := BlockMatrix[Outer[Times, BlockMatrix[Outer[Times, a, b]], c]]
```

called by

```
Table[ $\Sigma_n = \text{Apply}[g3, \text{Take}[\text{Tuples}[\{w, x, y, z\}, 3], \{n+1, n+1\}]], \{n, 0, 63\}]$ .
```

B.2 The n-qubit super-operator

The super-operator governing the system dynamics can be generated as follows. First, use the above code to define the Σ_n 's as the n-qubit Pauli matrices. Then following the results of Chapter 2, the super-operator can be written,

$$M_{kji} = \frac{-i}{2^{N+1}} \text{Tr}([\Sigma_k, \Sigma_j] \Sigma_i),$$

while the dissipative portion of the Master equation requires that we evaluate

$$K_{kji} = \frac{-1}{2^{N+1}} \text{Tr}([\Sigma_k, \Sigma_j \Sigma_k] \Sigma_i).$$

Each of these has been defined to contain only 0's and ± 1 's. They can be explicitly evaluated in a straightforward manner with :

$$M[a_, b_, c_] := \frac{-i}{16} \text{Tr}[\Sigma_a \cdot \Sigma_b \cdot \Sigma_c - \Sigma_b \cdot \Sigma_a \cdot \Sigma_c]$$

and

$$K[a_, b_, c_] := \frac{-1}{16} \text{Tr}[\Sigma_a.\Sigma_b.\Sigma_a.\Sigma_c - \Sigma_b.\Sigma_a.\Sigma_a.\Sigma_c]$$

called according to

$$\text{Table}[M[a, b, c], \{a, 1, 4^n-1\}, \{b, 1, 4^n-1\}, \{c, 1, 4^n-1\}]$$

and similar for K.

The n-qubit Master equation in Bloch form is then produced by evaluating

$$r_i == \sum_{k=1}^{4^n-1} \sum_{l=1}^{4^n-1} \sum_{j=1}^{4^n-1} r_l \{ h_k M[k, l, i] - 16 a_j K[j, l, i] \}.$$

Appendix C

A wideband IQ modulator for microwave pulse generation

In building up our experimental apparatus to test the microwave controlled coupling schemes developed in chapter 3, we realized the need for affordable and high-performance microwave pulse generation equipment. Many of the devices used by physicists doing measurements in the microwave domain are based upon or adapted from core technologies developed for applications to commercial or military communications systems. As is often the case, we found that the commercially available devices did quite meet our needs, so we had to tinker a little bit. In the end, we designed and built a wideband I/Q modulator using a combination of off-the-shelf and standard order products from a handful of companies.

Microwave qubit measurements require pulses of various shapes, durations and duty cycles. A typical single qubit experiment will require at least two pulse channels, one for the READ pulses and one for the WRITE pulses; multiqubit experiments will in most cases require at least two channels per qubit. In our case, we were interested in pulses lasting from a few ns to a few μ s and having any shape we might wish

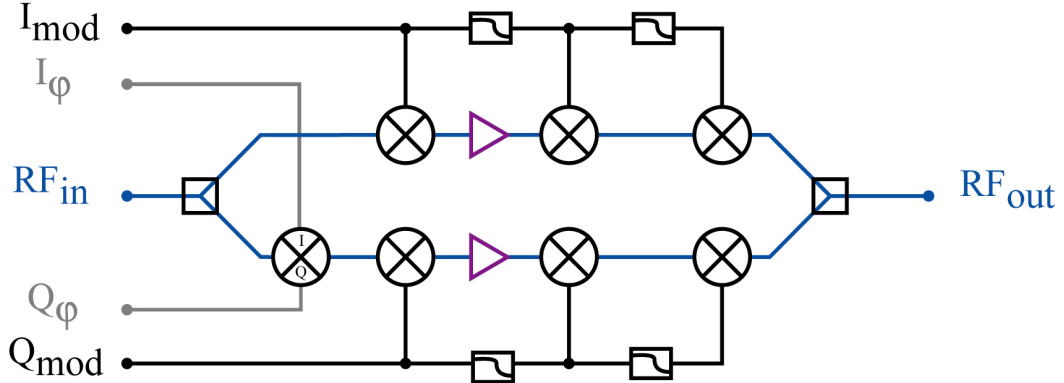


Figure C.1: Schematic black box modulator.

to create. We decided to work with CPS resonators at around 10GHz, and qubit frequencies lying either above or below the readout, so in order to be of general use for the series of measurements, and perhaps others, we wanted a pulse creation system with carrier bandwidth from 6-18GHz. and in the frequency range of 6-18GHz. Since direct digital synthesis of signals in the 5-20GHz range is not yet available [104], it is necessary to use analog electronics. There are several viable and common approaches. The standard technique is to use a continuous wave (cw) signal generator to produce a high level carrier signal, then to carve from this cw signal the desired pulse train by sending it through a modulator. The modulating signals and hardware may be either analog or digital. This general strategy is depicted in above. The experimentalist must find a way of implementing such a pulse creation system that meets the requirements and constraints of the particular experimental system, and hopefully in an flexible and affordable manner.

There are several well-known techniques in this regard, and there are several others which we explored in the course of our due diligence on this project, all of which I will outline here before moving to our final strategy, specific design considerations, the instrument assembly and finally test data.

For low-frequency applications any desired signal may be created by coupling random access memory loaded with waveform data to a microprocessor and a digital-to-analog converter (ADC). This is the *arbitrary waveform generator*, or AWG, found in some incarnation or another in most any physics lab. These instruments are purely digital, and this severely limits the available output frequencies. This is typically stated in terms of a sampling rate. A 1GS/s AWG may produce a signal with components up to 500MHz.

A single channel of our IQ modulator is shown schematically above. The unit is designed to be operated as a black box modulator. A microwave signal at the desired carrier frequency and pulse shaping signals centered at DC are supplied as inputs, and microwave pulses that are, ideally, a product of the inputs, emerge as output. Our design effectively implements a nuts-and-bolts version of the idealized IQ mixer. We achieve a modulation depth (or on/off ratio) of approximate 60dB over the full carrier range of 5-18GHz by cascading three mixing stages with different diode power levels and one amplification stage in each of the I and Q arms. Phase balance between the I and Q arms is achieved through a common IQ mixer inserted into the Q channel and controlled with DC voltages. The phase balance may be calibrated once and for all at each frequency and stored in an automated lookup table. The I and Q modulation channels have 4GHz bandwidth, allowing extremely fast pulse rise and fall times.

Our lab-built instrument's performance is similar to that of the only known commercially available device that meets this need: the 'wideband external I/Q inputs' option 016 on the Agilent E8267D-series vector signal generator. There, an on/off ratio of 80dB is achieved from 3.2-20GHz, with nodulation bandwidth of 2GHz. This is available only as a \$16.9k option on a typically \$60k instrument. Our device may be constructed for \$5k.

Bibliography

- [1] R. P. Feynman, "Simulating physics with computers," *Int. J. Theor. Phys.* 21, 467 (1982).
- [2] Seth Lloyd, "A Potentially Realizable Quantum Computer," *Science* 17 Vol. 261. no. 5128 (1993).
- [3] P. W. Shor, *Proceedings, 35th Annual Symposium on Foundations of Computer Science*, IEEE Press, Los Alamitos, CA (1994).
- [4] L. K. Grover, "A fast quantum mechanical algorithm for database search," *Proceedings, 28th ACM Symposium on Theory of Computation*, 212 (1996).
- [5] P. Shor, *Phys. Rev. A*, **52** 2493 (1995).
- [6] A. M. Steane, *Phys. Rev. Lett.*, **77** 793 (1996).
- [7] M. A. Nielsen and I. L. Chuang, *Quantum Computation and Quantum Information*, Cambridge, (2000).
- [8] Chetan Nayak, Steven H. Simon, Ady Stern, Michael Freedman, Sankar Das Sarma, "Non-Abelian anyons and topological quantum computation," *Reviews of Modern Physics*, 80 2008.

- [9] P. Zanardi and M. Rasetti, "Noiseless Quantum Codes," Phys. Rev. Lett. 79, 3306 (1997).
- [10] L. Viola and S. Lloyd, "Dynamical suppression of decoherence in two-state quantum systems," Phys. Rev. A 58, 2733 (1998).
- [11] P. Rebentrost, I. Serban, T. Schulte-Herbrüggen, and F. K. Wilhelm, "Optimal Control of a Qubit Coupled to a Non-Markovian Environment," Phys. Rev. Lett. 102, 090401 (2009).
- [12] A. Barenco, C. H. Bennett, R. Cleve, D. P. DiVincenzo, N. Margolus, P. Shor, T. Sleator, J. Smolin, and H. Weinfurter, Phys. Rev. A 52, 3457 (1995).
- [13] J. Preskill, *Notes on Quantum Computation*, <http://www.theory.caltech.edu/people/preskill/ph229J>. Preskill, (lecture notes for Physics 219/Computer Science 219 at Caltech).
- [14] A. Abragam, *Principles of Nuclear Magnetism*, Oxford, 1961.
- [15] C. P. Slichter, *Principles of Magnetic Resonance*, Springer, 1990.
- [16] L. M .K. Vandersypen and I. L. Chuang, Rev. Mod. Phys. **76**, 1037 (2004).
- [17] Daniel Loss and David P. DiVincenzo. "Quantum computation with quantum dots." Physical Review A, 57(1):120-126, Jan 1998.
- [18] C. Monroe, D. M. Meekhof, B. E. King, W. M. Itano, and D. J. Wineland. "Demonstration of a fundamental quantum logic gate." Physical Review Letters, 75(25):4714-4717, December 1995.
- [19] D. Kielpinski, C. Monroe and D. J. Wineland, "Architecture for a large-scale ion-trap quantum computer," Nature 417, 709-711 (13 June 2002).

- [20] I. H. Deutsch, G. K. Brennen, and P. S. Jessen. "Quantum computing with neutral atoms in an optical lattice." *Fortschritte Der Physik-Progress of Physics*, 48(9-11):925-943, 2000.
- [21] M. H. Devoret, *Quantum Fluctuations in Electrical Circuits*, Les Houches Session LXIII, Elsevier Science, (1997).
- [22] J. Koch, T. M. Yu, J. Gambetta, A. A. Houck, D. I. Schuster, J. Majer, A. Blais, M. H. Devoret, S. M. Girvin, and R. J. Schoelkopf, "Charge-insensitive qubit design derived from the Cooper pair box," *Phys. Rev. A* 76, 042319 (2007).
- [23] A. O. Niskanen, J. J. Vartiainen, and M. M. Salomaa, "Optimal Multiqubit Operations for Josephson Charge Qubits," *Phys. Rev. Lett.* 90, 197901 (2003).
- [24] Y. Nakamura, Yu. A. Pashkin, and J. S. Tsai, *Nature*, **398** (1999);
- [25] J. E. Mooij, T. P. Orlando, L. Levitov, Lin Tian, C. H. van der Wal, and S. Lloyd, *Science*, **285** (1999).
- [26] D. Vion, A. Aassime, A. Cottet, P. Joyez, H. Pothier, C. Urbina, D. Esteve and M.H. Devoret, *Science*, **296** (2002).
- [27] J. M. Martinis, S. Nam, J. Aumentado, and C. Urbina, *Phys. Rev. Lett.* **89**, 117901 (2002);
- [28] I. Chiorescu, Y. Nakamura, C. J. P. M. Harmans, and J. E. Mooij, *Science* **299** (2003);
- [29] V. Bouchiat, D. Vion, P. Joyez, D. Esteve, M. H. Devoret, *Physica Scripta T* 76, 165 (1998).

- [30] M.H. Devoret and J. M. Martinis, "Implementing Qubits with Superconducting Integrated Circuits," *Quant. Inf. Proc.* **3**, 163 (2004).
- [31] J. Clarke and F. K. Wilhelm, *Nature (London)* 453, 1031 (2008).
- [32] Yury Makhlin, Gerd Schön, and Alexander Shnirman, "Quantum-state engineering with Josephson-junction devices." *Rev. Mod. Phys.* 73, 357 (2001).
- [33] P. A. M. Dirac, *The Principles of Quantum Mechanics* (Oxford University Press, New York, 1958).
- [34] A. Einstein, B. Podolsky, N. Rosen, "Can quantum-mechanical description of physical reality be considered complete?" *Physical Review* 41, 777 (15 May 1935).
- [35] L. M. K. Vandersypen, M. Steffen, G. Breyta, C. S. Yannoni, M. H. Sherwood, and I. L. Chuang, "Experimental realization of Shor's quantum factoring algorithm using nuclear magnetic resonance." *Nature*, **414** 883–887 (20/27 December 2001) 883 (2001).
- [36] Matthias Steffen, M. Ansmann, Radoslaw C. Bialczak, N. Katz, Erik Lucero, R. McDermott, Matthew Neeley, E. M. Weig, A. N. Cleland, and John M. Martinis, "Measurement of the Entanglement of Two Superconducting Qubits via State Tomography," *Science* 313, Issue 5792, 1423-1425 (2006)
- [37] G. Lindblad, *Commun. Math. Phys.* 48, 119 (1976).
- [38] D Leibfried, R Blatt, C Monroe, D Wineland, "Quantum dynamics of single trapped ions." *Review of Modern Physics*, volume 75, 281 (2003).

- [39] C. F. Roos, M. Riebe, H. Häffner, W. Hänsel, J. Benhelm, G. P. T. Lancaster, C. Becher, F. Schmidt-Kaler, R. Blatt."Control and measurement of three-qubit entangled state." *Science* 304, 1478 (2004)
- [40] A. Shnirman, G. Schön, and Z. Hermon, "Quantum Manipulations of Small Josephson Junctions." *Phys. Rev. Lett.* 79, 2371 (1997).
- [41] D. V. Averin and C. Bruder, "Variable Electrostatic Transformer: Controllable Coupling of Two Charge Qubits." *Phys. Rev. Lett.* 91, 057003 (2003).
- [42] P. Bertet et al., *Phys. Rev. Lett.* 95, 257002 (2005).
- [43] Antti O. Niskanen, Yasunobu Nakamura, and Jaw-Shen Tsai, "Tunable coupling scheme for flux qubits at the optimal point." *Phys. Rev. B* 73, 094506 (2006).
- [44] T. Duty, D. Gunnarsson, K. Bladh, and P. Delsing, *Phys. Rev. B* **69**, 140503(R) (2004);
- [45] A. Guillaume *et al.*, *Phys. Rev. B* **69**, 132504 (2004);
- [46] Wallraff, A. et al. "Strong coupling of a single photon to a superconducting qubit using circuit quantum electrodynamics." *Nature* 431, 162–167 (2004).
- [47] *Quantum Computing and Quantum Bits in Mesoscopic Systems*, A.J. Leggett, B. Ruggiero, and P.Silvestrini, eds. (Kluwer Academic/Plenum, 2004).
- [48] Lorenza Viola, "Advances in decoherence control," *Journal of Modern Optics*, 10 Nov -15 Dec 2004, Vol. 51 16-18, 2357-2367.
- [49] J. B. Majer *et al.*, cond-mat/0308192;
- [50] A. J. Berkley, *et al.*, *Science*, **300** (2003).

- [51] Yu. A. Pashkin, T. Yamamoto, O. Astafiev, Y. Nakamura, D. V. Averin, J. S. Tsai, *Nature* **421** (2003).
- [52] T. Yamamoto, Yu. A. Pashkin, O. Astafiev, Y. Nakamura, J. S. Tsai, *Nature* **425** (2003).
- [53] B. L. T. Plourde *et al.*, *Phys. Rev. B* **70**, 140501 (2004).
- [54] M. Baur, S. Filipp, R. Bianchetti, J.M. Fink, M. Goppl, L. Steffen, P.J. Leek, A. Blais, and A. Wallraff, "Measurement of Autler-Townes and Mollow transitions in a strongly driven superconducting qubit," arXiv:0812.4384v1 [cond-mat.mes-hall].
- [55] S. Hartmann and E. Hahn, *Phys. Rev.* **128**, 2042 (1962).
- [56] Seth Lloyd, "Almost Any Quantum Logic Gate is Universal," *Phys. Rev. Lett.* **75**, 346 - 349 (1995).
- [57] Navin Khaneja, Roger Brockett, and Steffen J. Glaser, "Time optimal control in spin systems," *Phys. Rev. A* **63**, 032308 (2001).
- [58] C. H. Bennett, J. I. Cirac, M. S. Leifer, D. W. Leung, N. Linden, S. Popescu, and G. Vidal, "Optimal simulation of two-qubit Hamiltonians using general local operations," *Phys. Rev. A* **66**, 012305 (2002).
- [59] C. H. Bennett, A. W. Harrow, D. W. Leung, J. A. Smolin, "On the capacities of bipartite Hamiltonians and unitary gates," *IEEE Trans. Inf. Theory*, Vol. 49, No. 8, (2003) p.1895-1911. arXiv:quant-ph/0205057v4
- [60] G. Vidal, K. Hammerer, and J. I. Cirac, "Interaction Cost of Nonlocal Gates," *Phys. Rev. Lett.* **88**, 237902 (2002).

- [61] Jennifer L. Dodd, Michael A. Nielsen, Michael J. Bremner, and Robert T. Thew, "Universal quantum computation and simulation using any entangling Hamiltonian and local unitaries," Phys. Rev. A 65, 040301 (2002).
- [62] Lorenza Viola and Emanuel Knill, "Robust Dynamical Decoupling of Quantum Systems with Bounded Controls," Phys. Rev. Lett. 90, 037901 (2003).
- [63] R. Vijayaraghavan, personal communication.
- [64] F. Motzoi, J. M. Gambetta, P. Rebentrost, F. K. Wilhelm, "Simple pulses for elimination of leakage in weakly nonlinear qubits," arXiv:0901.0534v2.
- [65] P. Rebentrost and F.K. Wilhelm, "Optimal control of a leaking qubit," Phys. Rev. B 79, 060507(R) (2009) arXiv:0808.2680
- [66] J. A. Jones in *Quantum Entanglement and Quantum Information*, Les Houches Session LXXIX, Elsevier Science (2004).
- [67] D. Leung, Ph.D. Thesis, Stanford University, ArXiv e-print cs.CC/0012017.
- [68] J. I. Cirac and P. Zoller, Phys. Rev. Lett. **74**, 4091 (1995).
- [69] F. Bloch and A. Siegert, Phys. Rev. **57**, 522, 1940.
- [70] Andrew T. Sornborger, Andrew N. Cleland, and Michael R. Geller, "Superconducting phase qubit coupled to a nanomechanical resonator: Beyond the rotating-wave approximation," Phys. Rev. A 70, 052315 (2004).
- [71] E. Collin, *et al.*, Phys. Rev. Lett. 93, 157005 (2004)
- [72] D. M. Greenberger, M. Horne, and A. Zeilinger, in *Bell's Theorem, Quantum Theory, and Conceptions of the Universe*, M. Kafatos, ed. (Kluwer Academic, 1989).

- [73] Y. Nakamura, Yu. A. Pashkin, and J. S. Tsai, *Nature*, **398** (1999).
- [74] J. M. Martinis, S. Nam, J. Aumentado, and C. Urbina, *Phys. Rev. Lett.* **89**, 117901 (2002).
- [75] D. Vion, A. Aassime, A. Cottet, P. Joyez, H. Pothier, C. Urbina, D. Esteve and M.H. Devoret, arXiv e-print cond-mat/0209315.
- [76] I. I. Rabi, *Phys. Rev.* **51**, 652 (1937).
- [77] N. F. Ramsey, *Phys. Rev.* **78**, 695 (1950).
- [78] A. Blais, A. M. van den Brink, A. M. Zagoskin, *Phys.Rev. Lett.* **90**, 127901 (2003).
- [79] J. B. Majer, F. G. Paauw, A. C. J. ter Haar, C. J. P. M. Harmans, and J.E. Mooij, arXiv e-print cond-mat/0308192.
- [80] A. J. Berkley, H. Xu, R. C. Ramos, M. A. Gubrud, F. W. Strauch, P. R. Johnson, J. R. Anderson, A. J. Dragt, C. J. Lobb, F. C. Wellstood, *Science*, **300** (2003).
- [81] C. Cohen-Tannoudji, J. Dupont-Roc, and G. Grynberg, *Atom-Photon Interactions*, Wiley (1992).
- [82] D. Leung, Ph.D. Thesis, Stanford University, ArXiv e-print cs.CC/0012017.
- [83] I. L. Chuang, L. M. K. Vandersypen, X. Zhou, D. W. Leung, and S. Lloyd, *Nature*, **393** 143 (1998).
- [84] T. F. Jones and M. Mosca, *J. Chem. Phys.* **109**:1649-1653 (1998).
- [85] W. K.Wootters, Phys. Rev. Lett. 80, 2245 (1998),quantph/9709029.

- [86] D. Gottesman, arXiv e-print quant-ph/9807006.
- [87] A. Blais, J. Gambetta, A. Wallraff, D. I. Schuster, S. M. Girvin, M. H. Devoret, and R. J. Schoelkopf, "Quantum-information processing with circuit quantum electrodynamics," Phys. Rev. A 75, 032329 (2007).
- [88] C. Rigetti, R. Mosseri, and M. Devoret, Quant. Inf. Proc. **3**, 351 (2004).
- [89] D. Gottesman, Phys. Rev. A, **54** 1862 (1996).
- [90] P. Shor, Phys. Rev. A, **52** 2493 (1995).
- [91] H. K. Cummins, G. Llewellyn, and J. A. Jones, Phys. Rev. A **67** 042308 (2003), and references therein.
- [92] Mark Byrd and Daniel Lidar, "Bang–Bang Operations from a Geometric Perspective," Quantum Information Processing, Vol. 1, Nos. 1/2, April 2002.
- [93] A. C. Doherty, et. al., Phys. Rev. A **62**, 012105 (2000)
- [94] C. Ahn, A. C. Doherty and A. J. Landahl, Phys. Rev. A **65**, 042301 (2002).
- [95] D. Gottesman, personal communication.
- [96] D. Gottesman, *Stabilizer Codes and Quantum Error Correction*. Ph.D. thesis, California Institute of Technology, Pasadena, CA, 1997. arXiv e-print quant-ph/9705052.
- [97] M. A. Sillanpää, J. I. Park, and R. W. Simmonds, *Nature* **449** (2007).
- [98] Introduction to Superconductivity, 2nd Ed. , McGraw-Hill, NY, 1996.
- [99] P. J. Hore, J. A. Jones, S. Wimperis, *NMR: The Toolkit*, Oxford (2000).
- [100] somehting on the validity of the RWA

- [101] S. Ashhab et al., Phys. Rev. B 74, 184504 (2006).
- [102] Wilson PRL, Longitudinal dressed states
- [103] Bessel funciton dependence of Rabi freq on drive amplitude, italian guy.
- [104] something on the frequencies available for AWGs unsing direct digital synthesis.
- [105] C. Rigetti, A. Blais and M. Devoret, Phys. Rev. Lett. 94, 240502 (2005).
- [106] S. Ashhab and F. Nori, Phys. Rev. B 76, 132513 (2007).
- [107] T. F. Havel and C. J. F. Doran, arXiv preprint quant-ph/0403136.
- [108] Definition of concurrence for pure states
- [109] Bell, J. S., 1964, "On the Einstein-Podolsky-Rosen Paradox," Physics 1, 195-200.
- [110] Cauchy Shwartz Hornberg or something Bell type ineq
- [111] David Mermin Bell ineq
- [112] J. H. Plantenberg, P. C. de Groot, C. J. P. M. Harmans & J. E. Mooij, "Demonstration of controlled-NOT quantum gates on a pair of superconducting quantum bits." Nature 447 14 June 2007.
- [113] Niskanen et al, Science 4 May 2007 Vol. 316. no. 5825, pp. 723 - 726
- [114] H. Jirari and W. Pötz, Phys. Rev. A 74, 022306 (2006).
- [115] M. Wenin and W. Pötz, Phys. Rev. 74, 022319 2006.
- [116] Chad Rigetti and Michel Devoret, "Minimal tunable gates for superconducting qubits," in preparation.

- [117] Chad Rigetti and Michel Devoret, "Exploiting weak three-body effects to produce tripartite entanglement," in preparation.
- [118] N. D. Mermin, Physical review Letters, 65 1838 (1990)
- [119] PRL 98, 100504 (2007)
- [120] PRL 101, 180403 (2008).
- [121] B. R. Mollow, Phys. Rev. A 5 2217 (1972).
- [122] S. Girvin, personal communication.
- [123] L. Frunzio, A. Wallraff , D. Schuster, J. Majer, and R. Schoelkopf, "Fabrication and characterization of superconducting circuit QED devices for quantum computation," IEEE Transactions on Applied Superconductivity 15(2), 860-863 (Jun 2005).
- [124] Kavita Goverdhanam, Rainee N. Simons, and Linda P. B. Katehi, IEEE TRANSACTIONS ON MICROWAVE THEORY AND TECHNIQUES, VOL. 45, NO. 10, OCTOBER 1997.
- [125] Knorr and Kuchler, IEEE Transactions on Microwave Theory and Techniques, Vol. MIrr-23, NO. 7, July 1975
- [126] H. P. Büchler, A. Micheli and P. Zoller, "Three-body interactions with cold polar molecules," Nature Physics 3, 726 (2007)
- [127] <http://www.krytar.com/pdf/4060200.pdf>
- [128] Prabhakar Pradhan, George C. Cardoso, Jacob Morzinski, M. S. Shahriar, "Effects of the Bloch-Siegert Oscillation on the Precision of Qubit Rota-

- tions: Direct Two-Level vs. Off-Resonant Raman Excitation." arXiv:quant-ph/0402122v2 (2004).
- [129] Audrey Cottet, "Implementation of a quantum bit in a superconducting circuit," Ph.D. Thesis, l'Universite Paris VI, 2002.
- [130] David I. Schuster, "Circuit quantum electrodynamics," Ph.D. Thesis, Yale University, 2007.
- [131] Rajamani Vijayaraghavan, "Josephson Bifurcation Amplifier: amplifying quantum signals using a dynamical bifurcation," Ph.D. Thesis, Yale University, 2008.
- [132] Michael B. Metcalfe, "A new microwave resonator readout scheme for superconducting qubits," Ph.D. Thesis, Yale University, 2008.
- [133] Julie H. Love, "Resolved dynamics of single electron tunneling using the RF-SET," Ph.D. Thesis, Yale University, 2007.
- [134] Florian Mintert, "Measures and dynamics of entangled states," Dissertation der Fakultat fur Physik der Ludwig-Maximilians-Universitat Munchen, 2004.
- [135] Lieven k. Vandersypen, "Experimental Quantum Computation with Nuclear Spins in Liquid Solution," Ph.D. Thesis, Stanford University, 2001.
arXiv:quant-ph/0205193
- [136] The underpinning of each of these tools is the Heisenberg picture of quantum computers. As a whole, they define an approach which is extremely helpful in understanding the subtleties of quantum systems and the sources of their strange properties. In many ways, the standard paradigm for quantum computing drawn up by analogy with classical computing fails to capture the essential

subtleties faced by those concerned with actually building the machines. At the very least, those working towards practical devices would be well-served by complementing the standard paradigm with fluency in the Heisenberg representation of quantum computing and comfort in translating between the two.

- [137] B. D. Josephson, "Coupled Superconductors," Rev. Mod. Phys. 36(1P1), 216 (1964).
- [138] M. I. Dykman and M. A. Krivoglaz, "Fluctuations in Non-Linear Systems Near Bifurcations Corresponding to the Appearance of New Stable States," Physica A 104(3), 480–494 (1980).
- [139] I. Siddiqi, R. Vijay, F. Pierre, C. M. Wilson, L. Frunzio, M. Metcalfe, C. Rigetti, R. J. Schoelkopf, M. H. Devoret, D. Vion, and D. Esteve, "Direct observation of dynamical bifurcation between two driven oscillation states of a Josephson junction," Phys. Rev. Lett. 94(2), 027005 (2005).
- [140] I. Siddiqi, R. Vijay, M. Metcalfe, E. Boaknin, L. Frunzio, R. J. Schoelkopf, and M. H. Devoret, "Dispersive measurements of superconducting qubit coherence with a fast latching readout," Phys. Rev. B 73(5), 054510 (2006).
- [141] Yu. A. Pashkin et al., Nature 421, 823 (2003).
- [142] Juha J. Virtainen, Antti O. Niskanen, Mikio Nakahara, Martti M. Salomaa, "Acceleration of quantum algorithms using three-qubit gates," arXiv:quant-ph/0310165v2 2003.
- [143] N. Bergeal, R. Vijay, V. E. Manucharyan, I. Siddiqi, R. J. Schoelkopf, S. M. Girvin, M. H. Devoret, "Analog information processing at the quantum limit with a Josephson ring modulator," arXiv:0805.3452v1 [cond-mat.mes-hall] (2008).

- [144] L. DiCarlo, J. M. Chow, J. M. Gambetta, Lev S. Bishop, D. I. Schuster, J. Majer, A. Blais, L. Frunzio, S. M. Girvin, R. J. Schoelkopf, "Demonstration of Two-Qubit Algorithms with a Superconducting Quantum Processor," arXiv:0903.2030v1.
- [145] M. Metcalfe, E. Boaknin, V. E. Manucharyan, R. Vijay, I. Siddiqi, C. Rigetti, L. Frunzio, R. J. Schoelkopf, and M. H. Devoret, "Measuring the decoherence of a quantronium qubit with the cavity bifurcation amplifier," Physical Review B 76, 174516 (2007).
- [146] J. M. Chow, J. M. Gambetta, L. Tornberg, Jens Koch, Lev S. Bishop, A. A. Houck, B. R. Johnson, L. Frunzio, S. M. Girvin, and R. J. Schoelkopf, "Randomized Benchmarking and Process Tomography for Gate Errors in a Solid-State Qubit," Phys. Rev. Lett. 102, 090502 (2009).